Doctoral Thesis

博 士 論 文

The basic characteristics of summer sea breeze events in Sendai, Japan and their effects on outdoor thermal comfort

仙台夏期海風の基本特性と屋外温熱快適性に及ぼす影響に関する研究

March 2023

Tohoku Institute of Technology, Graduate school of Engineering, Department of Architecture

Shiyi Peng

2023 年 3 月

東北工業大学大学院 工学研究科 建築学専攻

彭 詩怡

CONTENTS

Chapter 1. Introduction 1

1.1. Research background.. 1

1.2. Research purposes 3

1.3. Research scopes 3

1.4. Structure of the thesis 5

1.5. Framework of this research 9

1.6. Creativity and innovation 10

Chapter 2. Presentation of the research tools and materials used in this thesis 11

2.1. Introduction 11

2.2. Meteorological data are obtained by observation method.................................. 12

2.2.1. Concept... 12

2.2.2. Arrangement of measurement points... 12

2.2.3. Measurement points description for METADATA.............................. 13

2.2.4. Description of measurement points for metadata in this study 14

2.3. Use WRF model to obtain meteorological data.. 19

2.3.1. Concepts 19

2.3.2. The WRF Modeling System Program Components WRF 20

2.3.3. Basics for Running the Model.. 21

2.3.4. WRF model and experimental design of this study.............................. 23

2.4. Visualize and analyze data with GIS software 25

2.4.1. Concepts 25

2.4.2. GIS-Software... 27

2.4.3. The data visualized and analyzed in this study using GIS software..... 29

2.5. Evaluation of outdoor thermal comfort using Rayman software 30

2.5.1. Concepts 30

2.5.2. Influencing factors of outdoor thermal comfort 31

2.5.3. Outdoor thermal comfort evaluation 36

2.5.4. PET theoretical basis and calculation 39

Chapter 3. Reproducibility analysis of WRF model in urban climate research 44

3.1. Introduction 44

3.2. data 45

3.2.1. Measurement data 45

3.2.2. Simulation data 47

3.3. Reproducibility analysis of WRF model data 48

3.3.1. Analysis of Bias, RMSE and Correlation 48

3.3.2. Error dynamics analysis 50

3.4. Conclusions 54

Chapter 4. Analysis and Mapping of Sea Breeze Event Time in Coastal Cities 56

4.1. Introduction 56

4.2. Basic Characteristics of Summer Sea Breeze Activity in Sendai 56

4.2.1. Representative Validation of the Study Period 56

4.2.2. Define the Research Month 57

4.2.3. August Sea Breeze Daily Temperature Characteristics 59

4.2.4. Temporal Characteristics of Sendai Sea Breeze Event 59

4.3. Identification of Sea Breeze Day 61

4.3.1. Data used to identify sea breezes 61

4.3.2. Specific methods for identifying sea breeze days 62

4.3.3. Case Study Day 62

4.4. Mapping the Time of Summer Sea Breeze Event in Sendai City 63

4.4.1. Sea Breeze Arrival Time 63

4.4.2. Sea Breeze Retreat Time 65

4.4.3. Duration of Sea Breeze 68

4.5. Conclusions 70

Chapter 5. Sea breeze cooling capacity in a coastal city 72

5.1. Introduction 72

5.2. Identification of west breeze day... 72

5.2.1. Identification of the West Breeze Day 72

5.2.2. Case Study Day 73

5.3. Calculation of Sea breeze cooling capacity 74

5.4. Results and Discussion 76

5.4.1. Sea breeze cooling capacity 76

5.4.2. Trend of sea breeze cooling capacity and cooling range over time...... 77

5.4.3. Dynamic analysis of sea breeze cooling capacity 81

5.4.4. Sea breeze cooling capacity and distance 91

5.4.5. Inland penetration distance of sea breeze cooling 94

5.4.6. Sea breeze strongest cooling point 99

5.5. Conclusions 102

Chapter 6. Effect of sea breeze on thermal comfort in coastal cities 104

6.1. Introduction 104

6.2. Comparison of environmental factors between sea breeze day and west breeze day 104

6.2.1. Calculation of air temperature and drawing of distribution chart 105

6.2.2. Calculation of radiation values and mapping of distribution 109

6.2.3. Calculation of wind speed and mapping of distribution......................113

6.2.4. Calculation of relative humidity and plotting of distribution 117

6.3. PET day change between sea breeze day and west breeze day 121

6.3.1. PET and SET* Maps 121

6.3.2. Analysis of the relationship between thermal comfort index and each environmental factor... 126

6.3.3. Analysis of the distribution characteristics of heat stress levels......... 135

6.4. Differential Analysis of Sea Breeze Day and West Breeze Day PET 154

6.4.1. Definition of PET DIF 154

6.4.2. Map of PET DIF distribution on Sea Breeze Day and West Breeze Day 155

6.5. Conclusion 164

Chapter 7. Conclusions and Future research topic 167

7.1. Conclusion 167

7.2. Future research topic 169

Reference 170

Acknowledgements 181

Published Papers List 182

Chapter 1. Introduction

1.1. Research background

According to the statistics of the United Nations (2019), it is estimated that by 2050, approximately 68% of the world's population will live in cities. With accelerating urbanization [1], urban environments have produced a series of environmental problems, such as urban heat islands [2,3], enhanced precipitation [4], and air pollution [5]. Global warming has become a worldwide problem, and the intensity and duration of high temperatures are increasing [6]. Due to the industrialization that has taken place since the last century, the extensive emissions of CO2 have become the major source of anthropogenic greenhouse gas. This is the main trigger that contributes to global warming. Urban sprawl has led to the formation of the urban heat island phenomenon. A 4 °C rise in temperature can be caused by the urban expansion seen in Arizona, U.S.A., illustrated by Georgescu et al. (2013) [7]. In the summer of 2018, there were approximately 90,000 heatstroke patients in Japanese metropolitan areas. Therefore, it is urgent to take measures to alleviate such urban problems [8]. Improving the heat island effect has become a key challenge to achieving urban sustainability [9].

Most coastal cities have developed into megacities owing to their superior geographical location and convenient transportation amenities [10]. Wind is the movement in the horizontal direction of the atmosphere caused by the difference in atmospheric pressure. During the day, the hot air on the land surface rises, and the cold air on the sea surface flows toward the land to supplement it, thus forming a sea breeze. Sea breezes can effectively alleviate the urban heat island effect[11], and its cooling effect not only improves human comfort levels, but also effectively reduces energy consumption[12]. For this reason, many scholars have conducted in-depth research on the basic characteristics of sea breezes and their relationships with the urban environment. In summer, sea breezes always prevail[13]. Due to the low-temperature sea breeze that provides convective cooling in coastal cities, the UHI effect of coastal cities is lower than inland cities[14].

The sea breeze is a mesoscale atmospheric phenomenon. In the morning, as the sun rises, the land gradually warms up after absorbing the sun's radiation, while the temperature of the ocean changes very little. This difference in thermal characteristics creates a contrast in air temperature between land and ocean. The resulting pressure gradient from the ocean to the land drives cold shallow ocean air inland, resulting in a sea breeze[15]. The greater temperature difference between land and sea in summer makes the sea breeze always prevail in coastal cities[13].

While the sea breeze cools down the temperature, it also brings pollution transport and heat wave diffusion to the coastal areas of many cities[16–19]. Over the past few decades, global heat wave events have increased each year, with most cities suffering stronger heat wave intensities that last longer [6]. The rise in heatwave events has been attributed to global warming [20] and urban sprawl resulting in high-density urban form with low-density vegetation cover and increasing artificial heat removal [21]. The urban heat island phenomenon threatens human health and comfort [22] and increases water and electricity resources [23].

According to the urban thermal balance, UHIs result from an individual or the combination of several factors such as the reduction in previous land cover, the increase in solar absorption and heat storage material, the increase in anthropogenic heat release, and the decrease in urban ventilation [21]. Targeting these causations, various efforts have been made to mitigate UHIs in urban planning and design [24–27]. Overall, starting from the cooling potential of wind (i.e. sea breeze), reasonable modifications towards urban morphology at the local scale can enable wind penetration and may potentially mitigate UHIs. Moreover, outdoor thermal comfort, a critical indicator to assess UHI mitigation, can be potentially improved [28]. The improvement of outdoor thermal comfort in cities is a result of the mitigation of urban heat islands, and there is an interaction between the urban micro-scale and mesoscale. As a result, efforts have been made to find ways and means of improving outdoor thermal comfort.

1.2. Research purposes

Human overexploitation of the Earth has changed the ground surface conditions and caused significant changes in the urban climate of coastal areas. Fortunately, it has been found that when wind speed reaches a certain threshold, it can effectively mitigate the urban heat island phenomenon even to the point of complete offset[29]. In particular, this refers to the cold wind from the sea and rivers[30]. Sea breezes are therefore seen as an efficient source of cooling that can mitigate urban heat islands[11]. The effect of wind on the control of urban temperature has been verified by long-term measurements, and it was found that the sea breeze entering the city reduces the urban temperature by about 4°C compared to the case without wind [31]. This not only improves human comfort but also effectively reduces energy consumption [12,32,33] and generates wind energy[34]. Therefore, studies related to sea breeze are very important.

1.3. Research scopes

Sendai is the capital city of Miyagi Prefecture and is the largest metropolis in north-east Japan, covering an area of 785.8 km2 (Fig. 1.1). The southeast is plain, the downtown is hilly, and the northwest is mountainous. The city stretches about 40 km from the southeastern coastline to the northwest. According to statistics, the population growth rate is relatively high. From 2010 to 2015, the growth rate reached 3.46%, and the population reached 1.08 million in 2015. Sendai has a mild subtropical monsoon climate, with hot summers (city latitude: 31°49’00.00” N; city longitude: 130°18’00.00” E). During the summer days, the wind from the southeast direction of the sea is the most frequent and can effectively reduce the urban temperature of Sendai. Most mountainous coastal cities have urban areas close to the coastline, while the city center of Sendai is about 9 km away from the coastline. Currently, the annual average temperature in Sendai is rising at a rate of 2.3 °C per 100 years. In addition, in terms of health damage, many people suffer from heatstroke annually. In summer, the number of heatstroke patients tends to increase on days when the temperature rises sharply from the previous day or days when the highest temperature exceeds 30 °C. It is therefore necessary to study the characteristics of the impact of sea breezes on the urban environment of Sendai.

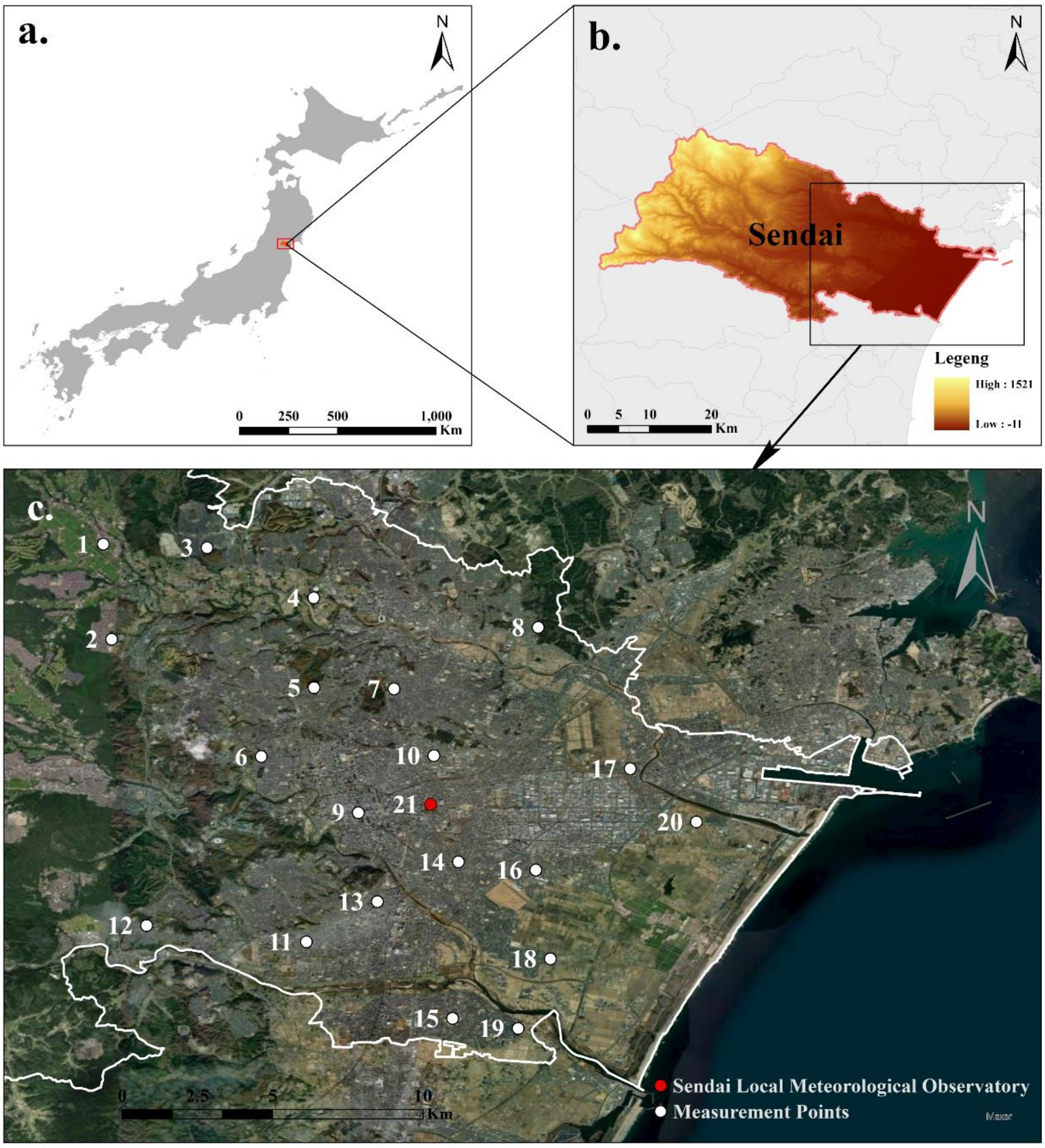

Fig. 1.1 *Map showing the location of Sendai and the distribution of temperature and humidity recorders and Sendai Local Meteorological Observatory in the study area. (a) Map of Japan; (b) Topography of Sendai area; (c) Distribution of temperature and humidity recorders on satellite maps.*

1.4. Structure of the thesis

This thesis consists of seven chapters, and it is organized as below:

Chapter One introduces the background of the thesis. It covers the progressive urbanization that has accelerated the urban environment's deterioration, leading to environmental problems such as urban heat islands. Based on the research background it is introduced, this investigates the effects of sea breeze on the urban environment and thus explore ways and means to improve outdoor thermal comfort.

Chapter Two evaluates the research methods and materials used in this study on the effects of sea breezes on the urban environment. There are many research methods and materials available, and of the wide variety of research methods and materials, there are different characteristics and strengths that apply to a variety of different research topics. This chapter focuses on all the research methods and materials used in this study. It mainly includes meteorological data acquisition and data visualization, and outdoor thermal comfort evaluation methods. The acquisition of meteorological data includes two ways: observation and software simulation.

Chapter Three is an analysis of the reproducibility of measured and modeled data. All the data analyzed in this thesis were obtained from mesoscale meteorological studies and predicted WRF model simulations, so it is necessary to analyze the reproducibility of the simulated and measured data. Firstly, access to the measured and modeled data is introduced, including the location and equipment selection of the measured points and the parameterization of the modeling software. The reproducibility and errors of the simulated data are analyzed in detail.

Chapter Four analyzes and maps the timing of sea breeze events in coastal cities. This chapter first summarizes the characteristics of summer sea breeze activity in Sendai, the study area, and then introduces the method of identifying sea breeze days. A temporal map of summer sea breeze events in Sendai was derived from the target day meteorological data simulated by mesoscale meteorological studies and predictive WRF models. The data were also visualized by using ArcGIS Pro to reproduce the sea breeze arrival time, sea breeze retreat time, and the distribution of sea breeze events in the study area.

Chapter Five is about the Sea breeze cooling capacity in a coastal city. This chapter defines how the sea breeze cooling capacity is calculated. The results of the calculations were visualized using ArcGIS Pro to generate a cooling map of sea breeze cooling capacity. The trends in hourly cooling capacity are also analyzed dynamically. The factors affecting sea breeze cooling capacity are discussed, as well as the hourly sea breeze maximum cooling point and the inland penetration distance of hourly sea breeze cooling during the time interval of sea breeze cooling action.

Chapter Six deals with the effect of sea breeze on thermal comfort in coastal cities. Firstly, the distribution of environmental factors affecting outdoor thermal comfort on sea breeze day and west breeze day are listed separately. Environmental factors include temperature, radiation, relative humidity, and wind speed. The source of all data is obtained from the WRF mode analog output. After analyzing the underlying environmental factors, the Rayman software was used to input each environmental factor, thus calculating the outdoor thermal comfort index, PET values, and SET* values for each simulation point on sea breeze day and west breeze day. The outdoor thermal comfort index mainly shows the values of each whole hour point during the sea breeze action time (i.e., 15 hours in total from 7:00 to 21:00), totaling 15 sets. The thermal comfort index of sea breeze day and west breeze day are plotted separately, and their respective variation characteristics and comparison characteristics with each other are analyzed. The distribution of heat stress levels at each point in time is also listed, and the specific distribution characteristics of their thermal comfort are analyzed. Finally, the difference between the outdoor thermal comfort index on sea breeze day and west breeze day is evaluated to analyze the improvement of thermal comfort on sea breeze day compared to west breeze day.

Chapter Seven summarizes the research conclusions and future research topics of this study. Firstly, the motion characteristics of sea breeze are obtained. According to the map of the temporal distribution of sea breeze events, the sea breeze blows landward at a slower rate in the coastal area and the rate increases with penetration inland. The arrival time of sea breeze is strongly influenced by inland rivers. From the map of sea breeze retreat time distribution, the direction of sea breeze retreat is related to the area of compact mid-rise and compact Low-rise and urban topography. The retreat of the sea breeze slows down significantly when it is close to highly urbanized areas. The sea breeze retreat speeds up until it is close to the coastal part. From the map of sea breeze duration distribution, the sea breeze duration is relatively evenly distributed in the area, and the sea breeze duration is the longest in the direction of sea breeze retreat.

The main conclusion drawn is that both the sea breeze cooling capacity and the cooling range show a rising and then decreasing trend, and reach a maximum at 10:00. It was also found that the distance of the action point from the coastline, the time of cooling effect occurrence, and inland rivers are important factors affecting the cooling capacity of sea breeze. The closer the action point is to the coastline, the greater the cooling capacity of the sea breeze. The positive impact of inland rivers on sea breeze cooling capacity. The area that produces the strongest cooling capacity per hour shows a strong negative correlation with the time of cooling effect onset and distance from the coast.

This study uses PET (Physiological Equivalent Temperature) values to respond to human heat stress levels and to describe human thermal comfort. Comfort is always lowest in urban areas on either sea or west breeze days, highest in coastal areas on sea breeze days, and highest inland on west breeze days. On sea breeze days there are different degrees of outdoor thermal comfort improvement values in different areas, with the longest duration and strongest degree of improvement in the coastal area. At 13:00, the strongest improvement in outdoor thermal comfort was obtained.

In future studies, more in-depth research can be conducted by adding measurement data analysis as well as questionnaires after identifying the study sites based on the findings of existing studies.

1.5. Framework of this research

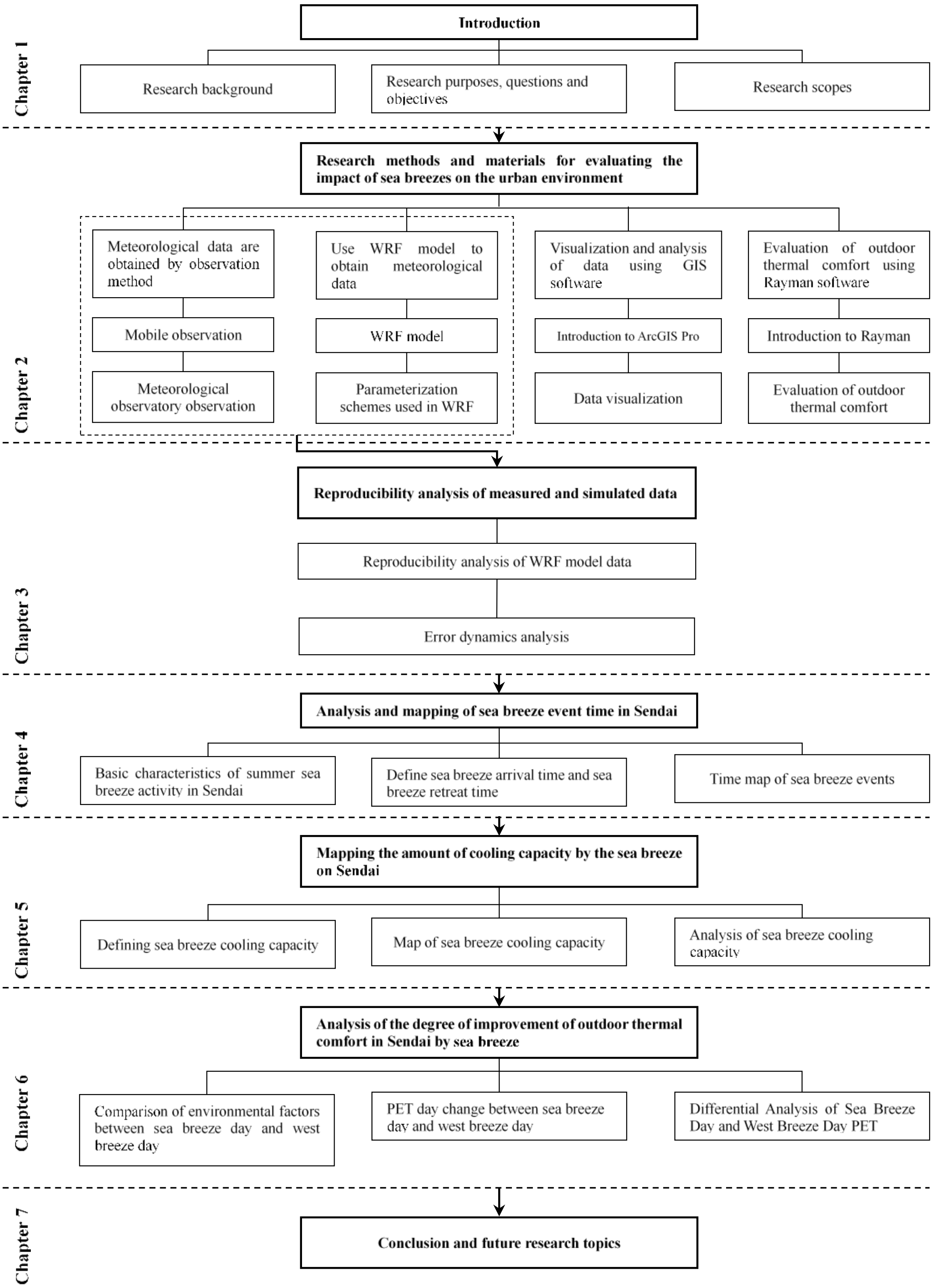

1.6. Creativity and innovation

The background of this study is accelerated urbanization, global warming, and urban heat island. The goal is to find ways to improve the comfort of the human living environment. Using the Sendai summer sea breeze as the main research object, I combined mesoscale sea breeze activity with microscale outdoor thermal comfort based on a comprehensive understanding of the action time and cooling capacity of the Sendai summer sea breeze. A new interpretation of the extent to which sea breeze improves the human living environment in coastal cities from the perspective of human comfort is presented.

In this study, I used WRF model simulation data as the research data, visualized the calculation results using ArcGIS Pro, and analyzed the temporal and spatial dynamics of sea breeze events and sea breeze cooling capacity. The different characteristics of sea breeze events in each area were analyzed in detail. It also defines the sea breeze cooling capacity and analyzes its influencing factors.

It was finally confirmed that inland rivers have a positive influence on the infiltration of sea breeze cold air to land in terms of speed, intensity, and extent; Regionally, sea breeze days have resulted in stronger and broader improvements in outdoor thermal comfort in coastal areas. In terms of time, the improvement in outdoor thermal comfort at night (after 21:00) covered almost the entire study area.

Chapter 2. Presentation of the research tools and materials used in this thesis

2.1. Introduction

Chapter Two evaluates the research methods and materials used in this study on the effects of sea breezes on the urban environment. There are many research methods and materials available, and of the wide variety of research methods and materials, there are different characteristics and strengths that apply to a variety of different research topics. This chapter focuses on all the research methods and materials used in this study. It mainly includes meteorological data acquisition and data visualization, and outdoor thermal comfort evaluation methods. The acquisition of meteorological data includes two ways: observation and software simulation.

Sea breezes have always been studied using observational data as well as numerical simulations. There are many ways to obtain data and analyze them. In the early days, sea breezes were analyzed from pure theory. Then, aircraft tracking [35] and LIDAR data inverse analysis [36] were used. In Japan, it has been concluded from the analysis of long-term multi-point test data that sea breezes in coastal areas mitigate temperature rises earlier than the inland areas of Sendai [37]. The cooling effect of the sea breeze on the built environment was found to be significant after field measurements in the Fukuoka area, and the sea breeze temperature increased, moving progressively deeper inland [38]. There are also many studies on the acquisition of data using numerical simulations. Simulations using mesoscale meteorological studies and forecasting WRF models have revealed that the urban heat island effect increases the temperature difference between the ocean and the land, thus enhancing the sea breeze effect. The cooling effect of sea breeze has been estimated from the wind speed values simulated by the WRF model. Urban environmental climate maps were also produced using the WRF calculations, reproducing the range of sea breeze cooling effects and the range of specific humidity rise effects [39].

2.2. Meteorological data are obtained by observation method

2.2.1. **Concept**

The heterogeneity of natural and artificial surfaces of urban environments implies that atmospheric observations require a network of measurements as dense as possible to adequately describe local climate conditions. The observation of urban climate can proceed through mobile measurements and stationary sites. However, due to the need to find suitable meteorological sites and instruments, the deployment and maintenance of fixed meteorological stations eventually lead to sparse data coverage for urban areas. Traditionally, meteorological measurements have not been taken in urban areas but in open areas representing larger regions. Many urban stations have been placed over short grass in open locations (parks, playing fields), and as a result, they are monitoring an environment of the type of modified rural. The simple classification of measuring sites contains categories for urban, downtown, suburban, and rural sites. The choice of measurement sites can be classified differently for different research purposes.

2.2.2. **Arrangement of measurement points**

A primary survey of the study area can document the presence of obstacles close to the measurement site. The main discrepancies are caused by unnatural surfaces and shading:

a) Obstacles around the screen influence the irradiative balance of the screen. A screen close to a vertical obstacle may be shaded from the solar radiation, “protected” against the night radiative cooling of the air by receiving the warmer infrared radiation from this obstacle, or otherwise influenced by reflected radiation.

b) Neighboring artificial surfaces may heat the air. Reflective surfaces (e. g., buildings, concrete surfaces, car parks) and water sources (e. g., ponds, lakes, and irrigated areas) should be avoided. Each climate parameter being measured at a site carries its considerations.

Facts to consider during the placement of a sensor in urban environments:

- Careful attention to radiation shielding and ventilation is highly recommended.
- Use of the same sensor assemblies (with/without shields and ventilation) inside a network is strongly advised to avoid inter-site differences.

The sensor should be relatively far from warm surfaces, walls, roads, or vehicles with hot engines and might receive reflected heat from glassed surfaces. Because urban environments are far dirtier than rural sites (in terms of dust, oils, and pollutants), thermometers and hygrometers require increased maintenance and frequent service. Yearly changing and calibration are strongly advised. The provision of shielding from extraneous sources of solar and long-wave radiation is also recommended.

2.2.3. **Measurement points description for METADATA**

Measurement points metadata should contain the following aspects of instrument exposure:

a) height of the instruments above the surface,

b) type of sheltering and degree of ventilation for temperature and humidity,

c) degree of interference from other instruments or objects (masts, ventilators),

d) microscale and top scale surroundings of the instrument, in particular,

i. the state of the enclosure’s surface, influencing temperature and humidity,

ii. nearby major obstacles (buildings, fences, trees) and their size,

iii. the degree of horizon obstruction for radiation observations,

iv. surrounding terrain roughness and major vegetation, influencing the wind,

v. all top-scale terrain features, such as small slopes, pavements, or water surfaces,

vi. Major mesoscale terrain features, such as coasts, mountains, or urbanization.

The survey of each site should be reviewed periodically, as environmental circumstances can change over some time. A systematic yearly visual check is recommended: If some aspects of the environment have changed, a new site description document should be included in the metadata file. A site update should be completed at least every five years.

2.2.4. **Description of measurement points for metadata in this study**

The measured data used in this study include meteorological observatory data and long-term multi-point measurement data in the research laboratory. The distance from the coast to Sendai Local Meteorological Observatory (38° 15′ 43.60″ N, 140° 53′ 49.52″ E), an urban area, is about 9 km. The south side of the meteorological observatory is a park, the north and east sides are covered by buildings, and the instruments are placed in the open space on the west side of the weather bureau building. Various meteorological variables were recorded, such as air temperature, humidity, wind direction and velocity, sunlight intensity, precipitation, and atmospheric pressure. All data can be obtained from the Japan Meteorological Agency, where the wind speed indicates its instantaneous and average values. The humidity measurement used an electronic hygrometer, and the thermometer was mounted at a height of 1.5 m above the ground. They were recorded at a frequency of 10 minutes.

Long-term multi-point test data were obtained from 20 temperature and humidity sensors (Fig. 2.1). The measuring instrument used a temperature and humidity recorder (T&D Corporation), and the frequency of data recording is set to 10 minutes (Fig. 2.2, Table 2.1). To avoid both rain and direct sunlight and to satisfy the need to record data in a naturally ventilated state, the measuring instruments were installed in an instrument shelter. All the instrument shelters were placed in the playgrounds of primary schools or parks within Sendai city (Fig. 2.1.c). The instrument shelters were placed away from trees and building walls to avoid local effects on measurements. Twenty measurement points extend inland from the city coast. A total of six measurement points were set up within 7 kilometers from the coast, with four points inland after 15 kilometers, and the rest of the points were distributed in the city.

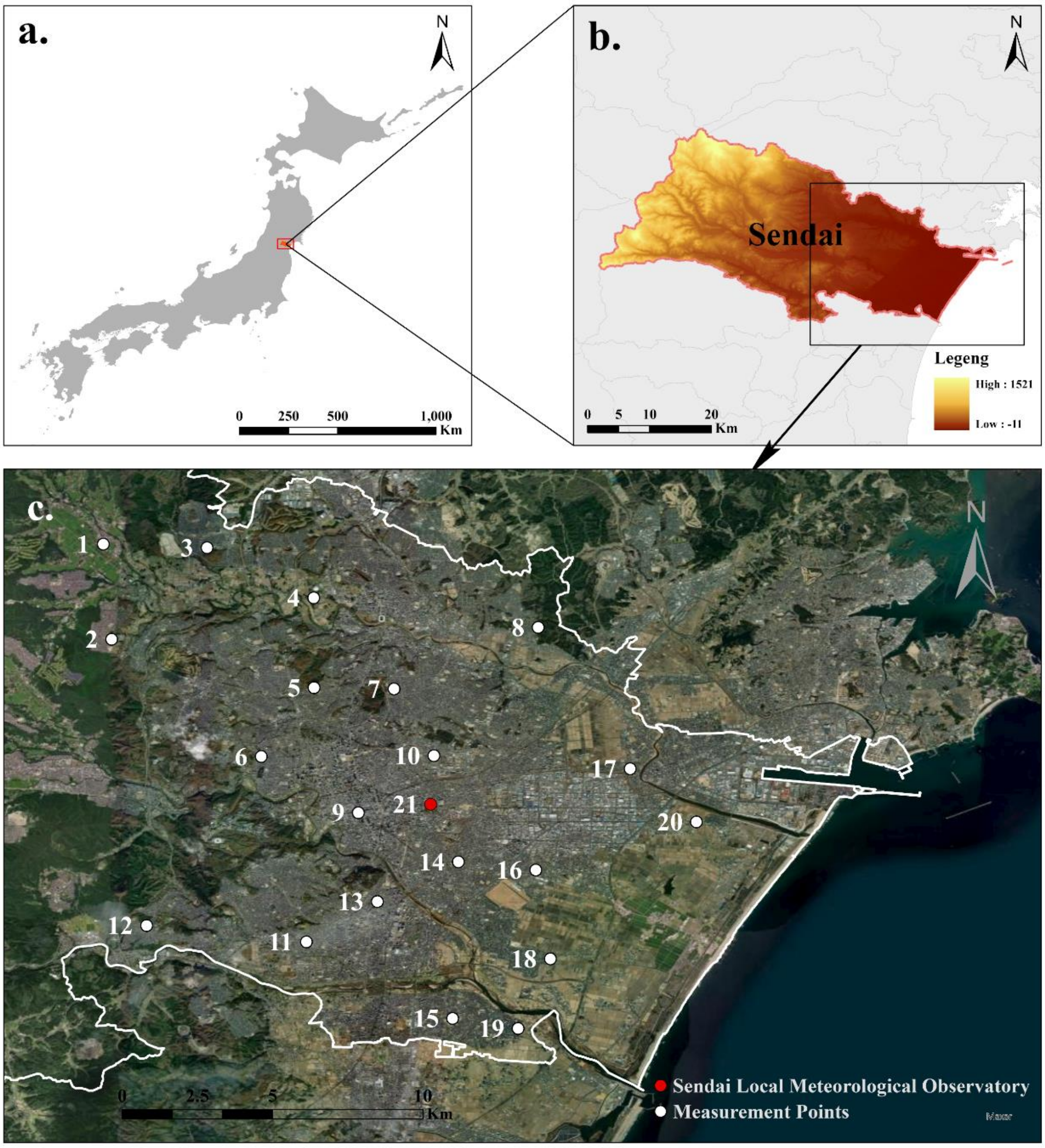

Fig. 2.1 *Map showing the location of Sendai and the distribution of temperature and humidity recorders and Sendai Local Meteorological Observatory in the study area. (a) Map of Japan; (b) Topography of Sendai area; (c) Distribution of temperature and humidity recorders on satellite maps.*

Fig. 2.2 *Installation status of the measuring equipment in the louver and temperature and humidity recorder, RH TR-72U.*

Table 2.1 *The instruments used at the measurement point, and the characteristics of the instrument placement and instrument setup.*

Measuring equipment	**Measurement equipment shelter**	**Time resolution**	**Observed elements**	**Ground surface**	**The function of surrounded area**
temperature and humidity recorder (T&D Corporation)	Louver	10min	T,RH	Lawn	playgrounds of Primary school

Table 2.2 records the number of the points, their latitude and longitude coordinates, and their distance from the coast. The location picture shows the following information about the site:

1. Location in Sendai City (location 1) ;

2. The main mesoscale terrain features within 1 km around the site (location 2) can directly reflect the urbanization and greening degree around the site ;

3. The specific location of the station in the primary school playground (location 3).

Table 2.2 *Measuring point location information*

ID	Station Name	Lon.	Lat.	Distance(Km)	Location 1	Location 2	Location 3
1	Nenoshiroishi	140.7966	38.3417	21.35			

2	Yakata	140.7992	38.3126	19.68			
3	Teraoka	140.8284	38.3406	18.92			
4	Nomura	140.8611	38.3253	15.65			
5	Kita-Sendai	140.8612	38.2978	13.91			
6	Kunimi	140.8450	38.2767	14.02			
7	Asahigaoka	140.8857	38.2974	12.15			
8	Tsurugaoka	140.9299	38.3162	10.15			
9	Higashi Nibancho	140.8748	38.2595	10.82			

10	Saiwaicho	140.8979	38.2770	10			
11	Nishitaga	140.8588	38.2199	11.63			
12	Hitokita	140.8099	38.2249	14.75			
13	Nagamachi	140.8806	38.2323	8.98			
14	Minamikoizumi	140.9054	38.2444	7.61			
15	Fukurobara	140.9037	38.1965	5.92			
16	Kabanomachi	140.9292	38.2419	5.6			
17	Takasago	140.9581	38.2730	5.27			

18	Rokugo	140.9336	38.2147	3.75			
19	Higashishiromaru	140.9238	38.1934	4.15			
20	Okada	140.9784	38.2567	2.83	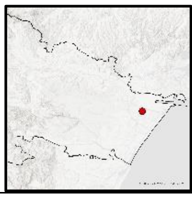		

2.3. Use WRF model to obtain meteorological data

2.3.1. **Concepts**

Weather Research & Forecasting Model (WRF)is a state-of-the-art mesoscale numerical weather prediction system designed for both atmospheric research and operational forecasting applications. The Advanced Research WRF (ARW) modeling system has been in development for two decades. The current release is Version 4, available since June 2018. It features two dynamical cores, a data assimilation system, and a software architecture supporting parallel computation and system extensibility.

The model serves a wide range of meteorological applications across scales from tens of meters to thousands of kilometers, including:

Idealized simulations (e.g. LES, convection, baroclinic waves)

Parameterization research

Data assimilation research

Forecast research

Real-time NWP

Hurricane research

Regional climate research

Fire research

Coupled-model applications

Teaching

The effort to develop WRF began in the latter 1990s and was a collaborative partnership of the National Center for Atmospheric Research (NCAR), the National Oceanic and Atmospheric Administration (represented by the National Centers for Environmental Prediction (NCEP), and the Earth System Research Laboratory), the U.S. Air Force, the Naval Research Laboratory, the University of Oklahoma, and the Federal Aviation Administration (FAA).

For researchers, WRF can produce simulations based on actual atmospheric conditions (i.e., from observations and analyses) or idealized conditions. WRF is currently in operational use at NCEP and other national meteorological centers as well as in real-time forecasting configurations at laboratories, universities, and companies.

2.3.2. **The WRF Modeling System Program Components WRF**

The Figure2.3 shows the flowchart for the WRF Modeling System Version 4.

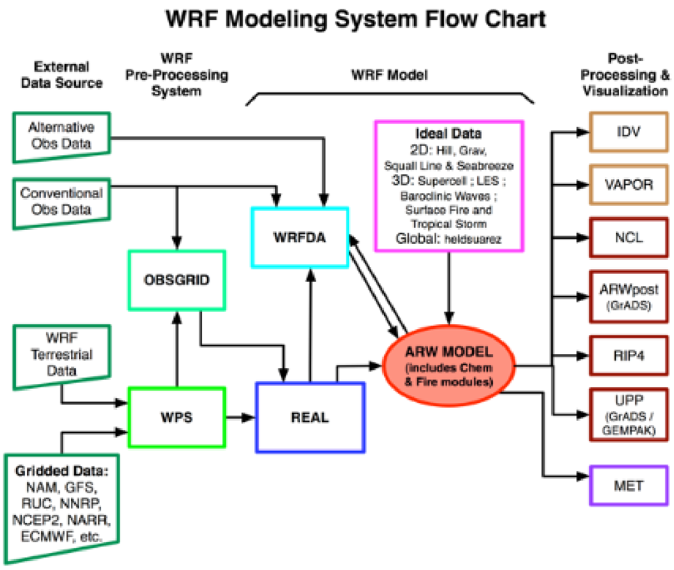

Fig. 2.3 Flowchart for the WRF Modeling System Version 4.

As shown in the diagram, the WRF Modeling System consists of these major programs:

Ⅰ The WRF Preprocessing System (WPS)

This program is used primarily for real-data simulations. Its functions include 1) defining simulation domains; 2) interpolating terrestrial data (such as terrain, land use, and soil types) to the simulation domain; and 3) describing and interpolating meteorological data from another model to this simulation domain.

Ⅱ WRF-DA

This program is optional but can be used to ingest observations into the interpolated analyses created by WPS. It can also be used to update the WRF model's initial conditions when it is run in cycling mode.

Ⅲ ARW solver

This is the primary component of the modeling system, which is composed of several initialization programs for idealized, and real-data simulations, and the numerical integration program.

Ⅳ Post-processing & Visualization tools

Several programs are supported, including RIP4 (based on NCAR Graphics), NCAR Graphics Command Language (NCL), and conversion programs for other readily available graphics packages.

2.3.3. **Basics for Running the Model**

The Figure2.4 is a description of the program flow during a typical model run:

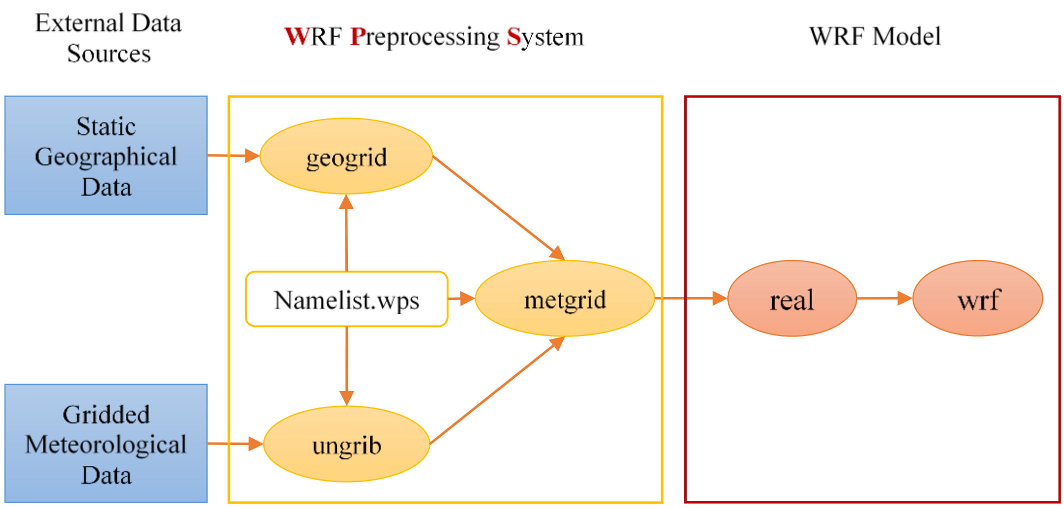

***Fig. 2.4** The process of running the model.*

WPS (WRF Preprocessing Systern)

Ⅰ geogrid. exe

Creates terrestrial data from static geographic data that is obtained from an external data source.

The simulation domain(s) are defined using the information specified by the user in the "share" and "geogrid" sections of the WPS name list. By default, in addition to computing latitude and longitude for every grid point, geogrid will interpolate soil categories, land use categories, terrain height, annual mean deep-soil temperature, monthly vegetation fraction, monthly albedo, maximum snow albedo, and slope category to the model grids.

Ⅱ ungrib. exe

Unpacks GRIB meteorological data (that is obtained from an external source) and packs it into an intermediate file format. Unpacking the data is controlled via the "share" and "ungrib" sections of the WPS name list.

Ⅲ namelist.wps

Namelist.wps file that is used for running the WRF Preprocessing system (which includes geogrid.exe, ungrib.exe, and metgrid.exe).

Ⅳ metgrid. exe

Interpolates the meteorological data horizontally onto your model domain. Output from metgrid. exe is used as input to WRF (through the real.exe program).

Ⅴ namelist.input

Namelist.input file that is used for running the WRF model (which includes real.exe, wrf.exe, tc.exe, and ndown.exe).

WRF Model

Ⅰ real.exe

This program vertically interpolates the met_em* files (generated by metgrid.exe), creates boundary and initial condition files, and does some consistency checks.

Ⅱ wrf.exe

Generates the model forecast.

2.3.4. **WRF model and experimental design of this study**

In this study, I used the Advanced Research Weather Research and Forecasting (ARW-WRF) model developed by the National Center for Atmospheric Research (NCAR) and the National Center for Environmental Prediction (NCEP) to numerically simulate the Sendai urban area [40,41]. The main physical settings of the model are shown in Table 2.3 These settings are similar to those used in a [39] study of the extent of sea breeze cooling in the Sendai area. Three nested domains were used in this simulation (Fig. 2.5). The outer square is domain 1, which consists of 37 × 28 grids with a spatial resolution of 9 km. Domain 2 consists of 43 × 34 grids with a spatial resolution of 3 km. The main analysis domain is domain 3, which consists of 31 × 28 grids with a spatial resolution of 1 km. A horizontal resolution of 1 km is widely used in numerical studies of urbanization and sea breeze [42,43]. The number of vertical layers used in this study was 30, and the urban canopy model and WSM 6-class graupel scheme [44] were used. Many planetary boundary layers (PBL) schemes are available, and some researchers have made detailed comparisons of the different schemes [45]. For this simulation, I used the Mellor–Yamada–Janjic model [46]. The Rapid Radiative Transfer Model for General circulation models (RRTMG) longwave scheme and Dudhia shortwave scheme in the general circulation model were used. The calculation period was from 1 to 10 August 2016. The simulated data in domain 3 finally generate 31 × 28 point data, and each point datum contains the values of temperature at 2 m above ground and specific humidity at 2 m above ground. The frequency of the numerical output is 10 min, which is the same as the measured data.

The external data required for the WRF model include land data and meteorological data. Among them, land data contains GIS data of topography, land use public facilities and other basic information of the national land. This study utilized data from the spatial digital land information released by the Japanese government with a resolution of 1 km.The meteorological data contains topographic, atmospheric, and sea surface water temperature data, etc. The final global operational analysis data (FNL) from NCEP (National Center for Environmental Prediction) was used.

Variable list：5-wave geopotential height，5-wave geopotential height anomaly，Absolute vorticity， Best (4 layers) lifted index， Cloud water， Cloud water mixing ratio， Convective available potential energy， Convective inhibition， Geopotential height， Geopotential height anomaly， Ice concentration， Ice cover， Land cover， Maximum temperature， Minimum temperature， Ozone mixing ratio， Planetary boundary layer height，Potential temperature，Precipitable water，Pressure，Pressure reduced to MSL， Relative humidity， Specific humidity， Surface lifted index， Temperature， Total cloud cover， Total ozone，u-component of wind，v-component of wind， Vertical speed shear， Vertical velocity (pressure)， Volumetric soil moisture content， Water equivalent of accumulated snow depth.

Table 2.3 Domains and Parameterization schemes used in WRF model experiments.

Calculation period	09:00 (JST) on August 1, 2016, to 09:00 (JST) on August 10, 2016 (sea breeze day) 09:00 (JST) on August 5, 2013, to 09:00 (JST) on August 15, 2013 (west breeze day)
Vertical grid	30 layers
Horizontal grid	Domain 1: 9 km, dimension 37 × 28 Domain 2: 3 km, dimension 43 × 34 Domain 3: 1 km, dimension 31 × 28
Meteorological data	NCEP re-analysis of global objective data
Land data	Digital national land information (resolution of 1000 m)
Microphysics	WSM 6-class graupel scheme
Radiation: Longwave Shortwave	Rapid radiative transfer model Dudhia shortwave
PBL scheme	Mellor-Yamada-Janjic TKE scheme
Surface scheme	Urban canopy model

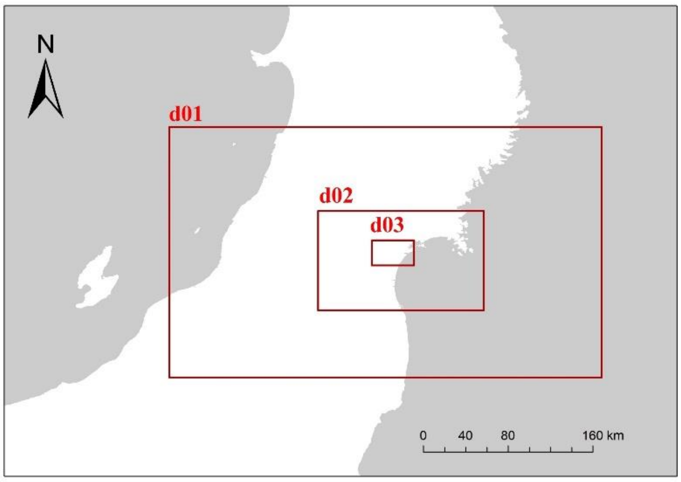

Fig. 2.5 *Definition of the three domains for the WRF model.*

2.4. Visualize and analyze data with GIS software

2.4.1. Concepts

Throughout history, almost all human activities have taken place on the Earth and are closely related to the Earth's surface location (i.e., geospatial location). With the increasing development and popularity of computer technology, Geography Information

System (GIS) plays an increasingly important role in people's production and life and has been widely used in different fields. In a strict sense, it is a computer system with the ability to centralize, store, manipulate, and display geo-referenced information.

Maps are often used to explore the Earth and exploit its resources. GIS technology, as an extension of map science, improves the efficiency and analytical capabilities of traditional maps. GIS technology is now becoming a fundamental tool for understanding the impact of environmental change over time as the scientific community identifies the environmental consequences of anthropogenic activities that affect climate change. GIS technology allows information from a variety of sources to be combined with existing maps and up-to-date information from Earth observation satellites along with the output of climate change models. This can help understand the impacts of climate change in the context of complex natural systems.

GIS belongs to the category of information systems that operate and process geo-referenced data. Georeferenced data describe the location and attributes of spatial elements on the earth's surface, two components of geographic data in GIS: spatial data, related to the geometric characteristics of spatial elements; and attribute data, providing information about spatial elements.

Geographic Information System (GIS), together with Global Positioning System (GPS) and Remote Sensing (RS), is called 3S. GIS is a data management system with a spatially specialized form of information system. Many disciplines benefit from GIS technology. In the history of development, John Snow depicted the cholera epidemic in London in 1854, using dots to represent individual cases, which was the first epidemic map to use a geographical approach. In 1967, the world's first truly operational GIS was developed in Ottawa, Ontario, Canada, by the federal Department of Forestry and Rural Development. Industry growth in the 1980s and 1990s spurred the rapid growth of UNIX workstations and personal computers with GIS applications. By the end of the 20th century, its rapid growth in a variety of systems had led to its consolidation and specification in a small number of relevant platforms. The active GIS market has led to low costs and continuous improvements in hardware and software for GIS components.

GIS systems are able to apply information from different sources in different forms. The basic requirement for the source data is to determine the location of the variables. The location is generally marked by the x, y, and z coordinates of longitude, latitude, and elevation. GIS data represents real-world objective objects in the form of digital data. There are multiple ways to enter data into a GIS in which it is stored in a digital format. And GIS can convert data into a different format by performing data reconstruction.

Projection is a fundamental part of map making. It is a mathematical method of converting information from a model of the earth, which converts a three-dimensional curved surface into a two-dimensional medium. Different projection systems are used for different types of maps, as each projection system has its own appropriate use. Among them, spatial analysis capability is the main function of GIS and the main feature that distinguishes GIS from computer mapping software. Spatial analysis is the study of spatial objects in terms of their spatial locations and connections, as well as the quantitative description of spatial objects. The modeling is done by data modeling, topology modeling, and network modeling.

2.4.2. **GIS-Software**

Geographic information is just a pile of digital records, which needs suitable software to represent it; at the same time, the creation of a geographic information database also depends on the help of suitable software to computerize geographic data. The market is now generally monopolized by two GIS giants, ESRI and MapInfo. One of them is ArcGIS, a series of GIS software produced by ESRI. The different application platforms are divided into desktop version and server version and mobile version. The desktop version of ArcGIS is composed of many application components. Using the example of ArcInfo, which contains full functionality, the application components would include:

ArcMap (is the most basic application component for cartography, editing, and map spatial analysis, but is mainly used for 2D spatial maps)

ArcCatalog (used to manage spatial data, for easy database design, and to record and display attribute data metadata)

ArcToolbox (the main collection of geographic data processing tools)

ArcGlobe (to display, edit, and analyze 3D spatial maps as a 3D stereoscopic globe)

ArcScene (display, edit, and analyze 3D spatial maps)

ArcReader (basic presentation tool)

In recent years ESRI has introduced a new desktop product, ArcGIS Pro. ArcGIS Pro will gradually replace ArcMap software. This product was released as part of Esri's ArcGIS 10.3 release. Compared to ArcGIS, ArcGIS Pro is ESRI's GIS product for the new era. It inherits the powerful data management, mapping, and spatial analysis capabilities of the traditional desktop software (ArcMap) on the original ArcGIS platform, but also has its own unique features.

Compared to traditional ArcGIS Desktop, ArcGIS Pro has the following advantages:

At the same time integrated with ArcMap, ArcSence, ArcGlobe, to achieve three-dimensional integration and synchronization.

A minimalist Ribbon interface style that allows the function buttons related to your current task to be tiled in the menu panel, making the software less difficult to use.

Allowing multiple map windows and multiple layout views to be opened, making it easy for users to quickly switch between tasks.

Support for 2-3D integrated data visualization, management, analysis and publishing, big data, task workflow, superb mapping, space-time cubes, etc..

Native 64-bit applications with multi-threaded processing support, greatly improving software performance.

Easily interface to the entire platform to visualize, edit, analyze, and share data from local, ArcGIS Online, or Portal for ArcGIS.

2.4.3. **The data visualized and analyzed in this study using GIS software**

This study used ArcGIS Pro version 2.7.0, a desktop product from ESRI. Data processed using this software include long-term multi-point measurements in the research laboratory and data simulated using the WRF model. Among them, both the measured point data and the WRF model simulation data have spatial location information, which meets the basic requirements of GIS software source data.

The specific locations of the long-term multi-point measurement data from the research lab were marked on the map using ArcGIS Pro. Using the distance measurement tool, you can easily measure the distance of each point from the coast. Because ArcGIS Pro can display satellite images of the area shown on the screen, it is possible to see the surroundings of each measurement point and visualize the distribution of each point.

The WRF model outputs temperature and specific humidity data at two meters above the ground in the study area, for a total of 31*28 points of data. Based on the movement characteristics of the sea breeze in the city, the temperature data at each point were used to calculate the time of arrival and retreat of the sea breeze from land at each point. The visualization of the sea breeze action on the map of the study area was achieved by using ArcGIS Pro to represent the time values on the map from light to dark blue. The velocity of sea breeze action was also calculated and analyzed by marking points of equal distance in each direction within the study area.

Temperature data simulated using the WRF model for west and sea breeze days were used to calculate the cooling capacity of the sea breeze at each point in the study area. The total sea breeze cooling and hourly sea breeze cooling at each point were calculated. ArcGIS Pro was used to show the magnitude of sea breeze cooling on the map of the study area in light to dark blue. This enabled the visualization of the sea breeze cooling capacity on the map.

2.5. Evaluation of outdoor thermal comfort using Rayman software

2.5.1. **Concepts**

People spend more than 90% of their average time indoors[47], leading to a dramatic increase in the energy consumed to create a comfortable indoor thermal environment. All over the world, people are now encouraged to spend more time outdoors. When people are directly exposed to the overall environment where air temperature (Ta), wind speed (Ws), relative humidity (RH) and radiation fluxes interact, the thermal physiological state of the human body is greatly affected, thus affecting the thermal comfort of the human body [48]. To create comfortable and healthy microclimate conditions, it is first necessary to better evaluate outdoor thermal comfort.

Microclimatic conditions inside urban areas depend on the result of the interaction of the regional climate with the whole urban area and the local characteristics of the urban development. Inadequate human thermal comfort conditions can affect the quality of life and the use of public open spaces. In the context of climate change and to improve the quality of life and health inside urban areas, urban planners are considering more and more the thermal component of climate to develop comfortable urban areas [49] .

Thermal comfort is the psychological state of mind that expresses people's satisfaction with the thermal surroundings and is usually referred to in terms of whether someone is feeling too hot or too cold. It can be also defined as the environmental condition that is acceptable to 80 % or more of the occupants within a space. Therefore, environmental conditions, metabolic processes, and personal sensations create a complex balance concerning human thermal comfort. Thermal discomfort can be more intense in urban areas, as temperature levels are higher in the center of a city than in its suburbs causing an urban heat island effect, especially when the wind is weak (bellow 5 m/s at 10 m high) [50] . This combination of high temperatures and poor ventilation reduces air quality and increases health risks affecting the quality of life in the cities. Especially during heat wave episodes, thermal stress can cause serious health problems and increase mortality and morbidity in humans [51] . The intrusion of cool air associated with sea breeze circulation increases the relative humidity and inhibits air temperature rise, hence ameliorating urban coastal environment and improving thermal comfort conditions with consequent effects on human health and even on plant physiology [52,53] 。

2.5.2. **Influencing factors of outdoor thermal comfort**

Outdoor thermal comfort is an important criterion to measure the overall comfort of the outdoor environment, and scholars at home and abroad have conducted a lot of research on the outdoor environment. Current research indicates that four environmental parameters of outdoor microclimate wind, light, heat, and humidity are important factors influencing outdoor thermal comfort [54–56] . Due to the complex and wide range of changes in outdoor environmental factors, especially solar radiation and wind speed, which are highly transient and dynamic, the effects of various environmental parameters on outdoor human thermal comfort have not been uniformly regular, and the impact results need further study.

Air temperature is a microclimate parameter that people can intuitively feel and make judgments about different temperatures, both hot and cold. The temperature difference between the external surface temperature of the human body and the air temperature directly affects the heat dissipation of the human body to the surrounding environment, the lower the air temperature, the greater the temperature difference, the greater the heat dissipation, and vice versa. Liu [55]. Observed long-term meteorological parameters and found that air temperature was the most critical parameter in determining outdoor thermal sensation. Air temperature has been identified as the most important climatic factor affecting outdoor thermal comfort [55,57–59], and it has been shown that in indoor thermal comfort studies, the air temperature can be directly used to evaluate the indoor hot and cold sensation when the indoor relative humidity is maintained between 40% and 60% is.

When the human body is in the outdoor environment, it is affected by the outdoor environment consisting of physical factors such as solar radiation, air temperature, surface temperature of surrounding objects, wind speed and relative humidity together, so a single air temperature factor cannot accurately represent the outdoor thermal comfort and thermal sensation. Among them, solar radiation not only itself will have an impact on human thermal comfort, but also will act with the surface temperature of surrounding objects to affect human radiation heat exchange, indirectly affecting the air temperature continues to affect human thermal comfort. Solar radiation mainly acts on the skin and vision, solar infrared radiation, in the cold season can give people a sense of warmth and comfort, but in the hot summer months make people feel hot and even burn the skin. UV radiation stimulates human skin and can cause UV allergy, pigmentation and even skin cancer; stimulating the retina can produce irritation and pain and other discomfort, and the intensity and duration of sunlight can even damage the retina. Too much light can produce visual fatigue.The average radiation temperature is defined as the average temperature of the external surface of the surrounding environment with respect to the radiation effect on the human body. It is a key parameter for calculating the radiative heat exchange between the human body and the surrounding environment, and directly reflects the intensity of solar radiation.

Solar radiation significantly affects human thermal comfort [60]. Moon [61] studied the thermal comfort in passenger compartments. The experimental results showed that solar radiation has a heating effect on the human body and the effect of solar radiation should be considered in the HVAC design. In 2019 Sharmin studied outdoor thermal comfort conditions through a field survey of the high-density tropical city of Dhaka and found that microclimatic conditions influenced by urban geometry were statistically correlated with thermal susceptibility voting (TSV), with air temperature, black-bulb temperature, and mean radiation temperature being the most important parameters (correlation coefficients r = 0.47, 0.45 and 0.44, respectively) [62]. Johansson considered shading conditions in his study [63] and found that solar radiation was an important factor affecting PET (physiological equivalent temperature).

Wind speed refers to the speed of airflow. The human body is in the outdoor environment, the surrounding air is always in a state of flow, and the flow rate is higher than a certain level before people can perceive it. When the wind speed acts on the human body, it mainly accelerates the convective heat exchange between the human body and the surrounding air, always increasing the heat exchange between the human body and the surrounding environment. But different ambient temperatures produce different levels of comfort. For example, in the hot summer, a windy environment will improve people's comfort and reduce the feeling of heat. But in the cold winter, the breeze will also intensify the cold feeling and be rejected by people. If the wind speed is too high, no matter what the season, it will bring discomfort, and stronger wind speed can also be harmful to society, such as "typhoons" or "tornados".

The relative humidity is the ratio of water vapor partial pressure in wet air to water vapor partial pressure in saturated wet air under the same temperature and atmospheric pressure. Some studies have found that when the humidity is between 30 to 70% does not have a significant impact on the human thermal sensation. However, when the background ambient temperature is higher, the higher relative humidity, reduces the evaporation rate of human sweat, reducing the amount of heat dissipated by the human body, and increasing the feeling of human stuffiness. When the background temperature of the environment is relatively low, the higher relative humidity reduces the thermal resistance of human clothing and accelerates the rate of heat exchange, making the body heat dissipation accelerated, a cold feeling increased. If the relative humidity is too low, the human body will feel that the surrounding environment is too dry. Therefore, to achieve human thermal comfort, the relative humidity range must be reasonably controlled.

More current studies show that solar radiation and air temperature are the decisive factors affecting outdoor thermal comfort, with wind speed and relative humidity being the weakest influences. Nikolopoulou conducted nearly 10,000 questionnaires at 14 different research sites in five different European countries and the results confirmed the close relationship between microclimate and comfort conditions, and that air temperature and solar radiation are important determinants [49]. Within urban areas, changes in radiation budget and wind patterns are responsible for significant spatial variations in thermal comfort. Thus, urban microclimate conditions are not only different from rural areas but also vary significantly over short distances (e.g., direct solar radiation exposure versus shaded locations). Local thermal comfort is influenced by the location and orientation of buildings and other urban elements such as vegetation [64,65], the materials used [66,67], and of course the interaction of the whole urban area with the regional climate.

However, some scholars disagree, Nikolopoulou considers wind speed as the second most important factor affecting pedestrian thermal sensation [56] and that increasing wind speed can reduce the air temperature in the inner city [68]. Metje and colleagues in 2008 [69] found a strong correlation between pedestrian comfort and WS, with comfort decreasing with increasing WS. They also found that for wind speeds above 5.0 m/s, the number of respondents who felt uncomfortable or very uncomfortable with the wind speed exceeded 60%. At lower wind speeds, 80% of the subjects rated the comfort level as acceptable. They also found that more than 60% of the subjects felt the wind, strong or very strong when the wind speed was >3.5 m/s. Kánto and colleagues in 2012 [70] studied the relationship between wind perception/preference voting and other variables in Szeged, Hungary. They found that the coefficient of determination of the linear regression fit between WS and mean wind perception vote was R2 = 0.713, the coefficient of determination of the regression between wind speed and mean wind preference vote was R2 = 0.843, between PET and mean wind perception vote was R2 = 0.31, and between PET and mean wind preference vote was R2 = 0.568. They also found that, among environmental variables, people were most sensitive to WS changes. In contrast, Viradigo and Velay-Dabat [71] found weak correlations between heat perception voting and temperature (r=0.31), relative humidity (r=0.12), and wind speed (r=null).

Wind can counteract the negative effects of solar radiation on thermal neutrality and thermal comfort, but as air temperature increases, the effect of wind diminishes, and when the air temperature is above 32°C, it is difficult to achieve thermal neutrality or thermal comfort by increasing wind speed [72] . Lai et al. found that solar radiation, wind speed, and relative humidity preferences are all air temperature dependent, and the higher the air temperature, the higher the preferred wind speed, the higher the required of solar radiation and relative humidity, and vice versa [54]. Cheng and colleagues [73] studied the effects of changes in wind speed and solar radiation on subjective heat perception in 2012. They found that under typical summer conditions in Hong Kong when Ta = 28°C and RH = 80%, an increase in wind speed from 0.3 m/s to 1.0 m/s corresponds to a 2°C drop in air temperature, and a person sitting in the shade wearing light summer clothing would need WS = 1.6 m/s to feel thermoneutrality. Memon and colleagues [74] studied 2010 the effect of 0.5 -4.0m/s ambient wind speed on Ta in an urban environment, and they found that Ta increased to 1.3C when the ambient wind speed decreased from 4.0m/s to 0.5m/s. Subjects could tolerate the outdoor heat better when solar radiation was lower. They preferred low radiation to moderate or high radiation, and the sensitivity of solar radiation to wind speed was calculated over different operating temperature ranges, and the subjects had different sensitivities to wind speed and solar radiation in overall operating temperature ranges and were more sensitive to changes in wind speed when the environment was warm [75].

The factors of human thermal comfort are influenced by a combination of microclimatic and personal factors. Among them, microclimatic parameters mainly include the four variables of wind, light, heat, and humidity mentioned above. And personal factors mainly include human metabolic rate and clothing thermal resistance. Microclimatic factors do not have a single effect in influencing the heat balance of the human body, but rather a combination of the factors. Personal factors can be controlled by human subjects and vary widely from person to person. The metabolic activity of the human body is an important basis for human life activities and also affects the thermal comfort of the body. Metabolism includes absorption, storage, and excretion of the body. Due to the complex regulatory mechanisms in the human body, it is possible to control the body temperature within a certain temperature range. If the body's self-regulation is too intense, discomfort can result. The thermal insulation of human body dressing can reduce the heat loss of the human body to a great extent. People adjust the thermal resistance between the human body and the surrounding environment by changing the amount of clothing, thus regulating the heat exchange between the human body and the surrounding environment. The unit of clothing thermal resistance is clo, and 1clo is equivalent to the clothing thermal resistance when people sit quietly in a room with 21℃, relative humidity close to 50%, and wind speed less than 0.05m/s.

In addition to the above factors, human heat sensation is also related to age gender, etc. Women are more sensitive to temperature changes, and the neutral temperature of women is 1°C higher than that of men. The metabolic rate of the human body decreases with age. At the same time, the evaporation rate of sweat on the skin's surface is reduced. Therefore, age also affects people's evaluation of thermal comfort. Older people prefer a warmer indoor environment. Geographical differences also affect the thermal comfort of the human body, and studies have shown that the thermal neutral temperature in cold areas is lower than that in mild areas.

2.5.3. **Outdoor thermal comfort evaluation**

In recent years, to improve the prediction accuracy of thermal comfort, in hot weather, the effects of air temperature, air humidity, wind speed, and radiation flux are taken into account. Domestic and foreign scholars have conducted continuous research and improvement on the thermal comfort evaluation index. Four climatic variables are required for thermal comfort assessment: air temperature, wind speed, mean radiant temperature, and relative humidity. However, the models do not always give accurate results due to limitations in spatial resolution and in the methods used to consider environmental conditions (i.e., dynamic and radiative aspects). Virtually all of these variables come together in a complex way, and for more than 100 years, research has been conducted to quantify the importance of the thermal environment to humans through a comprehensive thermal climate index that expresses the impact of all of these factors on thermal comfort simultaneously.

Human biometeorological indicators have been developed to describe heat stress. Danish scholar Fanger proposed the famous human body heat balance equation in 1970 and proposed the most widely used international Predicted Mean Vote, (PMV). This index is based on the human body heat balance theory and the two-node model and can reflect the average voting value of most people for thermal environments. However, the predicted mean vote has a large error when applied to outdoor environments. In 1989, Jendritzky added processes such as solar radiation to modify the Predicted Mean Vote so that it could be applied to outdoor thermal environments. in 2000, Perceived Temperature (PT) was proposed to define the Predicted Mean Vote to achieve The reference ambient temperature when the predicted mean vote is the same as the actual environment. In Germany, in 1987, applied meteorologists such as Maver and Hoppe proposed the famous Munich human heat balance model (MIEM) based on a comprehensive consideration of thermoregulation processes, and proposed the Physiological Equivalent Temperature (PET). 2000, the dynamic In 2000, Dynamic Physiological Equivalent Temperature (dPET) was established based on the Munich Human Heat Balance Model, thus expanding the application of physiological equivalent temperature.

PET is one of the most commonly used thermal comfort indices, and it can be defined as the air temperature at which the body's thermal balance in a typical indoor environment (without wind and solar radiation) is the same as the core and skin temperature of the complex outdoor conditions being evaluated [76]. In addition, PET is a widely used standard for predicting changes in thermal composition in urban and regional planning studies [77].

PET is widely used not only in Central Europe and cold climate regions but also in other subtropical, tropical, and monsoon regions [78]. To justify the use of PET in the study area, it is important to note that this thermal index has also been tested and applied in Lisbon, a Mediterranean climate influenced by the Atlantic Ocean [79] and other Mediterranean regions. The relevance of this index is that, in addition to being based on meteorological parameters, it reproduces the human physiological response to the environment, making it possible to assess thermal conditions indoors and outdoors.PET is a realistic climate index describing the thermal environment, enabling laymen to assess the thermal component of the climate based on personal experience [76]. One of the problems of this approach is the difficulty of obtaining complete input data to calculate PET.

Several research works have been carried out for the application of PET in outdoor thermal environments and different locations [80,81], and PET values can be calculated to evaluate outdoor thermal environments using the available software package Rayman [82]. Most outdoor thermal comfort studies use various thermal comfort indicators such as physiologically equivalent temperature (PET), outdoor standard effective temperature (OUTSET*, and universal thermal climate index (UTCI), taking into account six thermal parameters: air temperature, humidity, wind speed, solar radiation, metabolic rate, and clothing thermal resistance. Among them, solar radiation is the most complex factor among the input parameters [83].

In 2002, the WMO Meteorological Commission established the Universal Thermal Climate Index (UTCI) based on a multi-node model of body thermoregulation. Its structure is complex and realistic, and it is now widely used in the world. In addition to this, a total of more than 165 different thermal indices have been proposed during the development of thermal comfort index research [84]. A search of different thermal indices on the web of Science website yielded the results shown in Fig. 2.6: among them, PET, UTCI, SET*, and PMV are the four most commonly used indices, which is consistent with the results of previous studies [55]. PET is the thermal climate index currently most applied to outdoor thermal comfort.

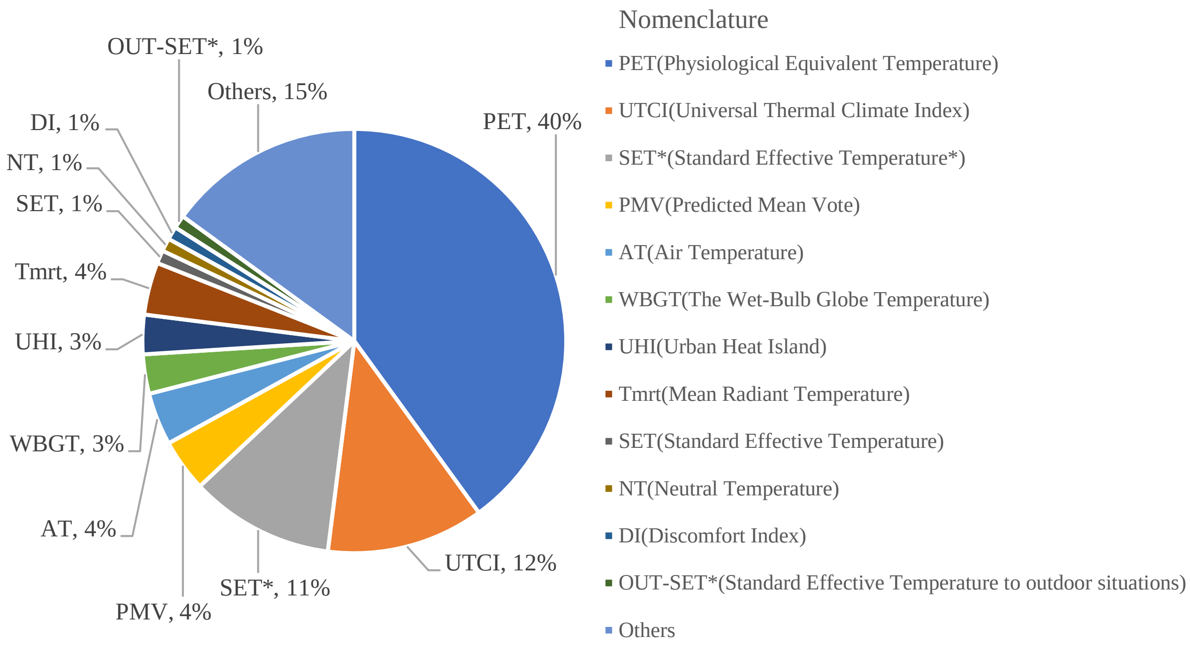

Fig. 2.6 *Frequency of thermal comfort index application in all studies.*

2.5.4. **PET theoretical basis and calculation**

The physiological equivalent temperature (PET) is the equivalent temperature of air temperature in a specific location (outdoors or indoors) with a typical indoor environment with core and skin temperature equal to the temperature under the assessed conditions. PET is based on the MEMI model (Munich Energy- balance Model for Individuals) to develop the metrics. The Munich Energy Balance Model (MEMI) is a thermo physiological model based on the heat balance equation of the human body, taking into account all basic thermoregulatory processes such as peripheral vasoconstriction or dilation and physiological sweating rate.

Human thermal equilibrium model：

$$M+W+R+C+E_D+E_{Re}+E_{Sw}+S=0 \qquad \textbf{(1)}$$

Where M is the metabolic rate (internal energy from food oxidation), W is the output of physical work, R is the net radiation of the body, C is the convective heat flow, the latent heat flow that evaporates water into water vapor diffused through the skin (imperceptible sweating), the sum of the heat flow that heats and humidifies inspired air prior to this, ESw the heat due to sweat evaporation, and the stored heat used to heat or cool the body mass flow. The individual terms in this equation have a positive sign if they result in an increase in energy to the body; they have a negative sign if there is a loss of energy (M is always positive; W, ED and Esw are always negative). All heat flows are in Watts.

In equation(1), some parameters depend on the average garment surface temperature, the average skin temperature, or the physiological sweat rate (all of the above parameters are influenced by environmental parameters), where the physiological sweat rate is both the basis for calculating Esw and a function of core temperature (core temperature depends on environmental conditions and activity). Therefore, to solve equation(1), the average surface temperature (Tcl), the average skin temperature (Tsk), and the core temperature (Tc) of the garment must first be obtained, and to obtain these three unknown quantities, two other equations are needed, which describe the heat transfer from the body core to the skin and from the skin surface to the clothing surface, respectively, equations (2) and (3):

$$F_{cs}=v_b\times\rho_b\times c_b b\times(T_c-T_{sk}) \qquad (2)$$

where,vb is the blood flow from the body core to the skin (l/s/m²), which is determined by the skin temperature and core temperature levels, ρb is the density of blood (kg/1), and cb is the specific heat capacity of blood (Ws/K/kg).

$$F_{cs}=(1/I_{cl})\times(T_{sk}-T_{cl}) \qquad (3)$$

where Icl is the clothing thermal resistance (Km2/W).

With equations (1), (2) and (3) and some heat physiological assumptions, it is possible to calculate the thermal state of the human body (i.e., heat flow, body temperature and sweating rate) under any meteorological condition, with activity and clothing thermal resistance.

PET is similar to the definition of effective temperature ET*, but according to the MEMI model, PET is defined as follows: when the human body (male, height 180 cm, weight 75 kg, clothing thermal resistance 0.9 clo, metabolic rate 80 W) is in a certain environment, his core temperature and skin temperature is equal to when in a typical room (average radiation temperature equal to air temperature, water vapor pressure equal to 1200 Pa, air velocity equal to 0.1 m/s), then the air temperature of this typical room is equal to the physiological equivalent temperature PET, the concept of PET allows a person to relate his sensations in different environments to the sensations indoors, thus allowing a person unfamiliar with biometeorology to evaluate different outdoor thermal environments. For example, a person in the summer sun with an air temperature of 30°C, a mean radiation temperature of 60°C, a wind speed of 1 m/s, and a partial pressure of water vapor of 2100 Pa would have a PET of 43°C, i.e., the thermal state of a person in this lower summer sun is the same as in a typical indoor room at 43°C. PET has been used primarily by researchers to determine the correspondence between PET and thermal sensation in different regions scales, as well as to study neutral PET temperatures in different regions to compare outdoor thermal comfort in different regions.

PET has the advantage of having well-known units (degrees Celsius) that allow different people to quickly understand the current level of the outdoor thermal environment. The calculation process consists of the following steps.

(a), For a given combination of meteorological parameters, the thermal condition of the human body is calculated using the MEMI.

(b), The calculated values of mean skin temperature and core temperature are inserted into the model MEMI and a system of energy balance equations is calculated for the air temperature Ta (v = 0.1 m/s, VP = 12 hPa and Tmrt= Ta).

(c), The air temperature obtained when the above conditions are satisfied is equivalent to PET.

The Rayman model is commonly used to calculate PET values and was developed according to the German Society of Engineers guidelines. It calculates the radiant flux in urban buildings based on air temperature, air humidity, cloud cover, time and date, the emissivity of surrounding surfaces, and the solid angle ratio. The PET values for the thermal environment parameters are obtained by entering the initial parameters in the Rayman model: air temperature, air humidity, wind speed, cloud cover, date and time of the calculation, geographical location of the calculation site, and the age, sex, weight, height, activity intensity and clothing thermal resistance of the person. The input initial parameters for this study were air temperature, relative humidity, radiation, and wind speed. All data sources were obtained from the WRF model simulation's direct output or the calculation of the output values. And the PET was calculated using standardized data (i.e. Age:35 years, Height:1.75; Metabolic rate:80w/m2; Clothing:0.9; Weight:75 kg; Sex: male).

PET values in different numerical intervals represent different degrees of heat sensation in the human body. To better interpret the results of PET calculations, PET was classified, and the table of heat sensation degrees used in this study is as follows (Table 2.4)：

Table 2.4 Thermal sensation classes for human beings.

PET（℃）	Thermal Perception	Grade of physical stress
> 41	Very hot	Extreme heat stress
35-41	Hot	Strong heat stress
29-35	Warm	Moderate heat stress
23-29	Slightly warm	Slight heat stress
18-23	Comfortable	No thermal stress
13-18	Slightly cool	Slight cold stress
8-13	Cool	Moderate cold stress
4-8	Cold	Strong cold stress

≤4	Very cold	Extreme cold stress

Chapter 3. Reproducibility analysis of WRF model in urban climate research

3.1. Introduction

With the progress of society and the economy, rapid urbanization has brought more convenience to human life. And too rapid urbanization has brought about changes in urban climate and even environmental degradation. In the face of global urbanization and global warming, urban climate issues have arisen. Over the past few decades, global heat wave events have increased each year, with most cities suffering stronger heat wave intensities and lasting longer. The rise in heatwave events has been attributed to high-density urban forms with low-density vegetation cover and increasing artificial heat dissipation due to urban sprawl [85]. As a result, the urban environment has attracted great attention worldwide.

In recent years, the Weather Research and Forecasting (WRF) model has become a popular tool for mesoscale urban climate studies. In the study of urban climate, because the city scale is large and the number of observation points is small, the WRF (Weather Research and Forecasting) model can reproduce the urban climate. Therefore, more and more researchers are applying WRF models to urban climate simulations.

For example [46] used the mesoscale WRF model to analyze the relationship between summer city size, coastal land use， and air temperature rise with distance from the coast in five coastal cities in Japan with different sizes and coast land use mesoscale cities in Germany. [86] used WRF to map wind and temperature distribution patterns and create an urban environmental climate map (UECM). Peng used the WRF calculation results to produce an urban environmental climate map, reproducing the range of the sea breeze cooling effect and the range of specific humidity rise effect [39].

The WRF model is usually used in large-scale numerical weather prediction, while the mesoscale urban climate research is relatively small compared with the weather prediction scale, so there is a certain difference between the simulated results and the real values. The magnitude of the difference reflects the agreement rate between the simulated and measured values. Meso-scale WRF model, the data are output according to a set frequency, making the data temporal and spatial in nature. However, the data may exhibit varying degrees of variability in rates across time and space. Therefore, this thesis provides a detailed discussion of the repeatability of the simulated and measured values from the perspective of time series and spatial locations.

3.2. data

The data used in this chapter are from August 5, 2016 (Sea Breeze Day). Because the main topic of this study is the effect of sea breeze on the urban environment, the sea breeze day was chosen as the study day when doing the reproducibility analysis of the measured data and the simulated data. Among them, the determination of the study day and its climatic conditions recorded at the weather station, including the specifics of insolation, air temperature, wind speed, and wind direction, see Section 4.3 Identification of sea breeze.

3.2.1. **Measurement data**

Long-term multi-point measurement sites were set up in the outdoor playgrounds of elementary schools in Sendai, with a total of 20 sites (Fig. 3.1, Table 3.1). The measurement points were placed away from buildings and trees. The data is acquired through temperature and humidity sensors placed inside the instrument shelters for recording. The recording frequency of the measuring instrument is set to ten minutes.

The measured points penetrate inland from the coast. The nearest point is 2.83 ㎞ from the coast, and the farthest point is 21.35km from the coast. The study area was divided into three regions according to the distance of each measurement point from the coast, and the degree of urbanization. I define the measured points (point 15 - point 20) within a range of seven kilometers from the coast as the coastal area. The measured points within seven to fifteen kilometers from the coast (point 5 - point 14) are defined as the urban area. The measured points within the range of fifteen to twenty-two kilometers from the coast (point 1 - point 4) are defined as the inland area.

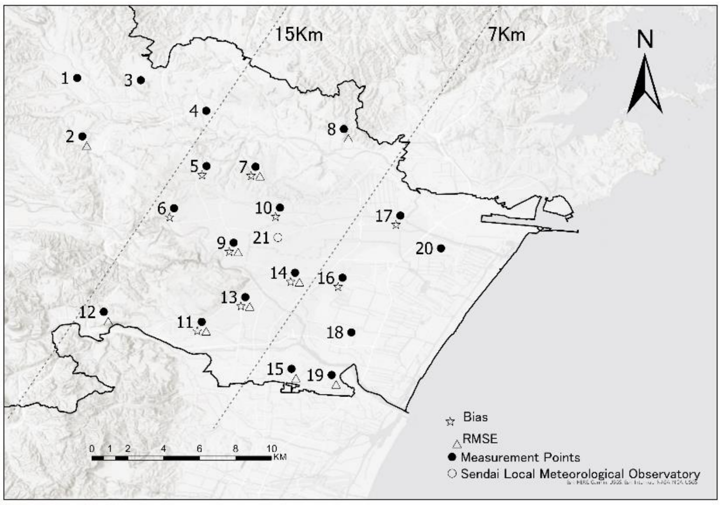

Fig. 3.1 *Map showing the location of Sendai and the distribution of temperature and humidity recorders and Sendai Local Meteorological Observatory in the study area. The extent of coastal areas, urban areas and inland areas are also indicated separately.*

Table 3.1 *Temperature and humidity recorder, and Sendai Local Meteorological Observatory information, including ID, name, coordinates and distance from the coast in the direction of prevailing winds.*

ID	Name	Lon.	Lat.	Distance(Km)
1	Nenoshiroishi	140.79660	38.34173	21.35
2	Yakata	140.79917	38.31259	19.68
3	Teraoka	140.82839	38.34062	18.92
4	Nomura	140.86110	38.32529	15.65
5	Kita-Sendai	140.86121	38.29776	13.91
6	Kunimi	140.84500	38.27667	14.02
7	Asahigaoka	140.88570	38.29738	12.15
8	Tsurugaoka	140.92988	38.31623	10.15
9	Higashi Nibancho	140.87478	38.25946	10.82
10	Saiwaicho	140.89793	38.27696	10
11	Nishitaga	140.85883	38.21992	11.63
12	Hitokita	140.80989	38.22493	14.75
13	Nagamachi	140.88062	38.23226	8.98
14	Minamikoizumi	140.90545	38.24443	7.61
15	Fukurobara	140.90368	38.19646	5.92
16	Kabanomachi	140.92917	38.24194	5.6
17	Takasago	140.95810	38.27296	5.27
18	Rokugo	140.93361	38.21472	3.75
19	Higashishiromaru	140.92375	38.19338	4.15
20	Okada	140.97840	38.25668	2.83
21	Observatory	140.89692	38.26209	9.43

3.2.2. **Simulation data**

In this study, a mesoscale weather research and forecasting (WRF) model was used to numerically simulate the study area. A total of three nested domains were set up (Fig. 2.5), each with spatial resolutions of 1km, 3km, and 9km from the inside out. The land data utilizes data from the Digital Land Information released by the Japanese government in space with a resolution of 1 km. The period for the calculation was set from August 1, 2016, to August 10, 2016. The numerical output frequency is the same as the measured data. The other main physical configurations of the model are shown in Table 2.3. See section 2.3 for all about software setup.

3.3. Reproducibility analysis of WRF model data

3.3.1. Analysis of Bias, RMSE and Correlation

The reproducibility analysis of the WRF model data was done using simulated data paired with actual measured point data for comparative analysis. This is because the simulation points are uniformly distributed in the simulation domain, while the measurement points are randomly distributed in the playgrounds of each elementary school in Sendai. Therefore, the simulated and measured points have some deviation in position and do not coincide exactly. Because the simulation points are uniformly covered over the entire study area, there will always be a point closest to the measurement point. Each measured point data is compared with the nearest simulated point data. Table 3.2 details the specific locations of the measured(ID) and simulated(FID) points and the distances between them.

Table 3.2 *The location of the measured and simulated points and the distance between them.*

ID	Station Name	Lon.	Lat.	FID	Lon.	Lat.	Distancd(Km)
1	Nenoshiroishi	140.7966	38.3417	731	140.7933	38.3416	0.29
2	Yakata	140.7992	38.3126	633	140.8047	38.3144	0.54
3	Teraoka	140.8284	38.3406	734	140.8279	38.3416	0.12
4	Nomura	140.8611	38.3253	671	140.8627	38.3235	0.24
5	Kita-Sendai	140.8612	38.2978	572	140.8627	38.2963	0.21
6	Kunimi	140.8450	38.2767	504	140.8395	38.2781	0.51
7	Asahigaoka	140.8857	38.2974	574	140.8858	38.2963	0.12
8	Tsurugaoka	140.9299	38.3162	644	140.9320	38.3144	0.27
9	Higashi Nibancho	140.8748	38.2595	441	140.8742	38.2600	0.08
10	Saiwaicho	140.8979	38.2770	509	140.8973	38.2781	0.14
11	Nishitaga	140.8588	38.2199	308	140.8627	38.2237	0.54
12	Hitokita	140.8099	38.2249	303	140.8049	38.2237	0.46
13	Nagamachi	140.8806	38.2323	343	140.8858	38.2328	0.46
14	Minamikoizumi	140.9054	38.2444	378	140.9089	38.2419	0.41
15	Fukurobara	140.9037	38.1965	213	140.9089	38.1965	0.45
16	Kabanomachi	140.9292	38.2419	380	140.9320	38.2419	0.25
17	Takasago	140.9581	38.2730	481	140.9551	38.2691	0.51
18	Rokugo	140.9336	38.2147	281	140.9319	38.2146	0.15
19	Higashishiromaru	140.9238	38.1934	214	140.9204	38.1965	0.45
20	Okada	140.9784	38.2567	450	140.9782	38.2600	0.37

In this study, the reproducibility of the measured and simulated data was analyzed by Bias, RMSE and correlation and error analysis. Bias is used to indicate the degree of fit between the simulated and real values. The smaller the absolute value, the higher the degree of fit and vice versa. Define the average value of all simulated points covered in the range of real measurement points as S (Simulated) and the measured value of each measurement point as Mn (Measured), then the calculation of deviation is calculated as Biasn = S - Mn. RMSE (Root Mean Squared Error), a measure of accuracy, is often used to measure the difference between the simulated or estimated value of a model and the measured value. The formula is as follows:

$$\mathrm{RMSE} = \sqrt{\frac{\sum_{i=1}^{n}\left(X_{mea,i} - X_{sim,i}\right)^2}{n}}$$

The results of Bias, RMSE, and correlation calculations are presented in Table 3.3. Based on the data analysis it can be concluded that the correlation of all points is strong. After ranking the Bias and RMSE difference values from largest to smallest, the top ten with large differences are indicated in Fig. 3.1 and Table 3.3. The top ten absolute values of all Bias values are marked with ▲, and the top ten RMSE values are marked with ★. The points where the different values of Bias and RMSE are simultaneously larger appear at points 7, 9, 11, 13, and 14. As can be seen in Figure 3.1, all five points are distributed in urban areas. It can be seen that the higher the degree of urbanization, the higher the difference. This is the same conclusion reached in the previous study.

***Table 3.3** Results of precision inspection for temperature numerical computation*

ID	Location	Bias[℃]	RMSE[℃]	Correlation
1	Nenoshiroishi	-0.55	0.68	0.981
2	Yakata	-0.88	0.82 ☆	0.973
3	Teraoka	-0.76	0.82	0.974
4	Nomura	-0.13	0.43	0.993
5	Kita-Sendai	-1.36 △	0.57	0.984
6	Kunimi	-1.81 ▲	0.53	0.985
7	Asahigaoka	-1.72 ▲	0.99 ★	0.945
8	Tsurugaoka	-0.62	1.09 ★	0.945
9	Higashi Nibancho	-2.49 ▲	1.00 ★	0.936
10	Saiwaicho	-1.53 ▲	0.58	0.979
11	Nishitaga	-2.05 ▲	0.99 ★	0.939
12	Hitokita	-0.24	0.88 ★	0.969
13	Nagamachi	-2.13 ▲	0.86 ☆	0.950
14	Minamikoizumi	-2.15 ▲	0.88 ★	0.937
15	Fukurobara	-0.84	1.03 ★	0.912
16	Kabanomachi	-1.29 △	0.53	0.969
17	Takasago	-1.36 △	0.80	0.957
18	Rokugo	-1.20	0.82	0.926
19	Higashishiromaru	-0.60	1.34 ★	0.802
20	Okada	-0.59	0.75	0.939

3.3.2. **Error dynamics analysis**

Based on the data derived in section 3.3.1, it is clear that the difference between the measured and simulated data have area characteristics. The difference at each point show that there are different degrees of influence on the simulated values of mesoscale urban climate at different geographical locations and urban environments. In order to assess the errors between numerical simulations and measured values at different locations and times, a dynamic analysis of the errors was done for the whole study area and for each of the three regions for 24 hours a day. Where the error is defined by defining the nth measured value of A measured point is An, and the nth simulated value of B, the nearest simulated point with A measured point, is Bn, then the nth comparison difference of A, B points. That is, Xn = Bn - An. The error is calculated by taking the average value of temperature at each time point, separately for the whole area and the three area.

After observing the dynamic graph of the entire area error (Fig. 3.2), it is found that the error values are negative except for the two local periods of 4:00-6:00 and 22:00-24:00, which are positive values. Such a result means that the simulated value is lower than the measured value most of the time. The error values start to increase gradually at 6:00 and start to decrease after reaching a peak at 10:00. After that, the error value is maintained at a certain level from 12:00-13:30 and then decreases rapidly. At 15:00 it started to rise again and at 16:30 it started to fall once again. From the total 24-hour time period, 63.89% of the period, error value is between 0℃-1℃, and mainly concentrated in the two time periods of 0:00-7:00 and 17:30-24:00. 10.42% of the period, the error value is between 2℃-3℃ and mainly concentrated in 9:10-11:40. The remaining 25.69% of the period had error values between 1°C and 2°C.

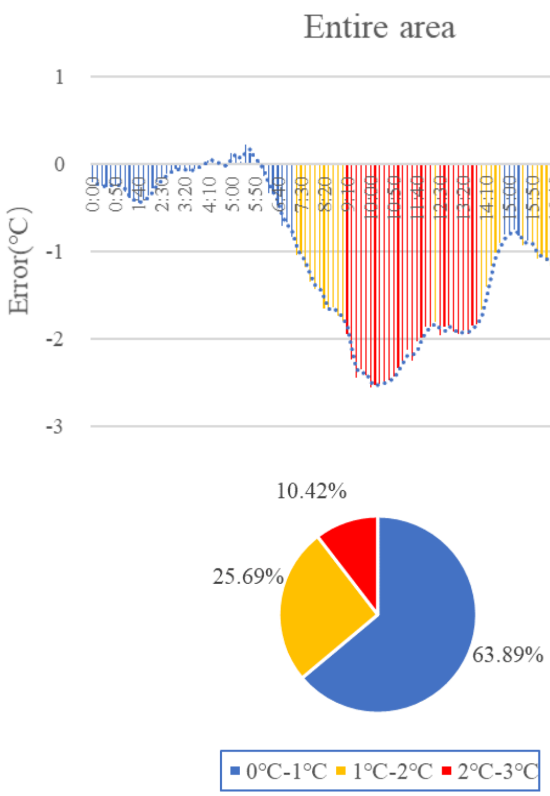

Fig. 3.2 *The error dynamic curve for the entire area.*

After observing the dynamic graph of the error in the inland area (Fig. 3.3), After observing the dynamic graph of the error in the inland area (Fig. 3.3), it is found that the error values show negative values in the time period of 7:00-20:00 and positive values in the rest of the time period. Such results indicate that in the inland area, the simulated values appear low in the daytime and high in the morning and night. The error value starts to change from positive to negative at 6:00, and the first lowest peak occurs at 9:30, then decreases until 11:00 when it rises again, and rapidly decreases after stabilizing in a certain range from 12:30-14:00. From the total 24-hour time period, 68.75% of the time period, the error value is between 0℃-1℃, mainly concentrated in the two time periods of 00:00-8:40 and 15:00-21:40. Only 2.08% of the time periods had error values between 2°C and 3°C, distributed among several data in the 12:00-14:00 time period. The remaining 29.17% of the time period had error values between 1°C and 2°C.

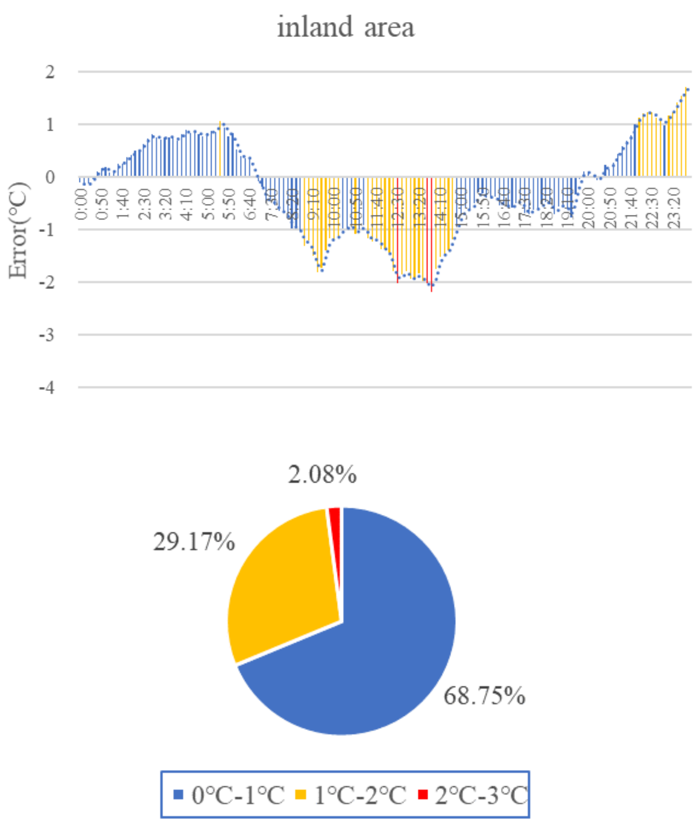

***Fig. 3.3** The error dynamic curve for the inland area.*

Observation of the error dynamics plot for the urban area shows that all simulated values show low results (Fig. 3.4). The error values start to increase from 6:00, reach a peak at 11:00. A slowdown in the descent occurred at 12:30, followed by another rapid descent at 14:00. It then started to rise again at 15:00 and dropped again at 17:00. From the total 24-hour time period, 54.86% of the period, the error value is between 0℃-1℃, mainly concentrated in the two time periods of 00:00-6:40 and 18:00-24:00. In 21.53% of the time periods, the error value was between 2° C-3° C, concentrated in 9:30-14:00. The remaining 23.61% of the time periods, the error value was between 1°C-2°C.

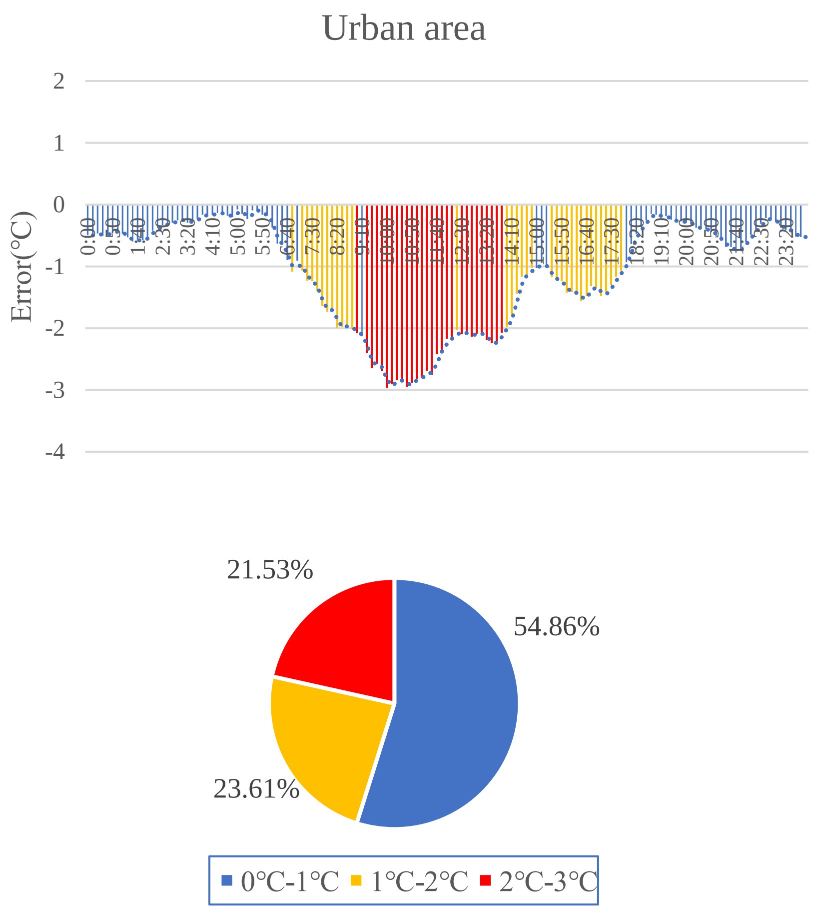

Fig. 3.4 *The error dynamic curve for the urban area.*

Observation of the dynamic graph of the coastal area error shows that almost all the simulated values show low results (Fig. 3.5). Only two very low positive values were observed between 19:00-20:00 and 22:30-24:00. The error value increases rapidly at 7:00, reaching a peak at 10:30. The error value then starts to decrease, with a small increase at 15:00 and a decrease again at 16:30. Looking at the total 24-hour time period, 61.11% of the period, the error value was between 0°C and 1°C and occurred in a similar period to the urban area. 14.58% and 7.64% of the periods showed error values greater than 2°C, concentrated between 8:30-13:00. The error values of 3℃-4℃ appeared at 9:40-11:00, and the largest error value was -3.75℃, which appeared at 10:10. For the remaining 16.67% of the period, the error value was between 1° C and 2° C.

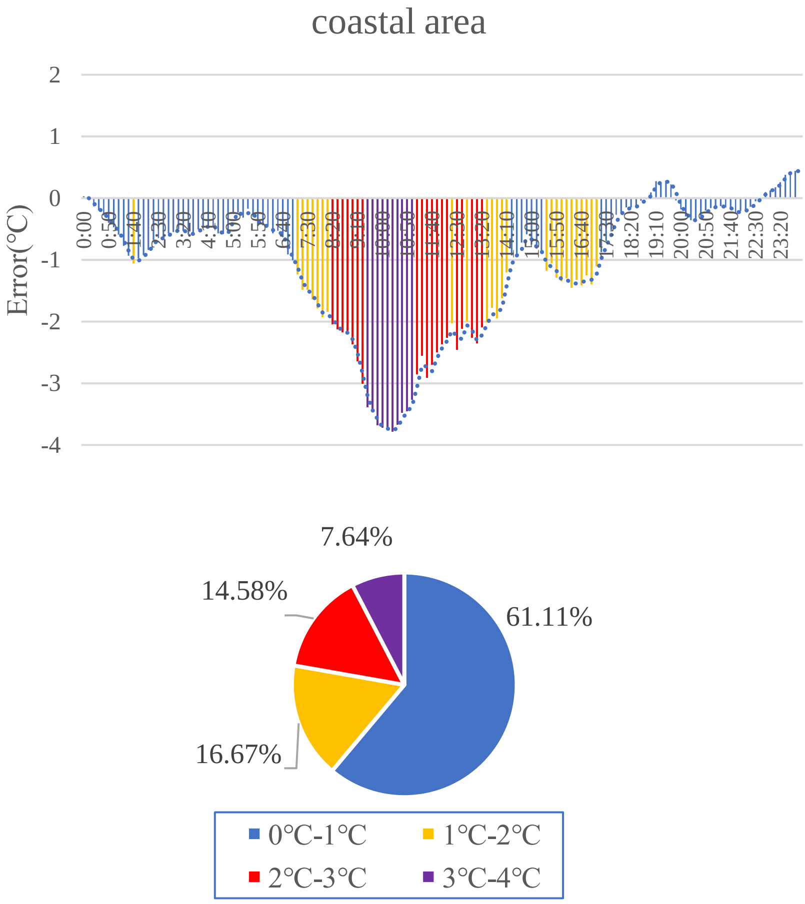

Fig. 3.5 The error dynamic curve for the coastal area.

3.4. Conclusions

In the reproducibility analysis of the WRF model data, it was concluded that there was a large correlation between the simulated and measured values at all points. Among the three areas, the urban area has the highest difference value. In the error dynamics analysis, the simulated values are always lower than the measured values in the rest of the area, except for the local period in the inland area. During the day, higher errors always occur around the 10:00-12:00 time period. And among the three areas, the coastal area locally presents higher error values and the inland area has the lowest error values.

Chapter 4. Analysis and Mapping of Sea Breeze Event Time in Coastal Cities

4.1. Introduction

Chapter Four analyzes and maps the timing of sea breeze events in coastal cities. This chapter first summarizes the characteristics of summer sea breeze activity in Sendai, the study area, and then introduces the method of identifying sea breeze days. A temporal map of summer sea breeze events in Sendai was derived from the target day meteorological data simulated by mesoscale meteorological studies and predictive WRF models. The data were also visualized by using ArcGIS Pro to reproduce the sea breeze arrival time, sea breeze retreat time, and the distribution of sea breeze events in the study area.

4.2. Basic Characteristics of Summer Sea Breeze Activity in Sendai

As Sendai is the subject of this thesis, it is necessary to analyze its climatic characteristics in detail, especially the characteristics of summer sea breeze activity. After defining August as the study month, the analysis focuses on the temperature characteristics of Sendai's August sea breeze days and summarises the temporal characteristics of Sendai's sea breeze events.

4.2.1. **Representative Validation of the Study Period**

In this Chapter, data from Sendai's local meteorological observatory were used to analyze and organize the climate characteristics of Sendai city in summer. The study period was chosen to be three years, 2018-2020. And the three-year study period (summer 2018-2020) was compared with two periods of twelve years (summer 2010-2021). After screening out the summer sea breeze days of the two periods, the daily mean temperature curves of the sea breeze days of the two periods overlapped (Fig. 4.1) Therefore, the results of the study are considered to be a good representation of the temperature characteristics of the sea breeze days in Sendai city in summer for the study period.

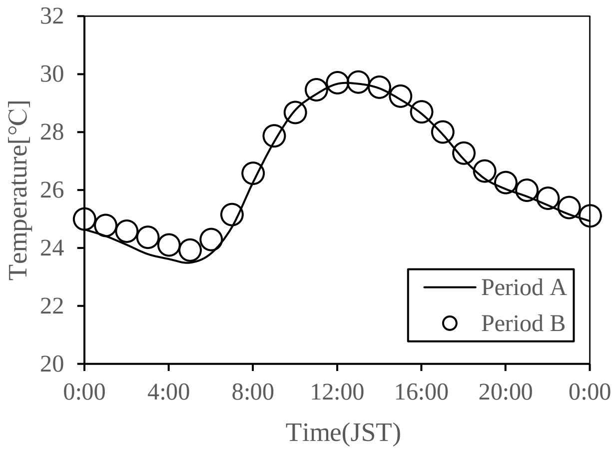

Fig. 4.1 *Average diurnal temperature fluctuations at Sendai Local Meteorological Observatory during period A (August 2010 to 2021) and period B (August 2018 to 2020) on sea breeze days.*

4.2.2. **Define the Research Month**

Sea breezes usually occur in warm seasons, and since the focus of this study is on sea breeze events, the statistics focus on the characteristics of hot summer weather. According to the 3-year monthly mean temperature curves of the study period (Fig. 4.2a), the highest monthly mean temperature in 2019 and 2020 occurred in August, and the highest monthly mean temperature in 2018 occurred in July, followed by August. Of these, the highest-temperature days in 2018 and 2020 occurred in August and the highest-temperature day in 2019 occurred in July (Fig. 4.2b). Finally, the number of days with maximum temperatures greater than 30°C in June, July and August for the three years of the study period was counted. Most of the days are concentrated in July, and August, with more than half of the days in 2019 and 2020 occurring in August. This shows that hot days are most common in August. Therefore, August was used as our focus month in this study (Fig. 4.3).

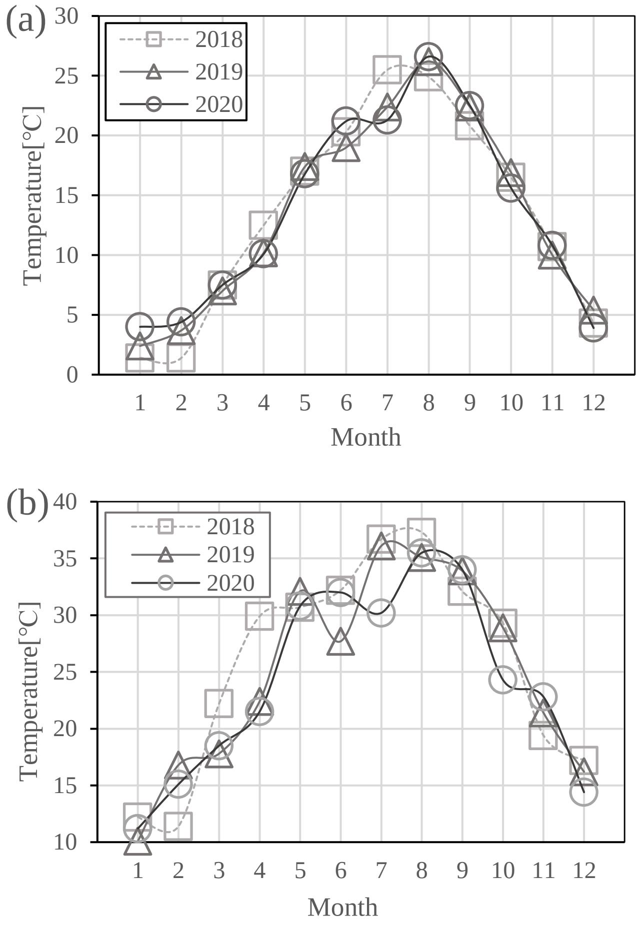

Fig. 4.2 *(a) The monthly average temperature from 2018 to 2020; (b) Monthly maximum temperature from 2018 to 2020.*

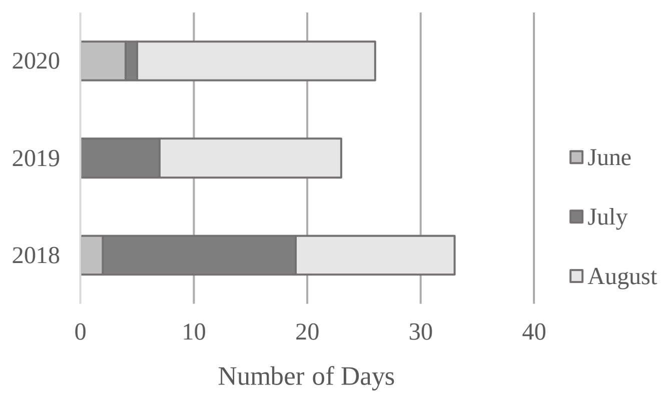

Fig. 4.3 *The number of days with a daily maximum temperature greater than 30 degrees Celsius in July–August–September from 2018 to 2020.*

4.2.3. **August Sea Breeze Daily Temperature Characteristics**

This section collates the temperatures for all sea breeze days during the study period (see Section 4.3 for the method of identification of sea breeze days). The number of sea breeze days increased each year from 2018 to 2020. In 2020, more than 20 days were defined as sea breeze days. Additionally, in any given year, more than half of the days identified as sea breeze days had high temperatures greater than 30°C (Fig. 4.4.). From this, it can be found that the temperature on sea breeze days is usually very high.

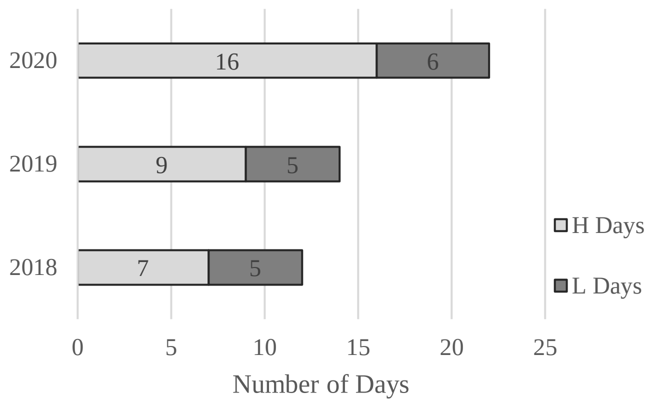

Fig. 4.4 *Number of days with maximum temperatures above 30 degrees Celsius (H Days) and below 30 degrees Celsius (L Days) for August 2018 to 2020 and defined as sea breeze days.*

4.2.4. **Temporal Characteristics of Sendai Sea Breeze Event**

Unlike the previous definition of sea breeze arrival and retreat times by wind conditions, this study determines the sea breeze arrival and retreat times based on the variation of sea breeze daily temperature and specific humidity (Fig. 4.5). When the sun rises, the temperature of the land begins to rise, forming a pressure difference with the sea, and the air begins to move from the sea to the land. The wind blowing from the direction of the sea brings cold air, so the point at which the temperature starts to drop after sunrise is defined as the time when the sea breeze arrives. The continuous rise in temperature is suppressed when the sea breeze arrives, which lowers the city's temperature. Additionally, it also brings humidity. The temperature fluctuates in a constant range, and the humidity rises again after a significant drop at midday due to strong sunlight. Because of the weakening of insolation, the temperature starts to exceed the constant range, and the rate of decrease increases significantly. At this point, the specific humidity also drops sharply again, and this study defines this moment as when the sea breeze retreats.

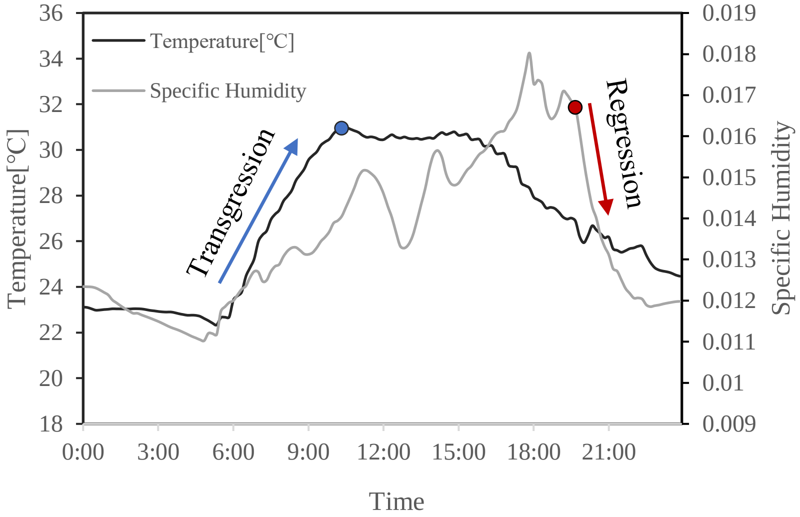

Fig. 4.5 *The diurnal temperature fluctuations and diurnal specific humidity fluctuations for August 5, 2016. The points pointed by the arrows show the time of arrival (blue points) and retreat of the sea breeze (red points).*

The total number of sea breeze days in August during the study period was 48 days. The sea breeze arrival time was distributed between 8:00-16:00, concentrated between 10:00-13:00, and 11:00 was the most common time for most days (Fig. 4.6 a).

Of all sea breeze days in August during the study period, the maximum temperature was greater than 30°C on a total of 32 days. The sea breeze arrival time on these days was distributed between 9:00 and 14:00, concentrated between 10:00 and 12:00, and 12:00 was the most common time for most days (Fig. 4.6 b).

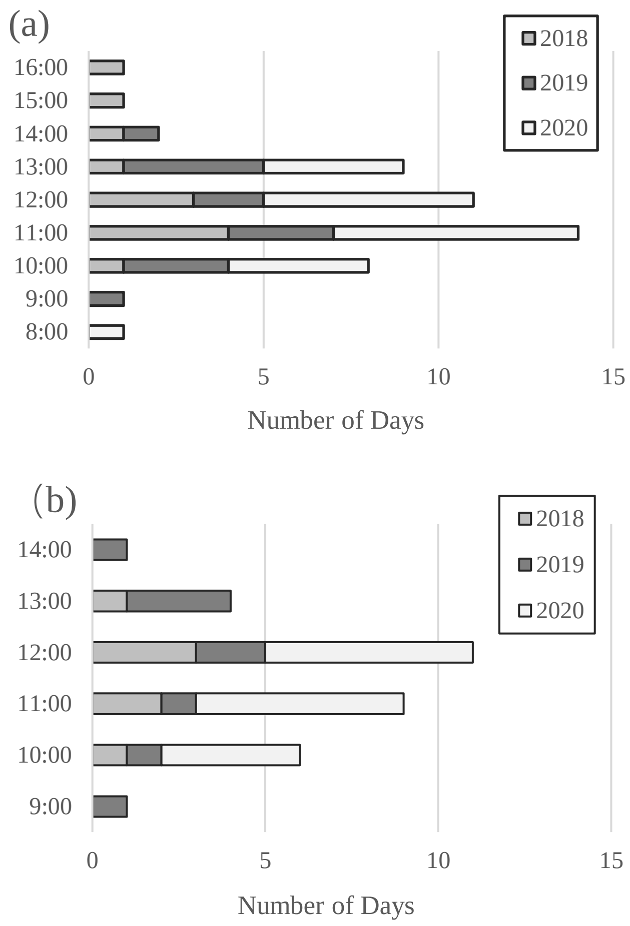

Fig. 4.6 *(a) Sea breeze arrival times for all sea breeze days in August from 2018 to 2020; (b) Sea breeze arrival times for August sea breeze days with maximum temperatures above 30 degrees Celsius from 2018 to 2020*

4.3. Identification of Sea Breeze Day

4.3.1. **Data used to identify sea breezes**

Sea breeze always appears in warm seasons. Therefore, only the summer season was selected as the study subject in this study. In Japan, June, July, and August are usually defined as summer. The historical records show that the highest frequency of high temperature occurs in August, therefore, August is used as the main subject of study. This study used data from Sendai Local Meteorological Observatory, long-term multi-point measurement data, and WRF model calculations. See Chapter 2 for a description of all data. Data from weather stations are used to analyze Sendai's climate and to select sea breeze days. The data are then collated by long-term multi-point measurement data for all sea breeze days. From the collated data, a day that can reflect most of the sea breeze day state is selected as the target study day; the sea breeze event time and characteristics are analyzed in detail, and finally, the sea breeze event map is drawn by the WRF model calculation data, in which the observed data and the WRF model calculation data are verified in detail.

4.3.2. **Specific methods for identifying sea breeze days**

In this study, the sea breeze days were determined from the data of meteorological observatory data downloaded from the Japan Meteorological Agency. The specific method is to determine the sea breeze day by the type of sea breeze and the change characteristics of meteorological variables after the occurrence of sea breeze. In addition, to exclude the interference of other factors, a sunny day was needed to identify the sea breeze day. Specifically, these include the following.

Sunshine: 40% or more of the possible sunshine hours.

Cloud: less than 5% cloud.

Rainfall: no rainfall.

Wind: wind blowing from the sea to the land lasting at least 2 hours.

Temperature: a drop in temperature lasting 1 hour or more after the start of the sea breeze.

4.3.3. **Case Study Day**

Based on the temporal characteristics of the Sendai sea breeze event in Section 4.2.4, the days when the sea breeze arrives at 11:00 or 12:00 are selected as the proposed study. Based on meeting the sea breeze day identification condition, to reduce the disturbance factor, in the daylight requirement, choose a day of all-day sunshine, and choose a day of stable wind direction after the sea breeze reaches the land. August 5, 2016, was finally chosen as the case study data for this study (Fig. 4.7).

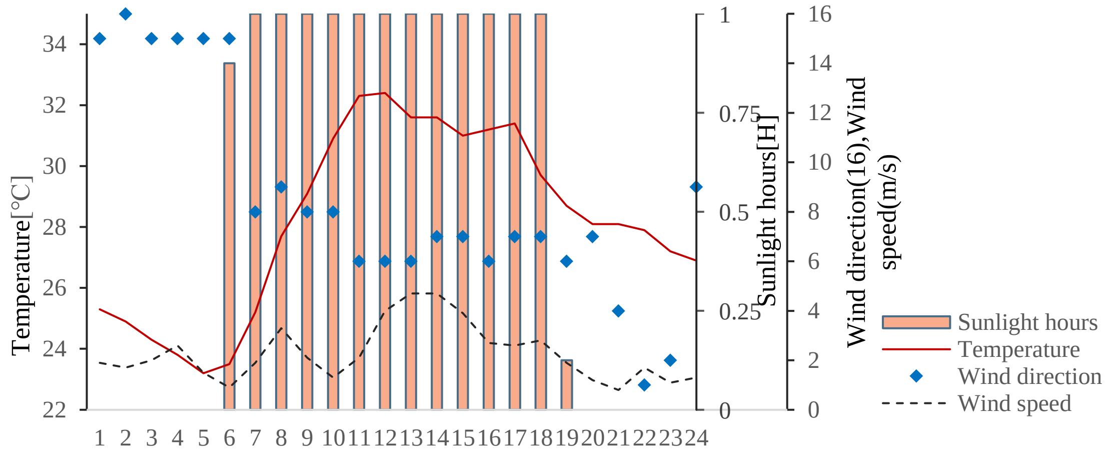

__Fig. 4.7__ Meteorological characteristics of the case study day (Aug.5.2016). Includes sunlight hours, temperature, wind direction, and wind speed.

4.4. Mapping the Time of Summer Sea Breeze Event in Sendai City

4.4.1. Sea Breeze Arrival Time

Using the sea breeze arrival time defined in Section 4.2.4, the temperature data generated by the WRF at each point were read to identify the sea breeze arrival time at each point. Finally, a sea breeze arrival distribution map was generated using ArcGIS Pro (Fig. 4.8a). See Section 2.4 for details on how to generate distribution maps with ArcGIS Pro. The following is a detailed discussion of the sea breeze arrival time distribution chart.

From 7:00 to 12:40, the sea breeze gradually penetrates inland from the coast (Fig. 4.8a). To analyze the velocity, the points in two directions (L1 and L2) are arranged separately (Fig. 4.8b). Figure 11c shows the location and environment of the points in the city. The points are consecutive, and both are spaced 1.5 km apart. The analysis of the sea breeze arrival time map and the line graph shows that all parts close to the coast have a slower sea breeze blowing towards the land. In the line graph, L1 shows (Fig. 4.8d) that the total time from point 1 (at 0 km) to point 4 (at 4.5 km) is 2 hours and 20 minutes, and the speed is uniform. From point 4, the pace starts to pick up, reaching point 13 inland (at 18 km) in a total of 2 hours and 40 minutes, a fast and even pace. L2 shows that the speed from point 1 (at km 0) to point 3 (at km 3) is about the same as L1. The speed increased rapidly from point 3, penetrating to point 10 (13.5 km) in just one hour, after which the speed began to decrease. Overall, L1 is slower than L2. L2 reaches point 13 (at km 18) one hour ahead of L1.

As can be seen in Fig. 4.8 b, for the region from point 6 to point 10 in the L2 direction, the penetration of the sea breeze inland is significantly accelerated. In Fig. 4.8c, it is found that points 6 to 10 are distributed near inland rivers. This is the same as the conclusion of Bastin's study that "inland rivers enhance the penetration of sea breeze inland" [87].

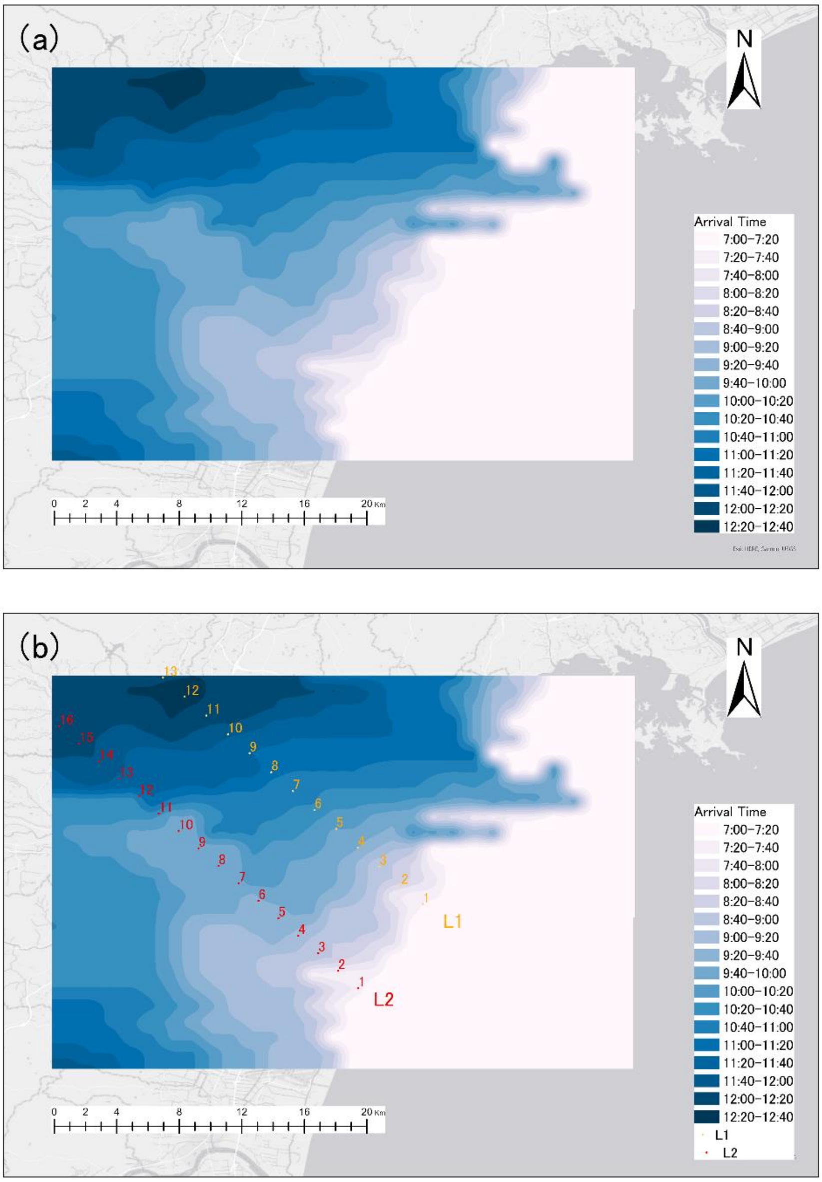

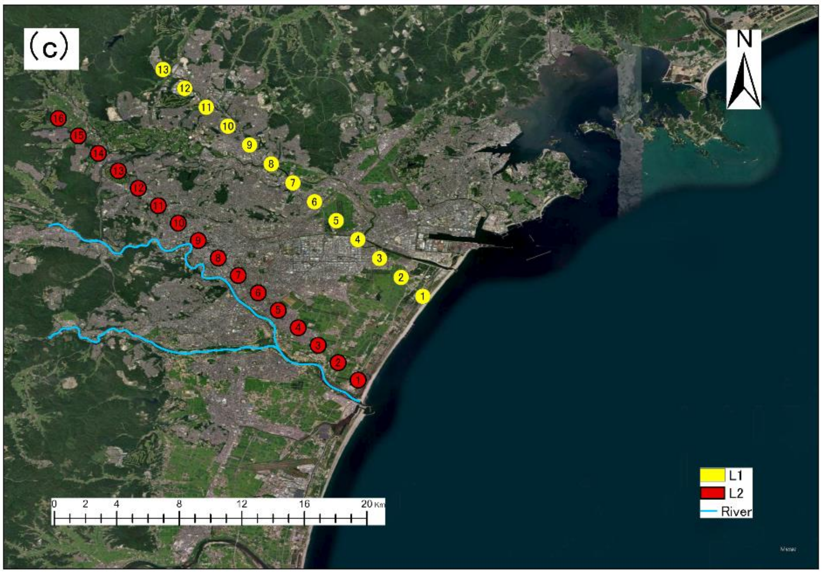

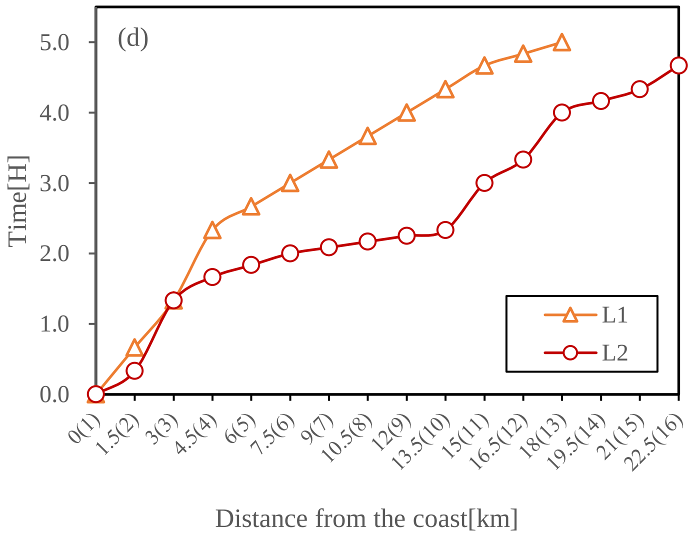

Fig. 4.8 *(a) Sea breeze arrival time map; (b) Distribution of points in the L1 and L2 directions on the sea breeze arrival time map; (c) Distribution of points in the L1 and L2 directions on the satellite map; (d) arrival times of points in the L1 and L2 directions.*

4.4.2. **Sea Breeze Retreat Time**

From 17:30 to 22:30, the sea breeze retreats towards the coast from inland areas, specifically from compact mid-rise and compact low-rise areas [88](Fig. 4.9a). With the retreat direction as the central point, the sea breeze retreat time was analyzed from three directions based on the topography of Sendai (Fig. 4.9b). Figure 4.9c shows the location and environment of the points in the city. According to Fig. 4.9d, it can be seen that L1 is obviously much faster than L2 and L3. The retreat from point 11 (at 15 km) to the coast took only 3 hours and was fast and even. Additionally, L2 and L3 used a total of 4 hours and 30 minutes to retreat from point 13 (at 18 km) to the coast. L2 began to decrease in speed at point 11 (at 15 km), increased in speed from point 9 (at 12 km) and retreated to the coast from point 5 (at 6 km) in just 30 minutes. L3 retreated from point 13 (at 18 km) to point 8 (at 10.5 km) at about the same speed as L1, but after point 8, the speed decreased significantly. The decrease continued until point 4 (at 4.5 km), where the speed started to increase until it reached the coast. From Fig. 4.9c, it can be found that the area where the retreat velocity of sea breeze decreases coincides with the urban edge, similar to Martilli's conclusion that "the roughness of the urban surface has a strong influence on the intensity of sea breeze"[89].

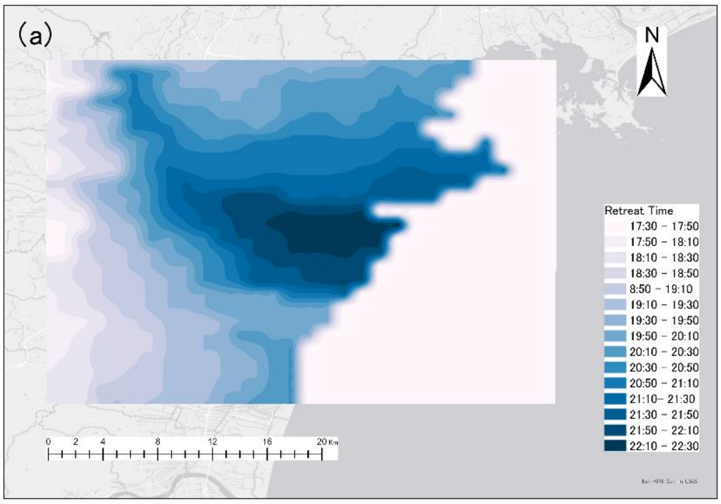

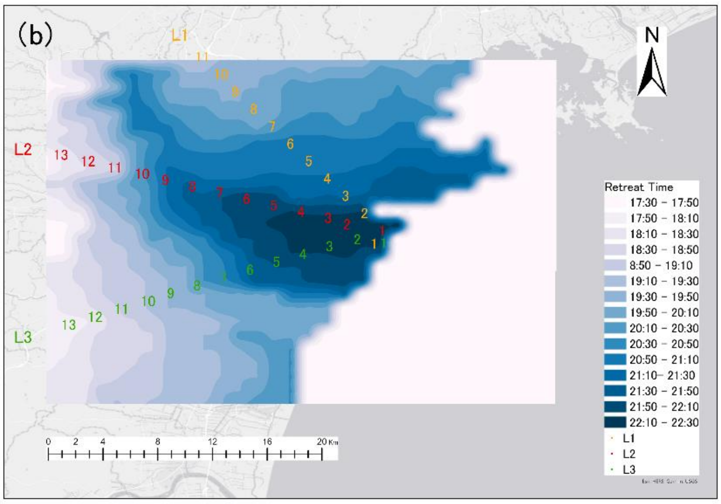
(b)
N
L1
L2
L3
Retreat Time
17:30 – 17:50
17:50 – 18:10
18:10 – 18:30
18:30 – 18:50
8:50 – 19:10
19:10 – 19:30
19:30 – 19:50
19:50 – 20:10
20:10 – 20:30
20:30 – 20:50
20:50 – 21:10
21:10– 21:30
21:30 – 21:50
21:50 – 22:10
22:10 – 22:30
0 2 4 8 12 16 20 Km

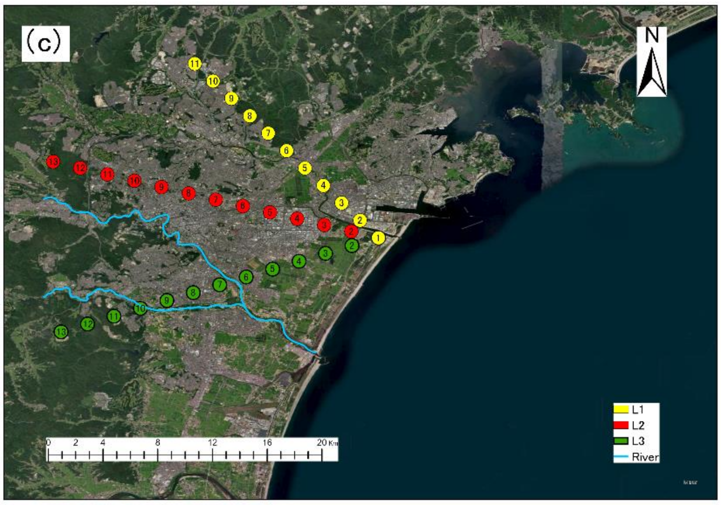
(c)
N
L1
L2
L3
River
0 2 4 8 12 16 20 Km

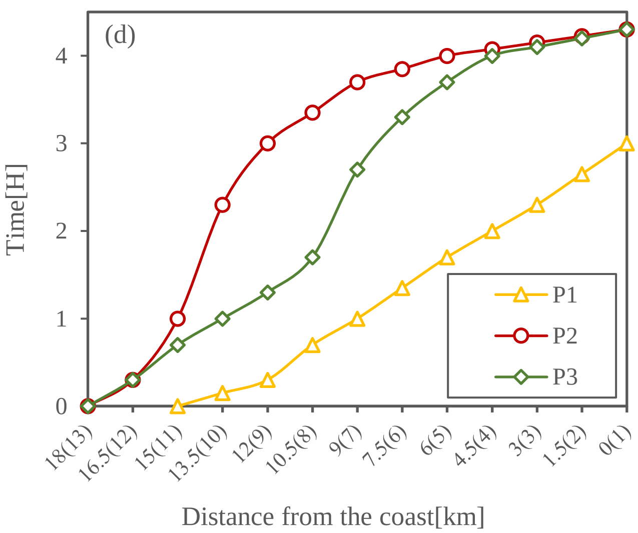
(d)
Time[H]
0
1
2
3
4
P1
P2
P3
18(13)
16.5(12)
15(11)
13.5(10)
12(9)
10.5(8)
9(7)
7.5(6)
6(5)
4.5(4)
3(3)
1.5(2)
0(1)
Distance from the coast[km]

Fig. 4.9 *(a) Sea breeze retreat time map; (b) Distribution of points in the L1, L2 and L3 directions on the sea breeze retreat time map; (c) Distribution of points in the L1, L2 and L3 directions on the satellite map; (d) The time when the L1, L2, and L3 directions retreat to each point.*

4.4.3. **Duration of Sea Breeze**

The sea breeze lasts for a minimum of 6 hours and up to 15 hours (Fig. 4.10a). As can be seen from Fig. 4.10b, the duration increases gradually from inland to coastal times. The histogram in all three directions shows that the increase in duration is uniform and continuous (Fig. 4.11a). Additionally, the total duration histogram showed that the cumulative duration of L1 and L3 was about the same. Additionally, in L2, the cumulative duration is about 13 hours longer than in L1 and L3 (Fig. 4.11b).

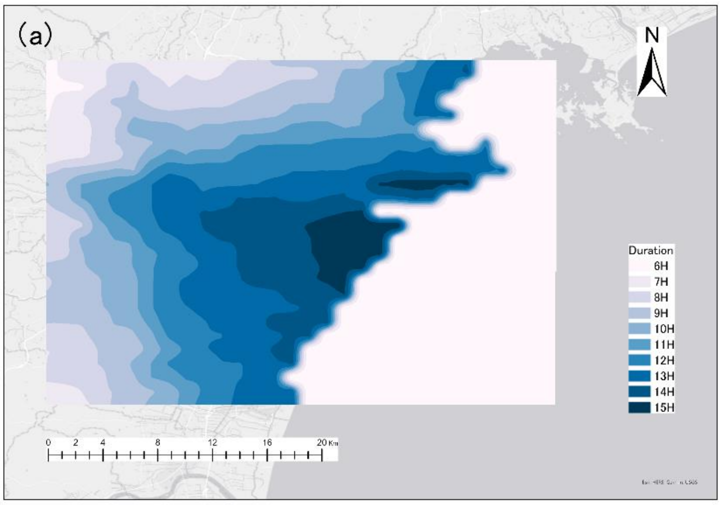

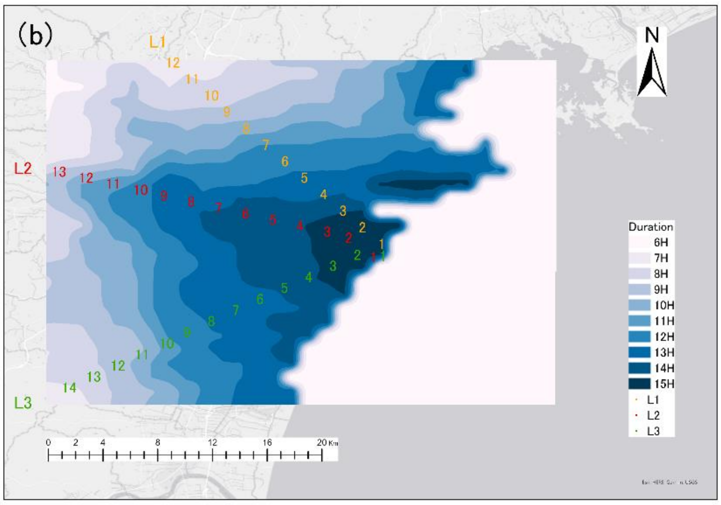

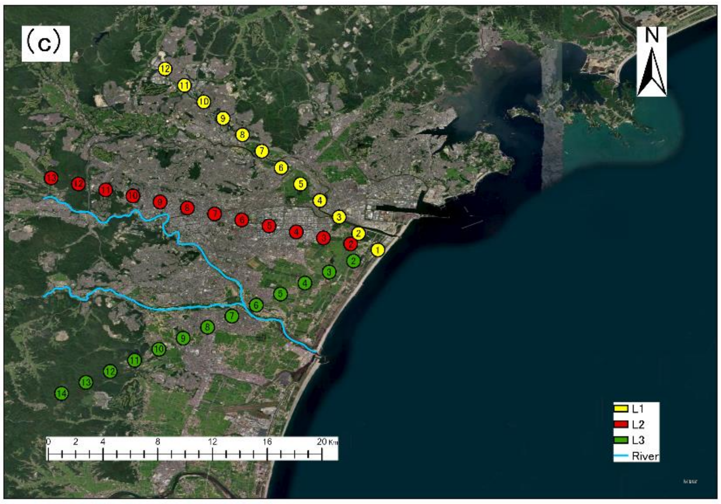

Fig. 4.10 *(a) Sea breeze duration time map; (b) Distribution of points in the L1, L2 and L3 directions on the sea breeze duration time map; (c) Distribution of points in the L1, L2 and L3 directions on the satellite map.*

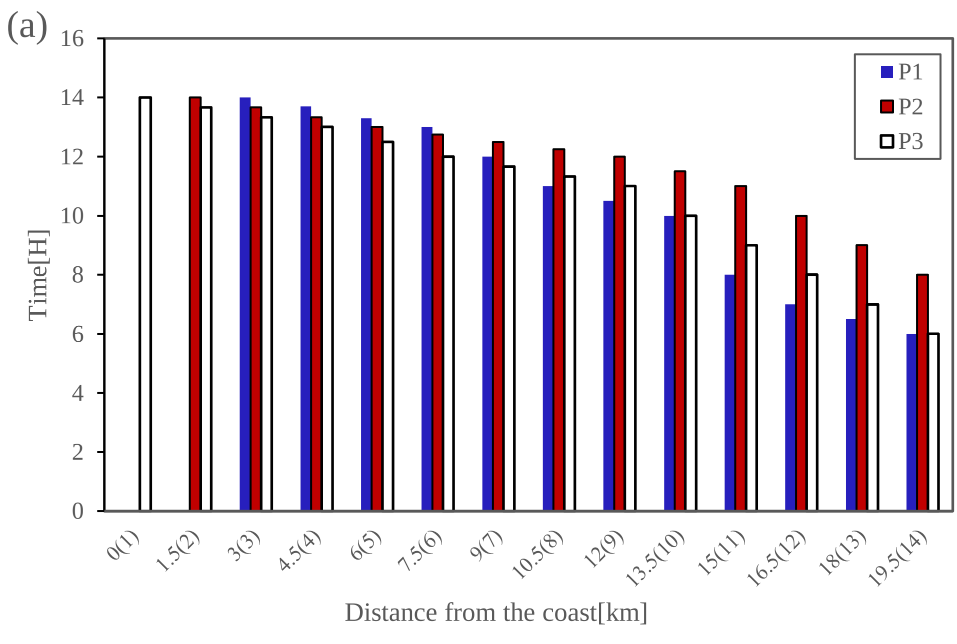

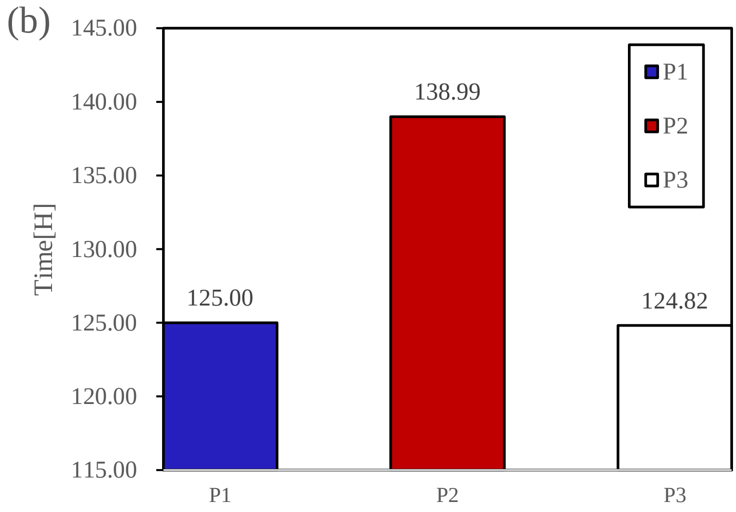

Fig. 4.11 *(a) The sea breeze duration at each point in the L1, L2 and L3 directions; (b) the sum of the sea breeze duration at all points in the L1, L2 and L3 directions.*

4.5. Conclusions

The sea breeze can effectively alleviate the summer heat in coastal cities. This study focuses on coastal cities and analyzes the temporal characteristics of the action of sea breeze in urban areas and the factors affecting its action. In the first stage, the long-term multi-point observation data were used to analyze their characteristics, and then the calculation results of temperature and specific humidity from the WRF mesoscale meteorological model were used to produce a map of the temporal distribution of sea breeze events. In the study, in the coastal part, the sea breeze blows landward at a slower rate, and the rate increases with penetration inland, as shown in the map of the sea breeze arrival time distribution. The arrival time of sea breeze is strongly influenced by inland rivers. From the map of sea breeze retreat time distribution, the direction of sea breeze retreat is related to the area of compact mid-rise and compact Low-rise and urban topography. The retreat of the sea breeze slows down significantly when it is close to highly urbanized areas. The sea breeze retreat speeds up until it is close to the coastal part. From the map of sea breeze duration distribution, the sea breeze duration is relatively evenly distributed in the area, and the sea breeze duration is the longest in the direction of sea breeze retreat. In this study, the visualization of the sea breeze event time can visualize the distribution of the sea breeze event time, which has enriched the basic research on the relationship between sea breeze and cities.

Chapter 5. Sea breeze cooling capacity in a coastal city

5.1. Introduction

Chapter Five is Sea breeze cooling capacity in a coastal city. This chapter defines how the sea breeze cooling capacity is calculated. The results of the calculations were visualised using ArcGIS Pro to generate a cooling map of sea breeze cooling capacity. The trends in hourly cooling capacity are also analysed dynamically. The factors affecting sea breeze cooling capacity are discussed, as well as the hourly sea breeze maximum cooling point and the inland penetration distance of hourly sea breeze cooling during the time interval of sea breeze cooling action.

5.2. Identification of west breeze day

The data used in this chapter include sea breeze day data and west breeze day data. Among them, the data related to sea breeze days are the same as those in Chapter Four Based on the characteristics of Sendai's summer sea breeze activity, days that were representative and qualified for the study were selected, and finally 5 August 2016 was chosen as the subject of the study. In this section, the focus is on the identification of west breeze days. Days with westerly winds in weather conditions similar to sea breeze days were selected for the study. Simulated data for west breeze days were obtained in the same way as for sea breeze days. The same way includes using the WRF model and applying the same settings. The difference between the simulated temperature data on a sea breeze day and a west breeze day was then calculated to quantify the cooling capacity of the sea breeze in coastal cities.

5.2.1. **Identification of the West Breeze Day**

As with the identification of sea breeze days, the first step is to determine the days when the west breeze blow by using meteorological observation data downloaded from the Japan Meteorological Agency. From these west breeze days, the type of sea breeze and the characteristics of changes in meteorological variables after the onset of the west breeze were used to finally identify the west breeze days. To try to exclude the interference of other factors, a sunny day was chosen to identify the west breeze day.

Specific conditions included the following.

Full sun, 40% or more of possible daylight hours.

Clouds: less than 5% clouds.

Rainfall: no rainfall.

Wind: West breeze lasting at least 2 hours.

5.2.2. **Case Study Day**

Using the above rules for identifying west breeze days, weather conditions similar to the selected sea breeze day were selected based on meeting the conditions for identifying west breeze days. This is because days with a west breeze occur much less frequently than sea breeze days. In theory, air currents always move from high pressure to low pressure, so the wind always blows from the side with lower temperatures to the side with higher temperatures. Therefore on days with plenty of sunshine and high temperatures, sea breezes blow on the vast majority of days. In the end, 10 August 2013 was chosen as the case study day using meteorological observation data downloaded from the Japan Meteorological Agency (Fig. 5.1). There was no rainfall all day on the case study day, and the maximum temperature was 34.9°C and the wind blew from land to sea from 10:00 to 17:00.

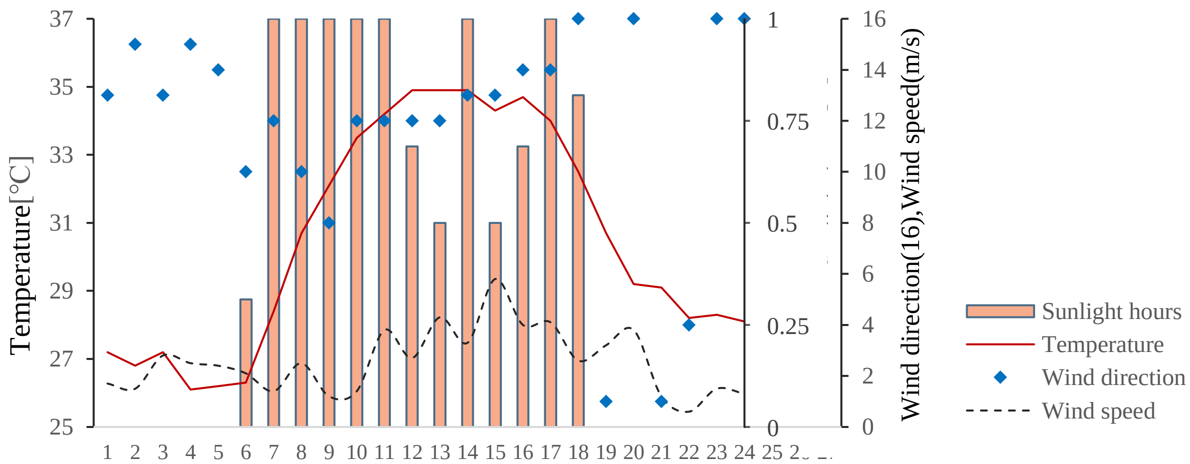

Fig. 5.1 *Meteorological characteristics of the case study day (10 August 2013). Includes sunlight hours, temperature, wind direction, and wind speed.*

5.3. Calculation of Sea breeze cooling capacity

Simulated temperature data for sea breeze days and west breeze days were calculated separately for the urban area of Sendai, Japan, using the WRF model. The difference between the simulated temperature data on a sea breeze day and a west breeze day is then derived to quantify the cooling capacity of the sea breeze in coastal cities. The difference in temperature between a sea breeze day and a west breeze day represents, under similar weather conditions, how much cooler the city is on a sea breeze day compared to a west breeze day. This study defines this difference as the cooling capacity of the sea breeze for coastal cities.

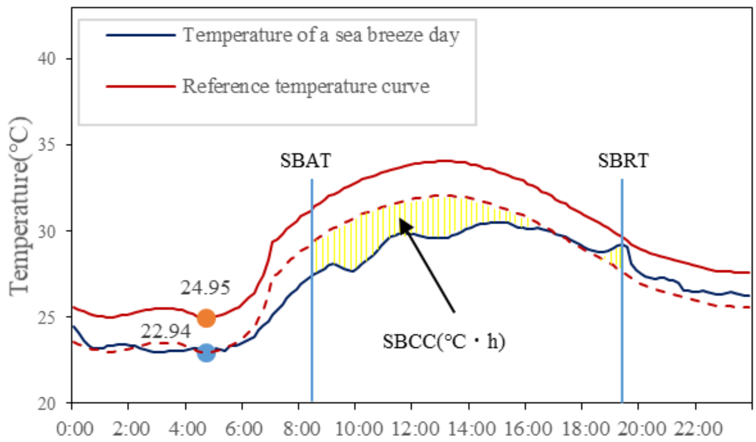

Fig. 5.2 *Sea breeze day (5 August 2016) temperature profile at the Sendai simulation point in the study area, west breeze day (10 August 2013) temperature profile and adjusted temperature profile. Yellow parts represent sea breeze cooling capacity.*

Although sea breeze days and west breeze days were chosen with similar weather conditions in mind. However, the temperature is usually influenced not only by the current weather conditions but also by the climatic phenomena that have occurred in the preceding period.

Overlapping the temperature profiles simulated at the same point in the WRF model for a sea breeze day and a west breeze day revealed that the temperature on the west breeze day was higher than that on the sea breeze day, despite the absence of sunlight in the early morning hours. In the absence of a sea breeze at night, the lower temperatures on sea breeze days compared to west breeze days are not due to the sea breeze and it is necessary to exclude the higher temperature values.

Therefore, all temperature values for a west breeze day need to be adjusted. This is done by extracting the lowest temperature value for the early morning hours of the west breeze day (the value at the orange point in Fig. 5.2) and finding the temperature value for the sea breeze day at the same time (the value at the blue point in Fig. 5.2). The difference between the two values is the value that needs to be reduced for the west breeze day as a whole. The difference between the two values is the overall reduction required for a west breeze day. After the temperature values for a west breeze day have been adjusted, the sea breeze cooling capacity is then calculated.

Sea breeze cooling capacity (SBCC) is the difference between the integration in time of the temperature on a west breeze day (WESTA) and the integration in time of the temperature on a sea breeze day (SEA). SBCC (°C h) is defined as the product of sea breeze cooling and the cooling duration (the shaded area in Fig. 5.2). The calculation is described in Eq. (1).

$$\text{SBCC}=\text{WESTA}-\text{SEA} \tag{1}$$

Where WESTA is the time integral of the adjusted westerly daily temperature profile and SEA is the time integral of the sea breeze daily temperature profile. They are defined by defining Eq.(2) and (3):

$$WESTA = \sum_{i=2}^{n} \frac{\left(T_{west(i-1)} + T_{west(i)}\right) \times \Delta t}{2} \tag{2}$$

$$SEA = \sum_{i=2}^{n} \frac{\left(T_{sea(i-1)} + T_{sea(i)}\right) \times \Delta t}{2} \tag{3}$$

Where Twest(i) and Tsea(i) are the west-adjusted daily temperature profile and the sea breeze-daily temperature profile at time step i, respectively, Δt is the time interval between adjacent time steps in the sea breeze event, and n is the number of time steps. The time step at each point is defined as the sea breeze duration at each point, calculated from the time of sea breeze arrival until the time of sea breeze retreat. The time is obtained by referring to Chapter Four's sea breeze action time diagram.

5.4. Results and Discussion

5.4.1. **Sea breeze cooling capacity**

Simulations in WRF mode based on the selected sea breeze days and west breeze days will result in data for a total of 1089 points. The geographical coordinates of each point and the temperature data are derived. The sea breeze cooling capacity is then calculated for each point. The sea breeze cooling is then imported into ArcGIS Pro to obtain a visual plan view of the sea breeze cooling in the simulated area (Fig. 5.3).

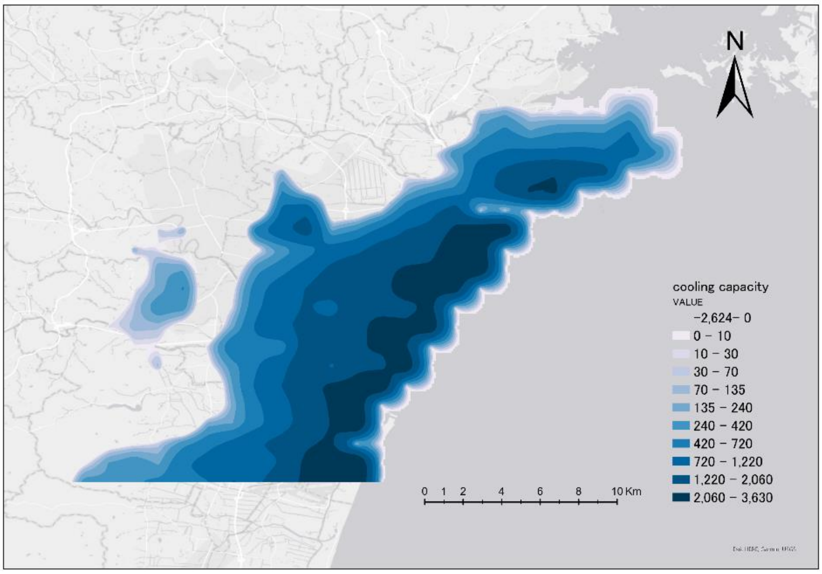

Fig. 5.3 *Plan view of all sea breeze cooling generated during the time of sea breeze action.*

As can be observed in Fig. 5.3, the blue area represents a positive sea breeze cooling, indicating that sea breeze cooling is generated at that point, with different shades of color representing different cooling intensities. It is observed that the magnitude of sea breeze cooling has certain characteristics. The cooling intensity of the sea breeze is highest along the coast and is gradually reduced as it penetrates inland.

5.4.2. **Trend of sea breeze cooling capacity and cooling range over time**

Chapter 4 concludes that the time of sea breeze action varies at each point and that the differences are mainly caused by the distance from the coast and the surrounding environment, especially inland rivers. The analysis was performed in one-hour increments during the time of sea breeze action to derive the characteristics of the sea breeze cooling capacity at each point. In the study area, the earliest time when the sea breeze acts is 7:00 and the latest time when it ends is 21:00. Therefore, the sea breeze cooling capacity was analyzed for a total of 15 hours from 7:00 to 21:00.

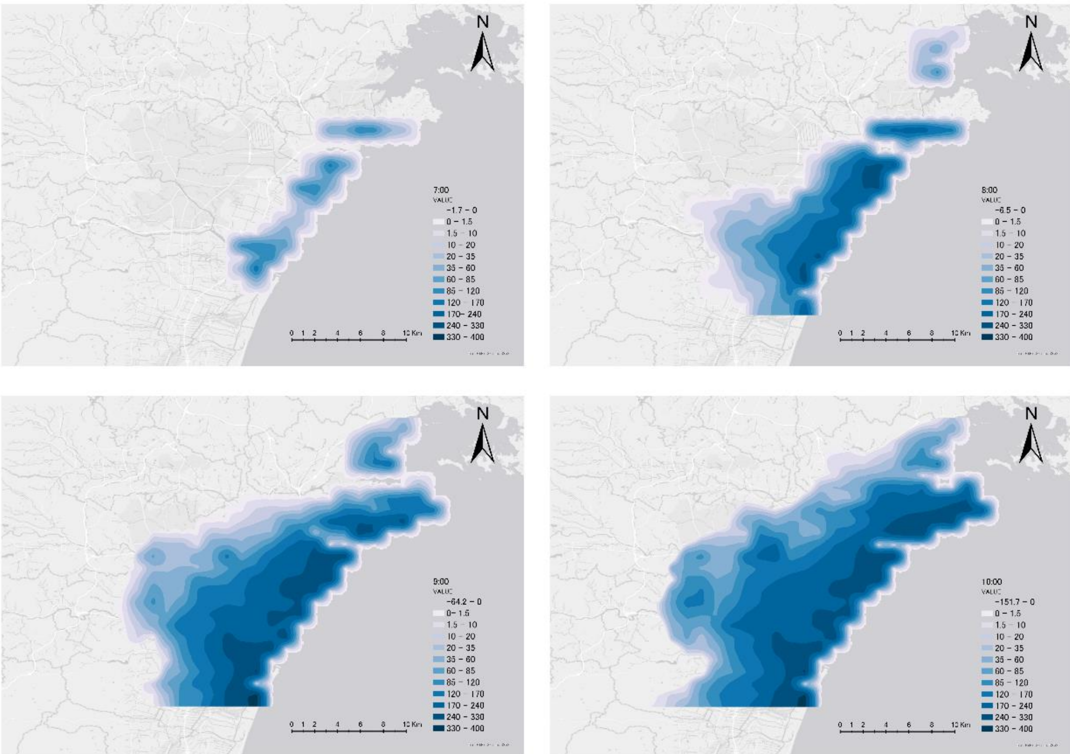

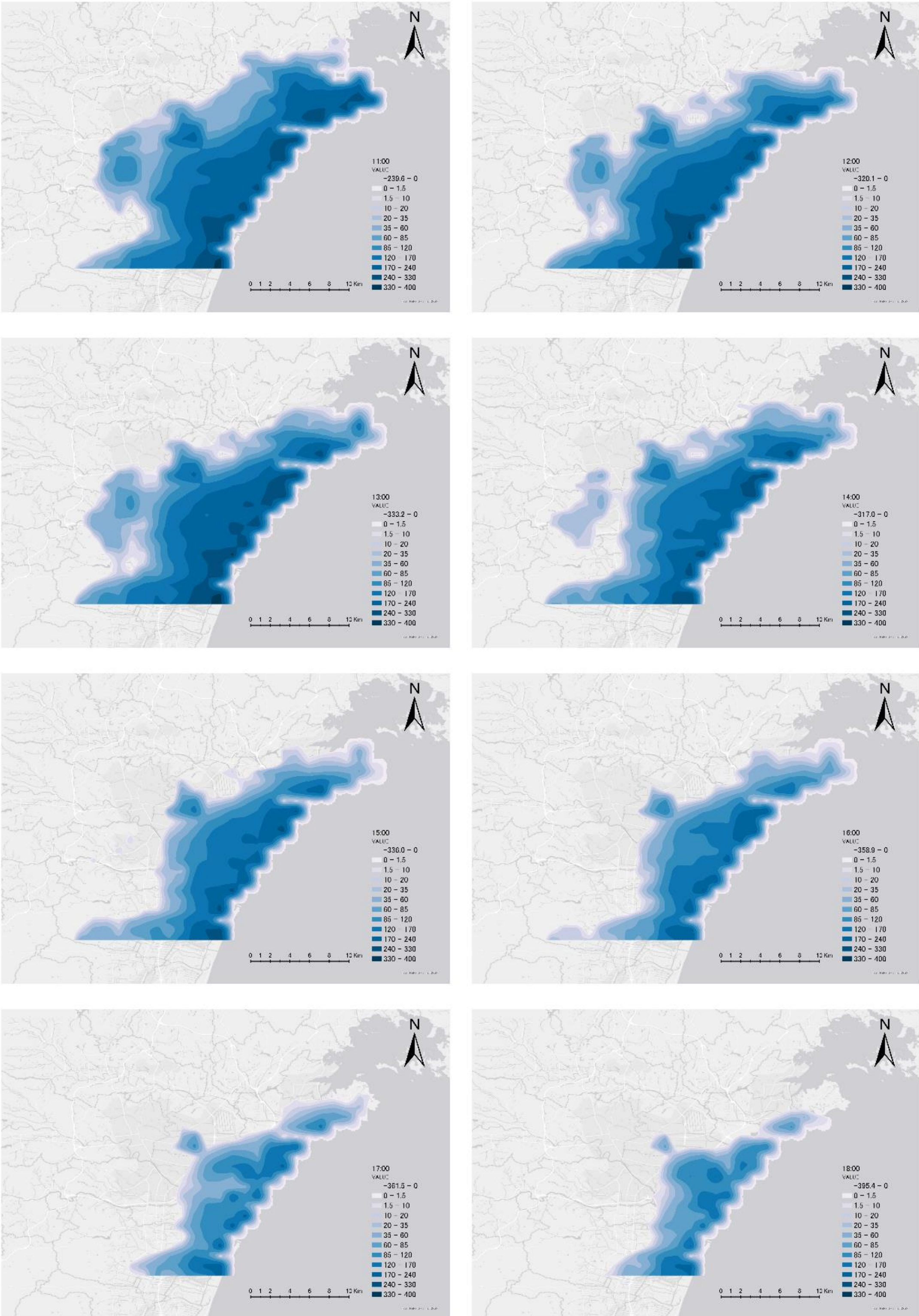
N
11:00
VALUE
−239.6 − 0
0 − 1.5
1.5 − 10
10 − 20
20 − 35
35 − 60
60 − 85
85 − 120
120 − 170
170 − 240
240 − 330
330 − 400
0 1 2 4 6 8 12 Km
12:00
−320.1 − 0
13:00
−333.2 − 0
14:00
−317.0 − 0
15:00
−336.0 − 0
16:00
−358.9 − 0
17:00
−361.5 − 0
18:00
−395.4 − 0

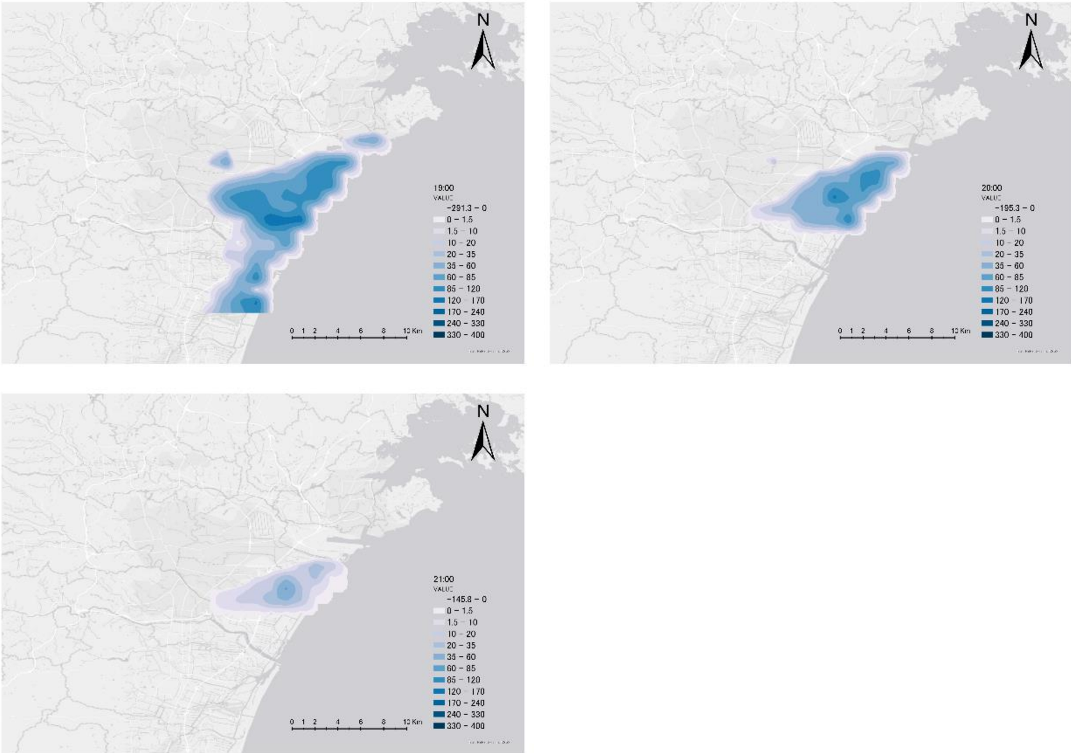

Fig. 5.4 *Plan view of sea breeze cooling capacity per hour.*

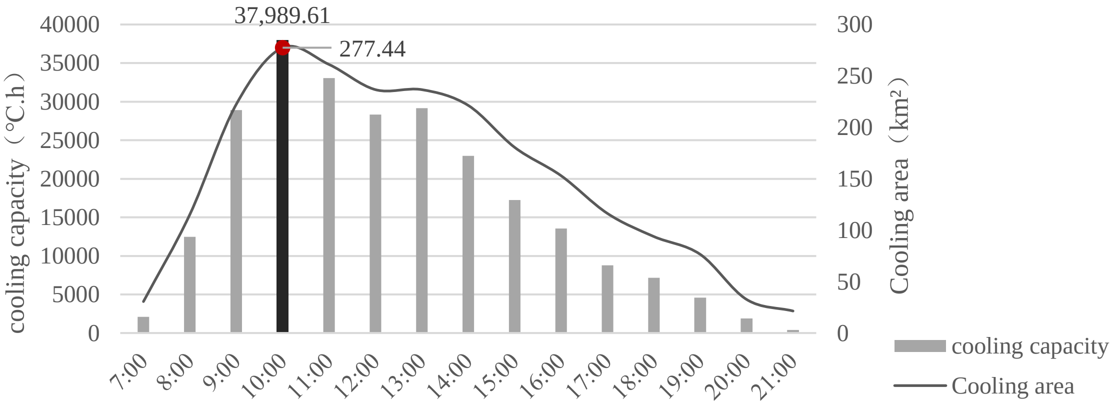

Fig. 5.5 *Sea breeze cooling capacity and cooling area per hour.*

Table 5.1 *Sea breeze cooling capacity and cooling area per hour.*

Time	cooling capacity (℃.h)	Cooling area (km²)
7:00	2092.99	30.6
8:00	12489.48	115.26
9:00	28891.49	222.36
10:00	37989.61	277.44
11:00	33062.05	261.12
12:00	28331.30	236.64
13:00	29149.13	236.64
14:00	22974.94	221.34
15:00	17250.13	180.54
16:00	13565.42	153
17:00	8760.34	116.28
18:00	7150.46	93.84
19:00	4600.70	76.5
20:00	1888.38	32.64
21:00	400.04	21.42

After visualizing the data using ArcGIS Pro, it is possible to visualize the process of the sea breeze cooling and its extent, starting from a small intensity and extent at 7:00 and gradually strengthening and spreading, before gradually weakening and shrinking (Fig. 5.4). It is also possible to see the geographical distribution of the sea breeze cooling range over the study area at different times of the day.

A statistical analysis of the data therein reveals (Fig. 5.5, Table 5.1) that both sea breeze cooling capacity and sea breeze cooling range show an upward and then downward trend. At 10:00, the sea breeze cooling capacity reached a maximum value of 37,989.61°C.h and the cooling area reached a maximum range of 277.44km². The rise from 7:00 to 10:00 was continuous and rapid, with the cooling volume rising from 2092.995°C.h to 37989.61°C.h in only three hours and the cooling range expanding from 30.6 km² to 277.44 km². The cooling volume at 10:00 was eighteen times stronger than the cooling volume at 7:00, while the cooling area expanded by nine times.

After 10:00 the cooling capacity and the cooling area begin to fall, at a slower rate between ten and 13:00, and show a small increase between 12:00 and 13:00. After 13:00, the cooling capacity and the cooling area show a continuous decline, and the rate of decline is more even.

5.4.3. **Dynamic analysis of sea breeze cooling capacity**

The description of the hourly sea breeze cooling planogram in terms of cooling capacity in each cooling intensity class interval and the cooling range allows the trend of the hourly variation in cooling capacity in each cooling intensity class interval and the cooling range as a percentage of the cooling intensity class to be derived (Fig. 5.6). This is used to specifically describe the variation in the hourly sea breeze cooling planes.

The description of the hourly sea breeze cooling planogram in terms of cooling capacity in each cooling intensity class interval and the cooling range allows the trend of the hourly variation in cooling capacity in each cooling intensity class interval and the cooling range as a percentage of the cooling intensity class to be derived (Fig. 5.6). This is used to specifically describe the variation in the hourly sea breeze cooling planes.

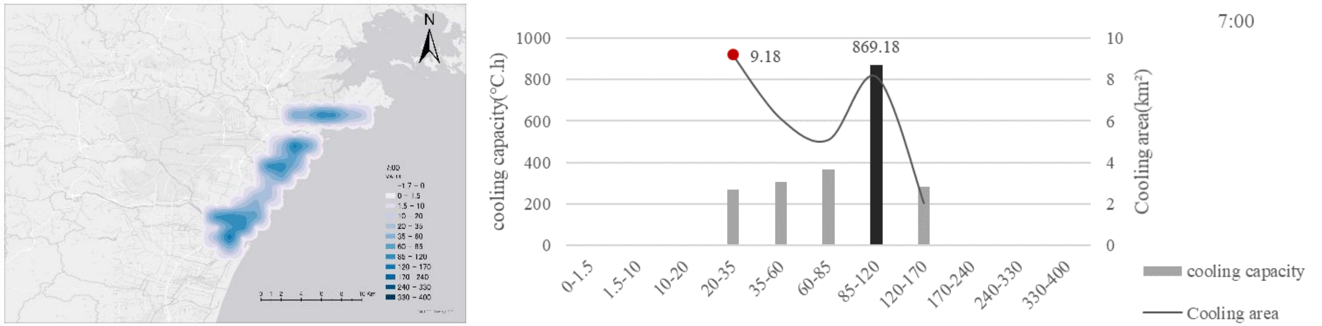
7:00
N
cooling capacity(°C.h)
Cooling area(km²)
1000
800
600
400
200
0
10
8
6
4
2
0
9.18
869.18
0-1.5
1.5-10
10-20
20-35
35-60
60-85
85-120
120-170
170-240
240-330
330-400
cooling capacity
Cooling area

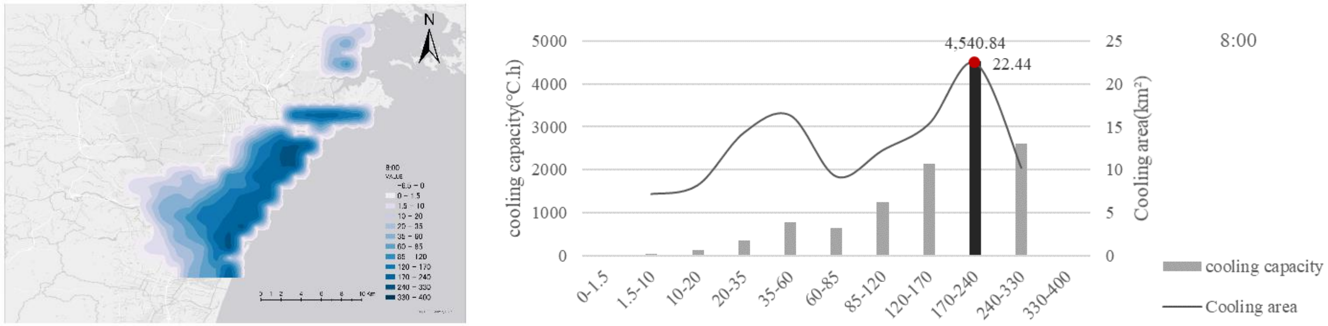
8:00
N
cooling capacity(°C.h)
Cooling area(km²)
5000
4000
3000
2000
1000
0
25
20
15
10
5
0
4,540.84
22.44
0-1.5
1.5-10
10-20
20-35
35-60
60-85
85-120
120-170
170-240
240-330
330-400
cooling capacity
Cooling area

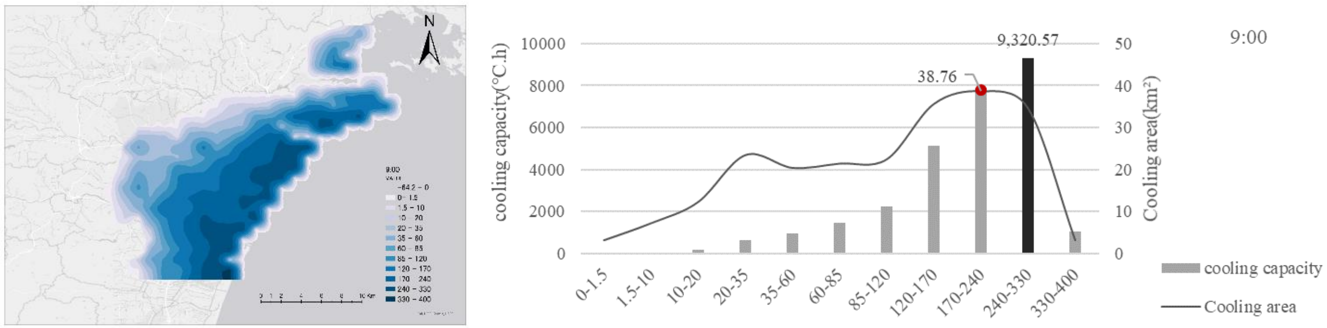
9:00
N
cooling capacity(°C.h)
Cooling area(km²)
10000
8000
6000
4000
2000
0
50
40
30
20
10
0
9,320.57
38.76
0-1.5
1.5-10
10-20
20-35
35-60
60-85
85-120
120-170
170-240
240-330
330-400
cooling capacity
Cooling area

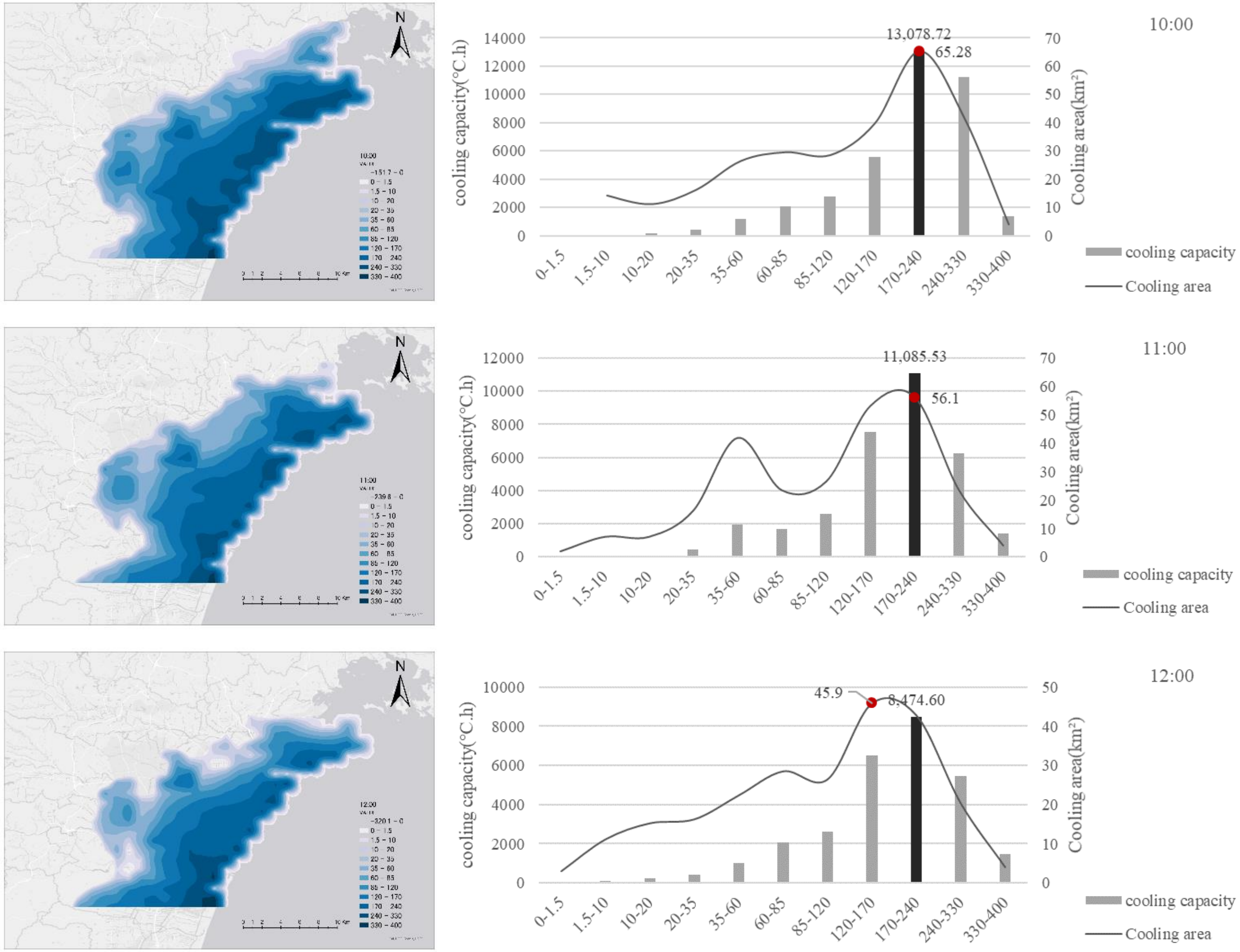
10:00
13,078.72
65.28
cooling capacity(°C.h)
Cooling area(km²)
0-1.5
1.5-10
10-20
20-35
35-60
60-85
85-120
120-170
170-240
240-330
330-400
cooling capacity
Cooling area
11:00
11,085.53
56.1
12:00
45.9
8,474.60

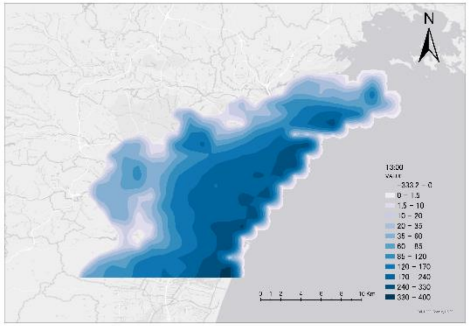

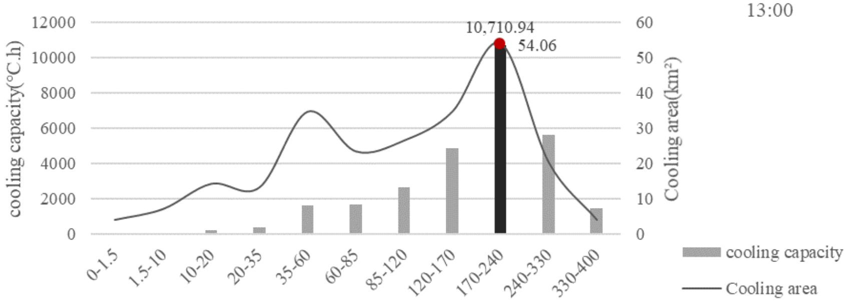

13:00

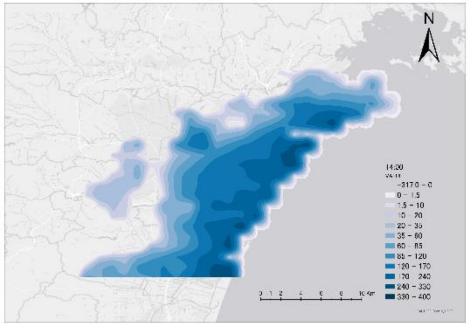

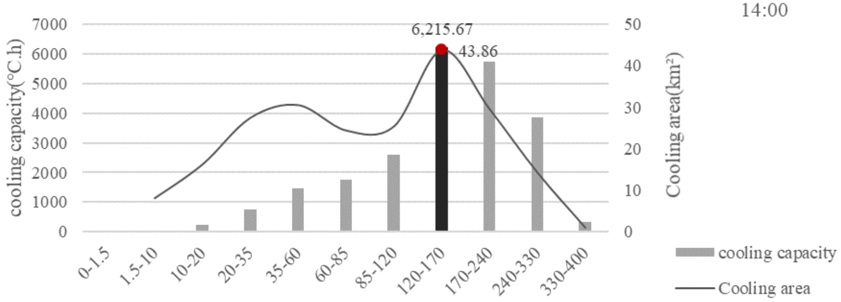

14:00

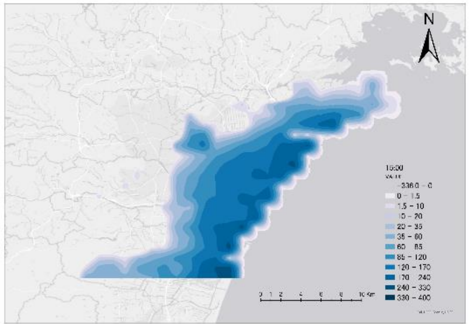

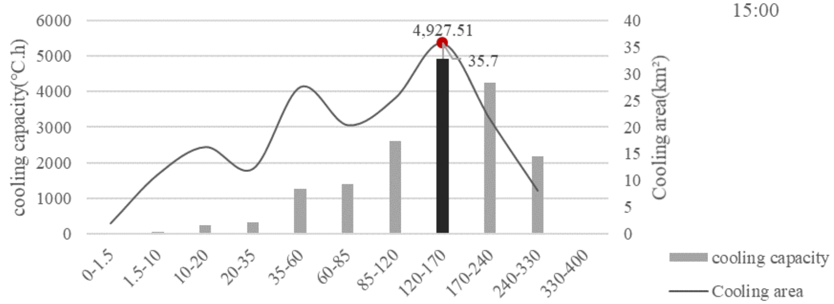

15:00

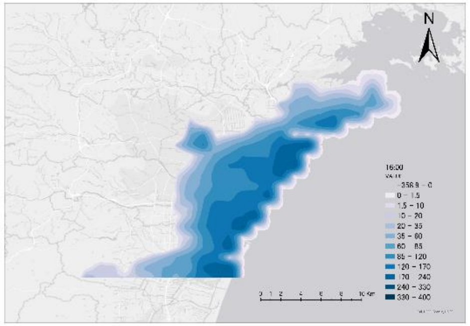

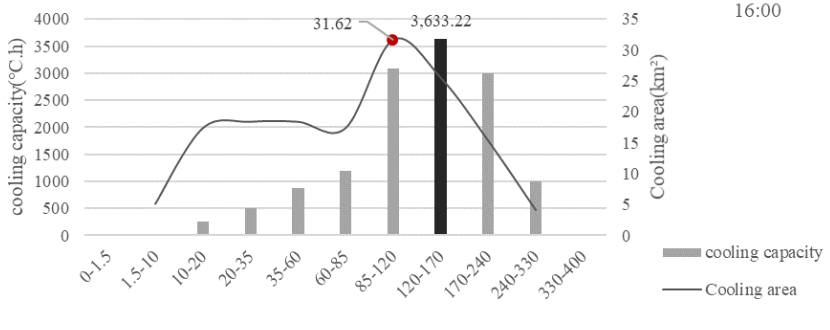

16:00

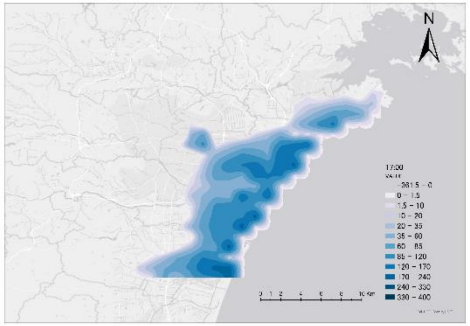

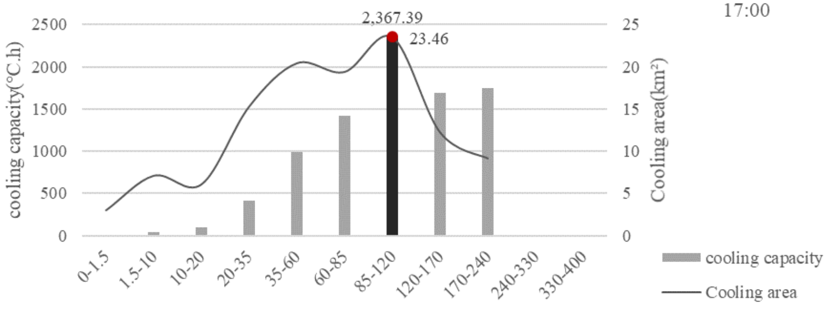

17:00

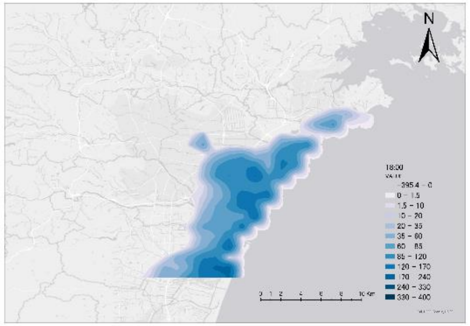

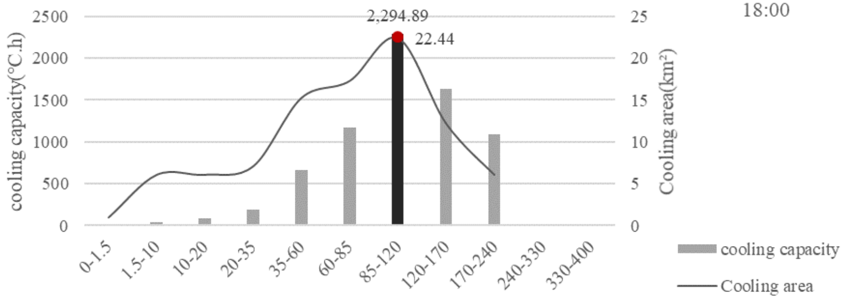

18:00

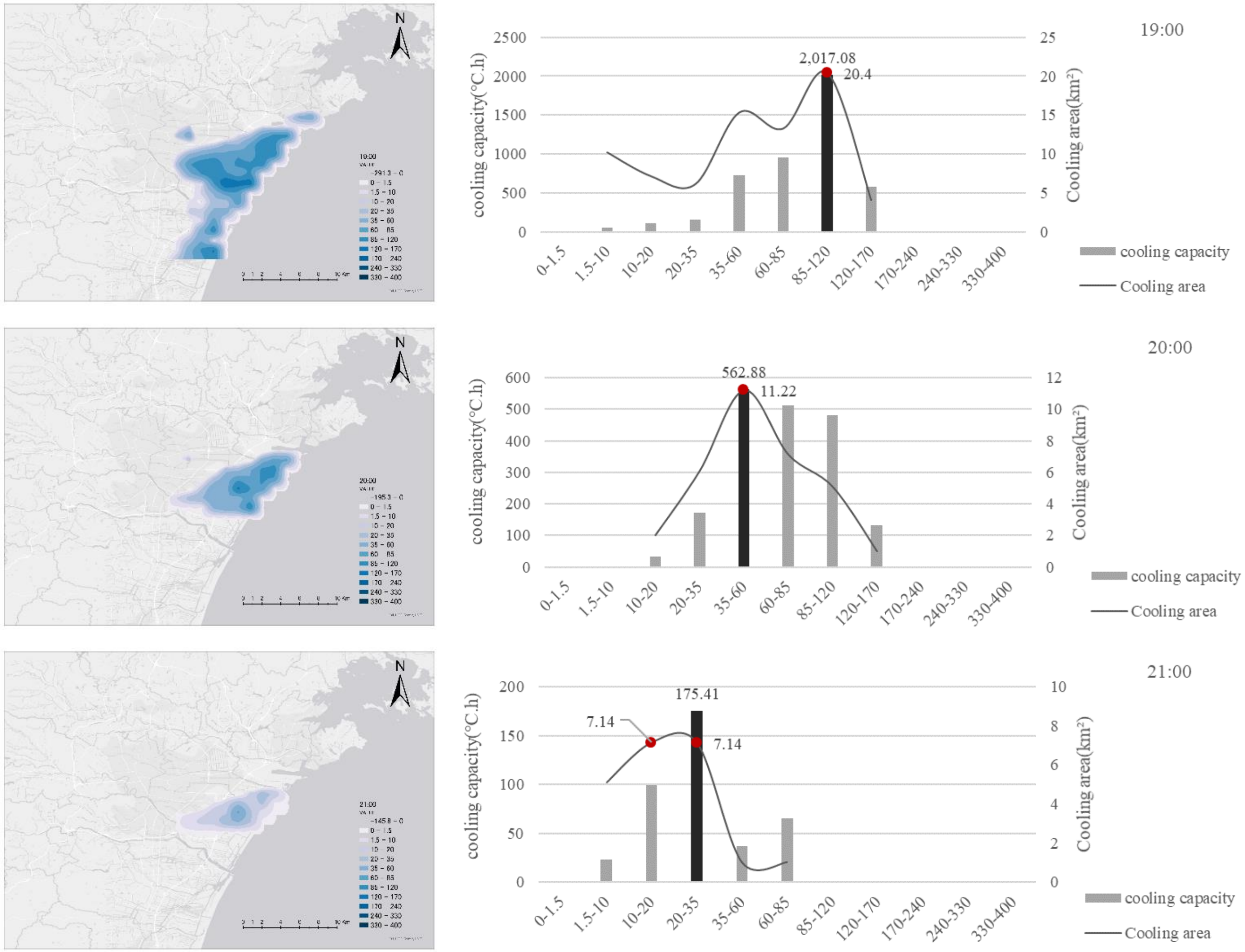

Fig. 5.6 *The amount of sea breeze cooling per hour with cooling area in each cooling intensity class interval.*

At 7:00, the sea breeze cooling levels were concentrated in the range 20-170°C.h. The strongest cooling levels in this time period were 120-170. Of all the levels, the 20-35 interval covered the widest area, totalling 9.18 km² and accounting for 30% of all the cooling areas. In the 85-120 interval the most cooling was generated, totalling 869.18 °C.h, or 42% of the total cooling.

At 8:00, the sea breeze cooling levels were concentrated in the range 1.5-330°C.h. The strongest cooling levels in this time period were 240-330.The strongest cooling levels increased from seven o'clock. Of all the classes, the 170-240 interval covered the widest area, totalling 22.44 km², or 19% of all cooling areas. The 170-240 interval produced the most cooling capacity, totalling 4540.84 °C.h and accounting for 36% of the total cooling.

At 9:00, all sea breeze cooling levels were covered, with the strongest cooling levels reaching the maximum interval 330-400 at this time of day. 170-240 covered the widest range of all levels, totalling 38.76 km² and accounting for 17% of all cooling areas. The 240-330 interval produced the most cooling capacity with a total of 9320.57 °C.h or 32% of the total cooling.

At 10:00, the sea breeze cooling classes are distributed between 1.5 and 400, with the strongest cooling classes being 330-400. of all the classes, the 170-240 zone covers the widest area, totalling 65.28 km², or 24% of all the cooling areas. The 170-240 zone produced the most cooling capacity, totalling 13,078.72 °C.h, or 34% of the total cooling.

At 11:00, all sea breeze cooling classes were covered, with the strongest cooling class being 330-400. Of all the classes, the 170-240 interval covered the widest area, totalling 56.1 km² and accounting for 21% of all cooling areas. The 170-240 zone produced the most cooling capacity, totalling 11085.53°C.h, or 34% of the total cooling.

At 12:00, all sea breeze cooling classes were covered, with the strongest cooling class being 330-400. Of all the classes, the 120-170 interval covered the widest area, totalling 45.9km², or 19% of all cooling areas. The 170-240 zone produced the most cooling capacity, totalling 8474.6°C.h, or 30% of the total cooling.

At 13:00, all sea breeze cooling classes were covered, with the strongest cooling class being 330-400. Of all the classes, the 170-240 interval covered the widest area, totaling 54.06km², or 23% of all cooling areas. The 170-240 zone produced the most cooling capacity, totaling 10,710.94°C.h, or 37% of the total cooling.

At 14:00, the sea breeze cooling classes were distributed between 1.5 and 400, with the strongest cooling class being 330-400. of all the classes, the 120-170 interval covered the widest area, totaling 43.86km², or 20% of all the cooling areas. The 120-170 zone produced the most cooling capacity, totaling 6215.67°C.h, or 27% of the total cooling.

At 15:00, the sea breeze cooling classes are distributed between 0-330, with the strongest cooling classes reduced to the 240-330 interval. Of all the classes, the 120-170 interval covered the widest range, totaling 35.7km², or 20% of all cooling areas. The 120-170 zone produced the most cooling capacity, totaling 4927.51°C.h, or 29% of the total cooling.

At 16:00, the sea breeze cooling classes are distributed between 1.5 and 330, with the strongest cooling classes in the 240-330 interval. Of all the classes, the 85-120 interval covered the widest range, totaling 31.62km², or 21% of all the cooling areas. The 120-170 zone produced the most cooling capacity, totaling 3633.22°C.h, or 27% of the total cooling.

At 17:00, the sea breeze cooling classes are distributed between 0-240, with the strongest cooling classes continuing to decrease to the 170-2400 zone. Of all the classes, the 85-120 interval covers the widest range, totaling 23.46km², or 20% of all cooling areas. The greatest amount of cooling was generated in the 85-120 interval, totaling 2367.39°C.h, or 27% of the total cooling.

At 18:00, the sea breeze cooling classes are distributed between 0 and 240, with the strongest cooling classes in the 170-240 zone. Of all the classes, the 85-120 interval covered the widest area, totaling 22.44km², or 24% of all cooling areas. The 85-120 zone produced the most cooling capacity, totaling 2294.89°C.h, or 32% of the total cooling.

At 19:00, the sea breeze cooling classes are distributed between 1.5 and 170, with the strongest cooling classes lowered to the 120-170 interval. Of all the classes, the 85-120 interval covered the widest range, totaling 20.4km², or 27% of all cooling areas. The 85-120 zone produced the most cooling capacity, totaling 2017.08°C.h, or 44% of the total cooling.

At 20:00, the sea breeze cooling classes are distributed between 10 and 170, with the strongest cooling classes in the 120-170 interval. Of all the classes, the 35-60 interval covered the widest area, totaling 11.22km², or 34% of all cooling areas. The 35-60 zone produced the most cooling capacity, totaling 562.88°C.h, or 30% of the total cooling.

At 21:00, the sea breeze cooling classes are distributed between 1.5 and 85, with the strongest cooling classes in the 60-85 zone. Of all the classes, the 10-20 and 20-35 intervals covered the widest range at 7.14km², accounting for 33% of all cooling areas. The 20-35 zone produced the most cooling capacity with a total of 175.41°C.h, representing 44% of the total cooling.

From the data tabulated in Table 5.2 and Table 5.3, the values distributed in the range 120-240 have the greatest impact on cooling capacity and cooling area of all cooling classes.

Table 5.2 *The share of different cooling grades in all cooling capacities and cooling area.*

cooling intensity class	cooling capacity(°C.h)	Cooling area(km²)
0-1.5	0.0001	0.0081
1.5-10	0.0024	0.0471
10-20	0.0087	0.0645
20-35	0.0225	0.0919
35-60	0.0576	0.1354
60-85	0.0740	0.1147
85-120	0.1226	0.1340
120-170	0.2046	**0.1587**
170-240	**0.2880**	**0.1587**
240-330	0.1911	0.0780
330-400	0.0285	0.0090

Table 5.3 Hourly values of cooling capacity and cooling area in each cooling class.

		0-1.5	1.5-10	10-20	20-35	35-60	60-85	85-120	120-170	170-240	240-330	330-400
7:00	cooling capacity				268.28	304.62	366.42	869.18	284.49			
	Cooling area				9.18	6.12	5.10	8.16	2.04			
8:00	cooling capacity		45.70	127.86	348.43	775.15	651.83	1255.15	2140.93	4540.84	2603.58	
	Cooling area		7.14	8.16	14.28	16.32	9.18	12.24	15.30	22.44	10.20	
9:00	cooling capacity	1.84	27.88	176.59	647.70	958.50	1474.33	2215.89	5132.72	7874.39	9320.57	1061.08
	Cooling area	3.06	7.14	12.24	23.46	20.40	21.42	22.44	35.70	38.76	34.68	3.06
10:00	cooling capacity		69.69	172.55	414.98	1189.31	2049.77	2785.42	5600.04	13078.72	11234.02	1395.10
	Cooling area		14.28	11.22	16.32	26.52	29.58	28.56	39.78	65.28	41.82	4.08
11:00	cooling capacity	1.84	49.33	87.68	425.03	1928.65	1674.08	2618.68	7540.35	11085.53	6258.43	1392.46
	Cooling area	2.04	7.14	7.14	16.32	41.82	23.46	26.52	53.04	56.10	23.46	4.08
12:00	cooling capacity	2.33	70.28	225.99	434.32	993.65	2074.93	2633.52	6489.58	8474.60	5459.52	1472.58
	Cooling area	3.06	11.22	15.30	16.32	22.44	28.56	26.52	45.90	42.84	20.40	4.08
13:00	cooling capacity	2.39	36.38	206.22	374.57	1587.90	1654.92	2660.22	4873.60	10710.94	5604.36	1437.63
	Cooling area	4.08	7.14	14.28	13.26	34.68	23.46	26.52	34.68	54.06	20.40	4.08
14:00	cooling capacity		52.22	238.26	748.21	1462.11	1739.90	2587.06	6215.67	5744.22	3854.31	332.98
	Cooling area		8.16	16.32	27.54	30.60	24.48	25.50	43.86	29.58	14.28	1.02
15:00	cooling capacity	2.81	62.60	236.96	332.28	1258.27	1401.92	2602.92	4927.51	4242.00	2182.85	
	Cooling area	2.04	11.22	16.32	12.24	27.54	20.40	25.50	35.70	21.42	8.16	
16:00	cooling capacity		23.44	258.89	496.93	874.66	1198.56	3086.08	3633.22	3003.43	990.19	
	Cooling area		5.10	17.34	18.36	18.36	17.34	31.62	25.50	15.30	4.08	
17:00	cooling capacity	3.14	43.40	99.54	412.35	992.07	1414.00	2367.39	1685.66	1742.78		
	Cooling area	3.06	7.14	6.12	15.30	20.40	19.38	23.46	12.24	9.18		
18:00	cooling capacity	0.45	36.39	84.36	187.54	657.57	1167.48	2294.89	1633.17	1088.61		
	Cooling area	1.02	6.12	6.12	7.14	15.30	17.34	22.44	12.24	6.12		
19:00	cooling capacity		58.34	108.26	160.11	729.05	951.35	2017.08	576.51			
	Cooling area		10.20	7.14	6.12	15.30	13.26	20.40	4.08			
20:00	cooling capacity			31.64	170.93	562.88	510.94	481.01	130.97			
	Cooling area			2.04	6.12	11.22	7.14	5.10	1.02			
21:00	cooling capacity		23.18	98.96	175.41	37.16	65.33					
	Cooling area		5.10	7.14	7.14	1.02	1.02					

5.4.4. **Sea breeze cooling capacity and distance**

This section focuses on the relationship between sea breeze cooling capacity and distance. Where distance is the distance from the point where the sea breeze cooling effect is generated, in the direction of the sea breeze, to the coastline. The total cooling capacity for all sea breeze cooling effects and the hourly sea breeze cooling capacity as a function of distance are discussed separately.

Table 5.4 summarises the correlation coefficients between sea breeze cooling and distance at all times. Of these, the absolute values of the correlation coefficients are less than 0.7 at 7:00, 19:00, and 21:00. all the remaining times have strong negative correlations.

Fig. 5.7 represents scatter plots and trend lines of total cooling capacity and hourly sea breeze cooling capacity versus distance for all sea breeze cooling effects. The formula and the value of R^2 are attached. All relationships show a positive correlation at seven o'clock in the morning and a very low fit with $R^2 = 0.0083$. The rest of the time shows a negative correlation and a good fit from 8:00 to 16:00.

Table 5.4 *Explain the correlation between cooling capacity and distance. Time zone is JST.*

ALL	-0.724
7:00	**0.091**
8:00	-0.817
9:00	-0.895
10:00	-0.849
11:00	-0.836
12:00	-0.824
13:00	-0.879
14:00	-0.856
15:00	-0.857
16:00	-0.847
17:00	-0.744
18:00	-0.721
19:00	**-0.517**
20:00	-0.756
21:00	**-0.206**

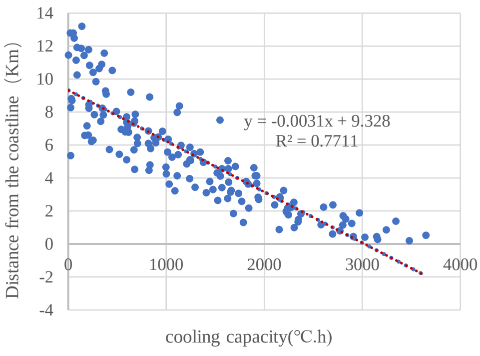

(1) 7:00-21:00

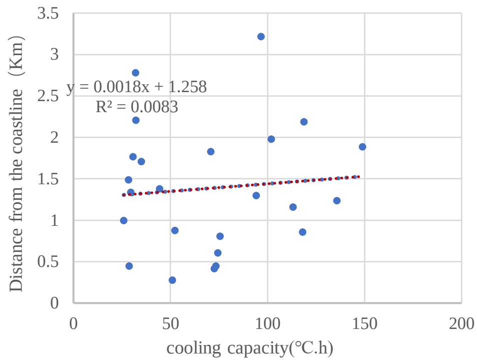

(2) 7:00

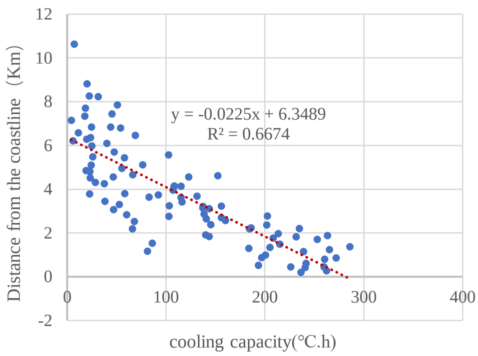

(3) 8:00

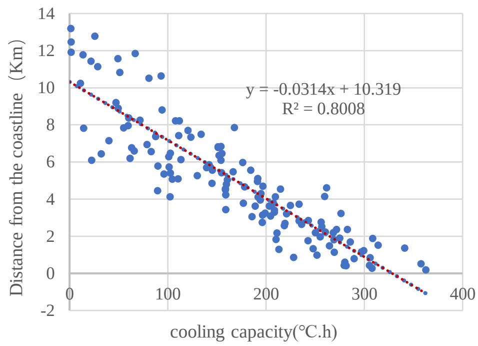

(4) 9:00

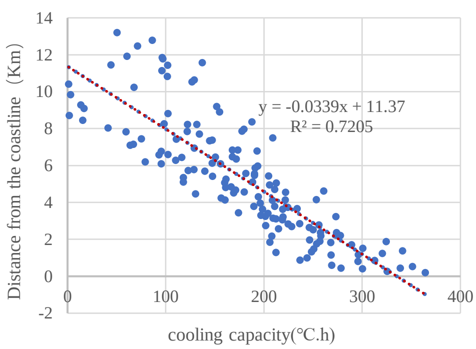

(5) 10:00

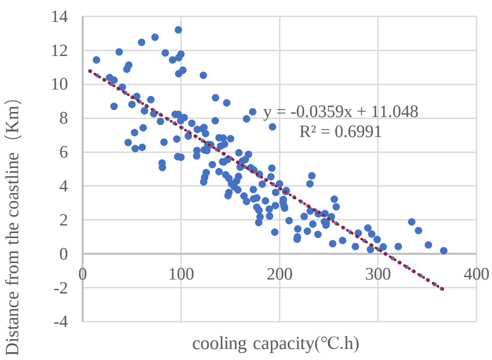

(6) 11:00

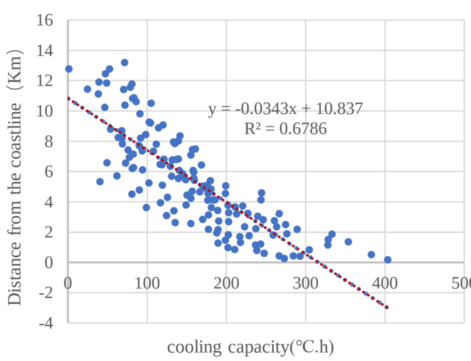

(7) 12:00

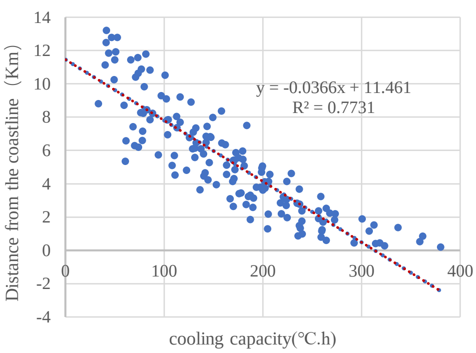

(8) 13:00

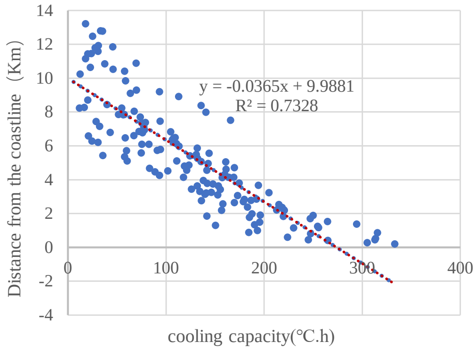

(9) 14:00

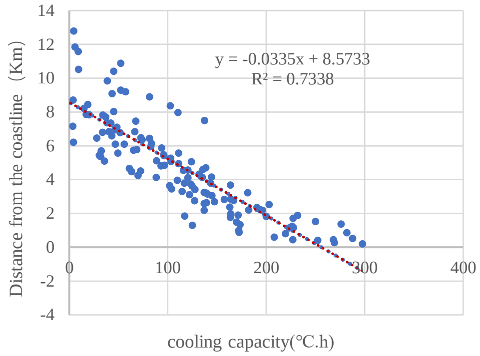

(10) 15:00

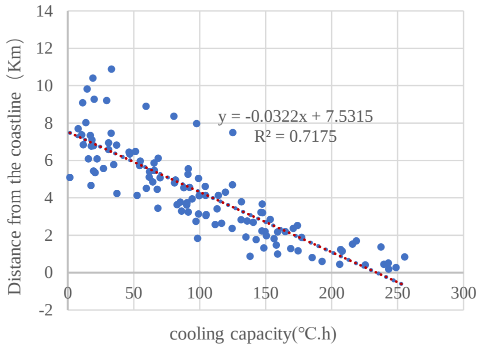

(11) 16:00

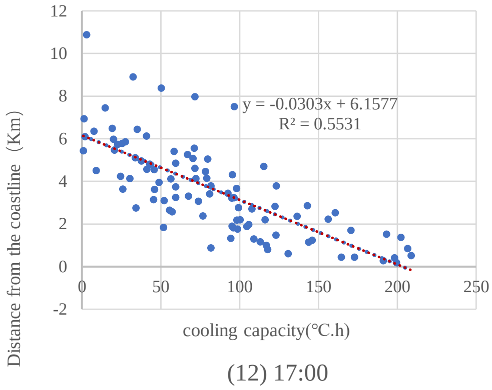

(12) 17:00

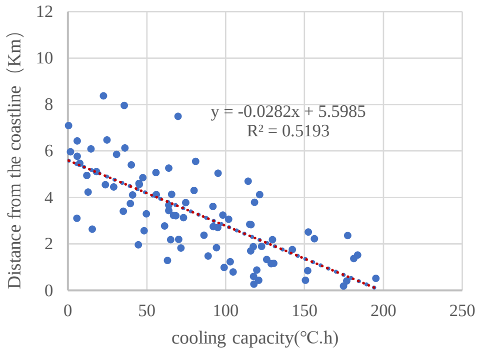

(13) 18:00

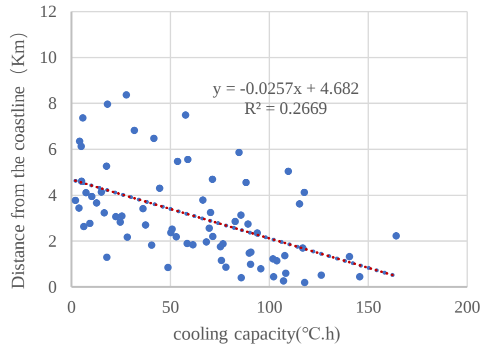

(14) 19:00

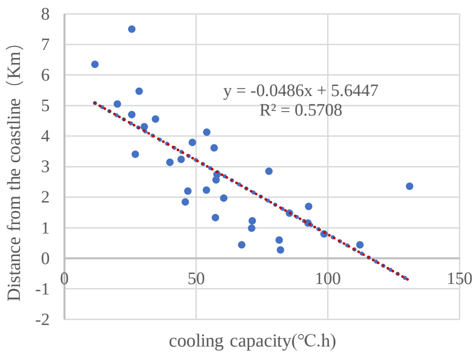

(15) 20:00

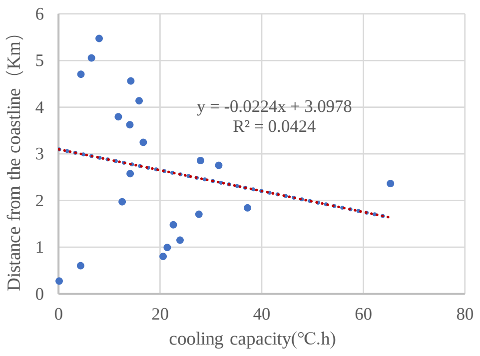

(16) 21:00

Fig. 5.7 Sea breeze cooling capacity as a function of distance.

5.4.5. **Inland penetration distance of sea breeze cooling**

To analyze the penetration process of the sea breeze cooling effect in the study area, the distance from the shore of the farthest point reached by the sea breeze cooling range per hour was counted. Based on the sea breeze cooling plan, the distance from the shore to the furthest point of the sea breeze cooling range was measured one by one, along the direction of the wind (Fig. 5.8).

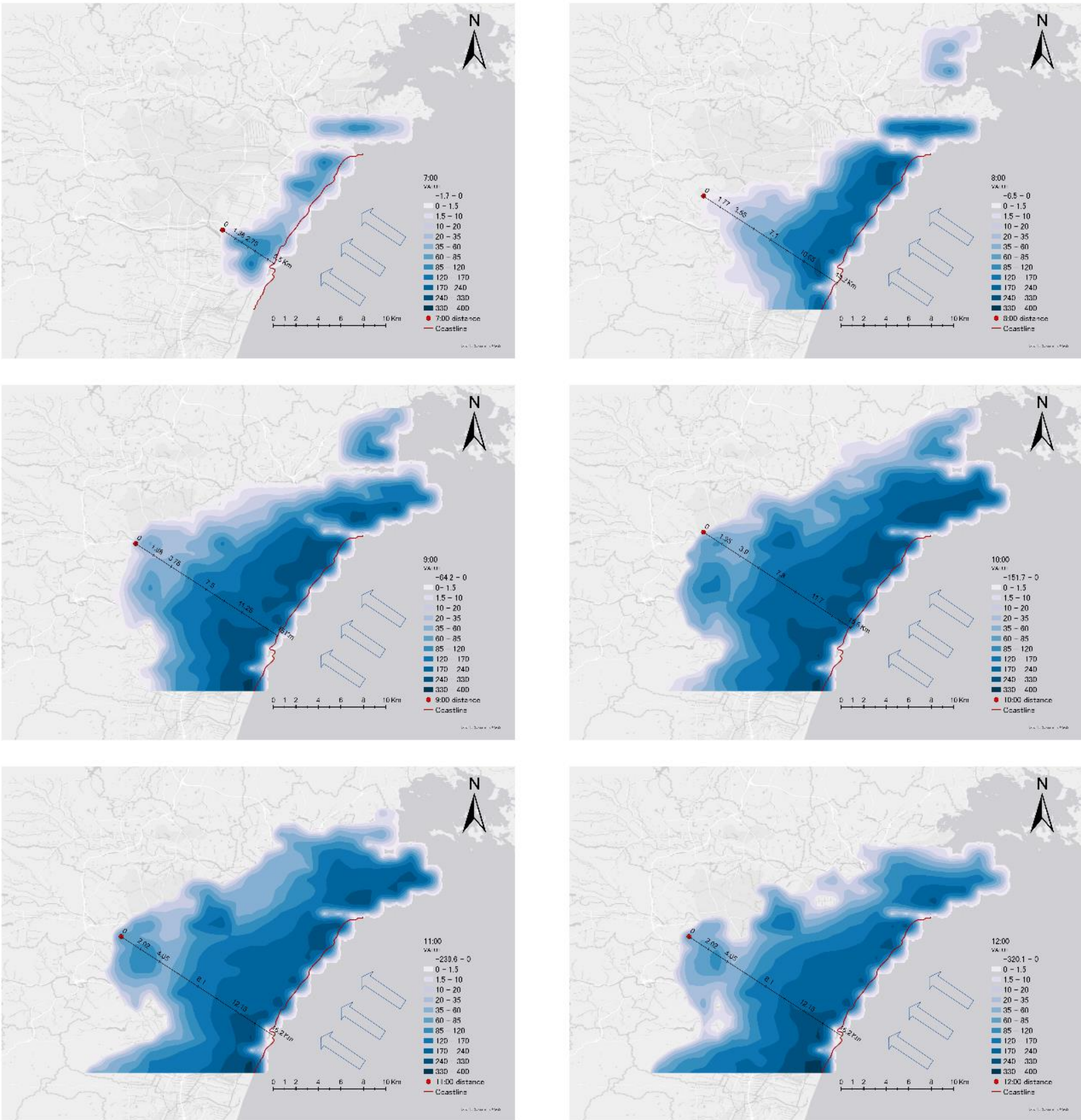

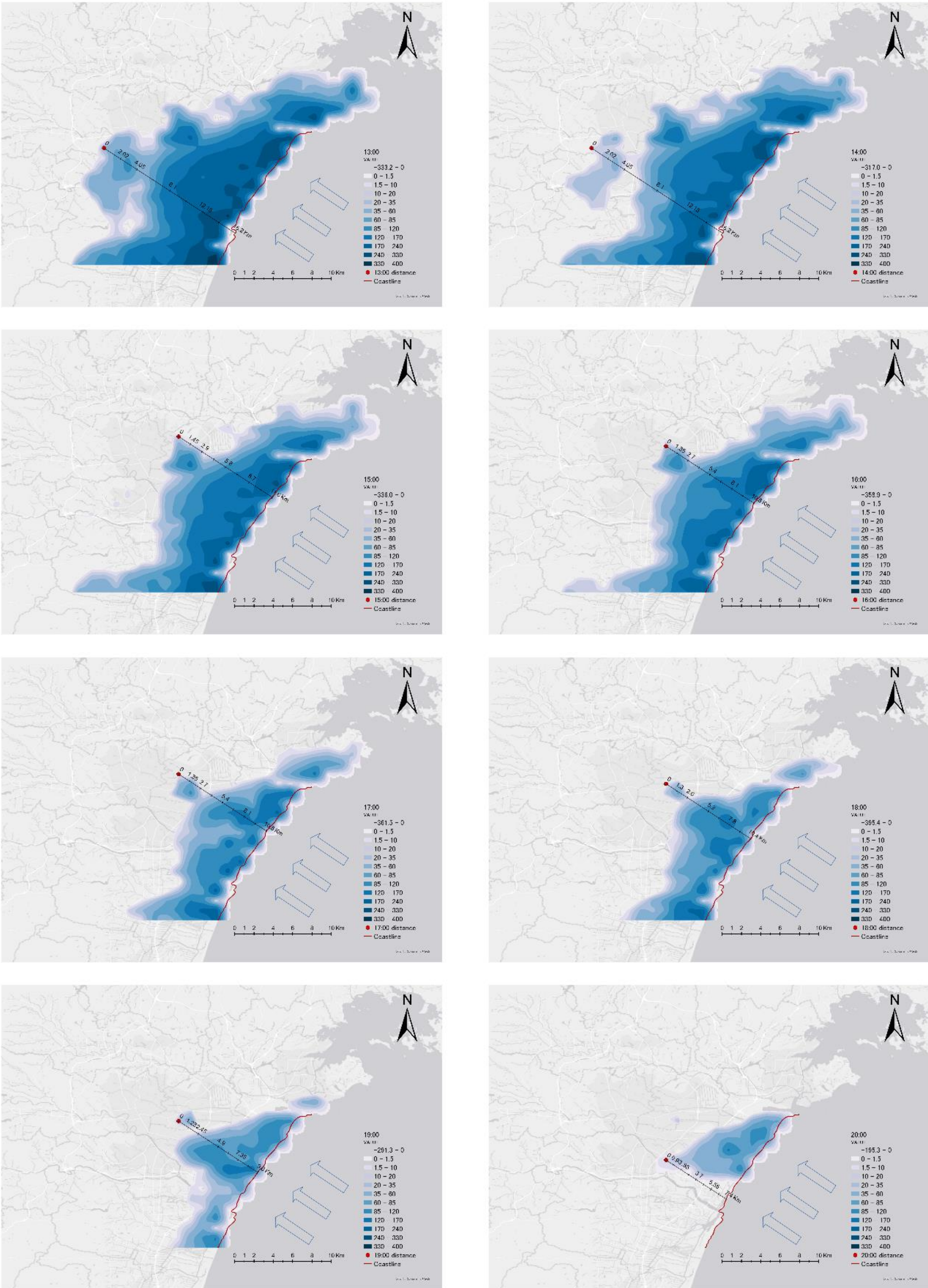
13:00
14:00
15:00
16:00
17:00
18:00
19:00
20:00

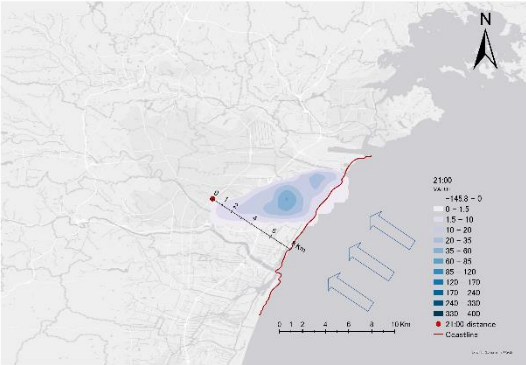

Fig. 5.8 *Distance to the furthest point of sea breeze cooling area penetration per hour.*

The farthest distance for cooling at 7:00 was 5.5 ㎞, and the distance grew rapidly to 14.2km at 8:00 and reached a maximum distance of 16.2km for cooling at 11:00, which continued until after 14:00, and then the distance shortened rapidly at 15:00. After that there has been a decreasing trend (Fig. 5.9). The relationship between cooling distance and time showed a positive correlation from 7:00 to 14:00(Fig. 5.10a), with a calculated correlation coefficient of 0.71, and a clear negative correlation from 15:00 to 21:00 (Fig. 5.10b), with a correlation coefficient of -0.92.

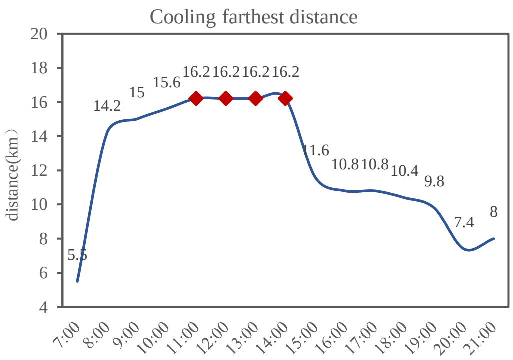

Fig. 5.9 *Furthest cooling distance and time.*

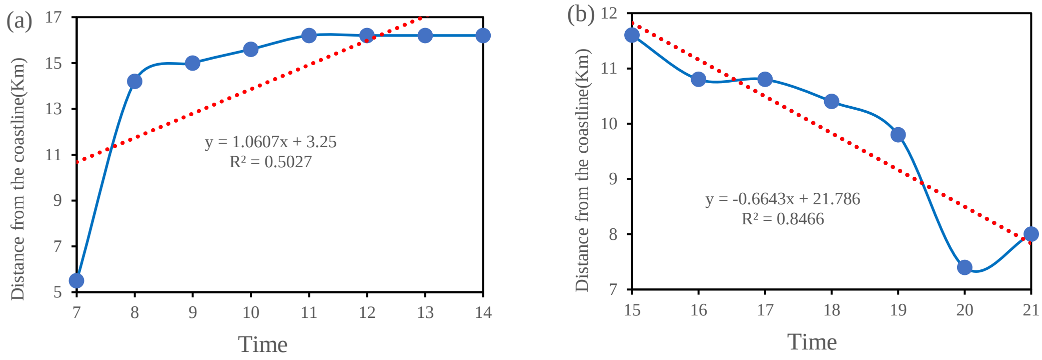

***Fig. 5.10**(a)7:00-14:00 Furthest cooling distance and time；(b)15:00-21:00 Furthest cooling distance and time.*

The points where the sea breeze cools the furthest distance from the 7:00-21:00 clock are represented on the map（Fig. 5.11）. A visual analysis of the distribution map alone reveals that the direction of cooling penetration follows the direction of the sea breeze, with a total of 10 points located close to inland rivers from 7:00-14:00 and 20:00-21:00, and a total of five points relatively far from inland rivers from 15:00-19:00. The points furthest away from sea breeze cooling have a stronger cooling capacity and a wider cooling range in the direction of the sea breeze. A detailed analysis of the inland rivers and the points with the furthest distance of sea breeze cooling is necessary.

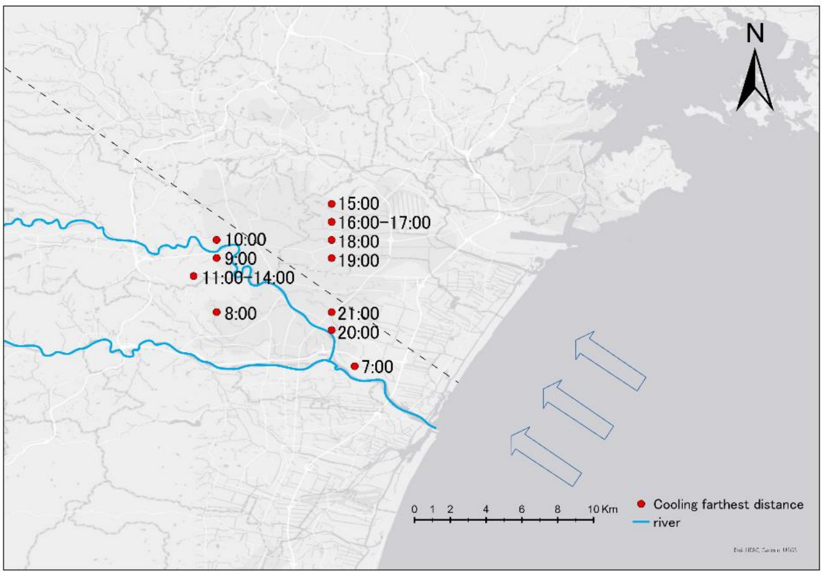

***Fig. 5.11** Hourly furthest cooling point on the map.*

Analyzing the relationship between the farthest points of the sea breeze cooling range and inland rivers about time, it can be seen that a total of ten points are closer to inland rivers in the time range of 7:00-14:00 and 20:00-21:00 under the entire sea breeze cooling action (Fig. 5.11), which is by the planimetric analysis. In the correlation analysis, the time range 7:00-14:00 shows a very weak positive correlation with a correlation coefficient of 0.38 (Fig. 5.13a). The time range 15:00-21:00 shows a strong negative correlation with a correlation coefficient of -0.93 (Fig. 5.13b). As the time value increases, the distance to the inland river gets closer.

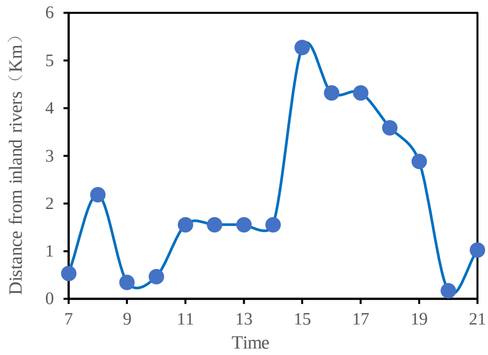

Fig. 5.12 *Distance of the farthest point of the sea breeze cooling area from an inland river as a function of time.*

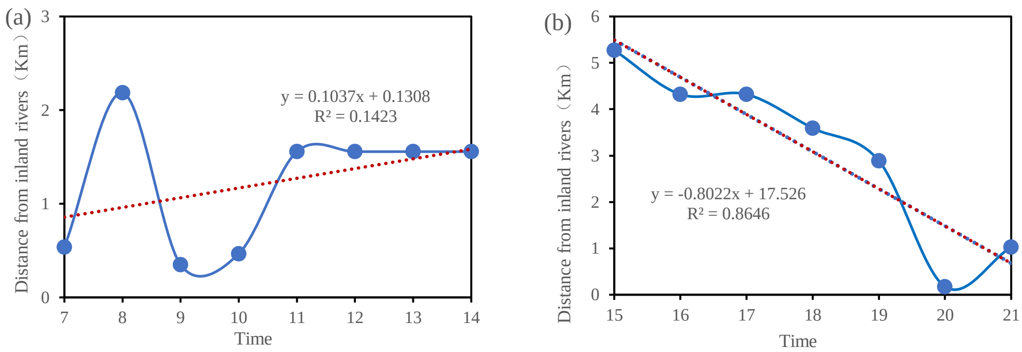

Fig. 5.13*(a)7:00-14:00 Distance of the farthest point of the sea breeze cooling area from an inland river as a function of time;(b)15:00-21:00 Distance of the farthest point of the sea breeze cooling area from an inland river as a function of time.*

The analysis revealed that in the range of the farthest distance of sea breeze cooling from 5km to 11km, the further the distance from the inland river, the further the sea breeze cooling distance (Fig. 5.14a). There is a strong positive correlation between them, with a correlation coefficient of 0.93. In the range of the farthest distance of sea breeze cooling from 11km to 17km, the closer the distance to inland rivers, the further the sea breeze cooling distance (Fig. 5.14b). There is a strong negative correlation between them with a correlation coefficient of -0.82. Therefore, the closer the point is to the inland rivers, the further the sea breeze cooling distance is when the sea breeze cooling distance is more than 11km.

The furthest range of sea breeze cooling exceeds 11km from 08:00-15:00. The hourly cooling capacity and cooling area analysis shows that of all the times with sea breeze cooling effect, the higher cooling capacity and the cooling area is found between 9:00-13:00. Therefore, it can be assumed that inland rivers have a positive effect on the cooling effect of sea breeze.

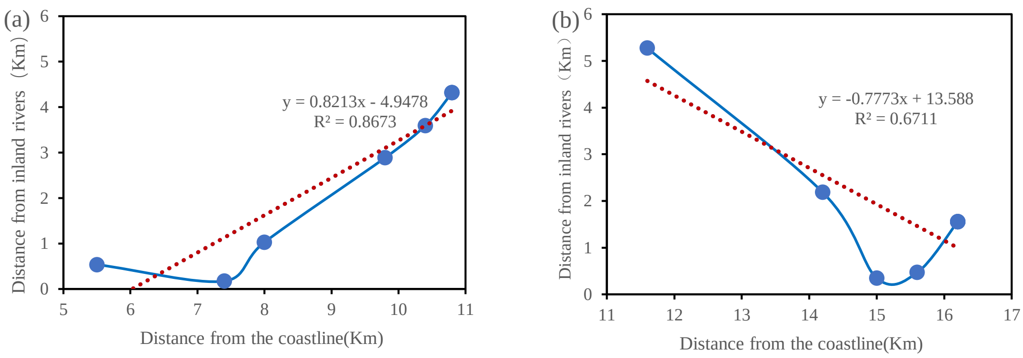

Fig. 5.14 *(a)The cooling area within a distance of 5 - 11 km, furthest cooling point to an inland river;* *(b) The cooling area within a distance of 11 - 17 km, furthest cooling point to an inland river.*

5.4.6. **Sea breeze strongest cooling point**

To analyze the points with the highest hourly sea breeze cooling capacity during the time of sea breeze cooling action, marked these points on a map as shown in Fig. 5.15. The values of the quantities potentially relevant to them were also counted (Table 5.5) and finally the correlations were analyzed (Table 5.6).

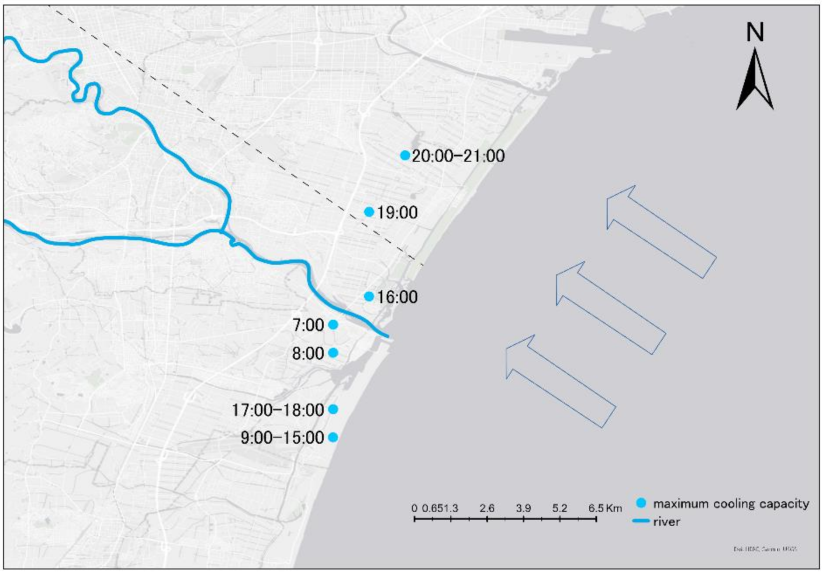

Fig. 5.15 *Location on the map of the point with the highest intensity of sea breeze cooling per hour.*

The results of the correlation analysis show (Table 5.6) that there is a strong correlation between the strongest cooling capacity and the two factors of time and distance from the coast. The strongest cooling capacity shows a strong negative correlation with time, with a correlation coefficient of -0.610. In the time interval produced by the cooling effect of the sea breeze, the value of the strongest cooling capacity decreases as time progresses backward. The strongest cooling capacity shows a strong negative correlation with the distance from the coast, with a correlation coefficient of -0.868. The closer the location of the strongest cooling point is to the coast, the larger the value of the strongest cooling value.

Table 5.5 *Hourly strongest cooling capacity, distance from inland rivers, and distance from the coastline.*

Time	Strongest cooling capacity	Distance from inland	Distance from the coastline
7:00	148.87	0.56	1.94
8:00	285.76	1.48	1.35
9:00	362.51	3.9	0.18
10:00	364.30	3.9	0.18
11:00	366.70	3.9	0.18
12:00	403.18	3.9	0.18
13:00	380.06	3.9	0.18
14:00	332.98	3.9	0.18
15:00	297.70	3.9	0.18
16:00	255.21	0.80	0.84
17:00	208.88	3.14	0.51
18:00	195.15	3.14	0.51
19:00	164.08	2.82	2.22
20:00	130.97	4.78	2.5
21:00	65.33	4.78	2.5

Table 5.6 *The relevance of the factors.*

Time	Strongest cooling capacity	Distance from inland rivers	Distance from the coastline
1			
-0.607	1		
0.387	0.146	1	
0.424	-0.868	-0.143	1

Analysis of the scatter plot of the sea breeze's strongest cooling capacity versus time shows that the overall trend follows a rising, flattening, and then falling process. At 12:00 the sea breeze's strongest cooling capacity reaches its maximum and then begins to decrease (Fig. 5.16). An analysis of the scatter plot of the sea breeze's strongest cooling capacity versus distance from the coast shows a strong negative correlation (Fig. 5.17).

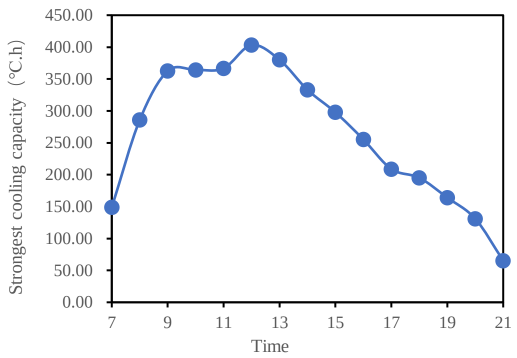

Fig. 5.16 *Strongest cooling capacity per hour of sea breeze.*

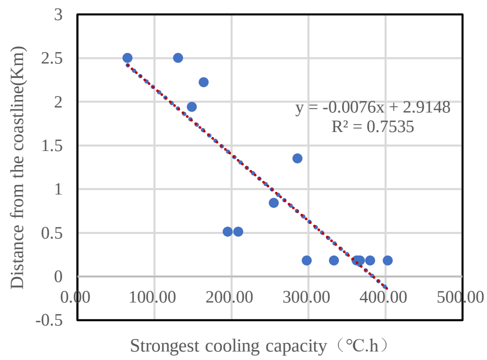

Fig. 5.17 *The sea breeze strongest cooling capacity in relation to the coastline.*

5.5. Conclusions

In this chapter, the difference between the temperature data on sea breeze days and west breeze days is defined as the cooling capacity of sea breeze for coastal cities. The characteristics of sea breeze cooling capacity and cooling range in time were analyzed in detail. The sea breeze cooling capacity and cooling range are described in detail by bar graphs and graphs. The values distributed in the range of 170-240 were eventually found to have the greatest effect on cooling capacity and cooling area.

The distance of the point of action from the coast, the time when the cooling effect occurs, and the inland rivers are important factors that affect the cooling capacity of the sea breeze. The analysis revealed that the closer the area is to the coast, the greater the sea breeze cooling capacity. The point where the cooling action of the sea breeze penetrates furthest into the land, the closer to the coastline and the closer to inland rivers, as the time increases between 15:00 and 21:00. Distance from inland rivers is positively correlated with the farthest distance of cooling when the farthest distance of sea breeze cooling is in the range of 5 km to 11 km. Distance from inland rivers is negatively correlated with the farthest distance of cooling when the farthest distance of sea breeze cooling is in the range of 11 km to 17 km. The area with the strongest cooling capacity per hour is negatively correlated with the time of occurrence of the cooling effect and the distance from the coast. Ultimately, it was concluded that inland rivers have a positive effect on the cooling effect of sea breeze.

Chapter 6. Effect of sea breeze on thermal comfort in coastal cities

6.1. Introduction

Chapter 6 deals with the effect of sea breeze on thermal comfort in coastal cities. Firstly, the distribution of environmental factors affecting outdoor thermal comfort on sea breeze day and west breeze day are listed separately. Environmental factors include temperature, radiation, relative humidity, and wind speed. The source of all data is obtained from the WRF mode analog output. After analyzing the underlying environmental factors, the Rayman software was used to input each environmental factor, thus calculating the outdoor thermal comfort index, PET values, and SET* values for each simulation point on sea breeze day and west breeze day. The outdoor thermal comfort index mainly shows the values of each whole hour point during the sea breeze action time (i.e., 15 hours in total from 7:00 to 21:00), totaling 15 sets. The thermal comfort index of sea breeze day and west breeze day are plotted separately, and their respective variation characteristics and comparison characteristics with each other are analyzed. The distribution of heat stress levels at each point in time is also listed, and the specific distribution characteristics of their thermal comfort are analyzed. Finally, the difference between the outdoor thermal comfort index on sea breeze day and west breeze day is evaluated to analyze the improvement of thermal comfort on sea breeze day compared to west breeze day.

6.2. Comparison of environmental factors between sea breeze day and west breeze day

Outdoor thermal comfort is an important criterion to measure the overall comfort of the outdoor environment, and scholars at home and abroad have conducted a lot of research on outdoor environments. Current research shows that the four environmental parameters of outdoor microclimate wind, light, heat, and humidity are important factors affecting outdoor thermal comfort. This study calculates the thermal comfort index using the Rayman model, which was developed according to the guidelines of the German Society of Engineers and which calculates the radiant flux in urban buildings based on air temperature, air humidity, cloudiness, time date, the emissivity of surrounding surfaces, and solid angle ratio. The input values for this study were air temperature, radiation, wind speed, and relative humidity. And standardized data were used to calculate the outdoor thermal comfort index (i.e. age:35 years, height:1.75; metabolic rate:80w/m2; clothing:0.9; weight:75 kg; sex: male).

6.2.1. **Calculation of air temperature and drawing of distribution chart**

The WRF model output value T2 is the thermodynamic temperature value at 2 m above the ground level of the simulation point, and the Celsius temperature can be obtained after calculation, and then it can be input into the Rayman software. From the conclusion of "Chapter 4: Analysis and Mapping of Sea Breeze Event Time in Coastal Cities", it can be seen that the sea breeze starts to invade from the sea to the land at 7:00 and retreats at 21:00. Therefore, we mainly analyze the characteristics of the temperature during the period when the sea breeze acts on land. From the findings of "Chapter 5 Sea breeze cooling capacity in coastal cities", it is clear that the sea breeze produces the widest range of cooling range and intensity at 10:00.

The average temperatures of all the simulated points in the whole area within the simulation range on sea breeze day and west breeze day are calculated separately and plotted into a graph which can be obtained (Fig. 6.1), the temperature on a west breeze day is generally higher than the temperature on a sea breeze day, and the temperature difference starts to decrease from 17:00.

Comparing the air temperature distribution between the sea breeze day and the west breeze day (Fig. 6.2), the comparison of temperatures is the same as in Figure 1, where the temperatures on west breeze day are generally higher than those on sea breeze day. On sea breeze day, the coastal areas always presented low-temperature values. Starting from 08:00, the closer inland, the higher the temperature values. From 17:00, the high-temperature areas started to move from the inland areas to the urban areas. On west breeze day, inland areas always presented low-temperature values. Coastal areas and urban areas presented high-temperature values.

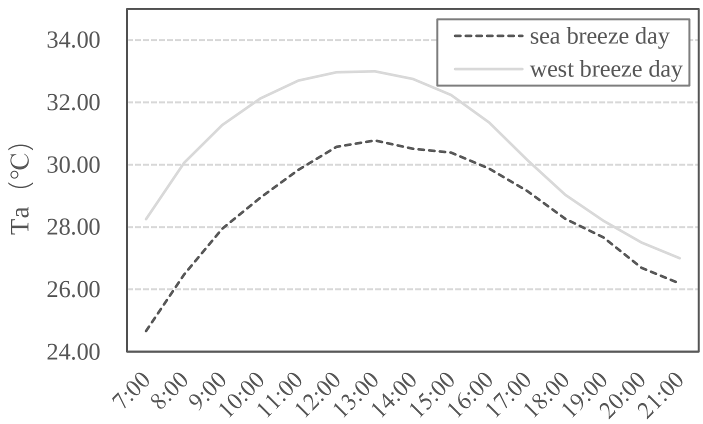

Fig. 6.1 *Average air temperature on sea breeze day and west breeze day*

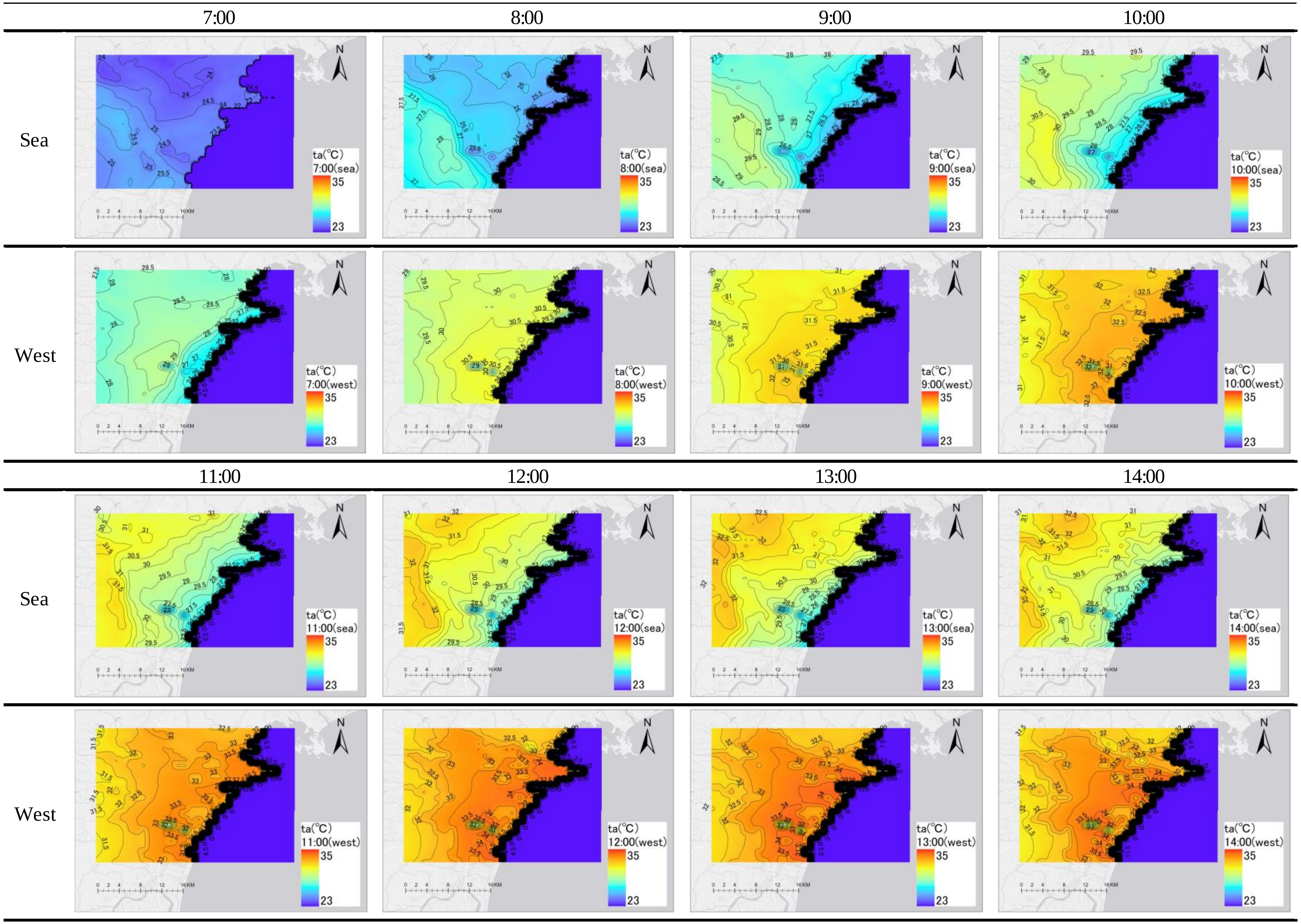
7:00
8:00
9:00
10:00
Sea
West
11:00
12:00
13:00
14:00
Sea
West
ta(°C)
35
23

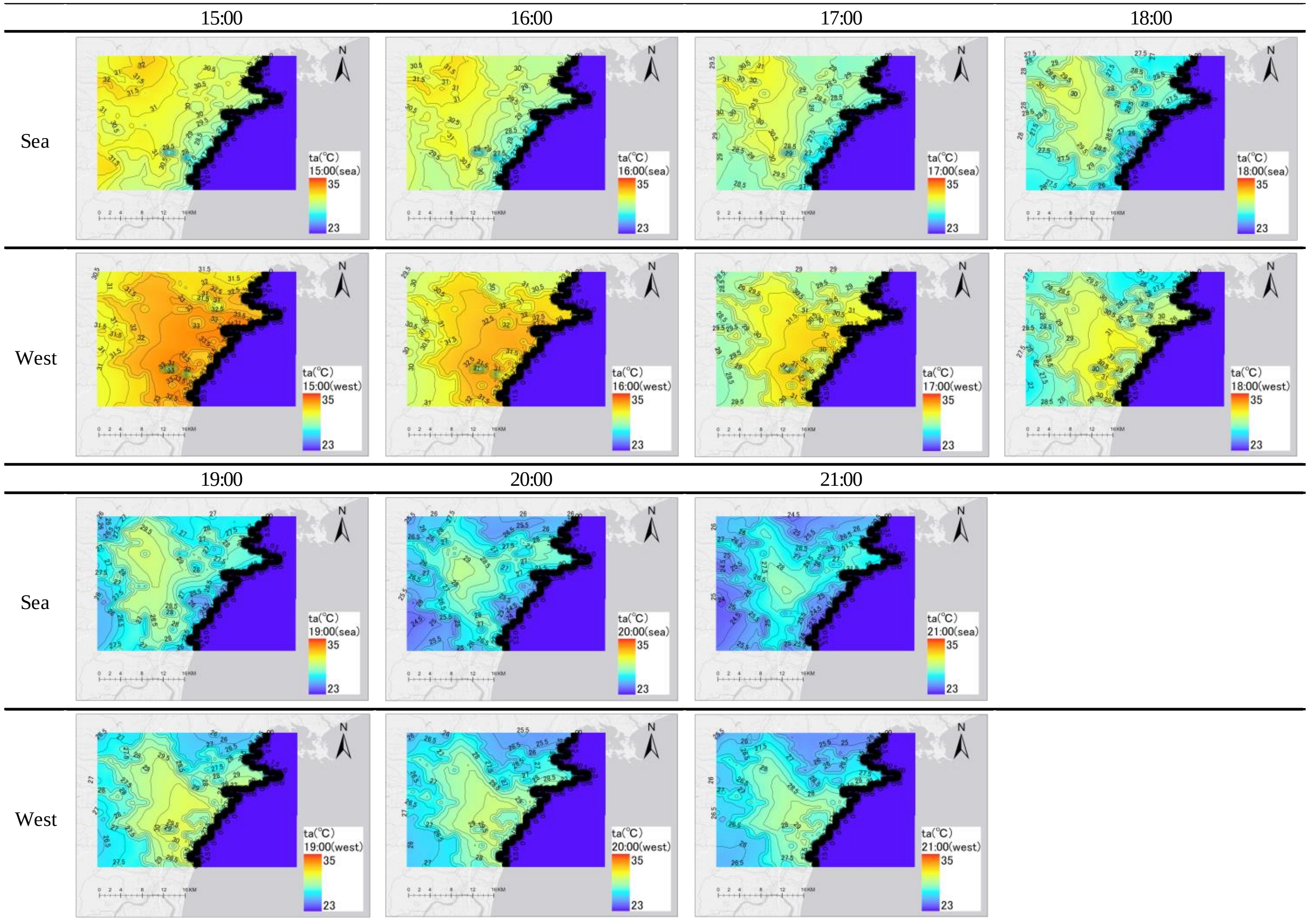

Fig. 6.2 *Map of temperature distribution between sea breeze day and west breeze day*

6.2.2. **Calculation of radiation values and mapping of distribution**

The SWDOWN (DOWNWARD SHORT WAVE FLUX AT GROUND SURFACE) in the WRF output variable is the amount of solar radiation at the Earth's surface that Rayman requires as input. This variable includes both direct and diffuse solar radiation. Therefore, this value can be entered directly into the Rayman software. The radiation values show a great difference between sea breeze day and west breeze days, but at 19:00 the radiation values are all 0. Therefore, only the radiation values from 7:00 to 18:00 are counted.

As can be seen from the average values of the study area at each momentary point for sea breeze day and west breeze day (Fig. 6.3), the radiation values for both sea breeze day and west breeze day increase from 7:00 and start to decrease after reaching a peak at 11:00. As a whole, the trend and the difference in the magnitude of the radiation averages between sea breeze day and west breeze day are not large. The difference between the radiation averages on sea breeze day and west breeze day is small during the period from 7:00 to 10:00, after which there is a slight increase in the difference.

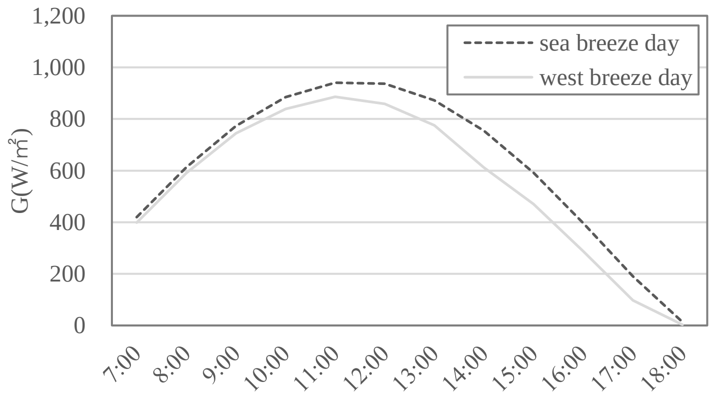

Fig. 6.3 *Radiation averaged over the study area at hourly moment points on sea breeze day and west breeze day.*

The difference between the maximum and minimum values of radiation at each hourly point in the study area on sea breeze day and west breeze day (Fig. 6.4) shows that the difference between the maximum and minimum values on sea breeze day are small, which means that the radiation values on land are high and average on the days of sea breeze day. On the west breeze day, the difference between the maximum and minimum values of radiation is larger from 12:00 onwards. That is to say, the average radiation value on the land on the day of the west breeze day is in different areas, and the radiation value varies greatly. Then, the radiation values at each moment of the sea breeze day and west breeze day were plotted into a radiation distribution map using ArcGIS Pro (Fig. 6.5) before further analysis.

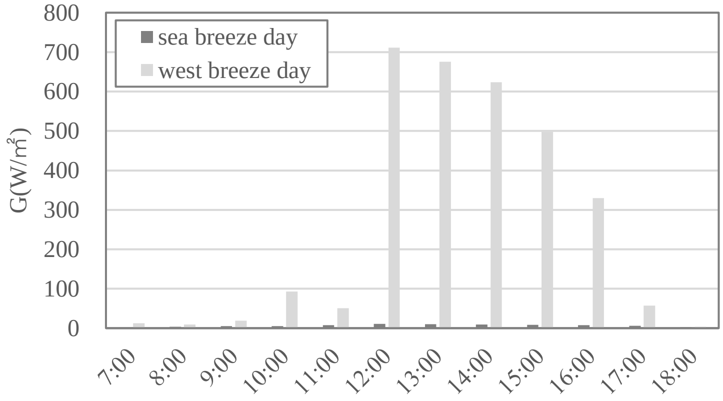

Fig. 6.4 *Difference between the maximum and minimum values of radiation in the study area at the hourly moment point on sea breeze day and west breeze day*

On sea breeze day, the radiation is high throughout the study area and the radiation values are well distributed. The radiation values in the study area are more evenly distributed between 7:00 and 9:00 on the west breeze day, with higher values in the north than in the south at 10:00. Lower radiation values were seen in urban areas at 11:00, and higher in the south between 12:00 and 13:00. 14:00 to 16:00 is when higher radiation values are more inland areas.

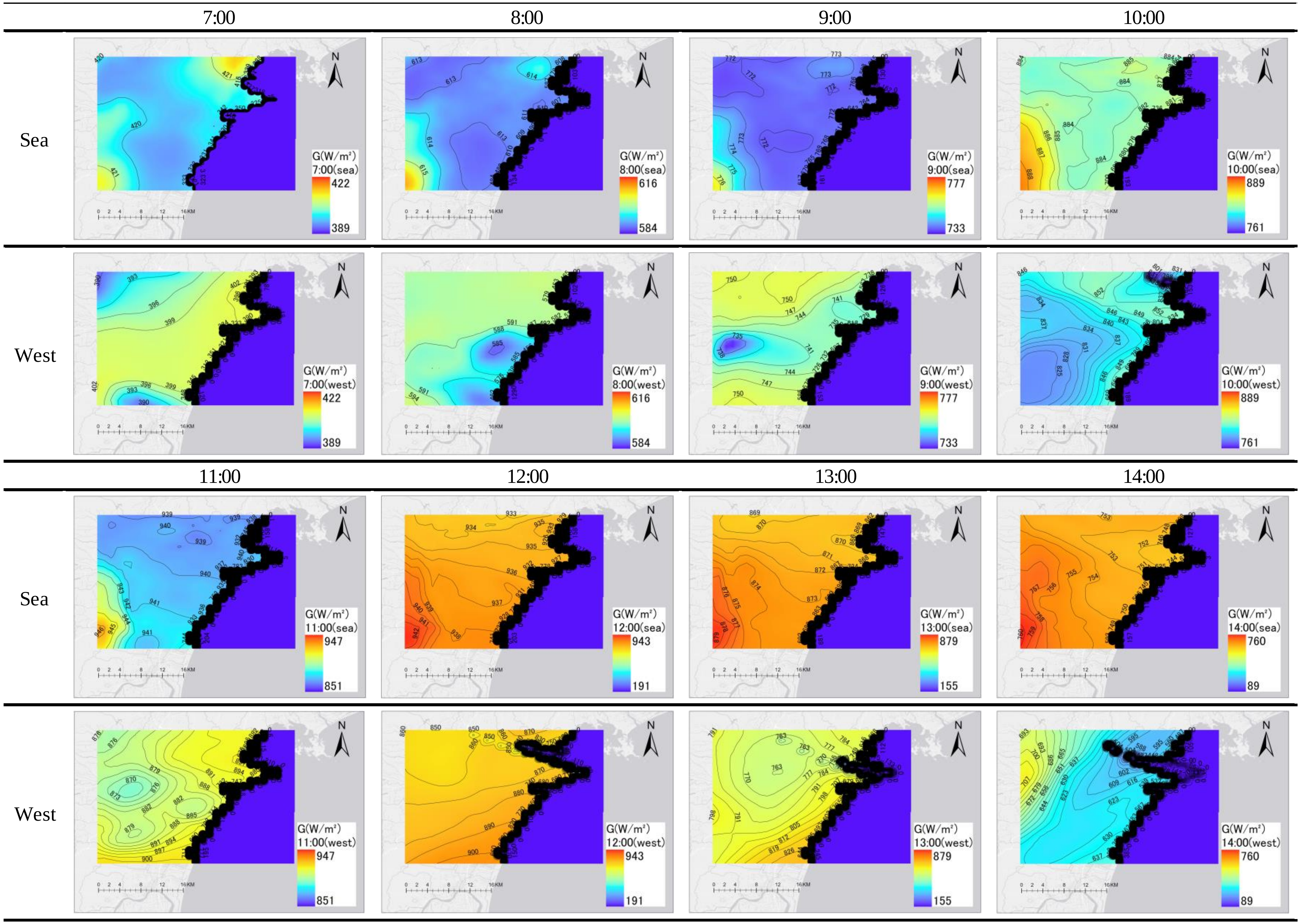
7:00
8:00
9:00
10:00
Sea
G(W/m²) 7:00(sea) 422 389
G(W/m²) 8:00(sea) 616 584
G(W/m²) 9:00(sea) 777 733
G(W/m²) 10:00(sea) 889 761
West
G(W/m²) 7:00(west) 422 389
G(W/m²) 8:00(west) 616 584
G(W/m²) 9:00(west) 777 733
G(W/m²) 10:00(west) 889 761
11:00
12:00
13:00
14:00
Sea
G(W/m²) 11:00(sea) 947 851
G(W/m²) 12:00(sea) 943 191
G(W/m²) 13:00(sea) 879 155
G(W/m²) 14:00(sea) 760 89
West
G(W/m²) 11:00(west) 947 851
G(W/m²) 12:00(west) 943 191
G(W/m²) 13:00(west) 879 155
G(W/m²) 14:00(west) 760 89
N
0 2 4 8 12 16KM

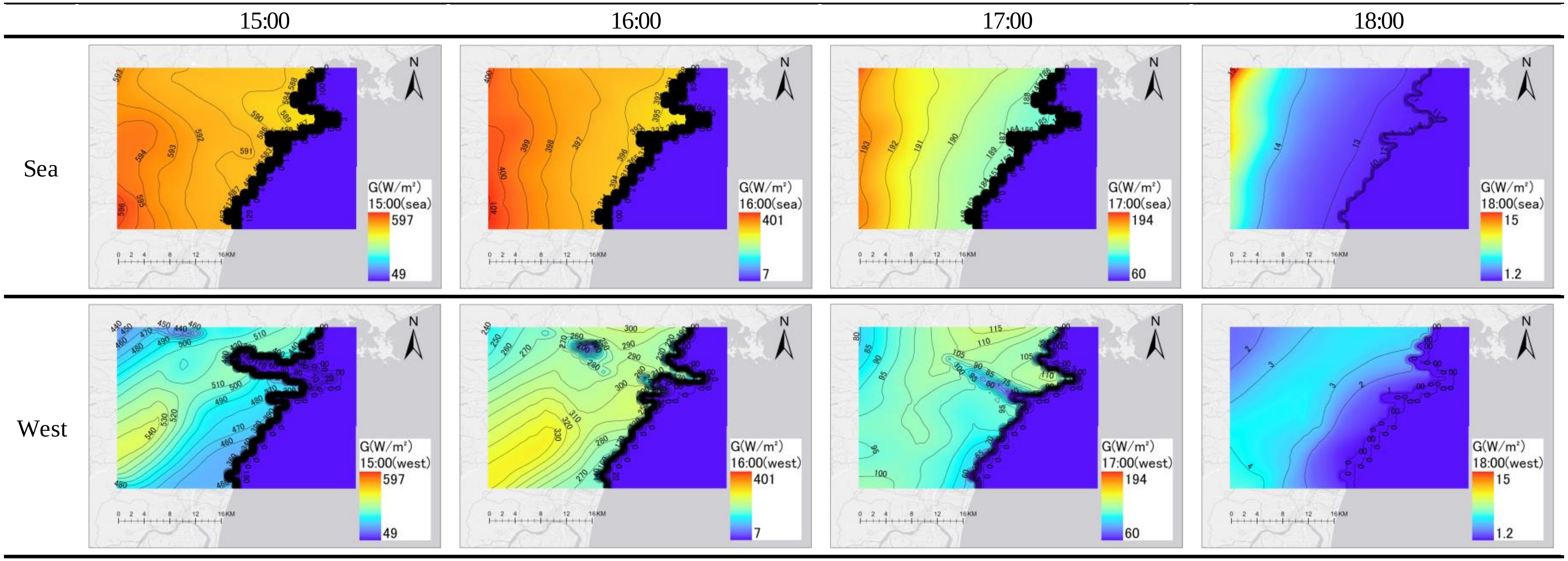

Fig. 6.5 *Map of the distribution of radiation values at hourly moment points on sea breeze day and west breeze day*

6.2.3. **Calculation of wind speed and mapping of distribution**

The WRF model output variable does not include horizontal wind speed. The horizontal wind speed can be obtained from U10 and Q10 calculations. U10 and Q10 represent 10m east wind speed and 10m north wind speed, respectively. Using the Pythagorean theorem, the 10m horizontal wind speed can be calculated：

$$V = \sqrt{U10^2 + Q10^2}$$

As can be seen from the wind speed averages (Fig. 6.6), on west breeze day the wind speed increases continuously from 07:00 until it reaches a maximum at 11:00, and from 16:00 the wind speed starts to weaken. The wind speed of the sea breeze day starts to increase continuously from 07:00 until it reaches the maximum at 13:00 and starts to weaken from 16:00. The wind speed on sea breeze day is always lower than the wind speed on west breeze day. The average wind speed on a sea breeze day is significantly lower than the average wind speed on a west breeze day. From 16:00 onwards, the gap starts to narrow gradually.

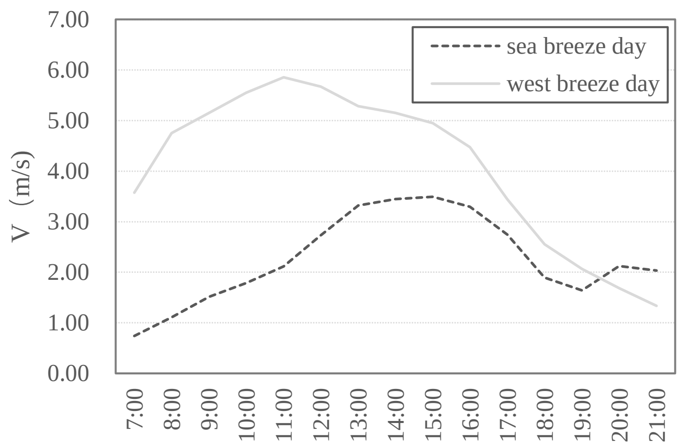

Fig. 6.6 *Average wind speed over the whole area on sea breeze day and west breeze day.*

The WRF modeling system supports NCAR command language (NCL) and can directly output the wind condition distribution map in the simulation area (Fig. 6.7). On the sea breeze day, the wind speed was low and irregular throughout the study area at

7:00. At 8:00, the wind speed blowing from the inland to the sea direction began to increase in the southwest region and at 9:00, the temperature in the area was high. At 9:00, the regularity of the wind blowing from the sea to the land direction started to increase, and at 10:00 it strengthened again, but after entering the urban area, the wind speed decreased and the direction was weak, and in the southwest area, the wind blowing from the inland to the sea direction made the sea breeze did not reach the area. Then the wind blowing from the sea directly to the land direction gradually strengthened until 14:00, when the sea breeze penetrated the whole study area except for the southwest region, but there was a significant decrease in wind speed as it penetrated inland. Starting at 19:00, the low wind speed was maintained and the wind began to blow from all directions toward the hot areas of the urban area.

On the west breeze day, the wind is always strong and at 7:00 it already has a strong regularity and can be roughly divided into two directions. The direction from the western inland to the eastern sea and the southwesterly wind in the sea area. Until 10:00, the wind blows in the direction from the land to the sea in the whole study area. Same as the sea breeze day, at 19:00, the low wind speed was maintained and the wind started to blow from all directions towards the hot areas of the city area.

	7:00	8:00	9:00	10:00
Sea	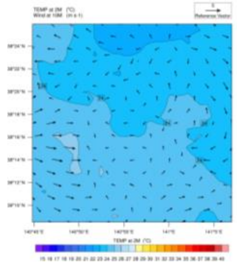	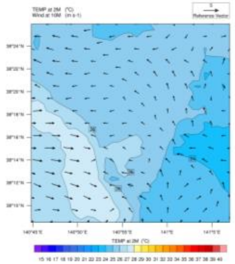	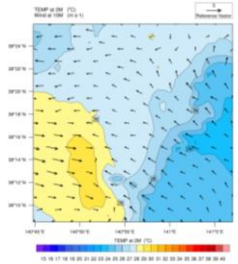	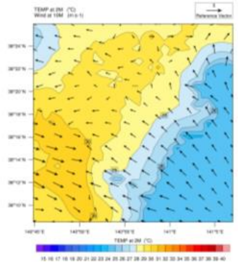
West	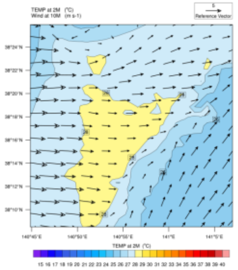	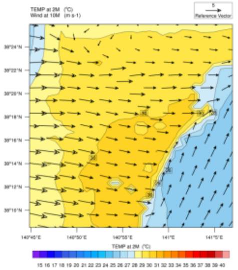	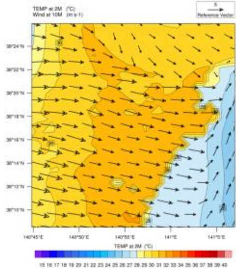	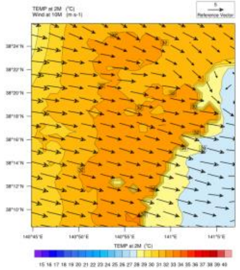

	11:00	12:00	13:00	14:00
Sea	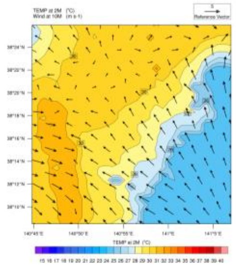	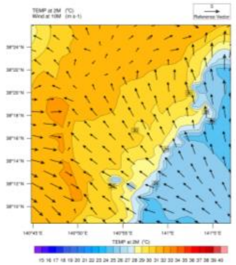	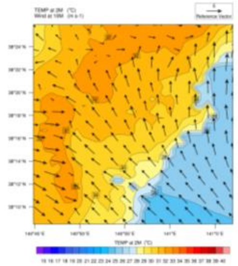	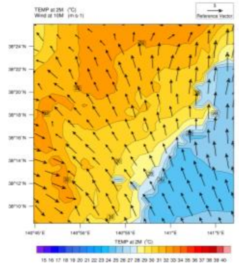
West	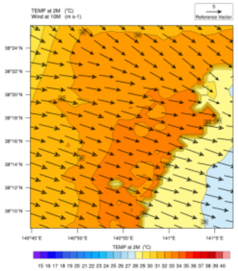	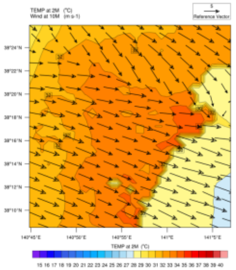	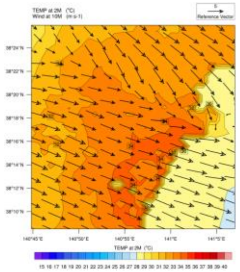	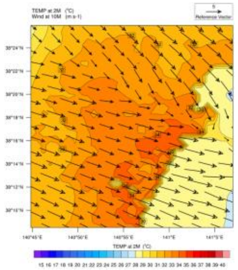

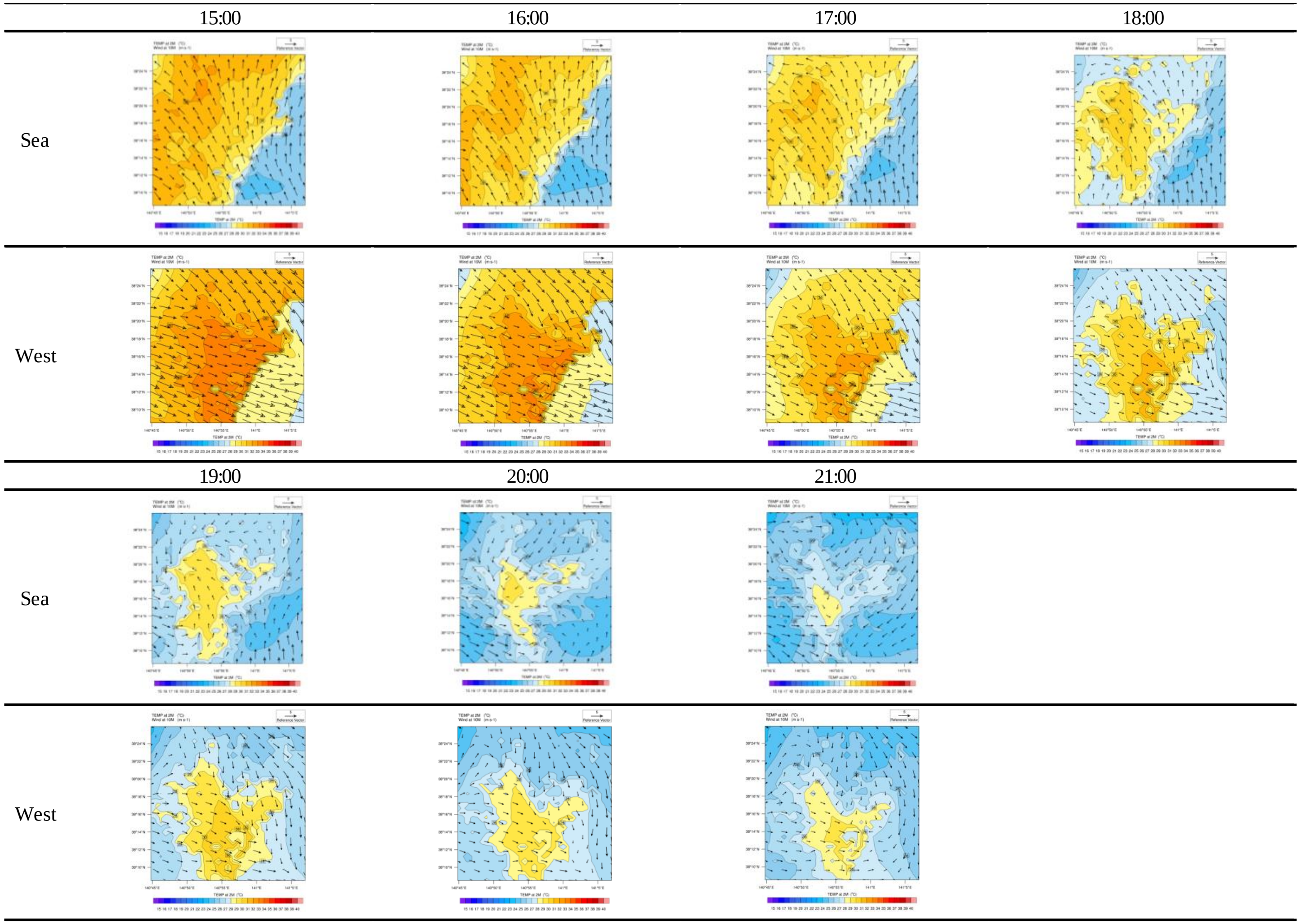

Fig. 6.7 *Map of wind speed distribution on sea breeze day and west breeze day.*

6.2.4. **Calculation of relative humidity and plotting of distribution**

Relative Humidity, expressed in RH. It refers to the percentage of water vapor pressure in the air and the saturation water vapor pressure at the same temperature, or the ratio of the absolute humidity of wet air to the maximum absolute humidity possible at the same temperature. It can also be expressed as the ratio of the partial pressure of water vapor in wet air to the saturation pressure of water at the same temperature.

NCEP surface flux data do not have RH and need to be calculated by specific humidity, air pressure and temperature, calculated by the formula

$$RH = 100\frac{w}{w_s} \approx 0.263pq\left[exp\left(\frac{17.67(T_2 - T_0)}{T_2 - 29.65}\right)\right]^{-1}$$

w vapor pressure I (Pa)

ws saturated vapor pressure (Pa)

q specific humidity (dimensionless)

p pressure (Pa)

T_2 temperature (K)

T_0 reference temperature (typically 273.16 K)

The average values of relative humidity for all simulated points over the whole area on sea breeze day and west breeze day were calculated separately, as shown in the figure (Fig. 6.8):

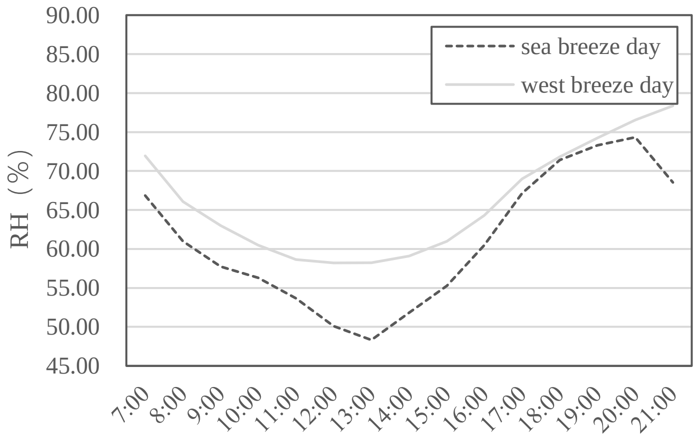

Fig. 6.8 *Average relative humidity of all simulated points over the whole area on sea breeze day and*

west breeze day

As a whole, from 07:00 to 17:00, the relative humidity on west breeze day is higher than that on sea breeze day, especially in the period from 07:00 to 13:00. The relative humidity on both days started to rise after a steady decline from 07:00 to 13:00. The relative humidity rises faster on sea breeze day than on west breeze day and begins to overlap between sea breeze day and west breeze day at 17:00.

The data obtained from the calculations were then plotted using ArcGIS Pro (Fig. 6.9), from which the regional characteristics of the relative humidity within the simulation were analyzed. The coastal area of the sea breeze day presented a higher relative humidity. The area of low relative humidity moves gradually from the inland area to the urban area. On the west breeze day, the inland area consistently shows higher relative humidity and the urban and coastal area have relatively lower present relative humidity.

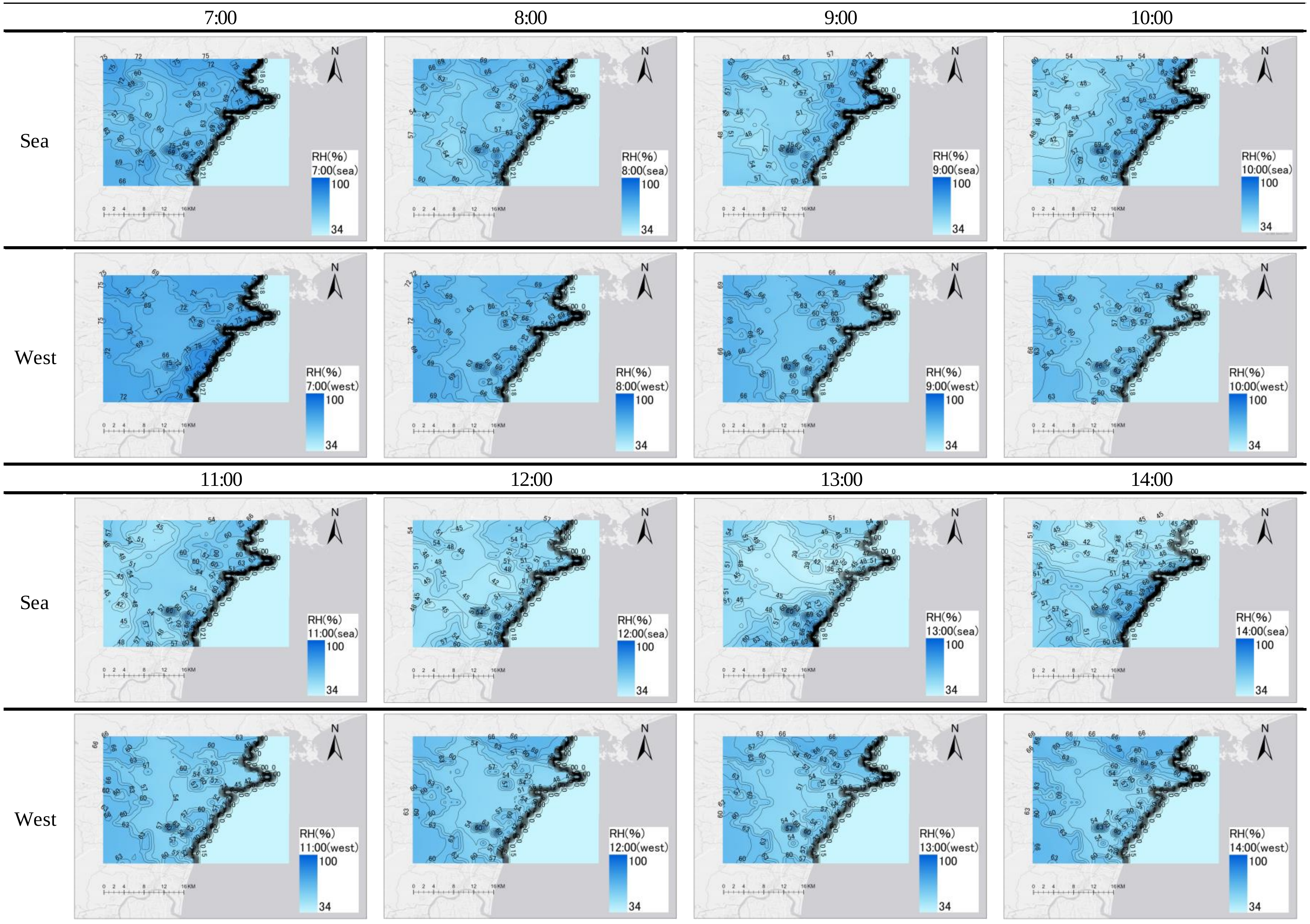
7:00
8:00
9:00
10:00
Sea
RH(%)
7:00(sea)
8:00(sea)
9:00(sea)
10:00(sea)
100
34
West
RH(%)
7:00(west)
8:00(west)
9:00(west)
10:00(west)
100
34
11:00
12:00
13:00
14:00
Sea
RH(%)
11:00(sea)
12:00(sea)
13:00(sea)
14:00(sea)
100
34
West
RH(%)
11:00(west)
12:00(west)
13:00(west)
14:00(west)
100
34
N
0 2 4 8 12 16KM

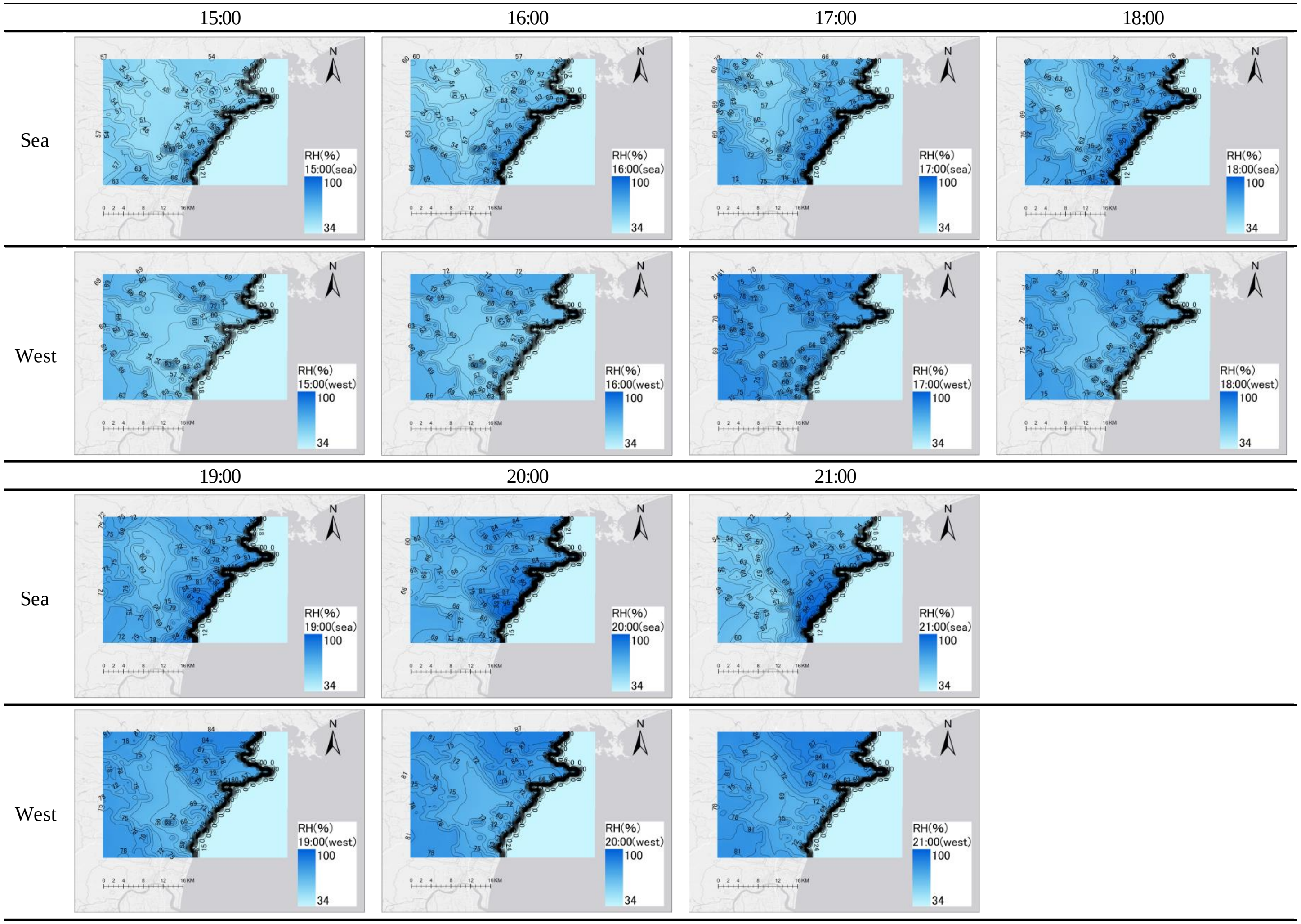

Fig. 6.9 *Map of relative humidity distribution on sea breeze day and west breeze day*

6.3. PET day change between sea breeze day and west breeze day

6.3.1. PET and SET* Maps

This study used the Rayman model to calculate PET values, the input initial parameters for this study were air temperature, relative humidity, radiation, and wind speed all data sources were obtained from the direct output of the WRF model simulation, or the output values were calculated. And standardized data were used to calculate PET (i.e. age:35 years, height:1.75; metabolic rate:80w/m2; clothing:0.9; weight:75 kg; sex: male). The results of the calculations are presented below as PET maps using ArcGIS Pro (Fig. 6.10).

Based on the PET map, a preliminary analysis of the characteristics of the daily variation of PET on sea breeze day and west breeze day was conducted. On the morning of the sea breeze day, high PET values were present in the western inland area and the northern inland area, with a significant decrease in the high PET values in the northern inland area until 13:00, and the high PET values in the western inland area persisted until 17:00. From 19:00, the high PET values started to move from the northern inland area to the urban area. Coastal areas show lower PET values from 09:00 onwards. On the west breeze day, the high PET values keep presenting in the coastal area and the urban area.

The SET* map (Fig. 6.11) presents the same pattern of thermal comfort changes as the PET map.

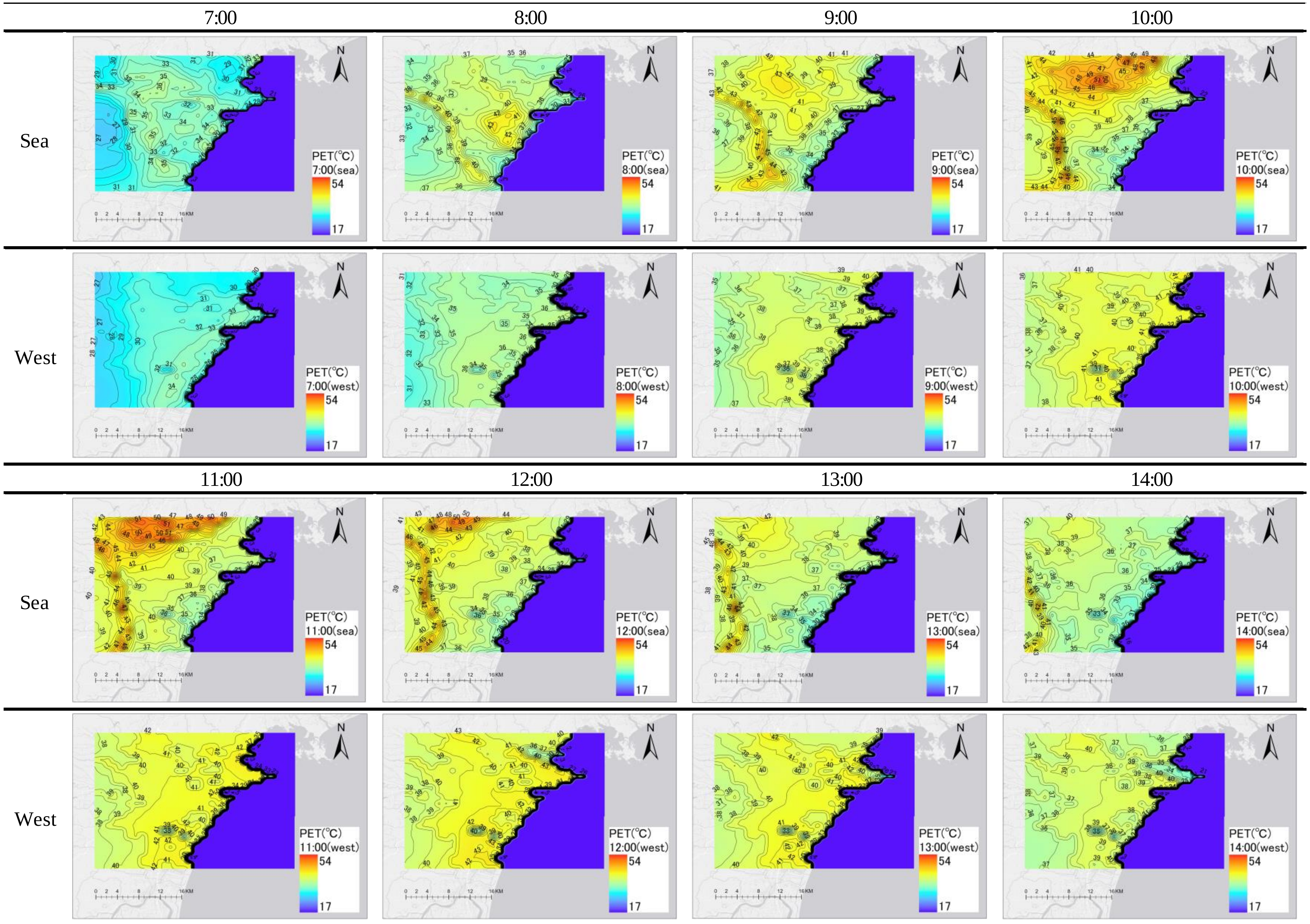
7:00
8:00
9:00
10:00
Sea
PET(℃) 7:00(sea)
PET(℃) 8:00(sea)
PET(℃) 9:00(sea)
PET(℃) 10:00(sea)
West
PET(℃) 7:00(west)
PET(℃) 8:00(west)
PET(℃) 9:00(west)
PET(℃) 10:00(west)
11:00
12:00
13:00
14:00
Sea
PET(℃) 11:00(sea)
PET(℃) 12:00(sea)
PET(℃) 13:00(sea)
PET(℃) 14:00(sea)
West
PET(℃) 11:00(west)
PET(℃) 12:00(west)
PET(℃) 13:00(west)
PET(℃) 14:00(west)
54
17
N
0 2 4 8 12 16KM

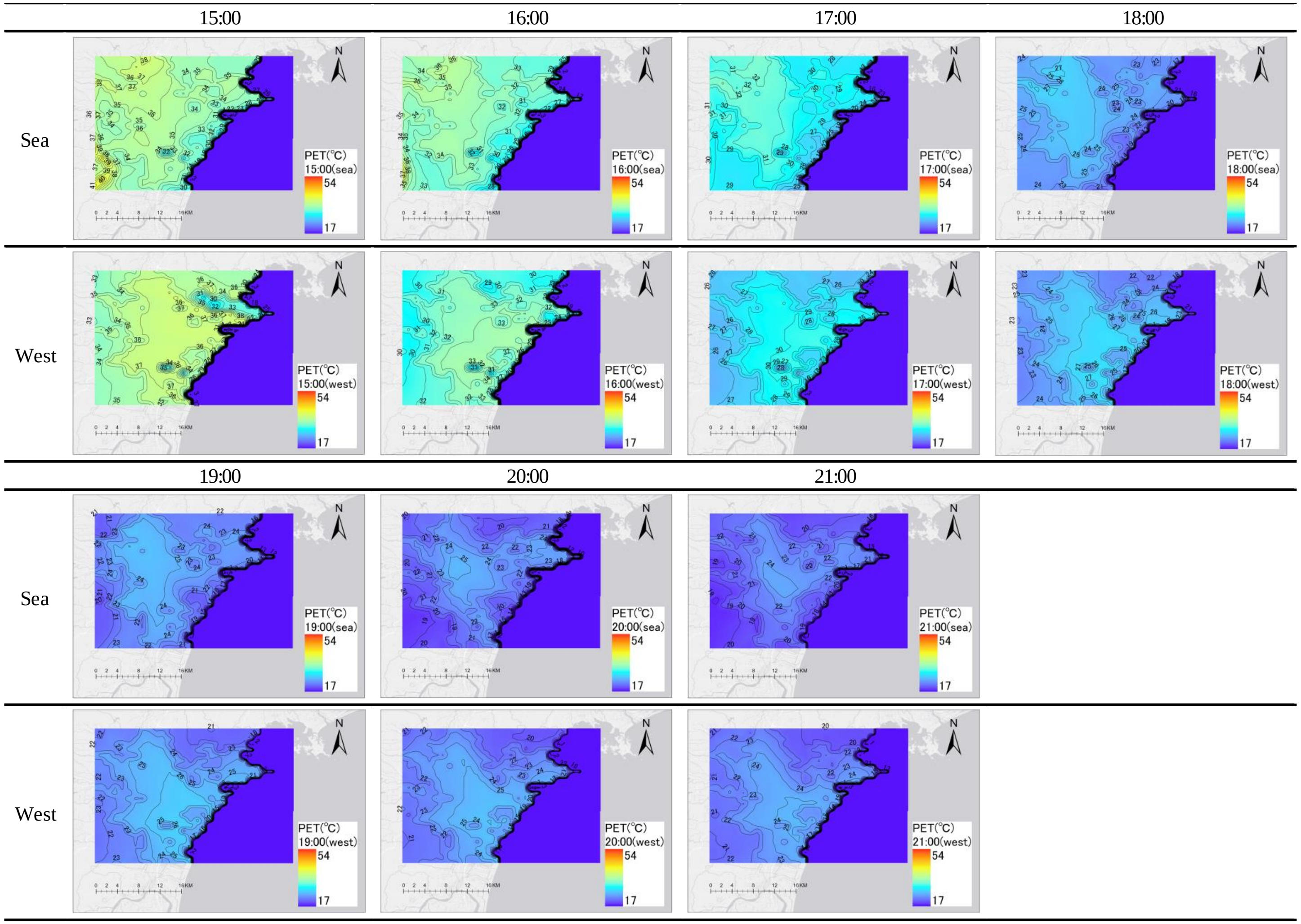

Fig. 6.10 *Map of PET distribution on Sea Breeze Day and West Breeze Day*

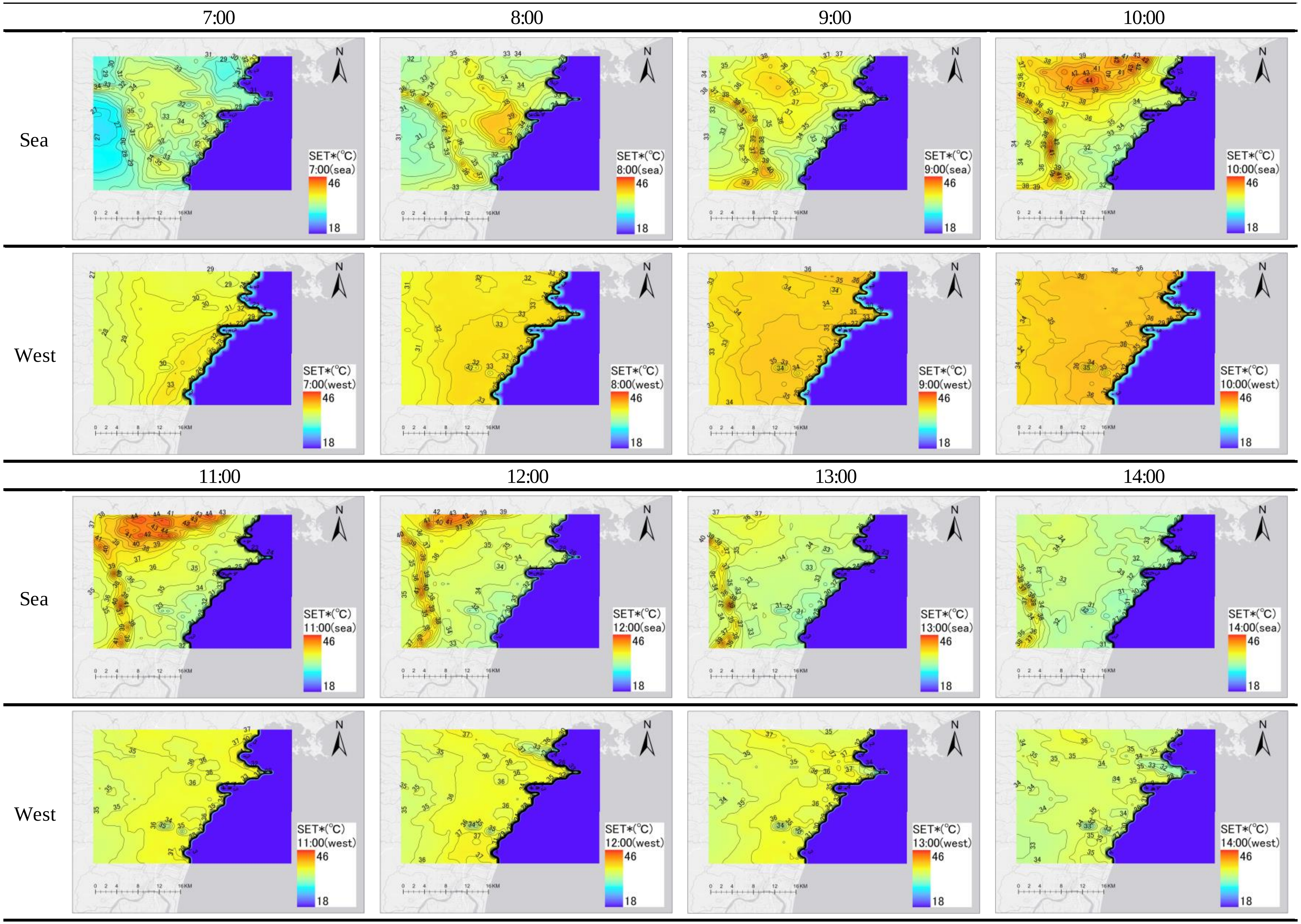
7:00
8:00
9:00
10:00
Sea
West
SET*(°C) 7:00(sea)
SET*(°C) 8:00(sea)
SET*(°C) 9:00(sea)
SET*(°C) 10:00(sea)
SET*(°C) 7:00(west)
SET*(°C) 8:00(west)
SET*(°C) 9:00(west)
SET*(°C) 10:00(west)
11:00
12:00
13:00
14:00
SET*(°C) 11:00(sea)
SET*(°C) 12:00(sea)
SET*(°C) 13:00(sea)
SET*(°C) 14:00(sea)
SET*(°C) 11:00(west)
SET*(°C) 12:00(west)
SET*(°C) 13:00(west)
SET*(°C) 14:00(west)
46
18
N
0 2 4 8 12 16KM

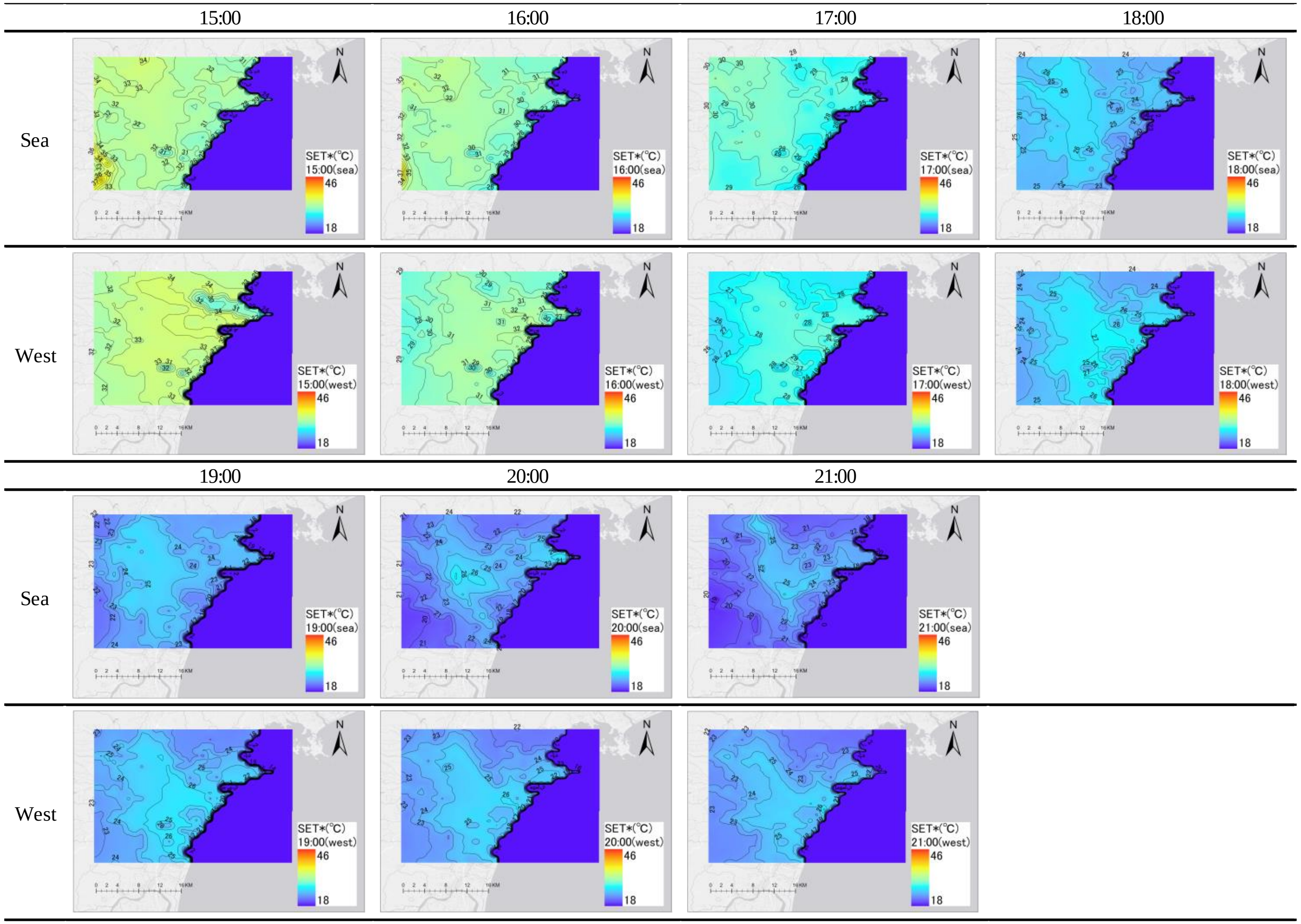

Fig. 6.11 *SET* Map of Sea Breeze Day and West Breeze Day*

6.3.2. **Analysis of the relationship between thermal comfort index and each environmental factor**

Because the results of the PET map and the SET* map are very similar, in this section, only the relationship between PET values and each environmental factor is analyzed for sea breeze days and west breeze day, respectively (Fig. 6.12/Fig. 6.13). The environmental factors specifically include temperature, wind speed, relative humidity, and radiation. Among them, temperature and wind speed are shown on the same map.

On the sea breeze day, the radiation values, wind speed, and temperature values are lower at 7:00 and the PET value distribution is more influenced by the relative humidity. The areas presenting lower relative humidity presented higher PET values.

At 8:00, in the local area along the coast near the urban area, low relative humidity and high PET values were presented. And at this time the radiation values started to increase, with the western inland area showing high radiation values and the wind blowing from the inland towards the sea, showing high PET values in this area. Such a phenomenon continued until 14:00.

At 10:00, the sea breeze blowing towards the land began to develop a consistent directionality, but in the northern inland area, the directionality of the sea breeze diminished and the wind speed was lower and the temperature was higher, presenting high PET values in this area. Such a phenomenon persisted until 15:00 when the sea breeze completely penetrated the entire study area before the PET values decreased. From 15:00 onwards, the radiation values decrease and the distribution of PET values is more influenced by the relative humidity. The areas presenting lower relative humidity presented higher PET values. On west breeze day, the higher the temperature the higher the region presents the lower the relative humidity, and the higher the PET values. And the regularity of the radiation values is not strong, and there is a clear territoriality of the high and low radiation values.

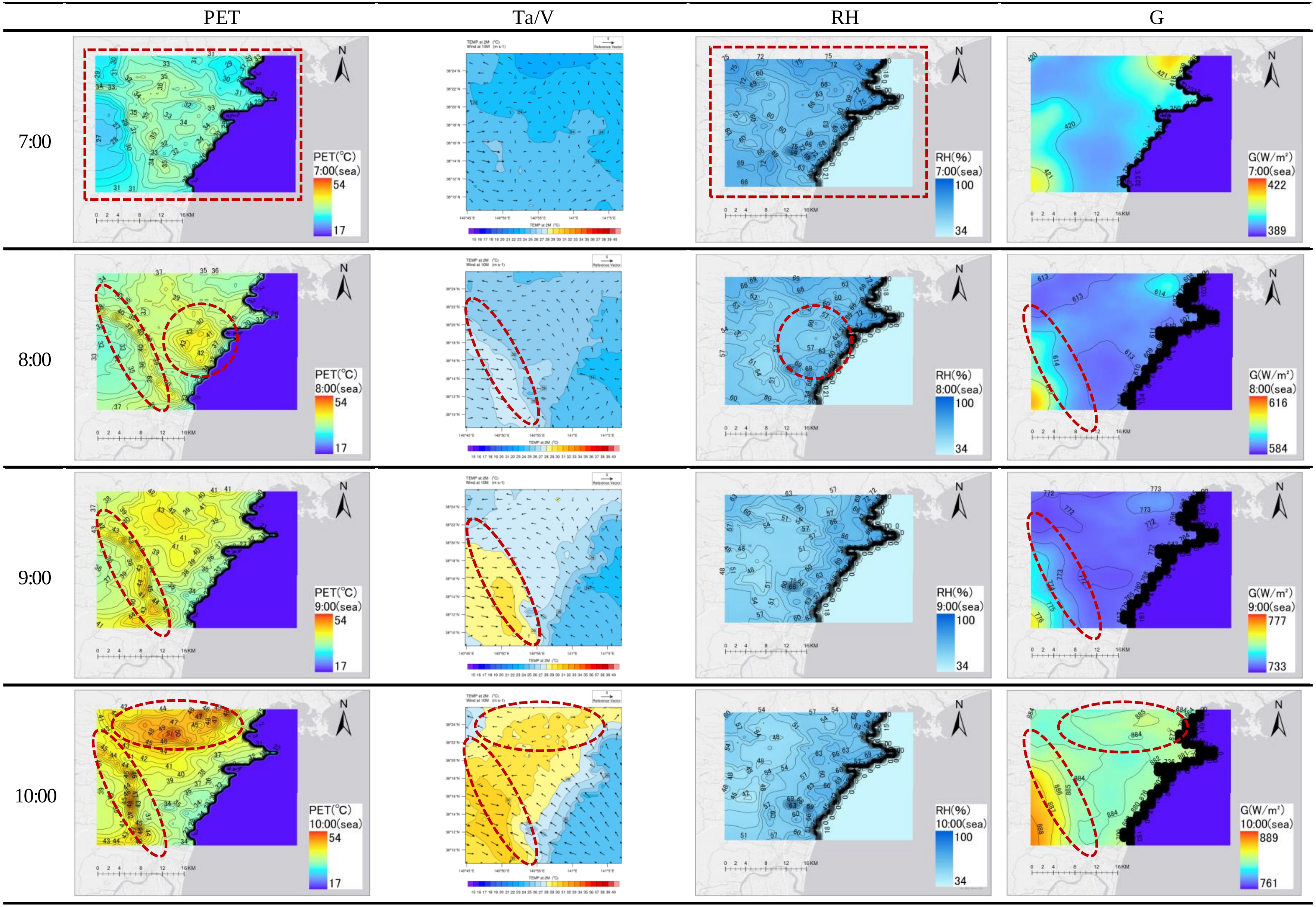
PET
Ta/V
RH
G
7:00
8:00
9:00
10:00
PET(℃)
7:00(sea)
54
17
RH(%)
7:00(sea)
100
34
G(W/m²)
7:00(sea)
422
389
PET(℃)
8:00(sea)
54
17
RH(%)
8:00(sea)
100
34
G(W/m²)
8:00(sea)
616
584
PET(℃)
9:00(sea)
54
17
RH(%)
9:00(sea)
100
34
G(W/m²)
9:00(sea)
777
733
PET(℃)
10:00(sea)
54
17
RH(%)
10:00(sea)
100
34
G(W/m²)
10:00(sea)
889
761
N
0 2 4 8 12 16KM

	PET	Ta/V	RH	G

11:00

12:00

13:00

14:00

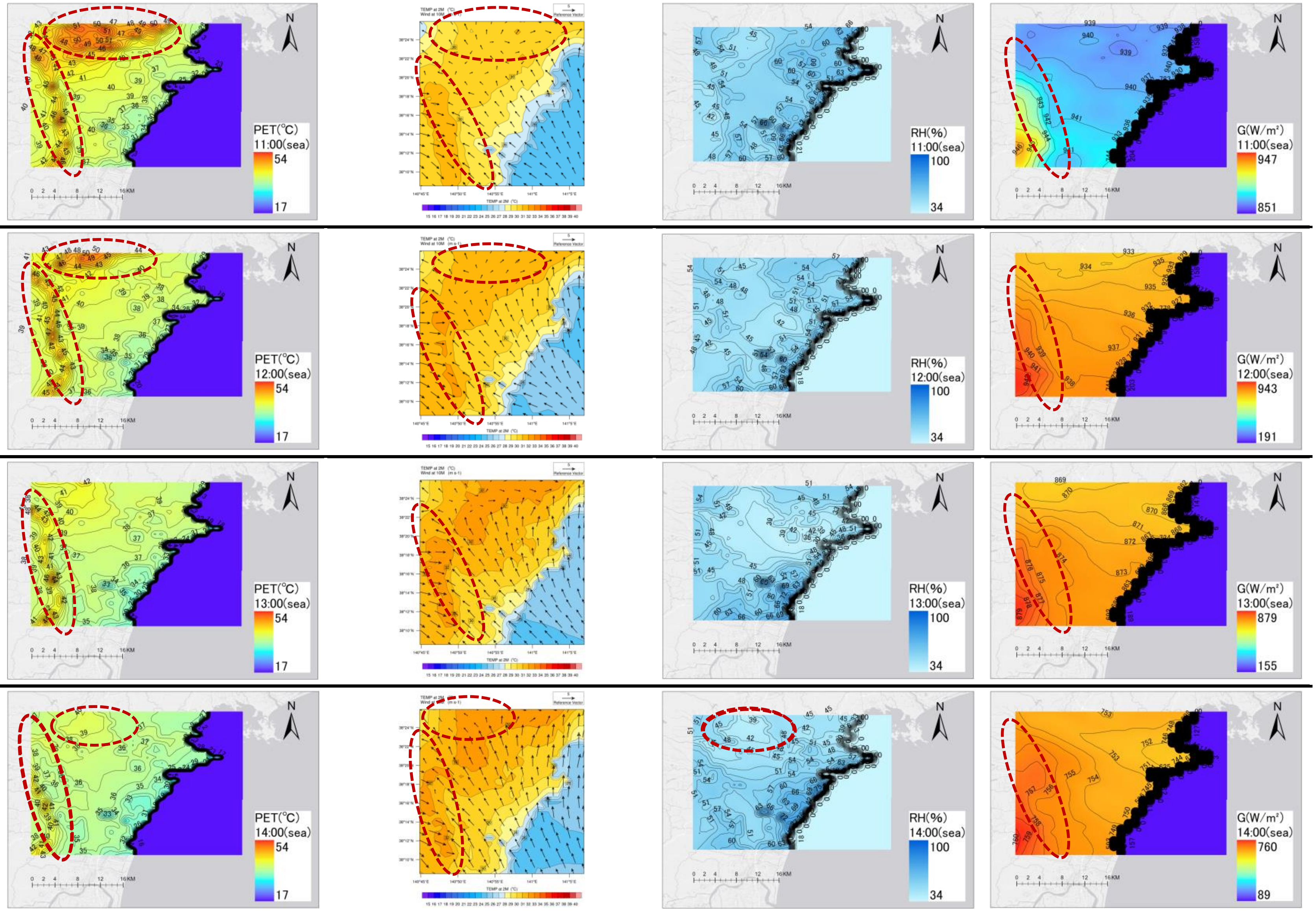

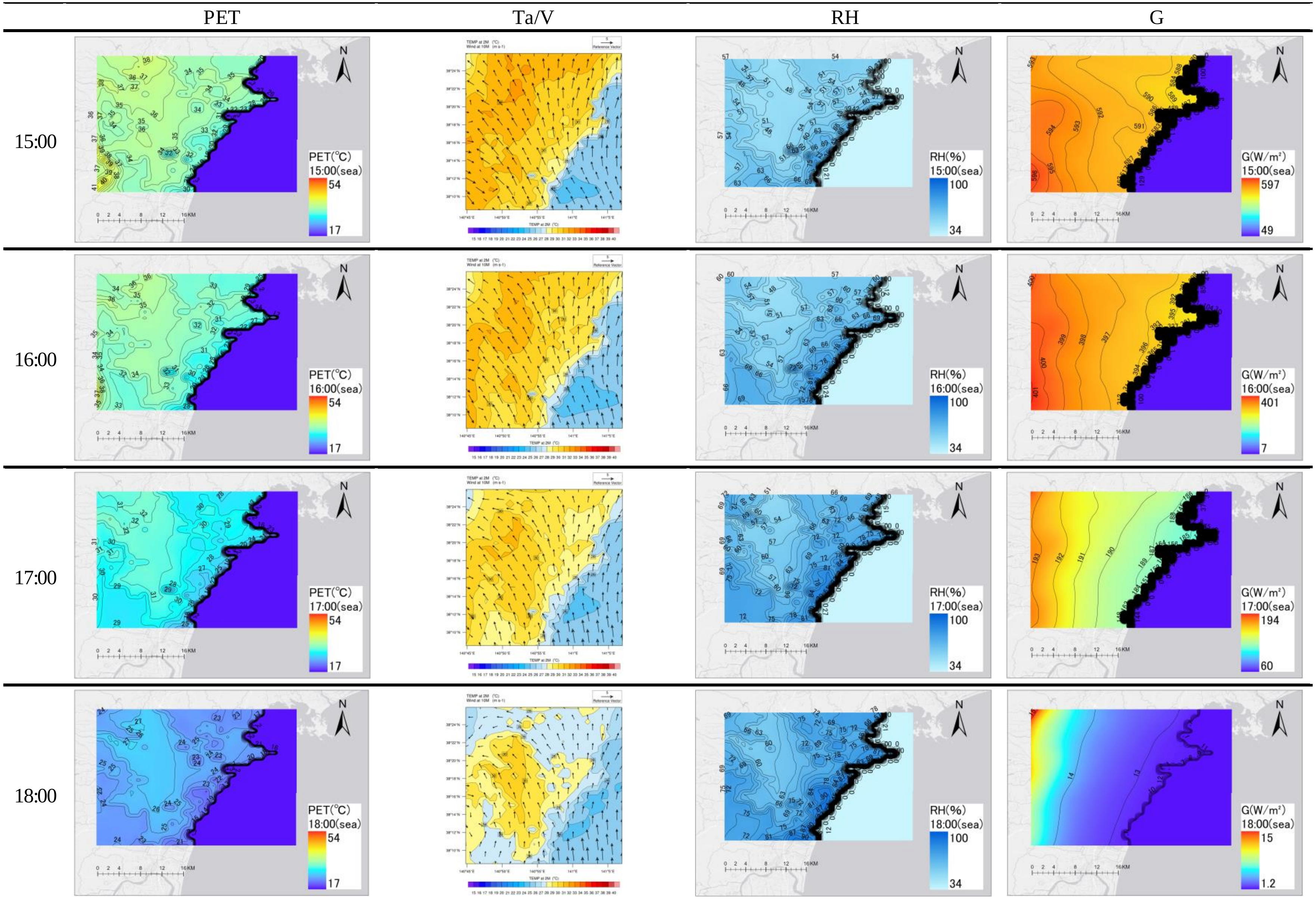
PET
Ta/V
RH
G
15:00
16:00
17:00
18:00
PET(℃)
15:00(sea)
54
17
RH(%)
15:00(sea)
100
34
G(W/m²)
15:00(sea)
597
49
PET(℃)
16:00(sea)
54
17
RH(%)
16:00(sea)
100
34
G(W/m²)
16:00(sea)
401
7
PET(℃)
17:00(sea)
54
17
RH(%)
17:00(sea)
100
34
G(W/m²)
17:00(sea)
194
60
PET(℃)
18:00(sea)
54
17
RH(%)
18:00(sea)
100
34
G(W/m²)
18:00(sea)
15
1.2

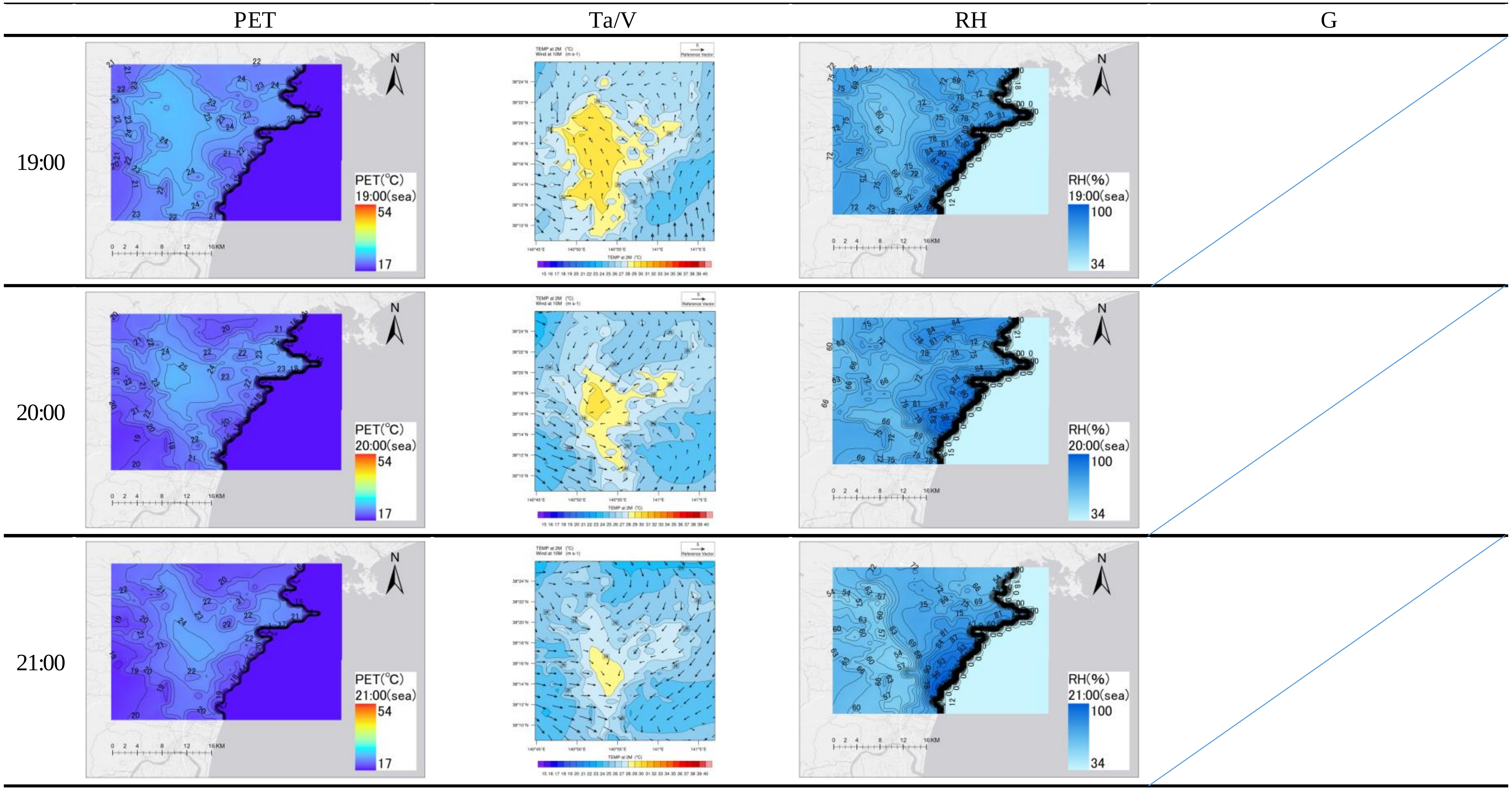

Fig. 6.12 *Thermal comfort index of sea breeze day with each environmental factor*

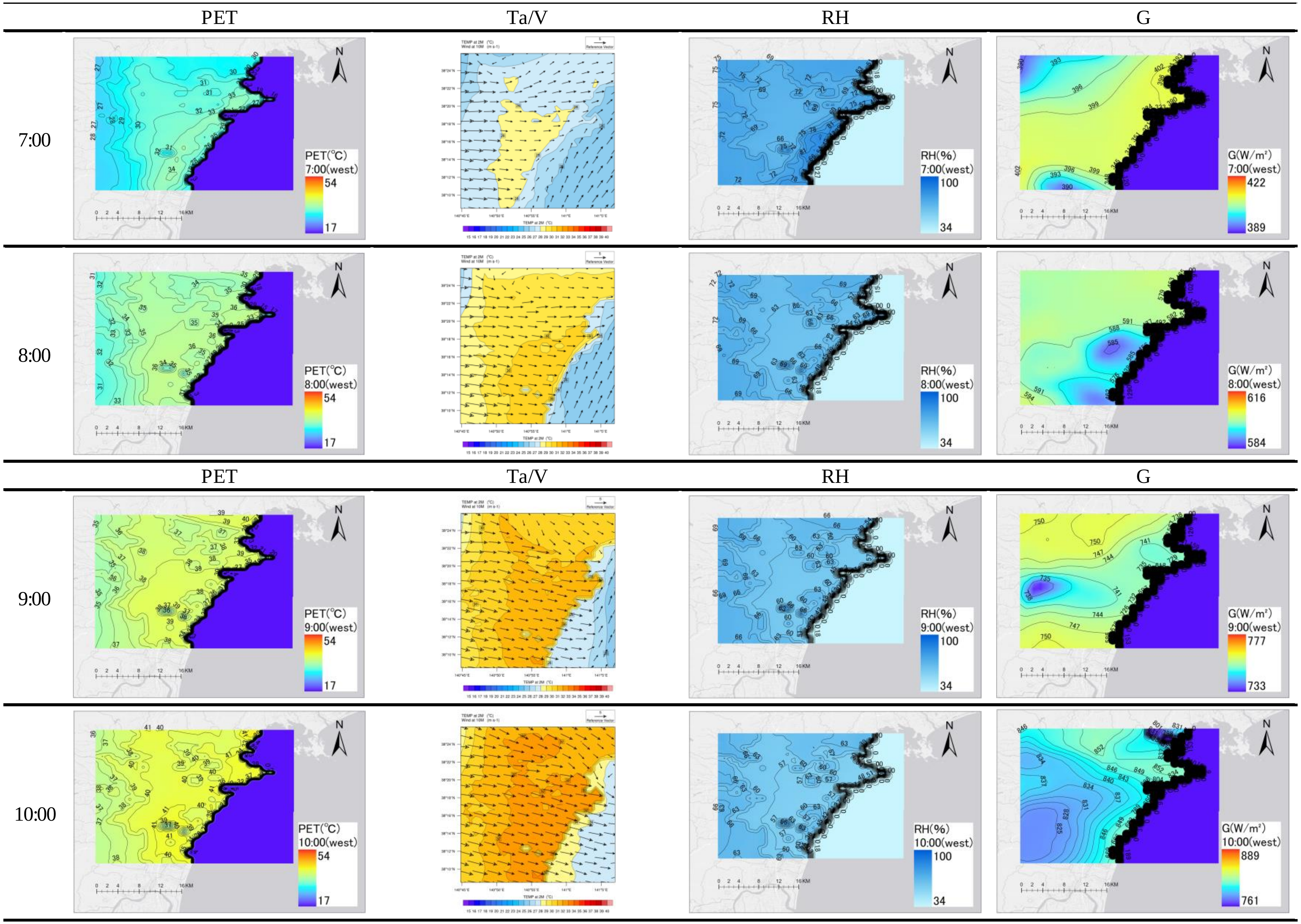
PET
Ta/V
RH
G
7:00
PET(℃) 7:00(west) 54 17
RH(%) 7:00(west) 100 34
G(W/m²) 7:00(west) 422 389
8:00
PET(℃) 8:00(west) 54 17
RH(%) 8:00(west) 100 34
G(W/m²) 8:00(west) 616 584
PET
Ta/V
RH
G
9:00
PET(℃) 9:00(west) 54 17
RH(%) 9:00(west) 100 34
G(W/m²) 9:00(west) 777 733
10:00
PET(℃) 10:00(west) 54 17
RH(%) 10:00(west) 100 34
G(W/m²) 10:00(west) 889 761

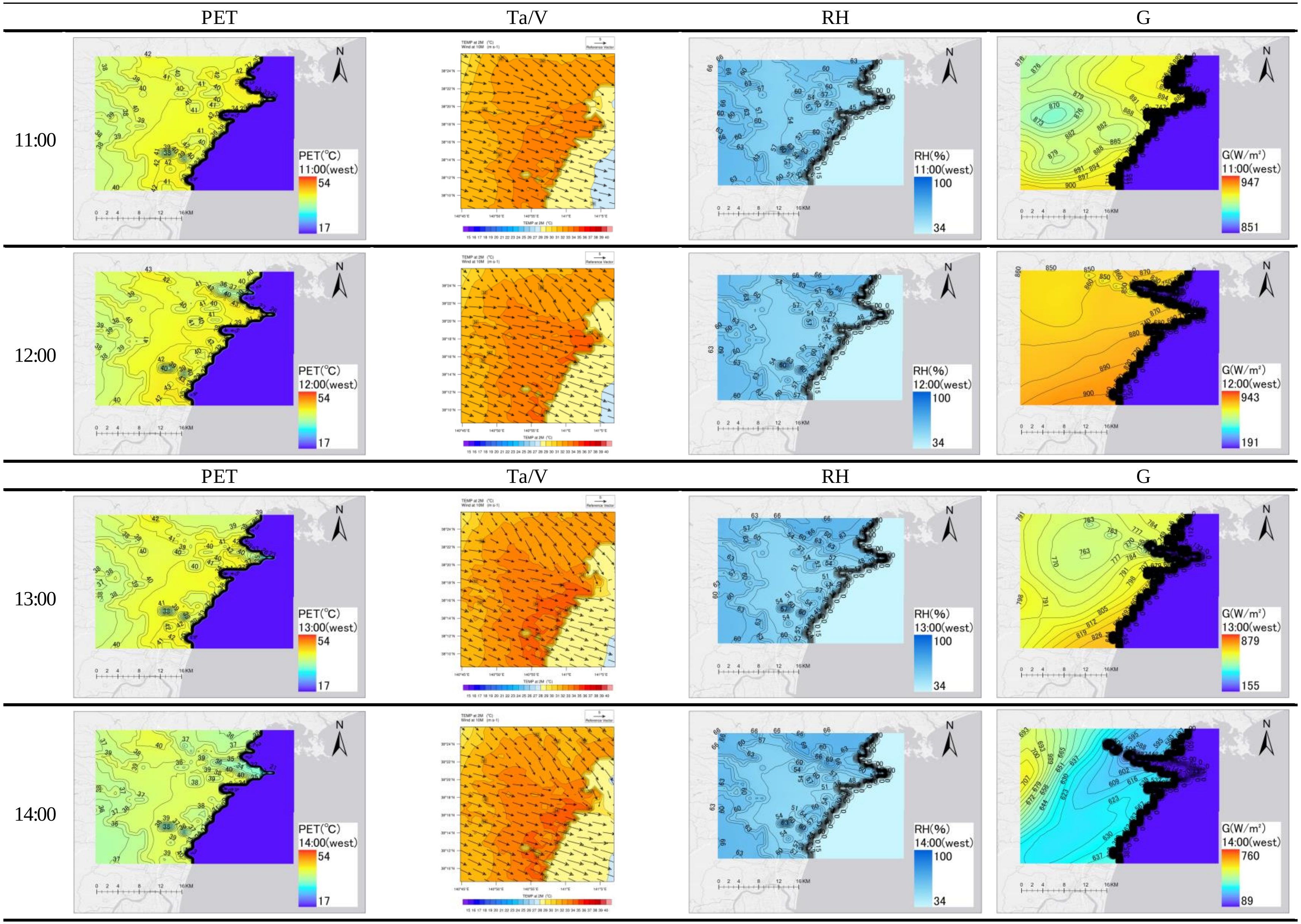
PET
Ta/V
RH
G
11:00
PET(℃) 11:00(west) 54 17
RH(%) 11:00(west) 100 34
G(W/m²) 11:00(west) 947 851
12:00
PET(℃) 12:00(west) 54 17
RH(%) 12:00(west) 100 34
G(W/m²) 12:00(west) 943 191
PET
Ta/V
RH
G
13:00
PET(℃) 13:00(west) 54 17
RH(%) 13:00(west) 100 34
G(W/m²) 13:00(west) 879 155
14:00
PET(℃) 14:00(west) 54 17
RH(%) 14:00(west) 100 34
G(W/m²) 14:00(west) 760 89

	PET	Ta/V	RH	G
15:00	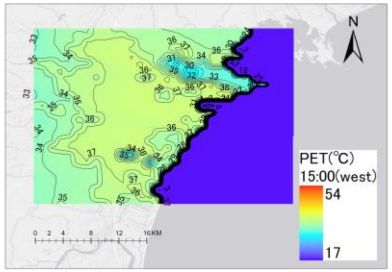	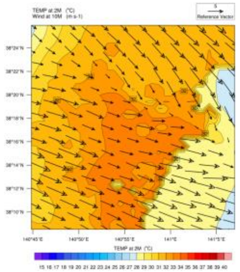	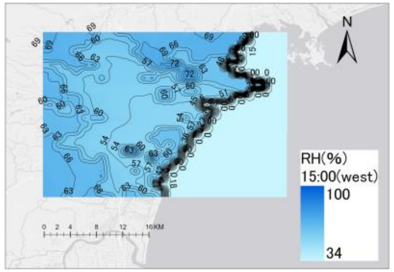	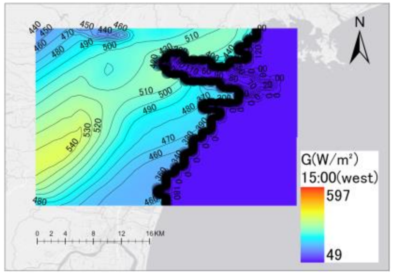
16:00	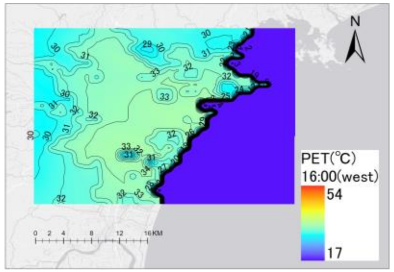	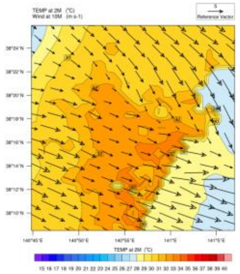	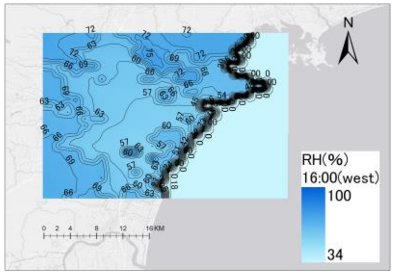	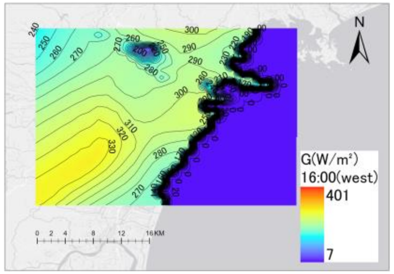

	PET	Ta/V	RH	G
17:00	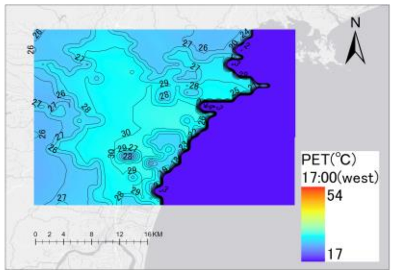	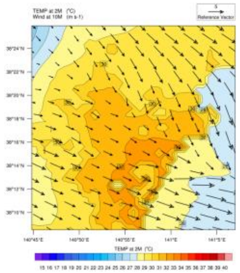	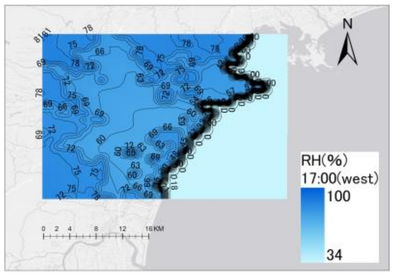	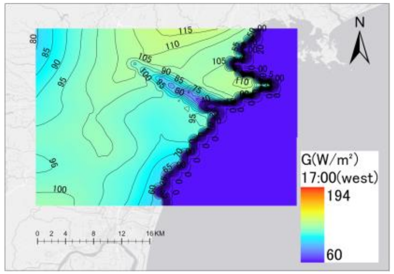
18:00	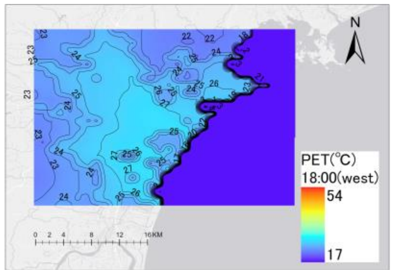	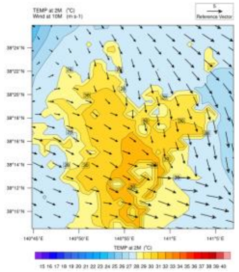	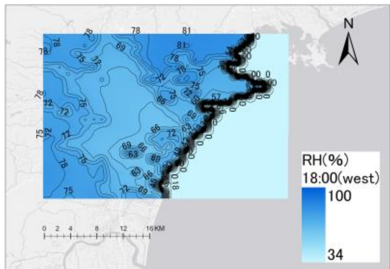	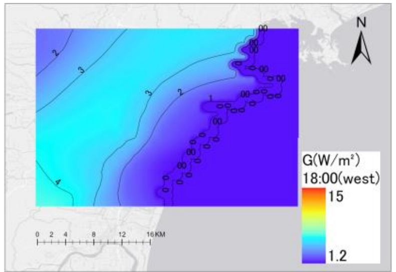

<table>
<tr><th></th><th>PET</th><th>Ta/V</th><th>RH</th><th>G</th></tr>
<tr><td>19:00</td><td>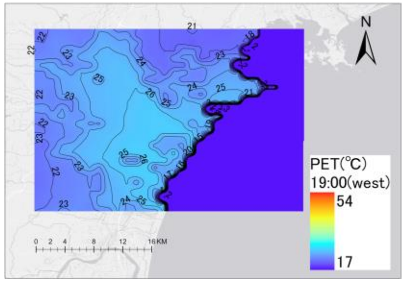</td><td>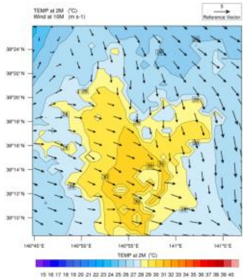</td><td>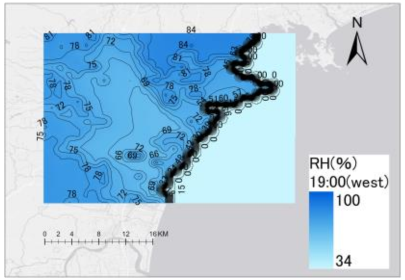</td><td></td></tr>
<tr><td>20:00</td><td>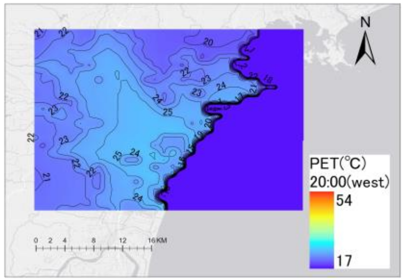</td><td>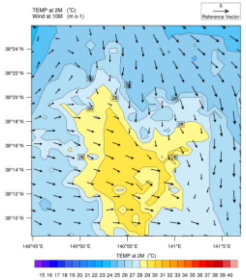</td><td>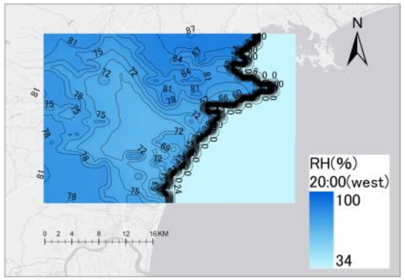</td><td></td></tr>
<tr><th></th><th>PET</th><th>Ta/V</th><th>RH</th><th>G</th></tr>
<tr><td>21:00</td><td>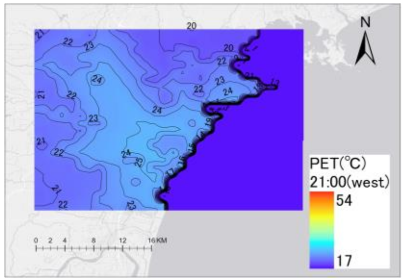</td><td>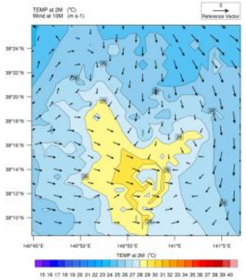</td><td>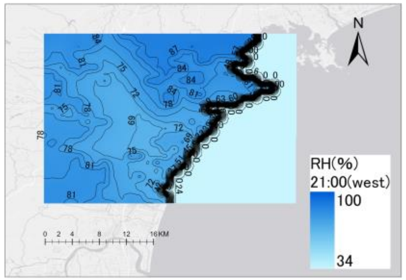</td><td></td></tr>
</table>

Fig. 6.13 *Thermal comfort index of west breeze day with each environmental factor*

6.3.3. **Analysis of the distribution characteristics of heat stress levels**

PET values in different numerical intervals represent different degrees of heat sensation in the human body. To better interpret the results of PET calculations, PET was classified, and the table of thermal perception degrees used in this study is as follows (Table 6.1):

Table 6.1 *Thermal perception classes for human beings.*

	PET（℃）	**Thermal Perception**	**Grade of physical stress**
a	> 41	Very hot	Extreme heat stress
b	35-41	Hot	Strong heat stress
c	29-35	Warm	Moderate heat stress
d	23-29	Slightly warm	Slight heat stress
e	18-23	Comfortable	No thermal stress
f	13-18	Slightly cool	Slight cold stress
g	8-13	Cool	Moderate cold stress
h	4-8	Cold	Strong cold stress
i	≤4	Very cold	Extreme cold stress

The analysis was performed separately for the entire study area, and the coastal, urban, and inland areas. The four areas were then analyzed in the aggregate for sea breeze day and west breeze day.

First, the mean PET values of the sea breeze day and the west breeze day were calculated for all points in the simulated area (Table 6.2, Fig. 6.14 a), and when plotted into a graph for analysis, it can be seen that the mean PET values of the sea breeze day are not significantly different from those of the west breeze day. In the time interval from 7:00 to 11:00, the mean PET value for the sea breeze day is slightly higher than the mean PET value for the west breeze day. in the time interval from 12:00 to 15:00, the mean PET value for the sea breeze day is slightly lower than the mean PET value for the west breeze day, with the maximum difference occurring at 13:00, at 1.78°C. in the time interval from 16:00 to 17:00, the mean PET value for the sea breeze day is slightly higher than the mean PET value for the west breeze day. The mean value of PET for the sea breeze day is slightly higher than that for the west breeze day. After that, the mean PET value of the sea breeze day is slightly lower than the mean PET value of the west breeze day.

Table 6.2 *PET averages of sea breeze day and west breeze day in the simulated area for (a) the entire area, (b) the inland area, (c) the urban area, and (d) the coastal area. (Where "Sea" represents sea breeze days, the "West" represents west breeze day, and DIF represents the difference between the value of west breeze day minus the value of sea breeze day.)*

	(a) entire area			(b) inland area			(c) urban area			(d) coastal area		
	Sea	West	DIF	Sea	West	DIF	Sea	West	DIF	Sea	West	DIF
7:00	31.77	30.57	-1.20	30.40	28.85	-1.55	32.15	30.39	-1.76	32.31	31.97	-0.34
8:00	36.42	34.60	**-1.81**	35.21	33.14	-2.07	36.76	34.51	-2.24	36.89	35.73	**-1.16**
9:00	39.04	37.83	-1.21	39.09	36.31	-2.78	40.47	37.98	-2.49	37.43	38.75	1.32
10:00	40.83	39.52	-1.31	42.49	38.22	-4.27	42.74	39.44	**-3.30**	37.56	40.52	2.96
11:00	40.96	40.34	-0.61	44.10	39.04	**-5.06**	42.06	40.22	-1.83	37.52	41.40	3.87
12:00	39.65	40.44	0.79	42.48	39.26	-3.22	40.03	40.49	0.46	37.23	41.21	3.99
13:00	38.09	39.87	**1.78**	40.01	38.77	-1.24	38.58	39.88	**1.30**	36.19	40.65	**4.46**
14:00	36.61	37.86	1.25	38.31	37.82	-0.50	37.13	37.80	0.67	34.83	37.95	3.12
15:00	34.94	35.62	0.68	36.22	34.84	-1.38	35.41	36.12	0.70	33.52	35.63	2.10
16:00	33.12	32.17	-0.95	34.57	30.91	-3.65	33.53	32.45	-1.07	31.66	32.75	1.08
17:00	29.74	27.94	-1.79	31.10	26.92	-4.19	29.98	28.01	-1.98	28.50	28.60	0.10
18:00	24.51	25.00	0.49	25.22	24.21	-1.01	24.88	25.06	0.18	23.61	25.50	1.89
19:00	23.23	23.87	0.64	22.96	23.20	0.24	23.67	23.81	0.14	22.93	24.41	1.48
20:00	21.83	23.06	1.23	21.40	22.50	1.10	21.76	22.95	1.19	22.22	23.59	1.38
21:00	21.14	22.55	1.41	20.57	22.12	**1.54**	21.12	22.39	1.27	21.57	23.05	1.48

In the inland area (Fig. 6.14 b), the mean PET value for the sea breeze day was always higher than the mean PET value for the west breeze day from 07:00 to 18:00. The mean PET value for the sea breeze day was significantly higher than the mean PET value for the west breeze day in the time interval from 09:00 to 12:00. At 11:00, the difference is the largest, and the PET mean of the sea breeze day is higher than the PET mean of the west breeze day by 5.06°C.

In the urban area (Fig. 6.14 c), the mean PET value for sea breeze day was higher than the mean PET value for west breeze day in the time interval from 7:00 to 11:00, and the difference narrowed compared to the inland area, and the maximum difference occurred in 10:00 with 3.3°C.

In the coastal area (Fig. 6.14 d), the mean PET values for sea breeze day were always lower than the mean PET values for west breeze day, except for the time interval between 7:00 and 8:00, when the mean PET values for sea breeze day were slightly higher than the mean PET values for west breeze day. Especially in the time interval from 10:00 to 15:00, the PET means of sea breeze day is significantly lower than that of west breeze day. At 13:00, the PET means of sea breeze day ergo PET mean is 4.46°C lower than that of west breeze day.

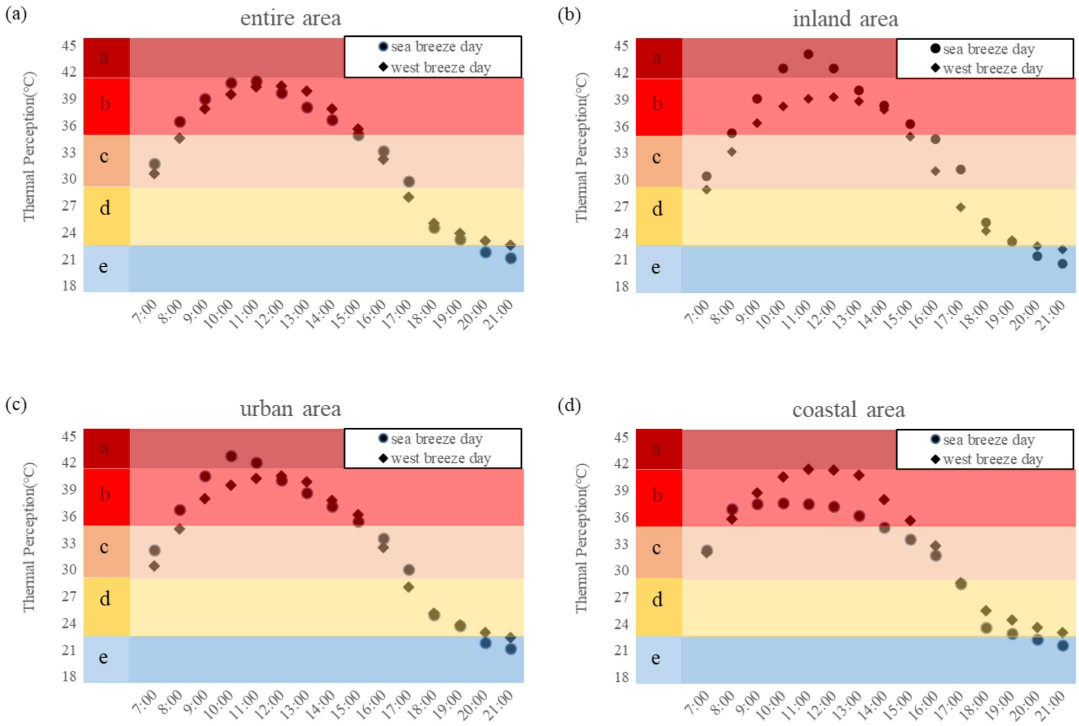

Fig. 6.14 *Thermal perception of the mean of sea breeze day and west breeze day PET for (a) the entire study area, (b) the inland area, (c) the urban area, and (d) the coastal area (a/b/c/d/e query table 1)*

The analysis comparing the thermal perception distribution of each area on sea breeze day and west breeze day separately (Fig. 6.15, Table 6.3) showed that on west breeze day, there was little difference in the thermal perception distribution of each area. The distribution of thermal perception in each area on sea breeze day differed greatly in the phase from 9:00 to 15:00. A higher distribution of thermal perception was presented in the inland area and a lower distribution of thermal perception was presented in the coastal area.

Table 6.3 *Mean PET values for (a) sea breeze day and (b) west breeze day in each area of the study area.*

	(a) sea breeze day				(b) west breeze day			
	inland	urban	coastal	entire	inland	urban	coastal	entire
7:00	30.40	32.15	32.31	31.77	28.85	30.39	31.97	30.57
8:00	35.21	36.76	36.89	36.42	33.14	34.51	35.73	34.60
9:00	39.09	40.47	37.43	39.04	36.31	37.98	38.75	37.83
10:00	42.49	42.74	37.56	40.83	38.22	39.44	40.52	39.52
11:00	44.10	42.06	37.52	40.96	39.04	40.22	41.40	40.34
12:00	42.48	40.03	37.23	39.65	39.26	40.49	41.21	40.44
13:00	40.01	38.58	36.19	38.09	38.77	39.88	40.65	39.87
14:00	38.31	37.13	34.83	36.61	37.82	37.80	37.95	37.86
15:00	36.22	35.41	33.52	34.94	34.84	36.12	35.63	35.62
16:00	34.57	33.53	31.66	33.12	30.91	32.45	32.75	32.17
17:00	31.10	29.98	28.50	29.74	26.92	28.01	28.60	27.94
18:00	25.22	24.88	23.61	24.51	24.21	25.06	25.50	25.00
19:00	22.96	23.67	22.93	23.23	23.20	23.81	24.41	23.87
20:00	21.40	21.76	22.22	21.83	22.50	22.95	23.59	23.06
21:00	20.57	21.12	21.57	21.14	22.12	22.39	23.05	22.55

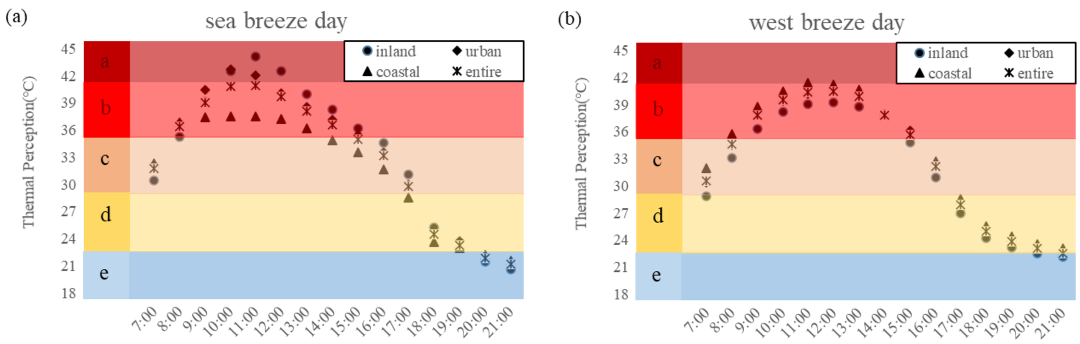

Fig. 6.15 *Thermal sensing of PET averages for (a) sea breeze day and (b) west breeze day in each area of the study area.*

After calculating the percentage of thermal perception level at each moment on sea breeze day and west breeze day separately, the sum of the percentage of each thermal perception level in all sea breeze action time periods was calculated and finally obtained in Fig. 6.16. From Fig. 6.16, it can be seen that there is some difference in the percentage of each thermal perception grade between sea breeze day and west breeze day. The percentages of sea breeze day in grade a (very hot), grade c (warm), and grade e (comfortable) were higher than those of west breeze day, and the rest of the grades were lower than those of west breeze day.

(a)

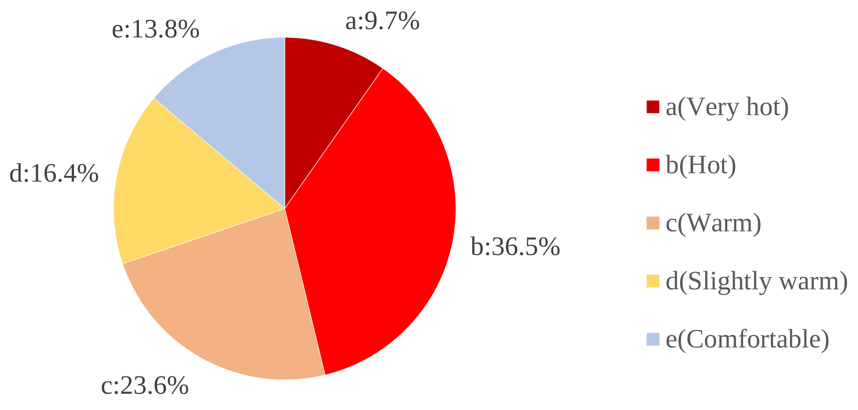

(b)

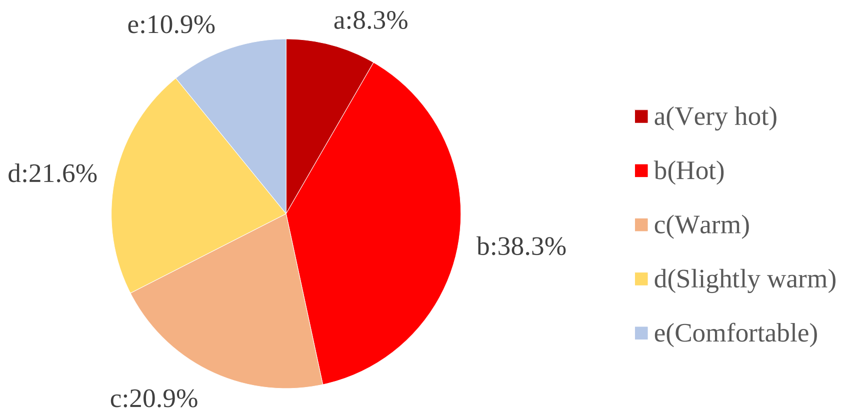

Fig. 6.16 *(a) Percentage of thermal perception level on sea breeze day; (b) Percentage of thermal perception level on west breeze day.*

The points of the different levels of thermal perception appearing at each moment of the sea breeze day and the west breeze day were marked on the map to further analyze the location of the appearance of the different levels of thermal perception (Fig. 6.17). The histogram can more clearly reflect the time of thermal perception (Fig. 6.18/Fig. 6.19).

On sea breeze day, the point of extreme heat stress started to appear from 8:00 and was present in 45.1% of the study area at 10:00. It is the time of the day when extreme heat stress occurs in the widest area of the entire day. From 10:00 onwards the area of extreme heat stress began to shrink until 17:00 when no area of extreme heat stress was present. And areas of extreme heat stress are always closer to inland areas. Extreme heat stress on west breeze day occurred in the time interval from 10:00 to 13:00. The most represented moment was 12:00, occurring in 41.5% of the study area, distributed in the coastal area and urban area.

Strong heat stress was present at the moment of 7:00 on the sea breeze day, scattered over a small number of areas in the study area. By 8:00, a large number of areas showed strong heat stress, with a distribution mostly concentrated in central urban areas. There was a tendency to expand the range of strong heat stress at 9:00, and after narrowing the range at 10:00, the range began to expand again at 11:00 until 13:00, when the area of strong heat stress reached its maximum area, with 81.5% of the points appearing within the study area. In the following two hours the range began to narrow until 17:00, when no areas of strong heat stress appeared. On west breeze day, strong heat stress appeared in the time interval between 8:00 and 15:00, and at 9:00 and 14:00 in almost the entire study area, 93.3% and 96.4% of the area, respectively. In the rest of the time interval, it was usually present in areas closer to the inland.

Moderate heat stress gives the feeling of warmth. At 7:00 on the sea breeze, day 78.5% of the area showed moderate heat stress, mainly distributed throughout the study area excluding the inland local area, and then the area started to shrink. Afterward, the areas of moderate heat stress did not appear in the urban area, as analyzed above at 8:00 when a large amount of strong heat stress was observed in the urban area. The phenomenon of moderate heat stress like this, which was concentrated only in small amounts in the coastal area, began to expand until 14:00 and spread from the coastal area to the inland area until 16:00 when moderate heat stress was presented in 87% of the study area. Moderate heat stress on west breeze day occurred in the time interval from 07:00 to 17:00. At 16:00, it appeared in 98.3% of almost the entire study area. 9:00 to 14:00 time intervals appeared only locally in a few areas. In the rest of the time interval, 77.7% of the area, except the western inland, was present at 7:00, the western and northern part of the inland at 8:00, the western inland and the local coastal area at 15:00, and the urban area at 17:00.

Slight heat stress is a stress response that is somewhat more comfortable than moderate heat stress. Slight heat stress was observed in a small number of areas inland on sea breeze days at 7:00. It reappeared until 16:00 and was distributed mainly in the coastal area. At 17:00 the range penetrates inland from the coast but does not include urban areas. At 18:00, the range spread to 86.9% of the study area. The missing part is mostly distributed in the coastal area. The range then began to gradually decrease centered on the urban area. Slight heat stress on west breeze day occurred at 07:00 and in the time interval from 15:00 to 21:00. The highest 81.9% of the area was distributed at 18:00. It appeared in the western part of the inland area at 07:00, only in a few localized areas from 15:00 to 16:00, in the western and northern part of the inland area and localized coastal areas at 17:00, and started to move towards urban and coastal areas at 18:00 and in the time interval from 19:00 to 21:00.

No thermal stress is the most comfortable environment for the human body. Sea breeze days began to appear at 18:00 in areas with no heat stress, mainly in coastal areas. The range then began to gradually expand, with the expansion concentrating on coastal and inland areas and excluding urban areas. Until 21:00 there was 81.5% of the area showed no heat stress. On the west breeze day, no thermal stress occurred in the time interval between 18:00 and 21:00, and in general in the western and northern parts of the inland area, with a maximum of 57.9% of the area at 21:00.

Slight cold stress gives the body a slightly cooler feeling. Such heat stress occurs only in a very small area at 21:00 on sea breeze day. The location of the distribution is close to the inland.

		a	b	c	d	e	f
PET（°C）		> 41	35-41	29-35	23-29	18-23	13-18
Thermal Perception		Very hot	Hot	Warm	Slightly warm	Comfortable	Slightly cool
Grade of physical stress		Extreme heat stress	Strong heat stress	Moderate heat stress	Slight heat stress	No thermal stress	Slight cold stress
7:00	sea	0.0%	7.0%	78.5%	14.5%	0.0%	0.0%
			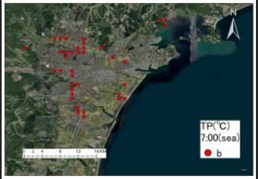	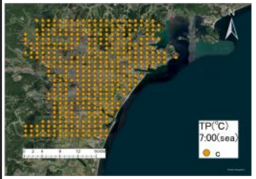	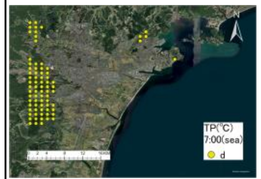		
	west	0.0%	0.0%	77.7%	22.3%	0.0%	0.0%
				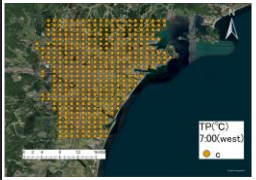			
8:00	sea	5.9%	63.8%	30.3%	0.0%	0.0%	0.0%
		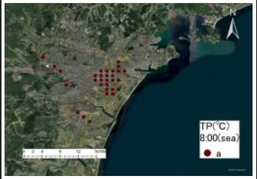	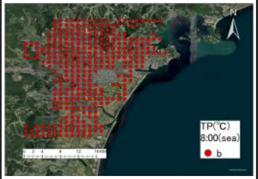				
	west	0.0%	52.4%	47.6%	0.0%	0.0%	0.0%
				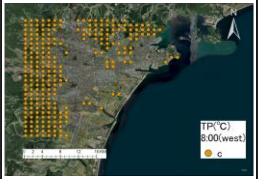			

		a	b	c	d	e	f
PET（°C）		> 41	35-41	29-35	23-29	18-23	13-18
Thermal Perception		Very hot	Hot	Warm	Slightly warm	Comfortable	Slightly cool
Grade of physical stress		Extreme heat stress	Strong heat stress	Moderate heat stress	Slight heat stress	No thermal stress	Slight cold stress
9:00	sea	22.9%	70.5%	6.7%	0.0%	0.0%	0.0%
		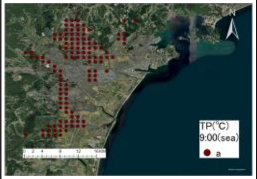	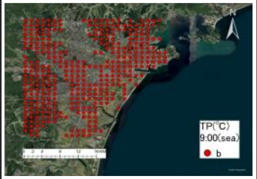	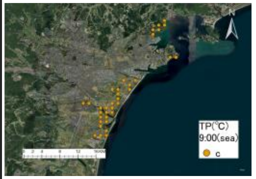			
	west	0.0%	93.3%	6.7%	0.0%	0.0%	0.0%
			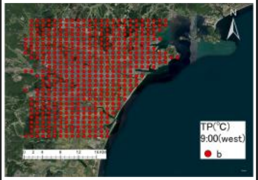	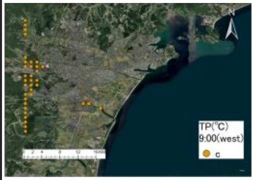			
10:00	sea	45.1%	47.8%	7.0%	0.0%	0.0%	0.0%
		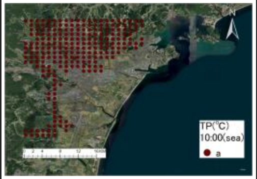	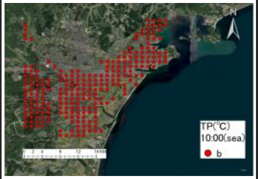	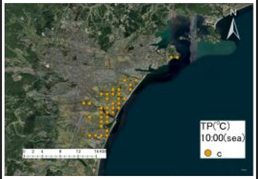			
	west	14.9%	84.6%	0.6%	0.0%	0.0%	0.0%
			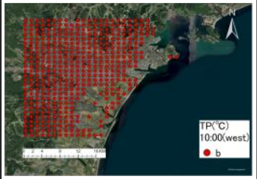	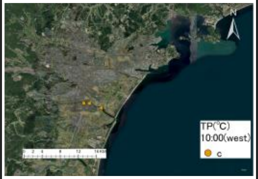			

		a	b	c	d	e	f
PET （°C）		> 41	35-41	29-35	23-29	18-23	13-18
Thermal Perception		Very hot	Hot	Warm	Slightly warm	Comfortable	Slightly cool
Grade of physical stress		Extreme heat stress	Strong heat stress	Moderate heat stress	Slight heat stress	No thermal stress	Slight cold stress
11:00	sea	37.5%	59.4%	3.0%	0.0%	0.0%	0.0%
		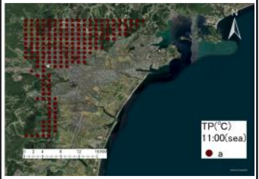		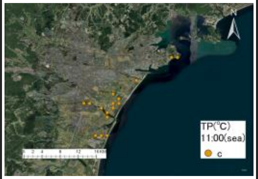			
	west	38.7%	60.8%	0.6%	0.0%	0.0%	0.0%
				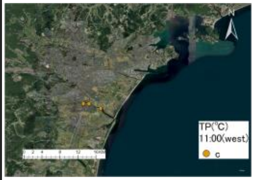			
12:00	sea	21.3%	74.3%	4.4%	0.0%	0.0%	0.0%
			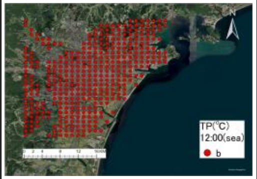	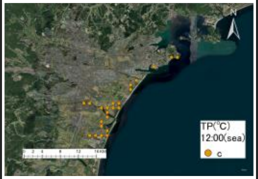			
	west	41.5%	57.7%	0.8%	0.0%	0.0%	0.0%
				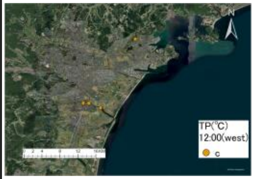			

		a	b	c	d	e	f
PET (°C)		> 41	35-41	29-35	23-29	18-23	13-18
Thermal Perception		Very hot	Hot	Warm	Slightly warm	Comfortable	Slightly cool
Grade of physical stress		Extreme heat stress	Strong heat stress	Moderate heat stress	Slight heat stress	No thermal stress	Slight cold stress
13:00	sea	9.7%	81.5%	8.8%	0.0%	0.0%	0.0%
		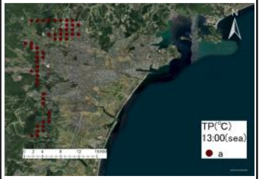	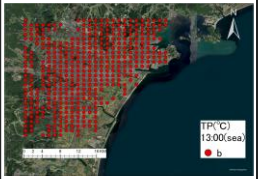				
	west	30.1%	69.1%	0.8%	0.0%	0.0%	0.0%
				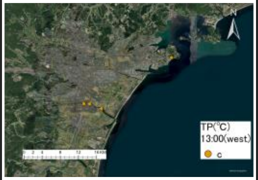			
14:00	sea	2.5%	80.0%	17.5%	0.0%	0.0%	0.0%
		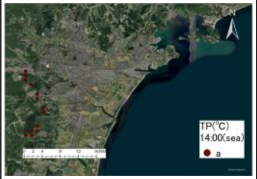	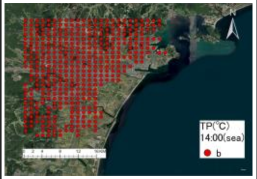				
	west	0.0%	96.4%	3.6%	0.0%	0.0%	0.0%
			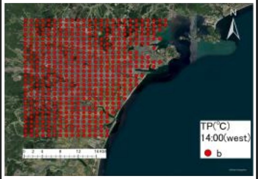				

		a	b	c	d	e	f
PET (°C)		> 41	35-41	29-35	23-29	18-23	13-18
Thermal Perception		Very hot	Hot	Warm	Slightly warm	Comfortable	Slightly cool
Grade of physical stress		Extreme heat stress	Strong heat stress	Moderate heat stress	Slight heat stress	No thermal stress	Slight cold stress
15:00	sea	0.8%	52.0%	47.2%	0.0%	0.0%	0.0%
		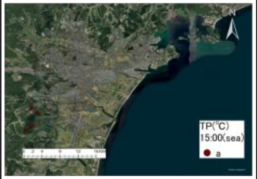	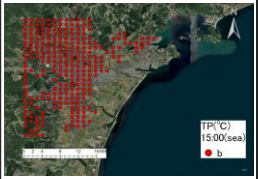	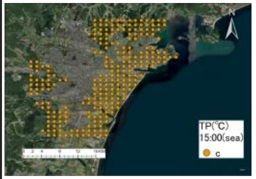			
	west	0.0%	60.0%	39.2%	0.8%	0.0%	0.0%
			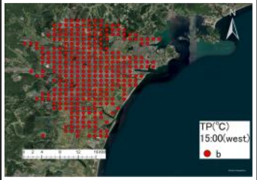		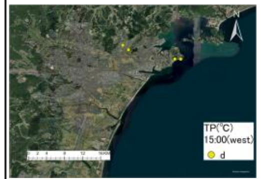		
16:00	sea	0.2%	10.9%	87.0%	1.9%	0.0%	0.0%
		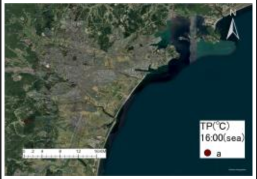	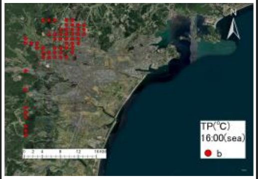	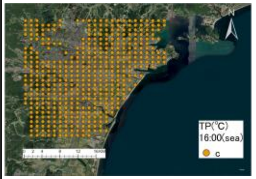			
	west	0.0%	0.0%	98.3%	1.7%	0.0%	0.0%
							

		a	b	c	d	e	f
PET (°C)		> 41	35-41	29-35	23-29	18-23	13-18
Thermal Perception		Very hot	Hot	Warm	Slightly warm	Comfortable	Slightly cool
Grade of physical stress		Extreme heat stress	Strong heat stress	Moderate heat stress	Slight heat stress	No thermal stress	Slight cold stress
17:00	sea	0.0%	0.0%	62.9%	37.1%	0.0%	0.0%
							
	west	0.0%	0.0%	37.1%	62.9%	0.0%	0.0%
							
18:00	sea	0.0%	0.0%	0.0%	86.9%	13.1%	0.0%
					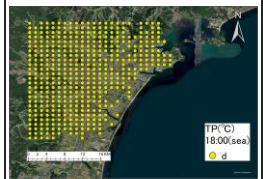		
	west	0.0%	0.0%	0.0%	81.9%	18.1%	0.0%
							

		a	b	c	d	e	f
PET（°C）		> 41	35-41	29-35	23-29	18-23	13-18
Thermal Perception		Very hot	Hot	Warm	Slightly warm	Comfortable	Slightly cool
Grade of physical stress		Extreme heat stress	Strong heat stress	Moderate heat stress	Slight heat stress	No thermal stress	Slight cold stress
19:00	sea	0.0%	0.0%	0.0%	53.1%	46.9%	0.0%
					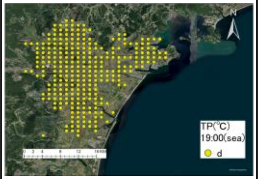	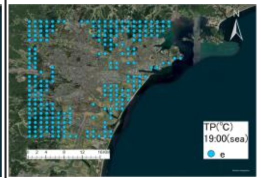	
	west	0.0%	0.0%	0.0%	61.7%	38.3%	0.0%
					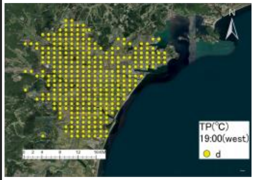		
20:00	sea	0.0%	0.0%	0.0%	33.9%	66.1%	0.0%
					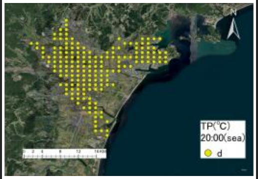	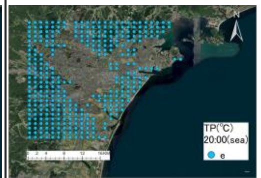	
	west	0.0%	0.0%	0.0%	51.2%	48.8%	0.0%
							

		a	b	c	d	e	f
PET（°C）		> 41	35-41	29-35	23-29	18-23	13-18
Thermal Perception		Very hot	Hot	Warm	Slightly warm	Comfortable	Slightly cool
Grade of physical stress		Extreme heat stress	Strong heat stress	Moderate heat stress	Slight heat stress	No thermal stress	Slight cold stress
21:00	sea	0.0%	0.0%	0.0%	18.3%	81.5%	0.2%
					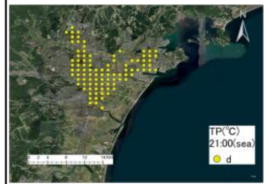	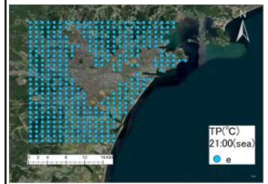	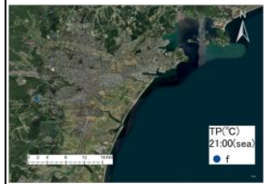
	west	0.0%	0.0%	0.0%	42.1%	57.9%	0.0%
					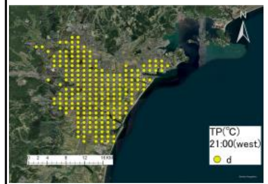	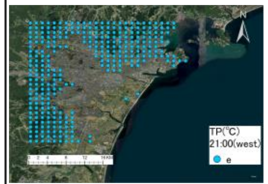	

__Fig. 6.17__ Distribution of the different levels of thermal perception occurring at each moment of a sea breeze day and a west breeze day

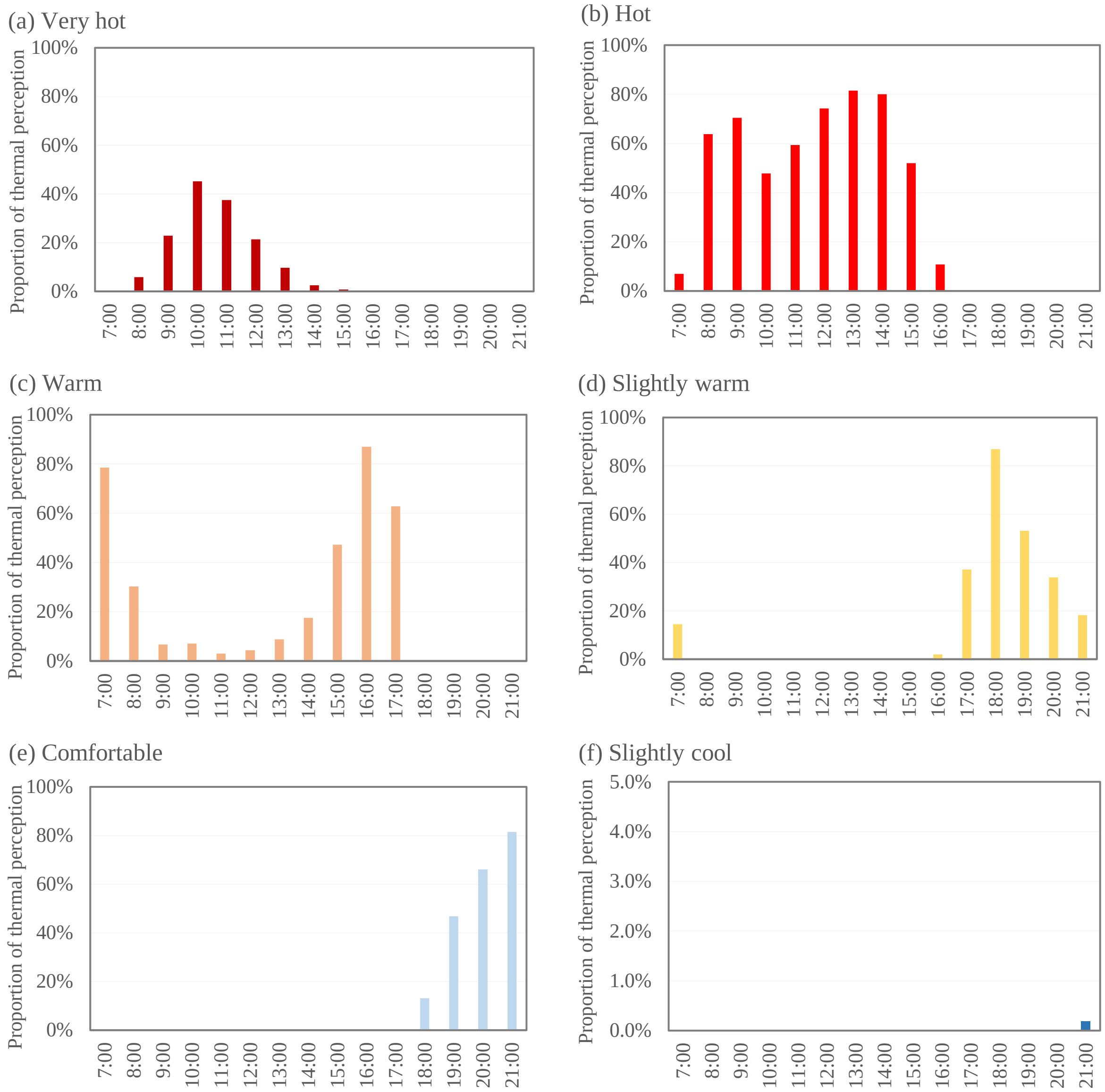

Fig. 6.18 *The percentage of sea breeze day thermal perception on the timeline.*

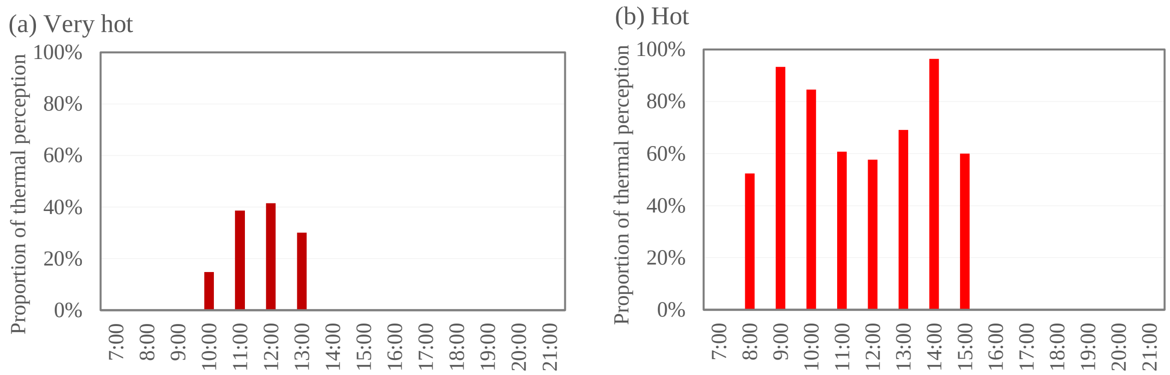

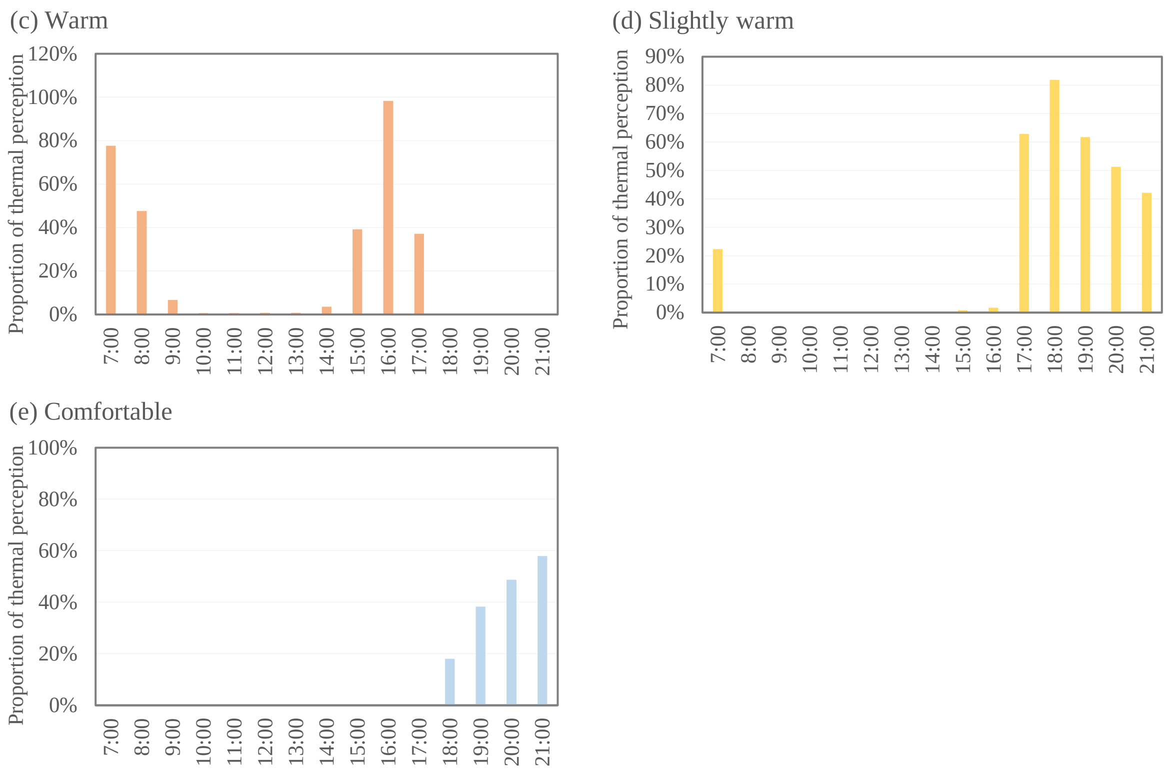

Fig. 6.19 *The percentage of west breeze day thermal perception on the timeline.*

Summarizing the distribution of all thermal perception on the map between the sea breeze day and the west breeze day, and doing further comparative analysis, it is concluded (Fig. 6.20) that at 7:00, both grade c (Moderate heat stress) and grade d (Slightly stress) appear, and the distribution areas are similar, but grade b (Strong heat stress) appears locally on the sea breeze day, but not on west breeze day. At 8:00 and 9:00, grade a (Extreme heat stress) was localized on sea breeze day but not on west breeze day. Grade a (Extreme heat stress) began to appear locally on west breeze day at 10:00, while grade a (Extreme heat stress) appeared on sea breeze days in most of the northern part of the study area. During the morning hours, more areas of discomfort appeared on sea breeze day than on west breeze day, to a greater extent.

During the period from 11:00 to 13:00, during the sea breeze day， grade a (Extreme heat stress) appeared in the area close to the inland, and the west breeze day appeared in the area close to the coastal area and the urban area. From 13:00 onwards, the sea breeze day has a relatively more comfortable grade c (Moderate heat stress) than the west breeze day in the coastal area. In general, the areas with higher comfort levels on sea breeze day are always close to the coastal area, while coastal areas always show lower comfort levels on west breeze day.

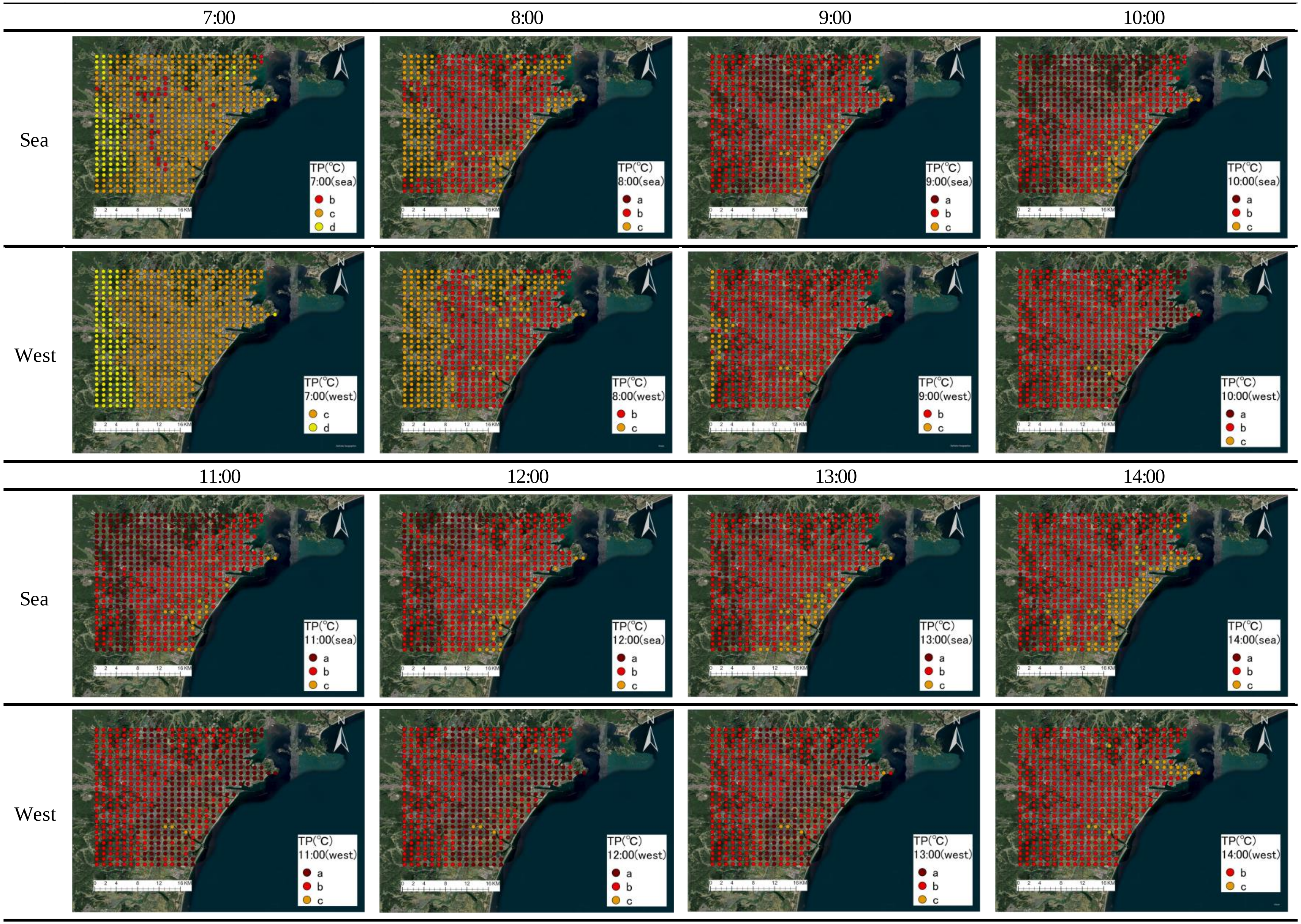
7:00
8:00
9:00
10:00
Sea
West
11:00
12:00
13:00
14:00
Sea
West
TP(°C)
7:00(sea)
b
c
d
TP(°C)
8:00(sea)
a
b
c
TP(°C)
9:00(sea)
a
b
c
TP(°C)
10:00(sea)
a
b
c
TP(°C)
7:00(west)
c
d
TP(°C)
8:00(west)
b
c
TP(°C)
9:00(west)
b
c
TP(°C)
10:00(west)
a
b
c
TP(°C)
11:00(sea)
a
b
c
TP(°C)
12:00(sea)
a
b
c
TP(°C)
13:00(sea)
a
b
c
TP(°C)
14:00(sea)
a
b
c
TP(°C)
11:00(west)
a
b
c
TP(°C)
12:00(west)
a
b
c
TP(°C)
13:00(west)
a
b
c
TP(°C)
14:00(west)
b
c

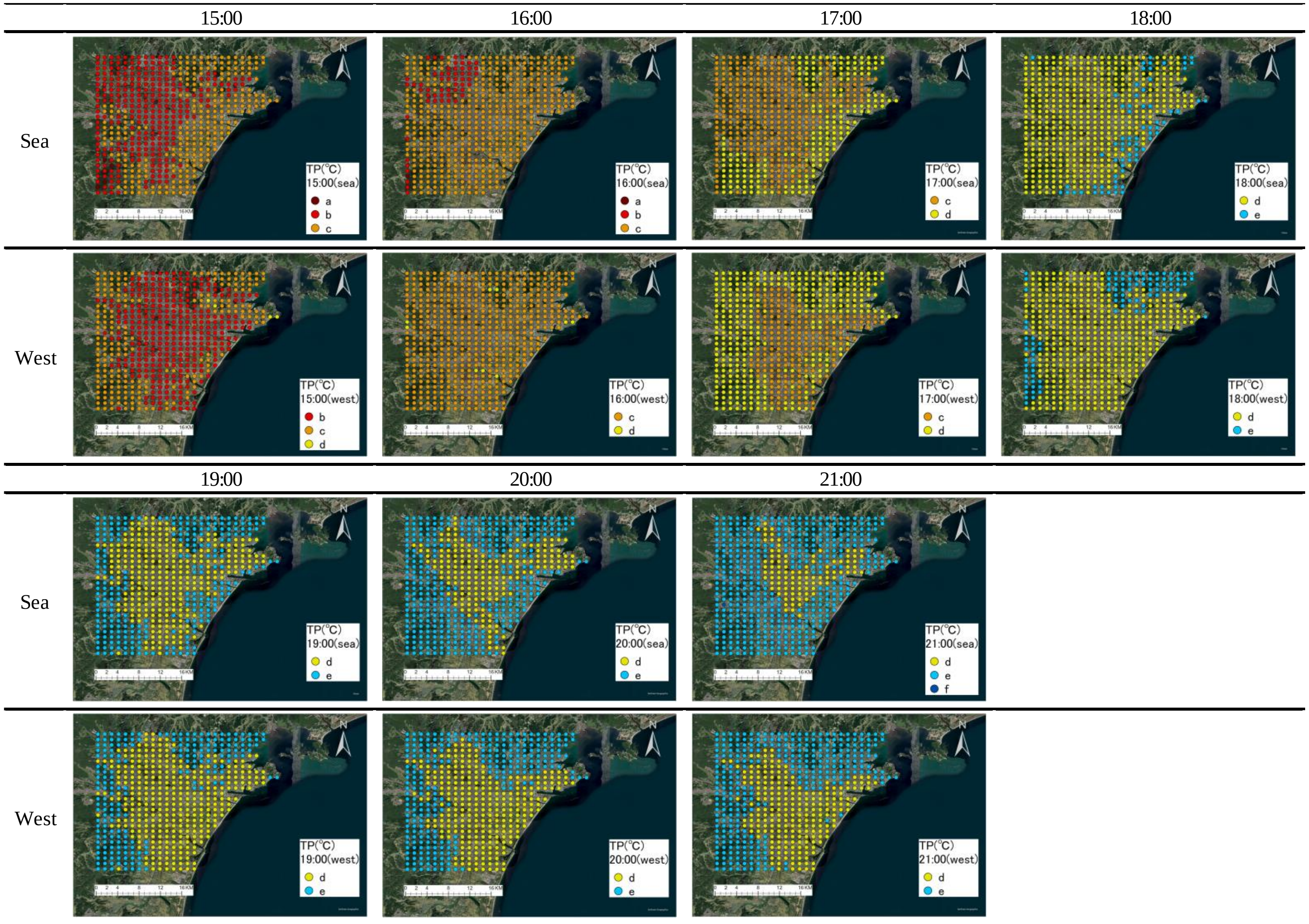

Fig. 6.20 *Distribution of heat stress levels per moment on sea breeze day and west breeze day.*

After making a stacked histogram of all moments of thermal perception, the distribution of each thermal perception over time was analyzed (Fig. 6.21). On sea breeze day (Fig. 6.21 a), from 07:00 to 15:00, many areas make people feel very hot and hot. From 15:00, the areas that make people feel warm gradually increase and appear slightly warmer and more comfortable 16:00, followed by a gradual expansion of the comfortable areas. In the area of 18:00 to 21:00 on west breeze day, there are fewer comfortable areas relative to sea breeze day.

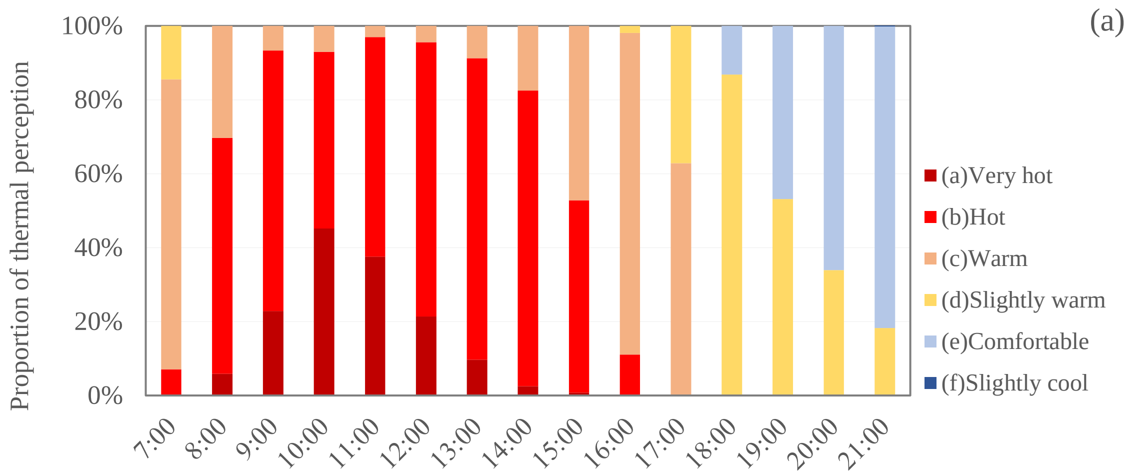

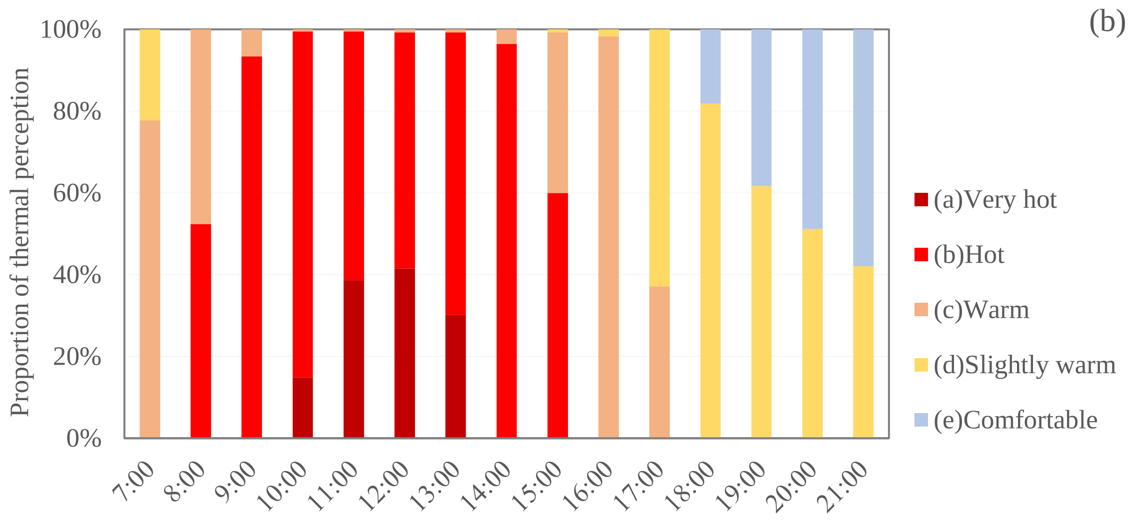

Fig. 6.21 *(a) Distribution of sea breeze daily thermal perception over time; (b) Distribution of west breeze daily thermal perception over time.*

6.4. Differential Analysis of Sea Breeze Day and West Breeze Day PET

6.4.1. **Definition of PET DIF**

If the PET values of two points are known, the higher the PET value the hotter and more uncomfortable the person feels in summer. Therefore, the difference between the two points is used to express the comfort level of PET. To analyze the degree of comfort on sea breeze days compared to west breeze days. All the PET values of the whole study area at each moment of the west breeze day, and all the PET values of the whole study area at each moment of the sea breeze day are corresponding to each other to find the difference, and the value with a positive statistical difference is the point where the sea breeze day is more comfortable than the west breeze day, and the expression is calculated as follows:

$$PET\ DIF_n = PET(WEST)_n - PET(SEA)_n$$

6.4.2. **Map of PET DIF distribution on Sea Breeze Day and West Breeze Day**

Use ArcGIS Pro to create a spatial distribution map with values (Fig. 6.22). The shades of blue are used to express the magnitude of the values.

Positive values of PET DIF appear at 7:00 in the coastal area, after which they gradually spread inland with time, but the range narrows from 16:00 to 17:00, and at 18:00 the spread area expands rapidly again until 21:00 when it is distributed almost with the whole study area. However, it can be seen that the range where positive values appear in urban areas is always less and, in the coastal area always has greater values.

	7:00	8:00	9:00
Sea	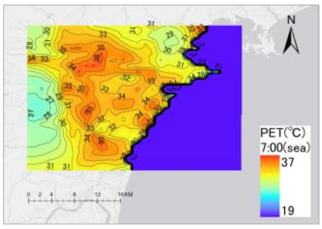	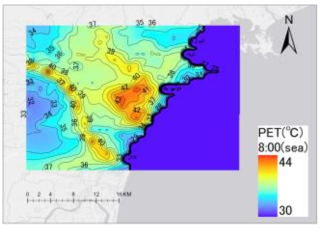	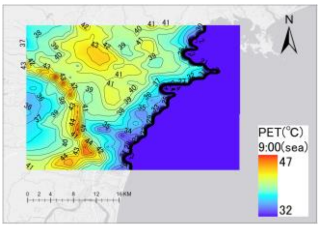
West	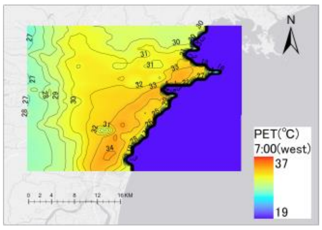	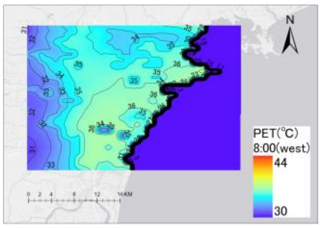	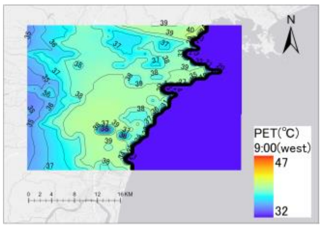
PET DIF	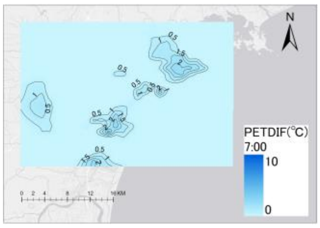	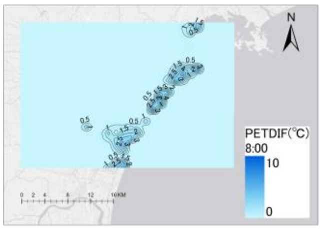	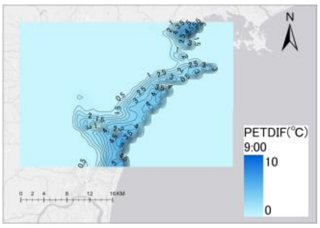

	10:00	11:00	12:00
Sea	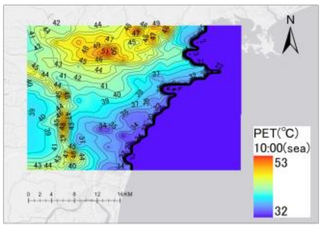	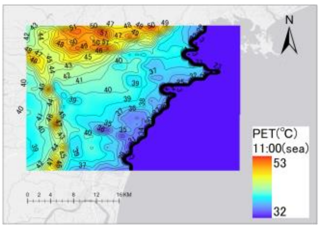	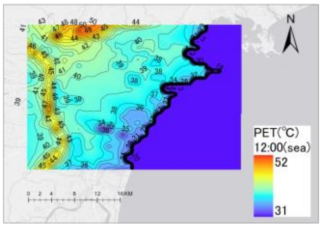
West	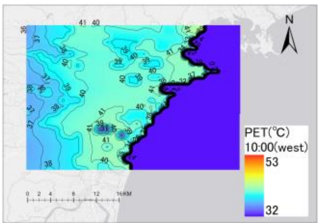	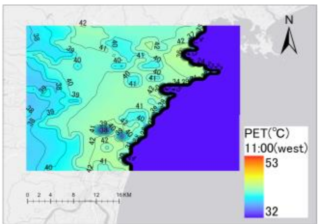	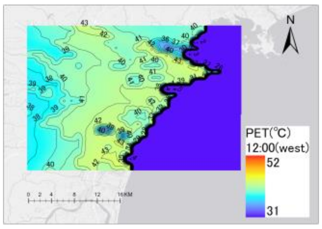
PET DIF	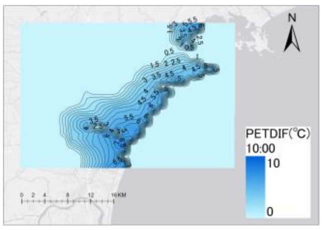	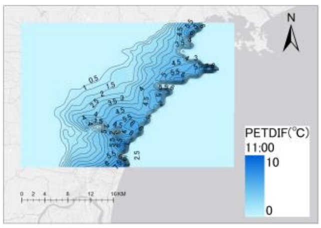	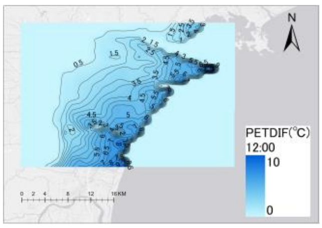

	13:00	14:00	15:00
Sea	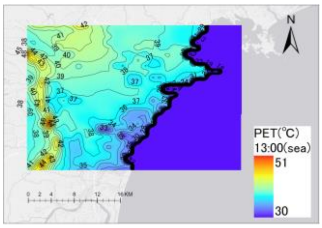	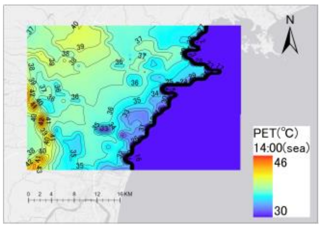	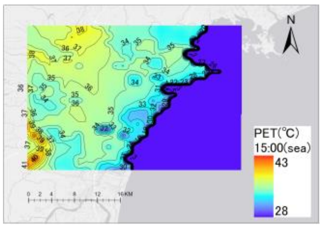
West	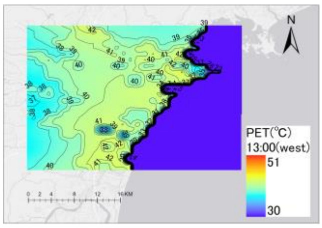	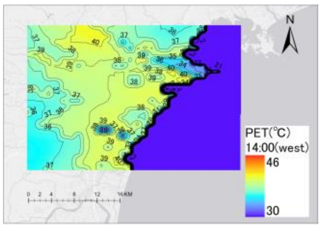	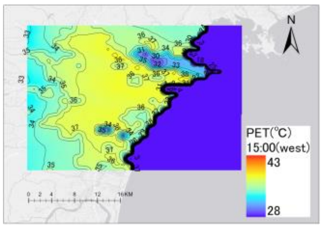
PET DIF	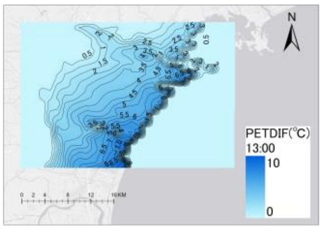	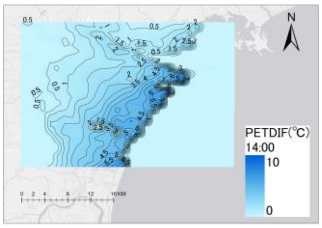	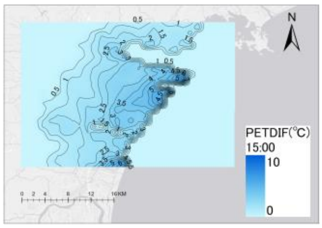
	16:00	**17:00**	**18:00**
Sea	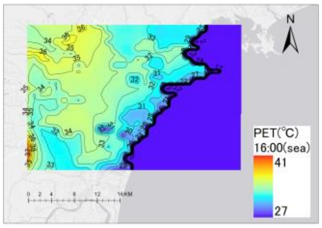	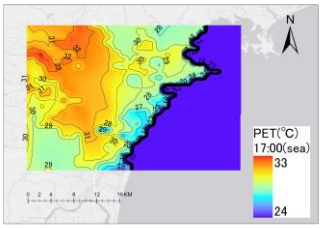	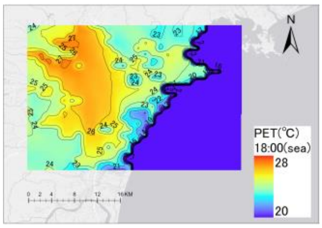
West	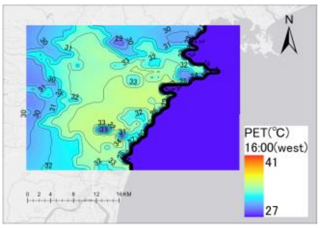	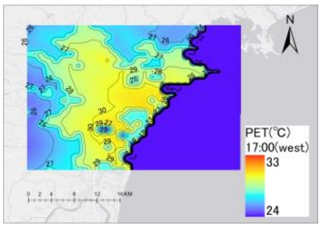	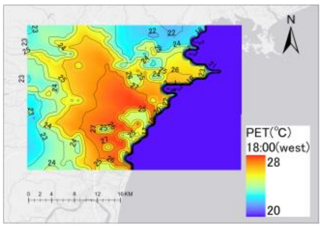
PET DIF	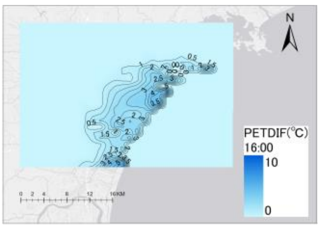	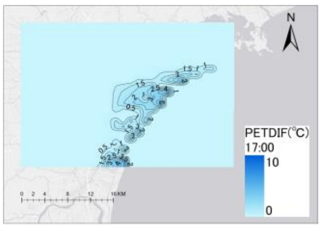	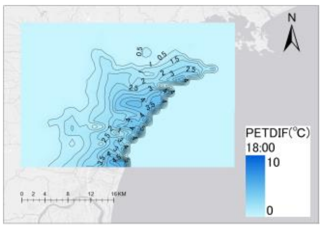

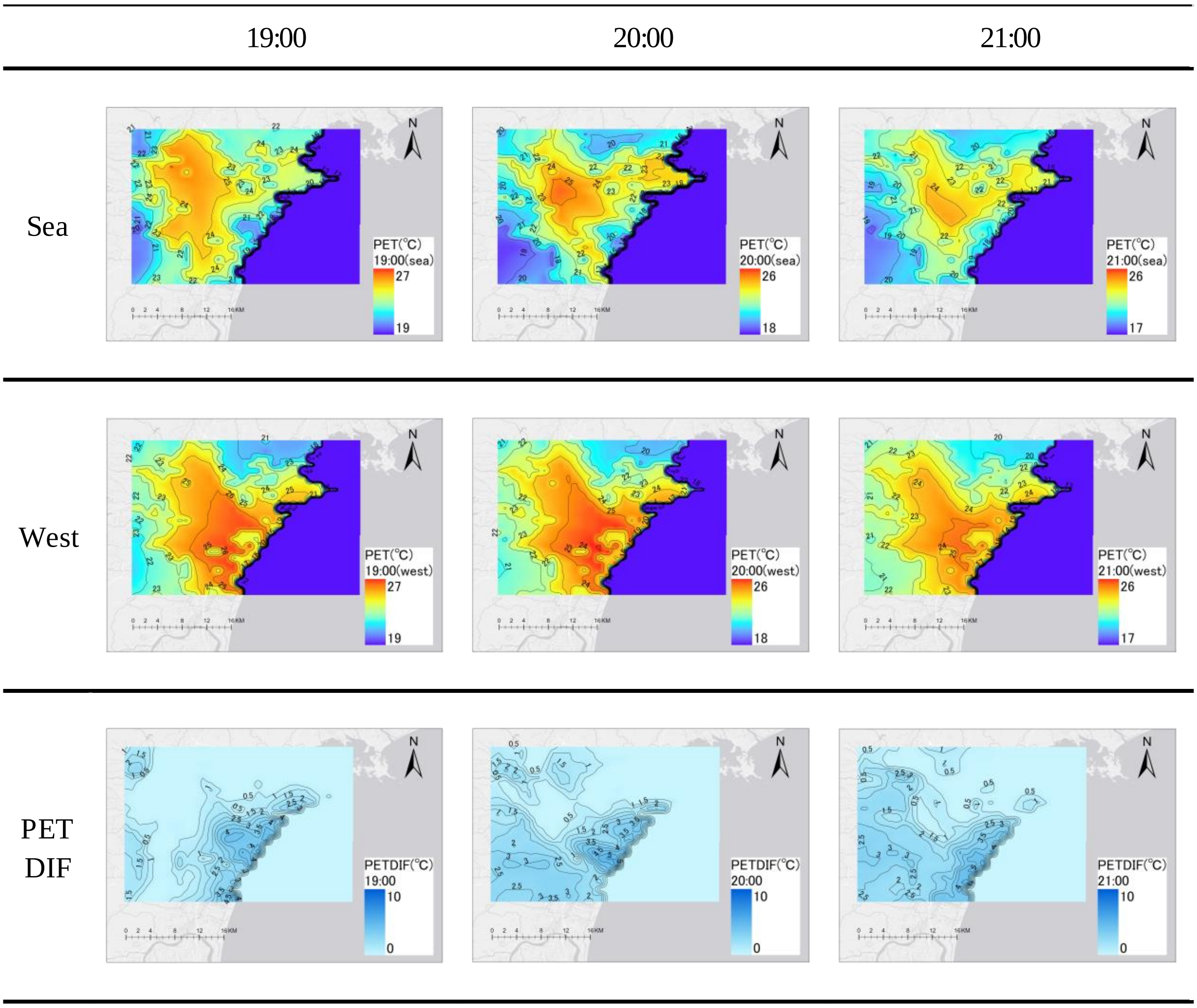

Fig. 6.22 *Map of PET DIF distribution on Sea Breeze Day and West Breeze Day*

Counting the sum of the positive PET DIF values at each moment, and the area of the distribution (Fig. 6.23), it can be observed that the sum and the area follow the same trend, starting to rise at 8:00 and starting to fall after reaching a peak at 14:00. Until 18:00 when it starts to rise once again.

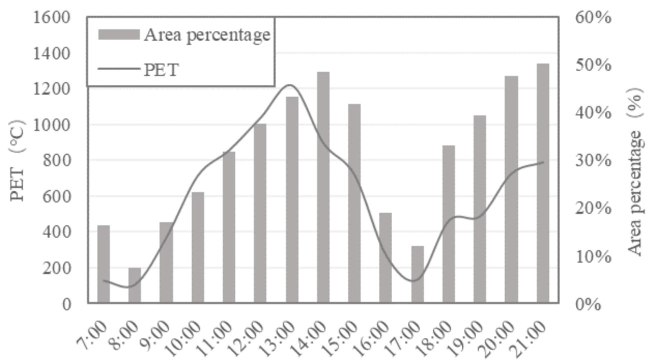

Fig. 6.23 *The ratio of the total PET DIF per moment value to the area producing positive PET DIF values.*

The average of the positive PET DIF values at each moment was then calculated to assess the change in the degree of comfort improvement on the sea breeze day compared to the west breeze day (Fig. 6.24). The average value continues to rise from 7:00 and remains at a higher level during the time interval from 10:00 to 13:00. After that it starts to decrease. The maximum mean value occurs at 10:00 with a mean value of 3.6°C.

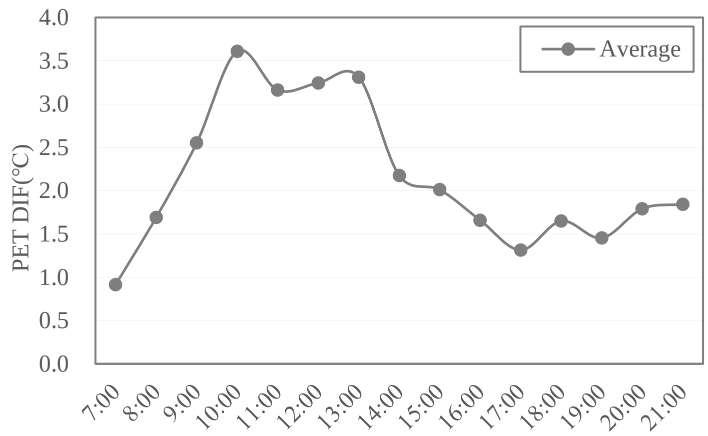

Fig. 6.24 *PET DIF mean value.*

SET* was analyzed in the same way, and according to Fig. 6.25/Fig. 6.26/Fig. 6.27, similar conclusions were drawn regarding PET. Among the mean values calculated for SET*, it was found that the SET* mean value has the same trend as the PET mean value, but is lower than the PET value. The maximum mean value also occurs at 10 points, but with a mean value of 2.2°C.

	7:00	8:00	9:00
Sea	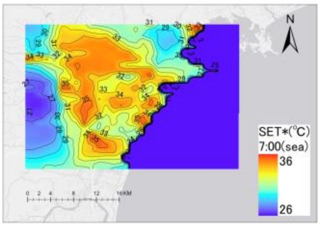	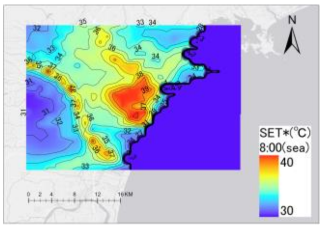	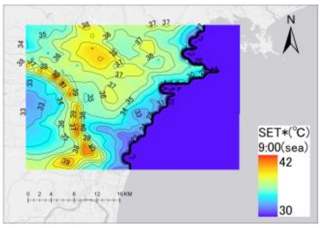
West	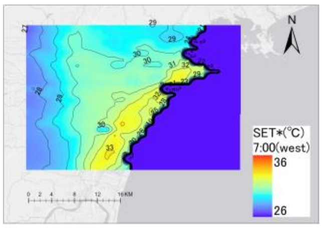	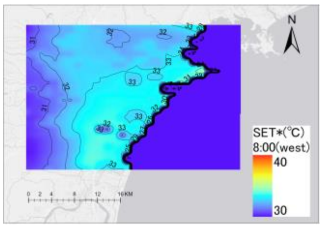	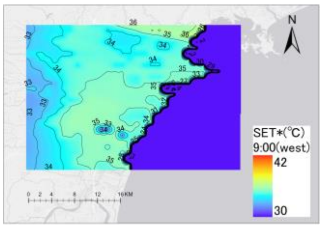
PET DIF	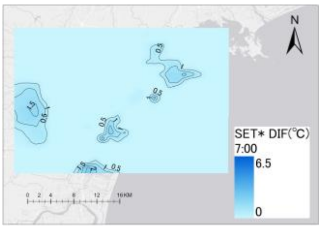	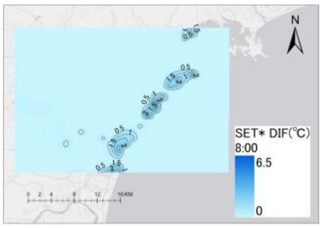	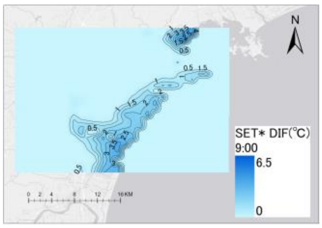
	10:00	11:00	12:00
Sea	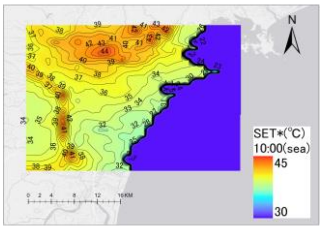	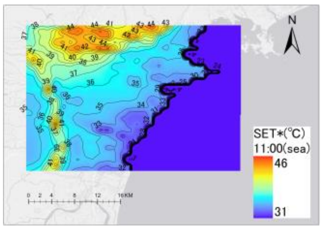	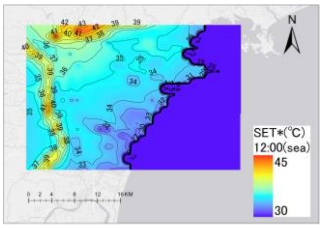
West	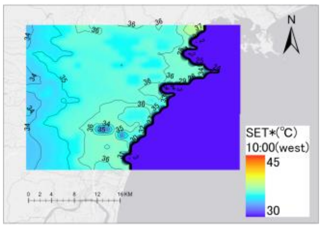	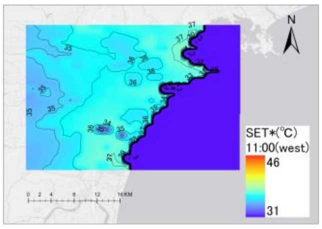	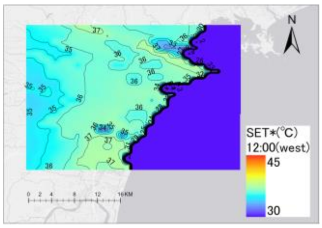
PET DIF	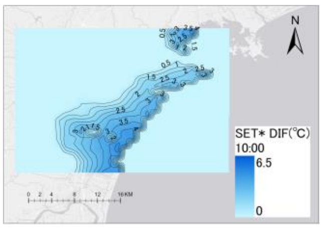	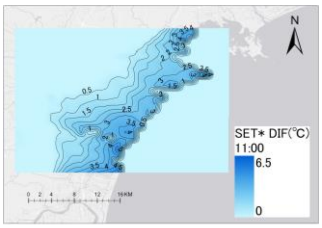	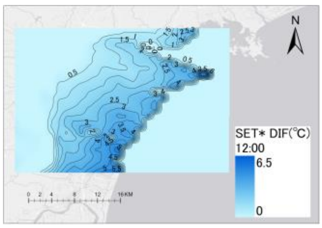

	13:00	14:00	15:00
Sea	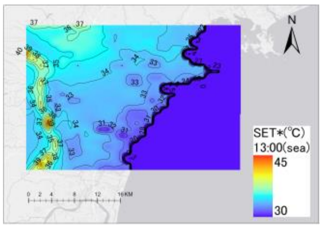	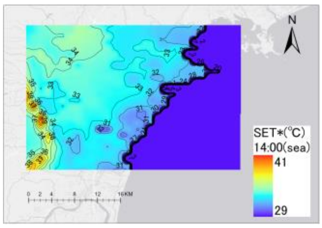	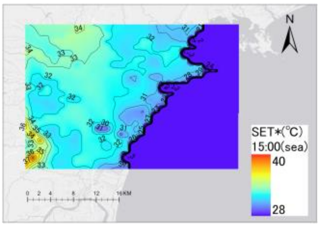
West	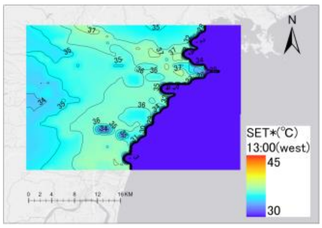	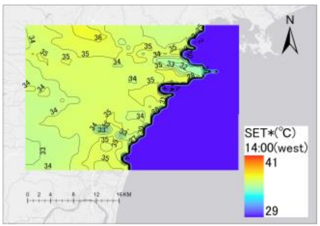	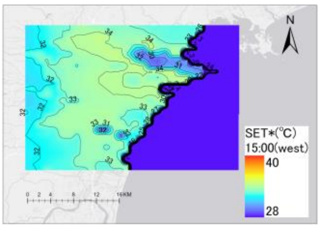
PET DIF	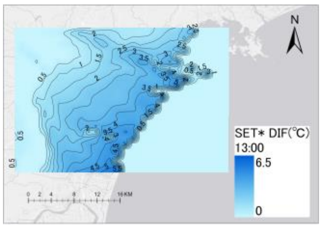	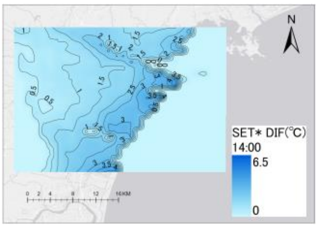	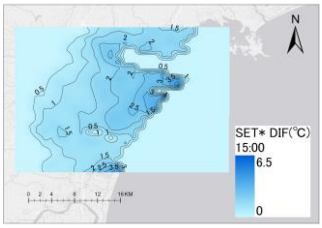
	16:00	17:00	18:00
Sea	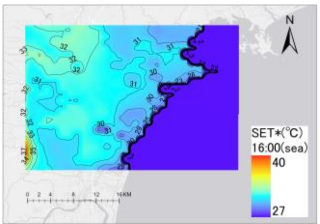	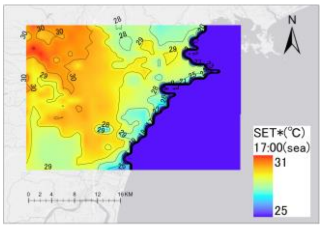	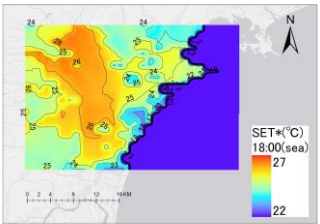
West	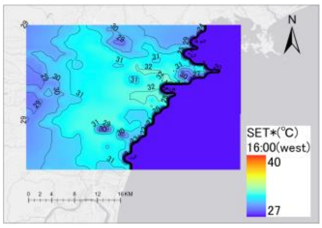	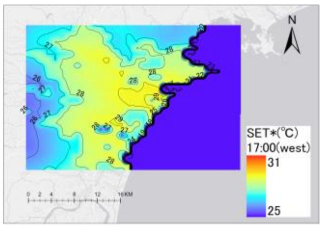	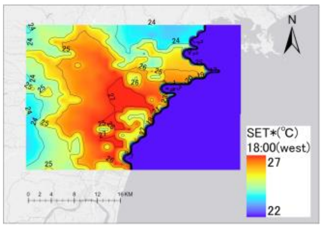
PET DIF	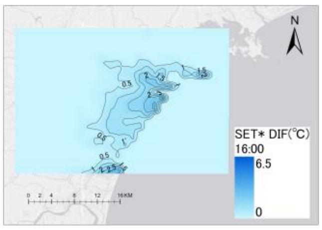	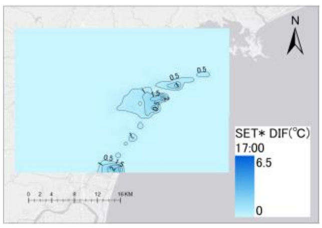	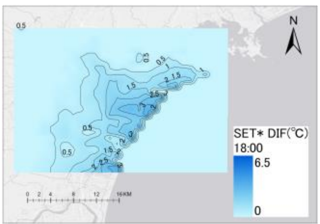

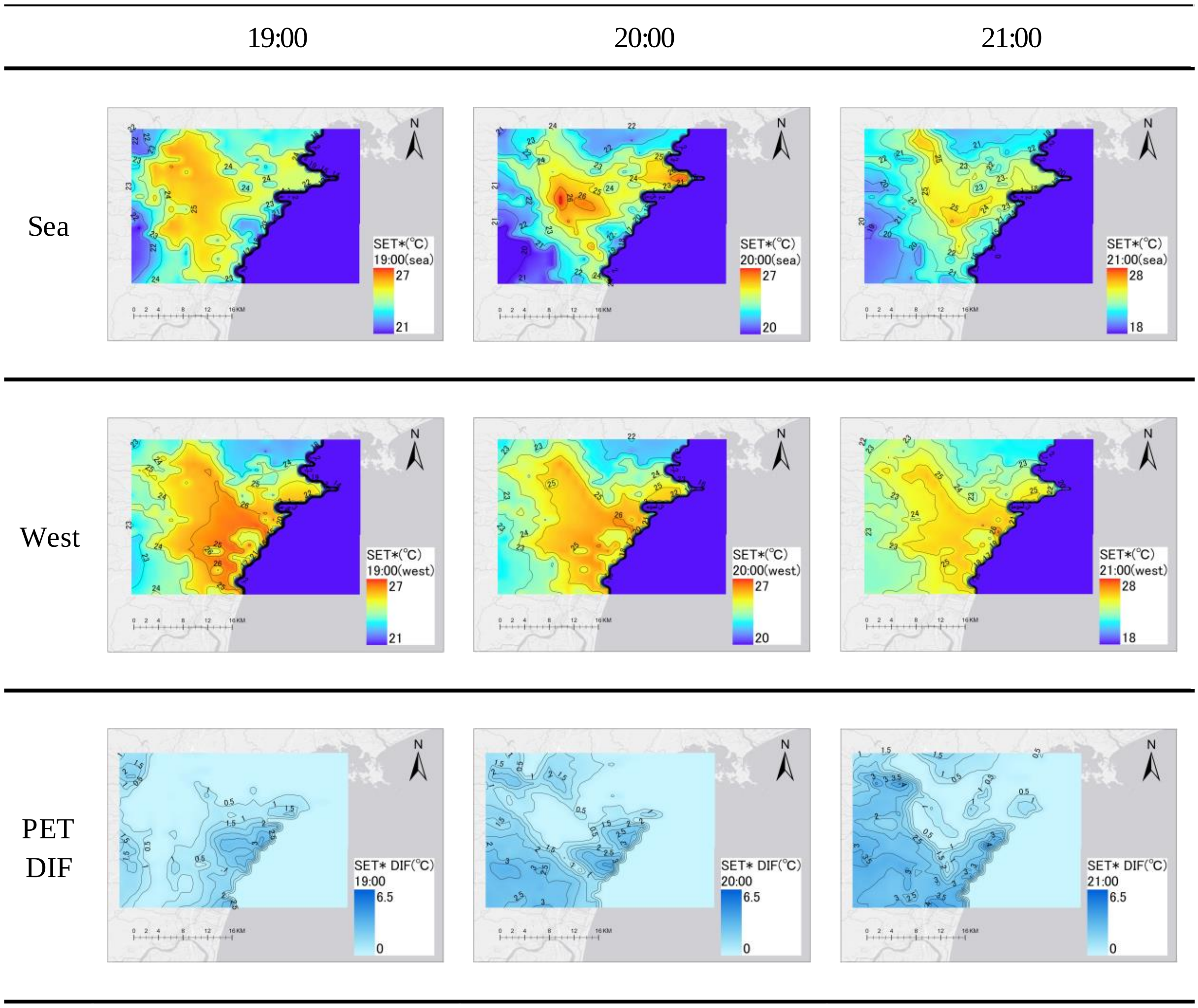

Fig. 6.25 *Map of PET DIF distribution on sea breeze day and west breeze Day.*

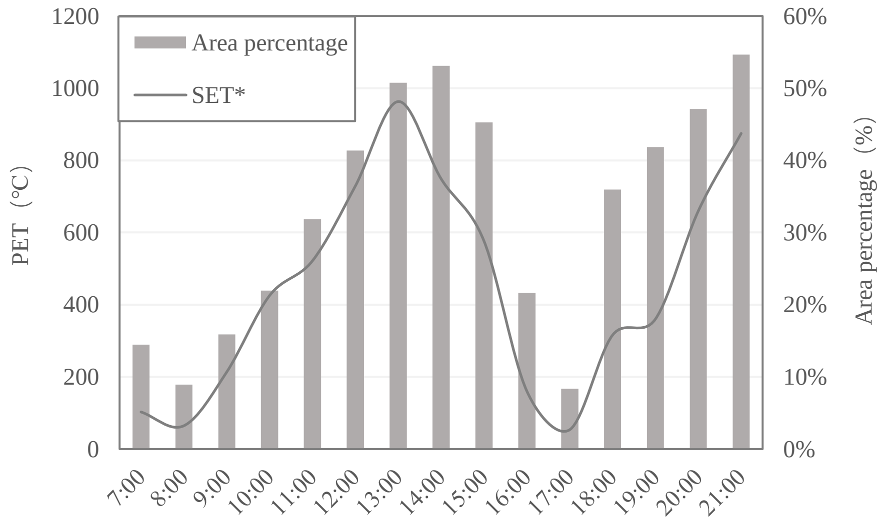

Fig. 6.26 *The ratio of the total SET* DIF per moment value to the area producing positive SET* DIF values.*

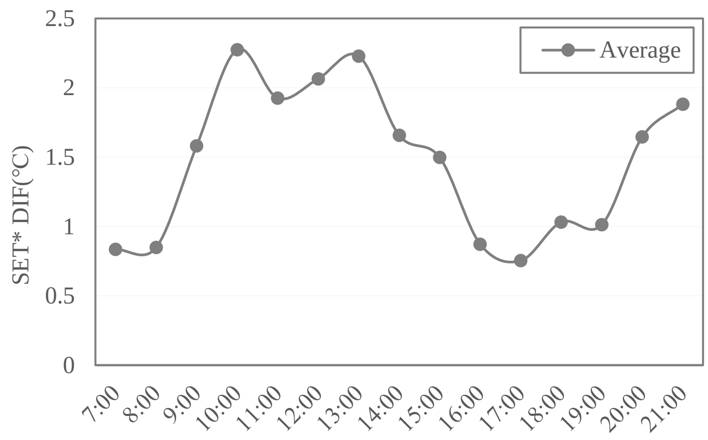

Fig. 6.27 S*ET* DIF mean value.*

In the previous analysis, it can be concluded that the improvement of thermal comfort in coastal cities by sea breeze day varies considerably from area to area. In the following, the mean values of PET DIF and SET* DIF per hour are analyzed for the entire area and inland area, urban area, and coastal area, respectively (Fig. 6.28).

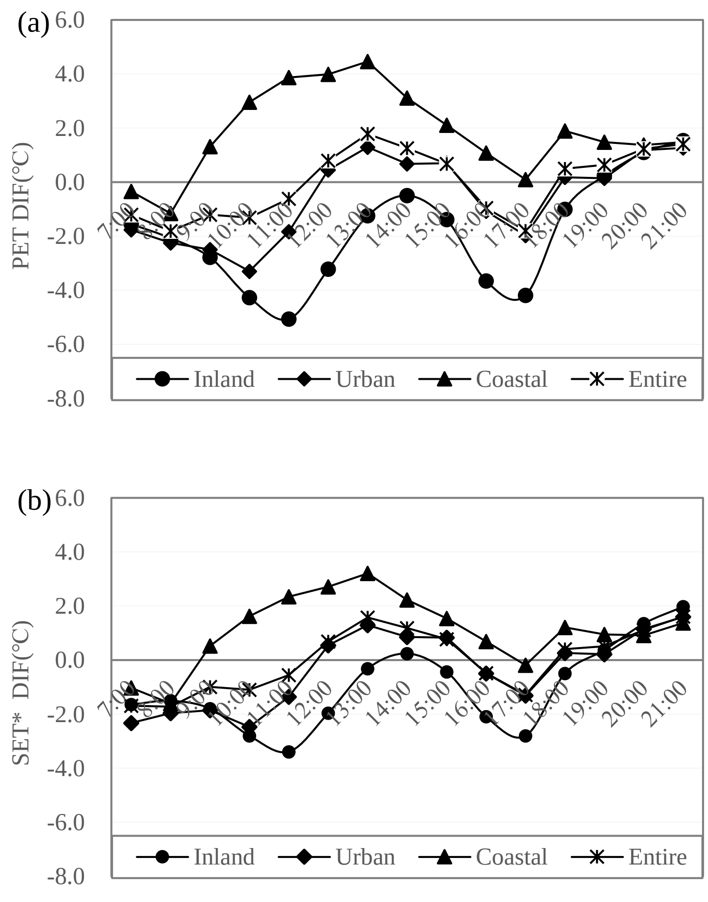

Fig. 6.28 *(a) Hourly average of PET DIF by area; (b) Hourly average of SET* DIF by area.*

The analysis shows that in each area, the PET DIF values have the same trend as the SET* DIF values, but the PET DIF values are larger and vary more strongly. And it is positive in the time interval from 19:00 to 21:00 in each area.

In Fig. 6.28(a), thermal comfort improvement is present throughout the area in the time interval between 12:00 and 15:00 and between 18:00 and 21:00. The maximum improvement occurs at 13:00 with a value of 1.8°C. In the inland area, except for the time interval from 19:00 to 21:00, there was no thermal comfort improvement and the PET DIF was negative. In urban areas, thermal comfort improvement was present in the time interval from 12:00 to 15:00 and from 18:00 to 21:00, with positive PET DIF values. The maximum improvement occurred at 13:00 with a value of 1.3°C. The improvement of thermal comfort was always present in the coastal area from 09:00 onwards and the improvement was large. The maximum improvement value appeared at point 13 with a value of 4.5°C.

In Fig. 6.28(b), thermal comfort improvement is present throughout the area in the time interval between 12:00 and 15:00 and between 18:00 and 21:00. The maximum improvement occurs at 13:00 with a value of 1.6°C. The inland area showed a weak thermal comfort improvement at 14:00 with a value of 0.2°C. The urban area showed thermal comfort improvement in the time interval between 12:00 and 15:00, and between 18:00 and 21:00, with a positive PET DIF value. The maximum improvement occurred at 13:00 with a value of 1.3°C. The improvement of thermal comfort was always present in the coastal area from 09:00 onwards and the improvement was large. The maximum improvement value appeared at point 13 with a value of 3.2°C.

6.5. Conclusion

(a) There are differences between sea breeze day and west breeze days in terms of underlying environmental factors. The basic environmental factors include temperature, radiation, wind speed and relative humidity:

In terms of temperature, the sea breeze day is overall lower than the west breeze day; the radiation values of the sea breeze are evenly distributed and have higher values, while the radiation values of the west breeze day are regional; in terms of wind speed, the wind speed values of the west breeze day are higher than the sea breeze day; the relative humidity is significantly higher on the west breeze day than on the sea breeze day before 17:00, and after that, the difference is small.

(b) On sea breeze day, there are large effects of wind direction and radiation values on outdoor thermal comfort; on west breeze day, there are large effects of temperature and relative humidity on outdoor thermal comfort.

During the time interval from 8:00 to 14:00 on sea breeze day, the higher radiation values in the western inland local area with the wind blowing from the western inland towards the eastern sea concentrated thermal discomfort in the area. In the northern part of the study area, the area not penetrated by the sea breeze also presented thermal discomfort. On a west breeze day, the higher the temperature presented, the lower the relative humidity presented the thermal discomfort phenomenon.

(c) On sea breeze days, the distribution of heat perception is territorial; on west breeze days, the distribution of heat perception is more similar in all regions.

On west breeze days, there was little difference in the distribution of thermal perception among the areas. On sea breeze days, the heat perception distribution of the areas went to establish at the time from 9:00 to 15:00 with a large difference. A higher distribution of thermal perception was presented in the inland area and a lower distribution of thermal perception was presented in the coastal area.

（d）Comfort is always lowest in urban areas on either sea or west breeze days, highest in coastal areas on sea breeze days, and highest inland on west breeze days.

In the area of thermal perception distribution, the sea breeze day presented a stronger thermal perception in the inland area with the urban area before 19:00, especially in the local area of the inland. After 19:00, the comfort level in the inland part starts to increase, the urban part presents a more intense thermal perception and the most comfortable thermal perception in the coastal area. Urban areas on west breeze day always presented a more intense thermal perception, with the most comfortable thermal perception in inland areas.

(e) On sea breeze days there are different degrees of outdoor thermal comfort improvement values in different areas, with the longest duration and strongest degree of improvement in the coastal area. At 13:00, the strongest improvement in outdoor thermal comfort was obtained.

Chapter 7. Conclusions and Future research topic

7.1. Conclusion

With accelerated urbanization, global warming and the urban heat island phenomenon. People are increasingly eager to have a comfortable living environment. This study aims to find ways to improve the comfort of the human living environment, using Sendai, Japan as the research target. After analyzing the reproducibility of the WRF model simulation data using long-term multi-point actual measurement data, the temporal characteristics of Sendai summer sea breeze events and sea breeze cooling capacity were visualized, and the temporal and spatial dynamics were analyzed. The main findings are summarized below.

Because the main source of data used for the analysis in this study is the mesoscale WRF model, the reproducibility of its simulated data was analyzed. In the reproducibility analysis of the WRF model data, it was concluded that there was a large correlation between the simulated and measured values at all points. Among the three areas, the urban area has the highest difference value. In the error dynamics analysis, the simulated values are always lower than the measured values in the rest of the area, except for the local time period in the inland area. During the day, higher errors always occur around the 10:00-12:00 time period. And among the three areas, the coastal area locally presents higher error values and the inland area has the lowest error values.

To better analyze the extent to which the sea breeze acts on coastal cities, its motion characteristics are first analyzed. According to the map of the temporal distribution of sea breeze events, the sea breeze blows landward at a slower rate in the coastal area and the rate increases with penetration inland. The arrival time of sea breeze is strongly influenced by inland rivers. From the map of sea breeze retreat time distribution, the direction of sea breeze retreat is related to the area of compact mid-rise and compact Low-rise and urban topography. The retreat of the sea breeze slows down significantly when it is close to highly urbanized areas. The sea breeze retreat speeds up until it is close to the coastal part. From the map of sea breeze duration distribution, the sea breeze duration is relatively evenly distributed in the area, and the sea breeze duration is the longest in the direction of sea breeze retreat.

During the day, the movement of the sea breeze toward land brings moist, cold air, which dampens the rise in temperature in coastal cities. This study defines the calculation of sea breeze cooling capacity. The results of the calculations were visualized using ArcGIS Pro to generate a map of sea breeze cooling capacity. The main conclusion drawn is that both the sea breeze cooling capacity and the cooling range show a rising and then decreasing trend, and reach a maximum at 10:00. It was also found that the distance of the action point from the coastline, the time of cooling effect occurrence, and inland rivers are important factors affecting the cooling capacity of sea breeze. The closer the action point is to the coastline, the greater the cooling capacity of the sea breeze. The positive impact of inland rivers on sea breeze cooling capacity. The area that produces the strongest cooling capacity per hour shows a strong negative correlation with the time of cooling effect onset and distance from the coast.

The sea breeze moves regularly over land and produces a cooling effect, but does it have an improvement on the comfort of people living on land? This study uses PET (Physiological Equivalent Temperature) values to respond to human heat stress levels and to describe human thermal comfort. On sea breeze day, there are large effects of wind direction and radiation values on outdoor thermal comfort; on west breeze day, there are large effects of temperature and relative humidity on outdoor thermal comfort. On sea breeze days, the distribution of heat perception is territorial; on west breeze days, the distribution of heat perception is more similar in all regions. Comfort is always lowest in urban areas on either sea or west breeze days, highest in coastal areas on sea breeze days, and highest inland on west breeze days. On sea breeze days there are different degrees of outdoor thermal comfort improvement values in different areas, with the longest duration and strongest degree of improvement in the coastal area. At 13:00, the strongest improvement in outdoor thermal comfort was obtained.

7.2. Future research topic

In the reproducibility analysis of the WRF model data, it was found that there was some error between the simulated and measured values. The error occurs mainly in the period around 10:00-12:00. Among the three areas, the coastal area locally presents higher error values. Because WRF can set a variety of boundary conditions, more boundary conditions can be tried in the future to make the error value as low as possible.

In the comfort analysis, the PET (Physiological Equivalent Temperature) value is used to respond to the human heat stress level and describe human thermal comfort. Coastal areas, urban areas, and inland areas all have their characteristics. In future studies, more in-depth research can be conducted by adding measurement data analysis as well as questionnaires after identifying the study sites based on the findings of existing studies. However, because of the low frequency of west breeze day in Sendai, there is a limitation in the selection of the date.

Reference

1. Parnell, S.; Walawege, R. Sub-Saharan African Urbanisation and Global Environmental Change. *Global Environmental Change* **2011**, *21*, S12–S20, doi:10.1016/j.gloenvcha.2011.09.014.

2. Kusaka, H.; Hara, M.; Takane, Y. Urban Climate Projection by the WRF Model at 3-Km Horizontal Grid Increment: Dynamical Downscaling and Predicting Heat Stress in the 2070's August for Tokyo, Osaka, and Nagoya Metropolises. *Journal of the Meteorological Society of Japan* **2012**, *90*, 47–63, doi:10.2151/jmsj.2012-B04.

3. Santamouris, M. Analyzing the Heat Island Magnitude and Characteristics in One Hundred Asian and Australian Cities and Regions. *Science of the Total Environment* **2015**, *512–513*, 582–598, doi:10.1016/j.scitotenv.2015.01.060.

4. Seino, N.; Aoyagi, T.; Tsuguti, H. Numerical Simulation of Urban Impact on Precipitation in Tokyo: How Does Urban Temperature Rise Affect Precipitation? *Urban Climate* **2018**, *23*, 8–35, doi:10.1016/j.uclim.2016.11.007.

5. Saitoh, T.S.; Shimada, T.; Hoshi, H. Modeling and Simulation of the Tokyo Urban Heat Island. *Atmospheric Environment* **1996**, *30*, 3431–3442, doi:10.1016/1352-2310(95)00489-0.

6. Wang, S.; Zhu, J. Amplified or Exaggerated Changes in Perceived Temperature Extremes under Global Warming. *Climate Dynamics* **2020**, *54*, 117–127, doi:10.1007/s00382-019-04994-9.

7. Georgescu, M.; Moustaoui, M.; Mahalov, A.; Dudhia, J. Summer-Time Climate Impacts of Projected Megapolitan Expansion in Arizona. *Nature Climate Change* **2013**, *3*, 37–41, doi:10.1038/nclimate1656.

8. Yamamoto, Y. Measures to Mitigate Urban Heat Islands. *Environmental and Energy research Unit. Quaterly Review* **2006**, *18*, 65–83.

9. Corburn, J. Cities, Climate Change and Urban Heat Island Mitigation: Localising

Global Environmental Science. *Urban Studies* **2009**, *46*, 413–427, doi:10.1177/0042098008099361.

10. *United-Nations, 2018. World Urbanization Prospects. Department of Economic and Social Affairs, United Nation, New York.*; 2018; Vol. 12; ISBN 9789211483192.

11. He, B.J. Potentials of Meteorological Characteristics and Synoptic Conditions to Mitigate Urban Heat Island Effects. *Urban Climate* **2018**, *24*, 26–33, doi:10.1016/j.uclim.2018.01.004.

12. Lopes, A.; Lopes, S.; Matzarakis, A.; Alcoforado, M.J. The Influence of the Summer Sea Breeze on Thermal Comfort in Funchal (Madeira). A Contribution to Tourism and Urban Planning. *Meteorologische Zeitschrift* **2011**, *20*, 553–564, doi:10.1127/0941-2948/2011/0248.

13. Kolokotsa, D.; Psomas, A.; Karapidakis, E. Urban Heat Island in Southern Europe: The Case Study of Hania, Crete. *Solar Energy* **2009**, *83*, 1871–1883, doi:10.1016/j.solener.2009.06.018.

14. Yun, G.Y.; Ngarambe, J.; Duhirwe, P.N.; Ulpiani, G.; Paolini, R.; Haddad, S.; Vasilakopoulou, K.; Santamouris, M. Predicting the Magnitude and the Characteristics of the Urban Heat Island in Coastal Cities in the Proximity of Desert Landforms. The Case of Sydney. *Science of the Total Environment* **2020**, *709*, 136068, doi:10.1016/j.scitotenv.2019.136068.

15. Miller, S.T.K.; Keim, B.D.; Talbot, R.W.; Mao, H. Sea Breeze: Structure, Forecasting, and Impacts. *Reviews of Geophysics* **2003**, *41*, doi:10.1029/2003RG000124.

16. Pokhrel, R.; Lee, H. 16 Estimation of the Effective Zone of Sea/Land Breeze in a Coastal Area. *Atmospheric Pollution Research* **2011**, *2*, 106–115, doi:10.5094/APR.2011.013.

17. Dandou, A.; Tombrou, M.; Soulakellis, N. The Influence of the City of Athens on the Evolution of the Sea-Breeze Front. *Boundary-Layer Meteorology* **2009**, *131*, 35–51, doi:10.1007/s10546-008-9306-x.

18. Shen, L.; Zhao, C.; Ma, Z.; Li, Z.; Li, J.; Wang, K. Observed Decrease of Summer Sea-Land Breeze in Shanghai from 1994 to 2014 and Its Association with Urbanization. *Atmospheric Research* **2019**, *227*, 198–209, doi:10.1016/j.atmosres.2019.05.007.

19. Bei, N.; Zhao, L.; Wu, J.; Li, X.; Feng, T.; Li, G. Impacts of Sea-Land and Mountain-Valley Circulations on the Air Pollution in Beijing-Tianjin-Hebei (BTH): A Case Study. *Environmental Pollution* **2018**, *234*, 429–438, doi:10.1016/j.envpol.2017.11.066.

20. Brooke Anderson, G.; Bell, M.L. Heat Waves in the United States: Mortality Risk during Heat Waves and Effect Modification by Heat Wave Characteristics in 43 U.S. Communities. *Environmental Health Perspectives* **2011**, *119*, 210–218, doi:10.1289/ehp.1002313.

21. Stewart, I.D.; Oke, T.R. Local Climate Zones for Urban Temperature Studies. *Bulletin of the American Meteorological Society* **2012**, *93*, 1879–1900, doi:10.1175/BAMS-D-11-00019.1.

22. Golden, J.S.; Hartz, D.; Brazel, A.; Luber, G.; Phelan, P. A Biometeorology Study of Climate and Heat-Related Morbidity in Phoenix from 2001 to 2006. *International Journal of Biometeorology* **2008**, *52*, 471–480, doi:10.1007/s00484-007-0142-3.

23. Guan, H.; Soebarto, V.; Bennett, J.; Clay, R.; Andrew, R.; Guo, Y.; Gharib, S.; Bellette, K. Response of Office Building Electricity Consumption to Urban Weather in Adelaide, South Australia. *Urban Climate* **2014**, *10*, 42–55, doi:10.1016/j.uclim.2014.09.005.

24. Gunawardena, K.R.; Wells, M.J.; Kershaw, T. Utilising Green and Bluespace to Mitigate Urban Heat Island Intensity. *Science of the Total Environment* **2017**, *584–585*, 1040–1055, doi:10.1016/j.scitotenv.2017.01.158.

25. He, B.J.; Zhu, J.; Zhao, D.X.; Gou, Z.H.; Qi, J. Da; Wang, J. Co-Benefits Approach: Opportunities for Implementing Sponge City and Urban Heat Island Mitigation. *Land Use Policy* **2019**, *86*, 147–157, doi:10.1016/j.landusepol.2019.05.003.

26. He, B.J. Towards the next Generation of Green Building for Urban Heat Island Mitigation: Zero UHI Impact Building. *Sustainable Cities and Society* **2019**, *50*, 101647, doi:10.1016/j.scs.2019.101647.

27. Qi, J. Da; He, B.J.; Wang, M.; Zhu, J.; Fu, W.C. Do Grey Infrastructures Always Elevate Urban Temperature? No, Utilizing Grey Infrastructures to Mitigate Urban Heat Island Effects. *Sustainable Cities and Society* **2019**, *46*, 101392, doi:10.1016/j.scs.2018.12.020.

28. Ding, L., He, B., Craft, W., & Petersen, H. Cooling Sydney Strategy - Planning for Sydney 2050. **2019**.

29. Park, H.S. Features of the Heat Island in Seoul and Its Surrounding Cities. *Atmospheric Environment (1967)* **1986**, *20*, 1859–1866, doi:10.1016/0004-6981(86)90326-4.

30. Kim, Y.H.; Baik, J.J. Daily Maximum Urban Heat Island Intensity in Large Cities of Korea. *Theoretical and Applied Climatology* **2004**, *79*, 151–164, doi:10.1007/s00704-004-0070-7.

31. Rajagopalan, P.; Lim, K.C.; Jamei, E. Urban Heat Island and Wind Flow Characteristics of a Tropical City. *Solar Energy* **2014**, *107*, 159–170, doi:10.1016/j.solener.2014.05.042.

32. Emmanuel, R.; Johansson, E. Influence of Urban Morphology and Sea Breeze on Hot Humid Microclimate: The Case of Colombo, Sri Lanka. *Climate Research* **2006**, *30*, 189–200, doi:10.3354/cr030189.

33. Masuda, Y.; Ikeda, N.; Seno, T.; Takahashi, N.; Ojima, T. A Basic Study on Utilization of the Cooling Effect of Sea Breeze in Waterfront Areas along Tokyo Bay. *Journal of Asian Architecture and Building Engineering* **2005**, *4*, 483–487, doi:10.3130/jaabe.4.483.

34. Archer, C.L.; Colle, B.A.; Delle Monache, L.; Dvorak, M.J.; Lundquist, J.; Bailey, B.H.; Beaucage, P.; Churchfield, M.J.; Fitch, A.C.; Kosovic, B.; et al. Meteorology for

Coastal/Offshore Wind Energy in the United States: Recommendations and Research Needs for the next 10 Years. *Bulletin of the American Meteorological Society* **2014**, *95*, 515–519, doi:10.1175/BAMS-D-13-00108.1.

35. Hu, X.M.; Xue, M. Influence of Synoptic Sea-Breeze Fronts on the Urban Heat Island Intensity in Dallas-Fort Worth, Texas. *Monthly Weather Review* **2016**, *144*, 1487–1507, doi:10.1175/MWR-D-15-0201.1.

36. David E.Kingsmill Convection Initiation Associated with a Sea-Breeze Front, a Gust Front, and Their Collision. *Meteorologische Zeitschrift* **1995**, *123*, 2913–2933, doi:https://doi.org/10.1175/1520-0493(1995)123<2913:CIAWAS>2.0.CO;2.

37. JUNIMURA and WATANABE Study on the Effects of Sea Breeze for Decreasing Urban Air Temperature in Summer: Analyses Based on Long-Term Multi-Point Mea-Surements and Observed Wind Conditions. *Journal of Environmental Engineering AIJ* **2008**, *73(623)*, 93–99, doi:https://doi.org/10.3130/aije.73.93.

38. Katayama, T.; Hayashi, T.; Shiotsuki, Y.; Kitayama, H.; Ishii, A.; Nishida, M.; Tsutsumi, J.I.; Oguro, M. Cooling Effects of a River and Sea Breeze on the Thermal Environment in a Built-up Area. *Energy and Buildings* **1991**, *16*, 973–978, doi:10.1016/0378-7788(91)90092-H.

39. Peng, S.; Kon, Y.; Watanabe, H. Effects of Sea Breeze on Urban Areas Using Computation Fluid Dynamic—A Case Study of the Range of Cooling and Humidity Effects in Sendai, Japan. *Sustainability (Switzerland)* **2022**, *14*, doi:10.3390/su14031074.

40. Powers, J.G.; Klemp, J.B.; Skamarock, W.C.; Davis, C.A.; Dudhia, J.; Gill, D.O.; Coen, J.L.; Gochis, D.J.; Ahmadov, R.; Peckham, S.E.; et al. The Weather Research and Forecasting Model: Overview, System Efforts, and Future Directions. *Bulletin of the American Meteorological Society* **2017**, *98*, 1717–1737, doi:10.1175/BAMS-D-15-00308.1.

41. William C.Skamarock, Joseph B.Klemp, Jimy Dudhia, David O.Gill, Dale M.Barker, Wei Wang, J.G.P. *A Description of the Advanced Research WRF Version 3.*;

2005; ISBN NCAR/TN–468+STR.

42. Miao, Y.; Liu, S.; Chen, B.; Zhang, B.; Wang, S.; Li, S. Simulating Urban Flow and Dispersion in Beijing by Coupling a CFD Model with the WRF Model. *Advances in Atmospheric Sciences* **2013**, *30*, 1663–1678, doi:10.1007/s00376-013-2234-9.

43. Zheng, Y.; Miao, Y.; Liu, S.; Chen, B.; Zheng, H.; Wang, S. Simulating Flow and Dispersion by Using WRF-CFD Coupled Model in a Built-up Area of Shenyang, China. *Advances in Meteorology* **2015**, *2015*, doi:10.1155/2015/528618.

44. Hong, S.Y.; Dudhia, J.; Chen, S.H. A Revised Approach to Ice Microphysical Processes for the Bulk Parameterization of Clouds and Precipitation. *Monthly Weather Review***2004**,*132*,103–120, doi:10.1175/1520-0493(2004)132<0103:ARATIM>2.0.CO;2.

45. Xie, B.; Fung, J.C.H.; Chan, A.; Lau, A. Evaluation of Nonlocal and Local Planetary Boundary Layer Schemes in the WRF Model. *Journal of Geophysical Research Atmospheres* **2012**, *117*, 1–26, doi:10.1029/2011JD017080.

46. Takebayashi, H.; Tanaka, T.; Moriyama, M.; Watanabe, H.; Miyazaki, H.; Kittaka, K. Relationship between City Size, Coastal Land Use, and Summer Daytime Air Temperature Rise with Distance from Coast. *Climate* **2018**, *6*, doi:10.3390/cli6040084.

47. Höppe, P. Different Aspects of Assessing Indoor and Outdoor Thermal Comfort. *Energy and Buildings* **2002**, *34*, 661–665, doi:10.1016/S0378-7788(02)00017-8.

48. Fang, Z.; Lin, Z.; Mak, C.M.; Niu, J.; Tse, K.T. Investigation into Sensitivities of Factors in Outdoor Thermal Comfort Indices. *Building and Environment* **2018**, *128*, 129–142, doi:10.1016/j.buildenv.2017.11.028.

49. Nikolopoulou, M.; Lykoudis, S. Thermal Comfort in Outdoor Urban Spaces: Analysis across Different European Countries. *Building and Environment* **2006**, *41*, 1455–1470, doi:10.1016/j.buildenv.2005.05.031.

50. MariaKolokotroni，RenganathanGiridharan Urban Heat Island Intensity in London: An Investigation of the Impact of Physical Characteristics on Changes in Outdoor Air Temperature during Summer. *Solar Energy* **2008**, *82*, 986–998,

doi:https://doi.org/10.1016/j.solener.2008.05.004.

51. Papanastasiou, D.K.; Melas, D.; Bartzanas, T.; Kittas, C. Temperature, Comfort and Pollution Levels during Heat Waves and the Role of Sea Breeze. *International Journal of Biometeorology* **2010**, *54*, 307–317, doi:10.1007/s00484-009-0281-9.

52. Zhu, M.; Atkinson, B.W. Observed and Modelled Climatology of the Land-Sea Breeze Circulation over the Persian Gulf. *International Journal of Climatology* **2004**, *24*, 883–905, doi:10.1002/joc.1045.

53. Bonnardot, V.; Planchon, O.; Cautenet, S. Sea Breeze Development under an Offshore Synoptic Wind in the South-Western Cape and Implications for the Stellenbosch Wine-Producing Area. *Theoretical and Applied Climatology* **2005**, *81*, 203–218, doi:10.1007/s00704-004-0087-y.

54. Lai, D.; Guo, D.; Hou, Y.; Lin, C.; Chen, Q. Studies of Outdoor Thermal Comfort in Northern China. *Building and Environment* **2014**, *77*, 110–118, doi:10.1016/j.buildenv.2014.03.026.

55. Liu, W.; Zhang, Y.; Deng, Q. The Effects of Urban Microclimate on Outdoor Thermal Sensation and Neutral Temperature in Hot-Summer and Cold-Winter Climate. *Energy and Buildings* **2016**, *128*, 190–197, doi:10.1016/j.enbuild.2016.06.086.

56. Nikolopoulou, M.; Steemers, K. Thermal Comfort and Psychological Adaptation as a Guide for Designing Urban Spaces. *Energy and Buildings* **2003**, *35*, 95–101, doi:10.1016/S0378-7788(02)00084-1.

57. Xu, M. The Influence of Alliance Innovation Network Structure upon Enterprise Innovation: A Case Study of China’s Energy-Saving and Environment-Protection Industry. *International Journal of Business and Management* **2018**, *13*, 208, doi:10.5539/ijbm.v13n2p208.

58. Xu, M.; Hong, B.; Jiang, R.; An, L.; Zhang, T. Outdoor Thermal Comfort of Shaded Spaces in an Urban Park in the Cold Region of China. *Building and Environment* **2019**, *155*, 408–420, doi:10.1016/j.buildenv.2019.03.049.

59. Yao, J.; Yang, F.; Zhuang, Z.; Shao, Y.; Yuan, P.F. The Effect of Personal and Microclimatic Variables on Outdoor Thermal Comfort: A Field Study in a Cold Season in Lujiazui CBD, Shanghai. *Sustainable Cities and Society* **2018**, *39*, 181–188, doi:10.1016/j.scs.2018.02.025.

60. Yang, R.; Zhang, H.; You, S.; Zheng, W.; Zheng, X.; Ye, T. Study on the Thermal Comfort Index of Solar Radiation Conditions in Winter. *Building and Environment* **2020**, *167*, 106456, doi:10.1016/j.buildenv.2019.106456.

61. Moon, J.H.; Lee, J.W.; Jeong, C.H.; Lee, S.H. Thermal Comfort Analysis in a Passenger Compartment Considering the Solar Radiation Effect. *International Journal of Thermal Sciences* **2016**, *107*, 77–88, doi:10.1016/j.ijthermalsci.2016.03.013.

62. Sharmin, T.; Steemers, K.; Humphreys, M. Outdoor Thermal Comfort and Summer PET Range: A Field Study in Tropical City Dhaka. *Energy and Buildings* **2019**, *198*, 149–159, doi:10.1016/j.enbuild.2019.05.064.

63. Johansson, E. Influence of Urban Geometry on Outdoor Thermal Comfort in a Hot Dry Climate: A Study in Fez, Morocco. *Building and Environment* **2006**, *41*, 1326–1338, doi:10.1016/j.buildenv.2005.05.022.

64. Oliveira, S.; Andrade, H.; Vaz, T. The Cooling Effect of Green Spaces as a Contribution to the Mitigation of Urban Heat: A Case Study in Lisbon. *Building and Environment* **2011**, *46*, 2186–2194, doi:10.1016/j.buildenv.2011.04.034.

65. Ng, E.; Chen, L.; Wang, Y.; Yuan, C. A Study on the Cooling Effects of Greening in a High-Density City: An Experience from Hong Kong. *Building and Environment* **2012**, *47*, 256–271, doi:10.1016/j.buildenv.2011.07.014.

66. Doulos, L.; Santamouris, M.; Livada, I. Passive Cooling of Outdoor Urban Spaces. The Role of Materials. *Solar Energy* **2004**, *77*, 231–249, doi:10.1016/j.solener.2004.04.005.

67. Carnielo, E.; Zinzi, M. Optical and Thermal Characterisation of Cool Asphalts to Mitigate Urban Temperatures and Building Cooling Demand. *Building and Environment*

2013, *60*, 56–65, doi:10.1016/j.buildenv.2012.11.004.

68. Strømann-Andersen, J.; Sattrup, P.A. The Urban Canyon and Building Energy Use: Urban Density versus Daylight and Passive Solar Gains. *Energy and Buildings* **2011**, *43*, 2011–2020, doi:10.1016/j.enbuild.2011.04.007.

69. Metje, N.; Sterling, M.; Baker, C.J. Pedestrian Comfort Using Clothing Values and Body Temperatures. *Journal of Wind Engineering and Industrial Aerodynamics* **2008**, *96*, 412–435, doi:10.1016/j.jweia.2008.01.003.

70. Kántor, N.; Égerházi, L.; Unger, J. Subjective Estimation of Thermal Environment in Recreational Urban Spaces-Part 1: Investigations in Szeged, Hungary. *International Journal of Biometeorology* **2012**, *56*, 1075–1088, doi:10.1007/s00484-012-0523-0.

71. Villadiego, K.; Velay-Dabat, M.A. Outdoor Thermal Comfort in a Hot and Humid Climate of Colombia: Afield Study in Barranquilla. *Building and Environment* **2014**, *75*, 142–152, doi:10.1016/j.buildenv.2014.01.017.

72. Xie, Y.; Liu, J.; Huang, T.; Li, J.; Niu, J.; Mak, C.M.; Lee, T. cheung Outdoor Thermal Sensation and Logistic Regression Analysis of Comfort Range of Meteorological Parameters in Hong Kong. *Building and Environment* **2019**, *155*, 175–186, doi:10.1016/j.buildenv.2019.03.035.

73. Chen, X.; Xue, P.; Liu, L.; Gao, L.; Liu, J. Outdoor Thermal Comfort and Adaptation in Severe Cold Area: A Longitudinal Survey in Harbin, China. *Building and Environment* **2018**, *143*, 548–560, doi:10.1016/j.buildenv.2018.07.041.

74. Memon, R.A.; Leung, D.Y.C.; Liu, C.H. Effects of Building Aspect Ratio and Wind Speed on Air Temperatures in Urban-like Street Canyons. *Building and Environment* **2010**, *45*, 176–188, doi:10.1016/j.buildenv.2009.05.015.

75. Xie, Y.; Huang, T.; Li, J.; Liu, J.; Niu, J.; Mak, C.M.; Lin, Z. Evaluation of a Multi-Nodal Thermal Regulation Model for Assessment of Outdoor Thermal Comfort: Sensitivity to Wind Speed and Solar Radiation. *Building and Environment* **2018**, *132*, 45–56, doi:10.1016/j.buildenv.2018.01.025.

76. P., H. The Physiological Equivalent Temperature - a Universal Index for the Biometeorological Assessment of the Thermal Environment. *International journal of biometeorology* **1999**, *43*, 71–75.

77. Ohlert, M.; Baruchel, J.; Galez, P. Applications of a Universal Thermal Index: Physiological Equivalent Temperature. *Journal of Physics D: Applied Physics* **1995**, *28*, A78–A83, doi:10.1088/0022-3727/28/4A/015.

78. Lin, T.P.; Matzarakis, A. Tourism Climate Information Based on Human Thermal Perception in Taiwan and Eastern China. *Tourism Management* **2011**, *32*, 492–500, doi:10.1016/j.tourman.2010.03.017.

79. Andrade, H.; Alcoforado, M.J. Microclimatic Variation of Thermal Comfort in a District of Lisbon (Telheiras) at Night. *Theoretical and Applied Climatology* **2008**, *92*, 225–237, doi:10.1007/s00704-007-0321-5.

80. Gulyás, Á.; Unger, J.; Matzarakis, A. Assessment of the Microclimatic and Human Comfort Conditions in a Complex Urban Environment: Modelling and Measurements. *Building and Environment* **2006**, *41*, 1713–1722, doi:10.1016/j.buildenv.2005.07.001.

81. Thorsson, S.; Lindqvist, M.; Lindqvist, S. Thermal Bioclimatic Conditions and Patterns of Behaviour in an Urban Park in Göteborg, Sweden. *International Journal of Biometeorology* **2004**, *48*, 149–156, doi:10.1007/s00484-003-0189-8.

82. Fang, Z.; Lin, Z.; Mak, C.M.; Niu, J.; Tse, K.T. Investigation into Sensitivities of Factors in Outdoor Thermal Comfort Indices. *Building and Environment* **2018**, *128*, 129–142, doi:10.1016/j.buildenv.2017.11.028.

83. Watanabe, S.; Nagano, K.; Ishii, J.; Horikoshi, T. Evaluation of Outdoor Thermal Comfort in Sunlight, Building Shade, and Pergola Shade during Summer in a Humid Subtropical Region. *Building and Environment* **2014**, *82*, 556–565, doi:10.1016/j.buildenv.2014.10.002.

84. Li, J.; Liu, N. The Perception, Optimization Strategies and Prospects of Outdoor Thermal Comfort in China: A Review. *Building and Environment* **2020**, *170*, 106614,

doi:10.1016/j.buildenv.2019.106614.

85. Stewart, I.D.; Oke, T.R. Local Climate Zones for Urban Temperature Studies. *Bulletin of the American Meteorological Society* **2012**, *93*, 1879–1900, doi:10.1175/BAMS-D-11-00019.1.

86. Sasaki, Y.; Matsuo, K.; Yokoyama, M.; Sasaki, M.; Tanaka, T.; Sadohara, S. 03 Sea Breeze Effect Mapping for Mitigating Summer Urban Warming: For Making Urban Environmental Climate Map of Yokohama and Its Surrounding Area. *Urban Climate* **2018**, *24*, 529–550, doi:10.1016/j.uclim.2017.07.003.

87. Bastin, S.; Drobinski, P. 01Temperature and Wind Velocity Oscillations along a Gentle Slope during Sea-Breeze Events. *Boundary-Layer Meteorology* **2005**, *114*, 573–594, doi:10.1007/s10546-004-1237-6.

88. Zhou, X.; Okaze, T.; Ren, C.; Cai, M.; Ishida, Y.; Watanabe, H.; Mochida, A. 50 Evaluation of Urban Heat Islands Using Local Climate Zones and the Influence of Sea-Land Breeze. *Sustainable Cities and Society* **2020**, *55*, 102060, doi:10.1016/j.scs.2020.102060.

89. Martilli, A. 02 A Two-Dimensional Numerical Study of the Impact of a City on Atmospheric Circulation and Pollutant Dispersion in a Coastal Environment. *Boundary-Layer Meteorology* **2003**, *108*, 91–119, doi:10.1023/A:1023044100064.

Acknowledgements

Most of all, I would like to express my deepest gratitude and respect to my supervisor Prof. Hironori WATANABE for his excellent guidance, advice, and encouragement throughout the whole duration of my Ph.D. research. I would like to thank Prof. Hironori WATANABE, Prof. Lei Xu, Prof. Koji KAGIYA, and Associate Prof. Hiroshi OISHI for reviewing my paper and providing valuable comments.

Gratitude is particularly to my research labmate Yusuke KON for his help in WRF simulations. I would like to thank USGS and NASA for providing free Landsat data. In addition, I would like to thank Prof. Xue, and Mr. Suzuki of the university for their help in my life. Obviously, their contributions, guidance, and encouragement were crucial to the completion of this study.

This study was funded by the JSPS KAKENHI grant (no. China National Scholarship Council (JP19K04734); 202008540002).

I would like to thank the Tohoku Institute of Technology for the tuition waiver. I would also like to express my sincere gratitude to all my friends and classmates at Tohoku Institute of Technology for your inspiring conversations and emotional support. In particular, I would like to thank my classmate, Aqing Chen, who has helped me a lot in my life and in my studies since the first day of my enrollment. Finally, I am very grateful to my husband Lei Qi, for his dedication and care, and to my parents for their unconditional support and encouragement.

Published Papers List

- **Journal Papers (2 items)**

[2022]

[1] Peng, Shiyi, Yusuke Kon, and Hironori Watanabe. "*Effects of Sea Breeze on Urban Areas Using Computation Fluid Dynamic—A Case Study of the Range of Cooling and Humidity Effects in Sendai, Japan.*" Sustainability 14.3 (2022): 1074.

[2] Peng, Shiyi, and Hironori Watanabe. "*Analysis and Mapping of Sea Breeze Event Time in Coastal Cities: A Case Study of Sendai*." Atmosphere 13.9 (2022): 1484.

- **Conference papers (1 item)**

[2022]

[1] Peng, Shiyi, and Hironori Watanabe. "*Reproducibility analysis of WRF model in urban climate research，A case study of Sendai.* "AIUE2022: 19th international conference of Asia Institute of urban environment)."Journal of Asian urban environment (2022)